



# University of Leicester

The Application of Surface Coatings for  
Low Wear and Low Friction Performance  
Between Valve-train Components

**By Simon. D. A. J. Lawes**

*A thesis submitted to the University of Leicester  
for the Degree of Doctor of Philosophy*

*Submitted May 2009*

“The pessimist sees the glass as half empty...

The optimist sees the glass as half full...

The engineer sees that the glass has been poorly optimised, and immediately starts looking around for funding.”

*Anonymous*

## Abstract

The UK produces >150 million tonnes of CO<sub>2</sub> annually, a large proportion of which comes from the transport sector. The UK looks to lead the way in CO<sub>2</sub> emission reduction, committing to an 80% reduction by 2050. Meeting this target is going to be a huge challenge for engineers in all sectors of industry, and improved component efficiency will have a large role to play.

This study has looked at the three novel friction and wear reduction techniques that may find application in the valve-train component of the automotive internal combustion engine. The aim of this study has been to establish the effectiveness of a range of: i) diamond-like carbon (DLC) coatings; ii) carbon nitride (CN<sub>x</sub>) coatings, and; iii) ionic liquid based lubricants, at reducing friction and wear in the valve-train. The main focus of this work has been the study of thin, wear resistant, and lubricious DLC coatings. A range of DLC coatings have been investigated to determine their performance in an instrumented valve-train test rig and compared to coating mechanical properties. Similar work has been conducted with CN<sub>x</sub> coatings, which are also thin, wear resistant and lubricious, whilst maintaining a lower hardness to elastic modulus ratio. It has been confirmed in this work that coating adhesion, hardness and abrasion resistance are key to coating durability in the valve-train along with the novel observation that impact toughness, particularly resistance to high angle inclined impact, is a very important factor in determining coating lifetimes.

Also work has also been done to investigate the lubrication properties of ionic liquids. These liquids have very different chemistry to traditional hydrocarbon based lubricants but have demonstrated values of friction coefficient similar to that of engine oil. The mechanism by which these liquids are retained in the contact and provide lubrication bears further investigation.

## Acknowledgements

**I would like to thank all those who have supported me throughout my Ph.D studies:**

The EPSRC for their funding of my work, making this experience possible.

Jaguar Land-Rover Ltd. for their co-sponsorship of this work and their support both financial and personal. I'd like to give particular thanks to Paul Blake of Jaguar Land-Rover for his continual interest and insight.

Dr. Dennis Teer, Sue Field and Wayne Southall, of Teer Coatings Ltd. for helpful discussions.

Dr. Jonathan Housden of TecVac Ltd.

The Royal Academy of Engineers for their financial support of my work and supporting my presentation at the ICMCTF 2008 in San Diego.

Prof. Michael Fitzpatrick and Ian Norman of the Open University for their collaboration, assistance and the use of their nanoindenter.

Dr. Andrej Furlan and Prof. Lars Hultman of the Thin Film Physics Division, Linköping University, for their collaboration on our carbon nitride coating research.

From the University of Leicester I would like to thank:

Dr. Karl Ryder and Prof. Andrew Abbott of the Department of Chemistry, for their collaboration on our ionic liquid research.

Prof. Helen Atkinson and Dr. Simon Gill for their support and guidance.

All of our experimental staff, in particular Paul Williams, Graham Clark and Barry Kirkland for their advice, assistance and for not complaining when they were bothered on their lunch breaks.

Tony Forryan has earned a special mention for his helpful advice, his interesting conversation and his unwavering preferential treatment.

Huge thanks have to go to my supervisor Prof. Sarah Hainsworth, for her encouragement, guidance and, towards the end, her goading.

Almost last but by no means least, my family; who've generously forgiven my poor attendance at family gatherings during the last few, busy, years.

... and of course Carla, for her unending belief that one day it'll all be over and we can finally relax.

## Publications

1. S D A Lawes, S V Hainsworth, M E Fitzpatrick, Evaluation of The Tribological Properties of DLC for Engine Applications 2007 *J. Phys. D: Appl. Phys.* 40 5427-5437
2. S D A Lawes, S V Hainsworth, The Relevance of High-angle Inclined Impact Testing of DLC for Engine Valve-train Applications. Tribology 2008 (IMEchE) proceedings, (submitted to *Wear*, under review)
3. S D A Lawes, S V Hainsworth, P Blake, K Ryder, A Abbott, Lubrication of steel/steel contacts by choline chloride ionic liquids, 2009 Tribology Letters, DOI 10.1007/s11249-009-9495-6.
4. S D A Lawes, A Furlan, L Hultman, S V Hainsworth, Evaluation of The Tribological Properties of Carbon Nitride Coatings for Engine Applications (in preparation)
5. S D A Lawes, S V Hainsworth, M E Fitzpatrick, Mechanical and Tribological Properties of DLC Coatings and Automotive Engine Application Performance: A Comparison, (in preparation)

## Presentations

1. Tribology 2008 (IMEchE): Surface Engineering of Automotive Powertrains for Environmentally Friendly Transport
2. International Conference on Metallurgical Coating and Thin Films 2008, San Diego
3. Institute of Materials, Minerals and Mining - Young person's lecture competition 2009 - East-Midlands regional heats and UK final

## Nomenclature

$\alpha$	-	Camshaft angle (cam-tappet calculations)
$\beta$	-	Angle to point of camshaft (cam-tappet calculations)
E	-	Eccentricity
L	-	Cam lift
D	-	Tappet displacement
F	-	Combined force
T	-	Torque
$f_n$	-	Natural frequency
K	-	Stiffness
I	-	Moment of inertia
DLC	-	Diamond-like carbon
CN <sub>x</sub>	-	Carbon nitride
a-C	-	amorphous carbon
ta-C	-	tetrahedral amorphous carbon
a-C:H	-	Hydrogenated amorphous carbon
a-C:Me	-	Metal doped amorphous carbon
a-C:F	-	Flourine doped amorphous carbon
a-C:Si	-	Silicon doped amorphous carbon
L <sub>c</sub>	-	Scratch-adhesion critical load
S	-	Unloading stiffness (hardness)
P	-	Load
H	-	Displacement
E <sub>r</sub>	-	Reduced modulus
A <sub>r</sub>	-	Projected contact area
k	-	A constant
H	-	Hardness
H <sub>c</sub>	-	Combined hardness
H <sub>s</sub>	-	Substrate hardness
H <sub>f</sub>	-	Film hardness
$\beta$	-	Relative indentation depth (hardness)
t	-	Film thickness
a	-	Wear scar diameter
R	-	Radius of counterface

$V_c$	-	Volume loss, coating
$V_s$	-	Volume loss, substrate
$S$	-	Sliding distance (microabrasion)
$N$	-	Load (microabrasion)
$k_c$	-	Specific wear rate, coating
$k_s$	-	Specific wear rate, substrate
$I(D)$	-	Intensity of disorder peak
$I(G)$	-	Intensity of graphite peak
$m$	-	Gradient of photo-luminescent background
$R_a$	-	Surface roughness parameter, arithmetic mean of surface amplitude
DGnd	-	Directionally ground finish, produced by grinding wheel, uni-axial
Pol	-	Polished surface finish, produced by 6 $\mu$ m diamond solution
Gnd	-	Ground surface finish, produced by #800 SiC grit
$\alpha$	-	Angle from horizontal (inclined contact force calculations)
$P_{\text{applied}}$	-	Applied load
$P_{\text{norm}}$	-	Normal load
$P_{\text{tang}}$	-	Tangential load
$\mu$	-	Friction coefficient
$a$	-	Contact width (inclined contact force calculations)
$E^*$	-	Combined stylus and sample stiffness
$P_{\text{max}}$	-	Maximum contact force
$P(x)$	-	Contact load distribution
$x$	-	Position in contact

# Contents

<b><u>Foreword</u></b>	<b>i</b>	
<b><u>Abstract</u></b>	<b>ii</b>	
<b><u>Acknowledgements</u></b>	<b>iii</b>	
<b><u>Publications</u></b>	<b>iv</b>	
<b><u>Nomenclature</u></b>	<b>v</b>	
<b>1</b>	<b><u>Introduction – Environmentally responsible automobiles and engine tribology</u></b>	<b>1</b>
1.1	Environmental responsibility	1
1.2	Engine tribology	4
1.3	Thesis structure	5
1.4	Chapter references	8
<b>2</b>	<b><u>Valve-train and the cam-tappet test rig</u></b>	<b>10</b>
2.1	The automotive valve-train	10
2.2	Tribology of the cam-tappet contact in DOHC systems	12
2.3	The cam-tappet test rig	15
2.3.1	<i>Determining friction coefficient – modelling forces</i>	17
2.3.2	<i>Signal noise</i>	21
2.3.2.1	Initial findings	22
2.3.2.2	Investigating the source of the noise	24
2.3.3	<i>Data filtration</i>	32
2.4	Chapter references	34
<b>3</b>	<b><u>Carbon based coatings – Common properties and deposition processes</u></b>	<b>35</b>
3.1	<b>Properties of carbon based coatings</b>	<b>35</b>
3.1.1	<i>The role of electron bond hybridisation</i>	36
3.1.2	<i>The role of coating interlayers</i>	36
3.1.3	<i>The role of alloying elements</i>	38
3.1.3.1	The effect of hydrogen content	39
3.1.3.2	The effect of silicon and fluorine content	39
3.1.3.3	The effect of metal content	39
3.1.4	<i>Frictional properties</i>	40
3.1.4.1	Friction and wear – The role of hydrogen and the environment	40
3.1.4.2	Friction and wear – The role of localised graphitisation	41
3.1.4.3	Friction and wear – The role of transfer layer formation	42
3.1.4.4	Friction and wear – Interaction with oil based lubricants	43
3.2	<b>Deposition processes</b>	<b>43</b>
3.2.1	<i>Physical vapour deposition (PVD)</i>	44
3.2.1.1	Sputtering	45
3.2.1.2	Ion beam deposition	47
3.2.1.3	Cathodic vacuum arc	48
3.2.1.4	Pulsed laser deposition	49
3.2.2	<i>Chemical vapour deposition (CVD)</i>	50
3.2.2.1	Plasma enhanced chemical vapour deposition	51
3.3	Chapter references	52

<b>4</b>	<b><u>Experimental techniques and methodology</u></b>	<b>59</b>
4.1	Cam-tappet test rig	59
4.2	Adhesion	60
4.3	Hardness and modulus	62
4.4	Wear	64
4.4.1	<i>Abrasive wear</i>	64
4.4.2	<i>Sliding wear</i>	66
4.3	Impact wear resistance	67
4.4	Chapter references	69
<b>5</b>	<b><u>Microscopy, spectroscopy and spectrometry</u></b>	<b>71</b>
5.1	Microscopy and spectroscopy	71
5.1.1	<i>Optical microscopy</i>	71
5.1.2	<i>Scanning electron microscopy</i>	72
5.1.3	<i>Scanning probe microscopy</i>	74
5.2	Spectrometry	75
5.3	Chapter references	77
<b>6</b>	<b><u>Diamond-like Carbon</u></b>	<b>78</b>
6.1	History of development	79
6.2	Properties of DLC coatings	79
6.3	Valve-train study	81
6.3.1	<i>Coating selection – considerations</i>	81
6.3.2	<i>Study structure</i>	82
6.3.3	<i>Results</i>	84
6.3.3.1	Raman spectroscopy	84
6.3.3.2	Atomic force microscopy	87
6.3.3.3	Coating thickness measurement	88
6.3.3.4	Valve-train testing	89
6.3.3.5	Nanoindentation testing	97
6.3.3.6	Scratch-adhesion testing	99
6.3.3.7	Micro-abrasion testing	102
6.3.3.8	Reciprocating sliding wear	104
6.3.3.9	Micro-impact testing and simulation	106
6.3.4	<i>Collected results, comparison and discussion</i>	110
6.3.4.1	Valve-train performance, key coating properties	111
6.3.4.2	Role of impact	113
6.3.4.3	Role of surface finish	118
6.3.5	<i>Conclusions</i>	118
6.4	Future work	119
6.5	Chapter references	121
<b>7</b>	<b><u>Carbon nitride coatings</u></b>	<b>125</b>
7.1	CN <sub>x</sub> coatings - History of development and properties	126
7.2	Importance of hardness and elasticity in wear	128
7.3	Valve-train study	129
7.3.1	<i>Coating selection</i>	129
7.3.2	<i>Testing</i>	132
7.3.2.1	Valve-train testing	132

7.3.2.2	Mechanical and tribological testing	133
7.3.3	<i>Results</i>	134
7.3.3.1	Valve-train testing	134
7.3.3.2	Nanoindentation testing – H/E	135
7.3.3.3	Scratch-adhesion testing	138
7.3.3.4	Reciprocating sliding wear	139
7.3.4	<i>Discussion</i>	142
7.3.5	<i>Conclusions</i>	143
7.4	<b>Future work</b>	143
7.5	<b>Chapter references</b>	145
<b>8</b>	<b><u>Ionic liquid lubrication</u></b>	147
8.1	<b>Ionic liquids – development and properties</b>	147
8.2	<b>Lubrication feasibility study</b>	149
8.2.1	<i>Ionic liquid formation</i>	149
8.2.2	<i>Lubrication- test procedure</i>	150
8.2.3	<i>Lubrication - initial observations</i>	151
8.2.4	<i>Surface texturing</i>	153
8.2.5	<i>Wettability</i>	155
8.2.5	<i>Results and discussion</i>	156
8.3	<b>Conclusions and future work</b>	160
8.4	<b>Chapter references</b>	162
<b>9</b>	<b><u>Conclusions</u></b>	164
9.1	<b>In Summary</b>	164
9.2	<b>Findings and implications</b>	165
9.3	<b>Future work</b>	167

# CHAPTER 1

## Introduction

---

### **1. Introduction – Environmentally responsible automobiles and engine tribology**

#### **1.1 Environmental responsibility**

#### **1.2 Engine tribology**

#### **1.3 Thesis structure**

#### **1.4 Chapter references**

---

#### 1.1 Environmental responsibility

Since the beginning of industrialisation, human activity has been introducing high quantities of greenhouse gases into the atmosphere. Greenhouse gases absorb infrared radiation and cause heat to be retained within the Earth's atmosphere. The increasing amount of retained heat is accelerating climate changes, which are believed to be causing changes in sea level, increase in extreme weather conditions, harm to crop yields and damage to animal habitats. This is a major global concern and 182 nations, including the UK, have ratified the Kyoto protocol [1, 2], committing themselves to an international framework for the reduction of greenhouse gas emission. There are a number of gases that contribute towards the greenhouse effect: nitrous oxides (NO<sub>x</sub>), methane (CH<sub>4</sub>), carbon dioxide (CO<sub>2</sub>), ozone (O<sub>3</sub>) and chlorofluorocarbons (CFCs). NO<sub>x</sub> is the most potent absorber of infrared radiation, ~300 times more potent than CO<sub>2</sub>, methane next at ~21 times but these are present in much smaller quantities and CO<sub>2</sub> is the primary contributor to global warming. The Stern Review [3] published by the UK government in 2006 indicated that in order to stabilise CO<sub>2</sub> in the atmosphere below a level where the worst effects of climate change are avoided, a global reduction in CO<sub>2</sub> output of 25% (relative to 1990 levels) by 2050 would be required.

There are many human activities that have large scale greenhouse gas contributions, (see figure 1.1). The use of fossil fuels for generating power and providing transport are some of the largest contributors to CO<sub>2</sub> emission, with transport accounting for ~14% of the global output of CO<sub>2</sub>. This contribution is set to grow with the economic development of countries such as India and China. As these countries become more industrialised, the bulk transport infrastructure will grow and as the per capita income increases a higher proportion of the rapidly growing populations will be looking to purchase personal transport. This will lead to large emerging markets and equally large CO<sub>2</sub> contribution. Transport sector growth is not limited to developing countries. Over the past 20 years, the transport sector in Europe has grown steadily. Unlike many other emission contributing processes, such as agriculture and industry, the improvements in transport efficiency and emission reduction technologies have not been able to keep pace with sector growth (see figure 1.2). Transport in the EU contributes ~25% more harmful emissions now than it did in 1990 [4] and growth is predicted to continue [5]. The primary contribution within the transport sector is personal and passenger transport in the form of cars and vans and with a small contribution from motorcycles (see figure 1.3).

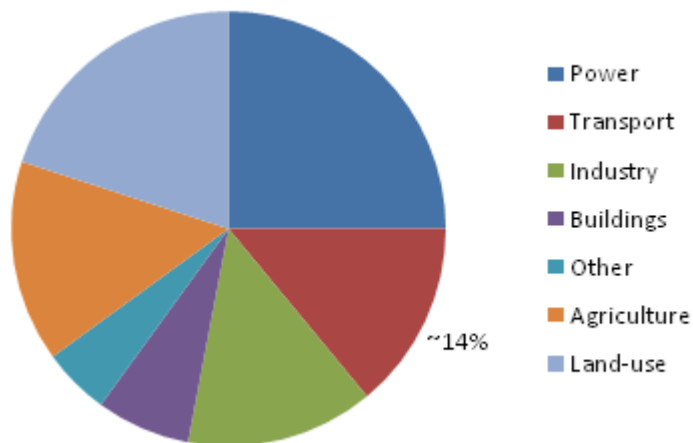


Figure 1.1 - Global sectoral greenhouse gas contribution in 2000. Emissions from power, transport and industry largely CO<sub>2</sub>. Source WRI 2006 [6]

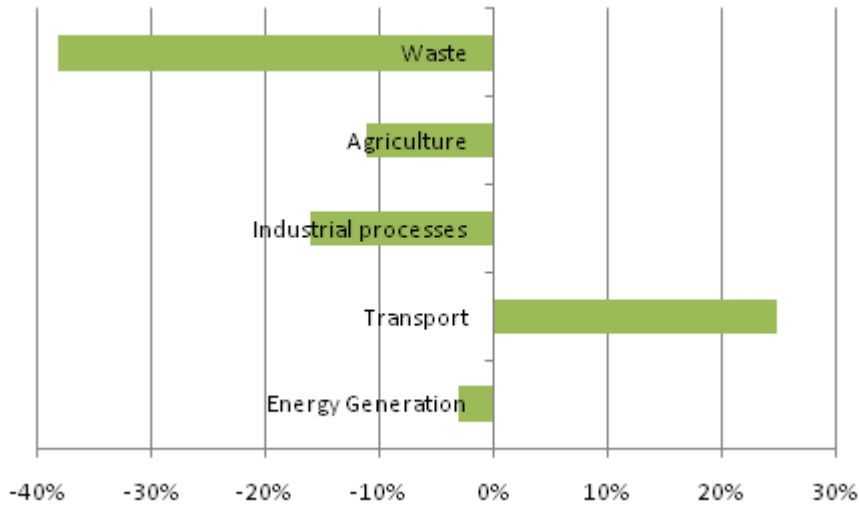


Figure 1.2 - EU greenhouse gas emissions growth 1990-2005. Source EEA 2006 [7]

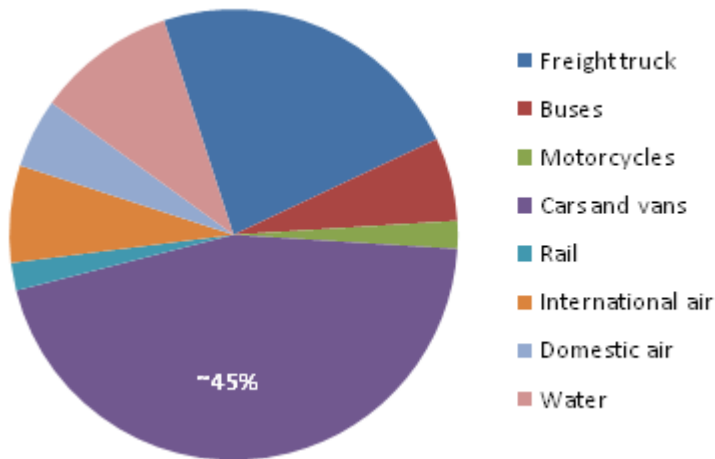


Figure 1.3 - Global transport CO<sub>2</sub> emission by mode in 2000. Source WBCSD 2004 [8]

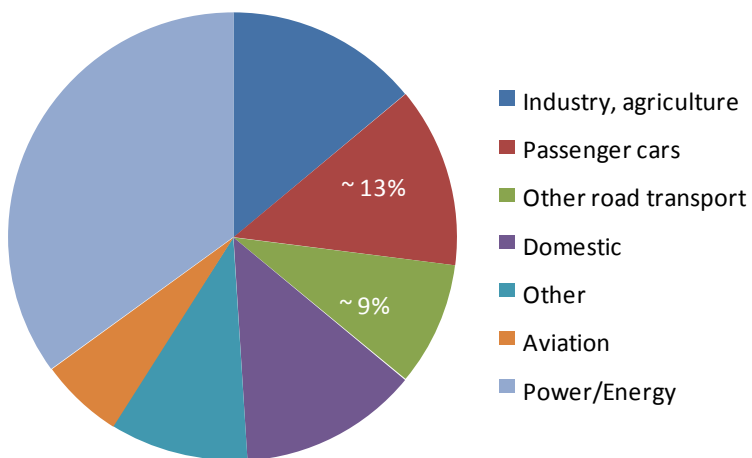


Figure 1.4 - Contributions to UK CO<sub>2</sub> emissions by sector in 2005. Source King Review, compiled from AEA/DEFRA [9]

Within the UK, the contributions to CO<sub>2</sub> emission by sector reflect those seen globally (see figure 1.4). The CO<sub>2</sub> emissions of developed countries such as the UK are unlikely to be the greatest threat to sustainability in the next forty years. However developed countries can make a great difference to future global emissions by the development of low emission technologies and leading by example. The Stern Review suggests that the UK aim for a 60-80% reduction in CO<sub>2</sub> emission by 2050 (relative to 1990 levels). If the UK is to reach the 60% reduction in CO<sub>2</sub> there is a very strong need to reduce the CO<sub>2</sub> output from passenger vehicles. The research in this thesis looks at reducing the energy losses to friction in the internal combustion engine as a way of improving fuel efficiency of vehicles and reducing their CO<sub>2</sub> contribution.

## 1.2 Engine tribology

There exist a number of studies of automotive energy losses by government funded reviews and independent research. Surveys of European vehicles have shown that only ~12% of the available power in the fuel is transferred to the wheels. Figures 1.5 and 1.6 show two example breakdowns of the vehicle losses [10, 11]. These studies indicate that the major losses are thermodynamic, ejecting heat by cooling to maintain operating conditions, and heat lost in the exhaust gases. The second greatest contribution is from mechanical losses in the power-train, divided roughly equally between engine losses and transmission losses.

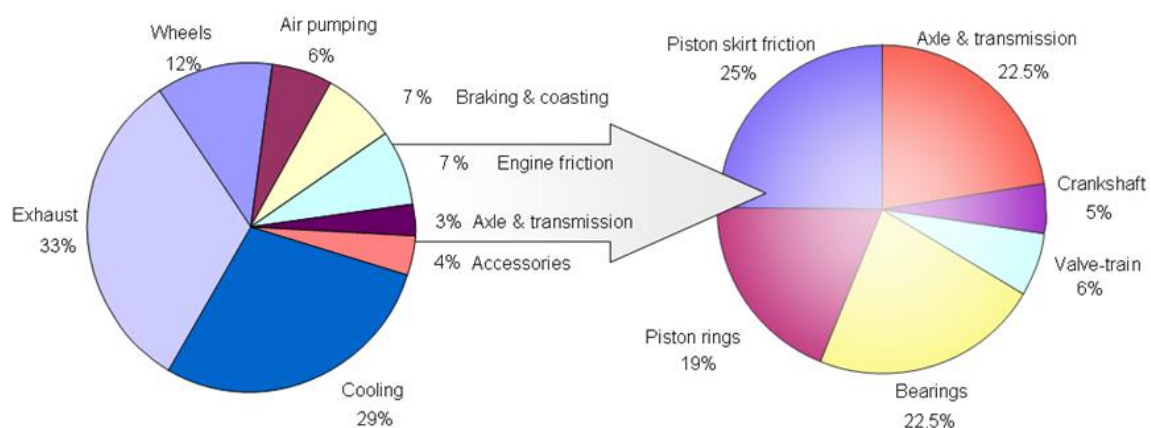


Figure 1.5 – Charts of typical energy losses from a light utility vehicle and detail of engine losses due to friction. Source [10].

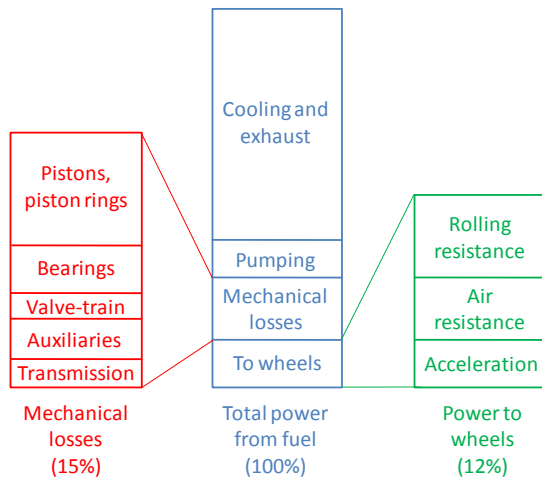


Figure 1.6 – Breakdown of energy losses in Volvo city driving test. [11]

Improvement of energy use in the vehicles engine is therefore critical for improving efficiency and reducing CO<sub>2</sub> emission. Typical approaches to improve efficiency include: the reduction of component mass by redesign and the use of lightweight materials; increase in the engine running temperature with less heat extraction; and the use of lower viscosity oils with friction modifying additives. These changes can all contribute towards a harsher environment for engine components. For example, higher operating temperatures or the use of lower viscosity oils can reduce oil film thickness and can increase wear rates. A common approach to wear management is the introduction of wear reducing additives to the oil package. However concern has emerged that some of these additives, such as zinc dialkyl dithio phosphate (ZDDP), have a damaging effect on the catalytic converter, and over time the catalytic converter becomes less effective and pollutant release increases. As pollution legislation becomes ever stricter, an alternative wear and friction reducing technology is needed.

### 1.3 Thesis structure

#### **The principle aim of this research is to:**

*“Investigate solutions to provide low-friction, low-wear contact conditions in the automotive engine valve-train without recourse to lubricant additives that are damaging to the catalytic converter.”*

This research will be investigating three such potential solutions, these are: (i) diamond-like carbon (DLC) coatings; (ii) carbon nitride (CN<sub>x</sub>) coatings and; (iii) ionic

liquid lubrication. The DLC and  $CN_x$  coating solutions (i and ii) are both concerned with depositing very thin ( $<4\mu m$ ), hard, wear-resistant, low-friction coatings onto components surfaces. These offer the possibility of reducing friction and improving wear resistance in component contacts, either removing the need for oil additives entirely or working with the oil additives and reducing the quantities required. Solution iii) is concerned with the use of a new chemistry of lubricant, ionic liquids, which could work with traditional oil-based additives or in time replace them and allow a departure from the chemistries that are known to harm the catalytic converter.

This study has been limited to the automotive value-train. The valve-train only accounts for between 6% and 10% of the frictional losses of the engine, with the largest frictional losses occurring in the piston assembly. The valve-train offers an opportunity to investigate possible techniques for improving friction and wear conditions in a relatively simple context. Much research is being conducted on reducing friction in the piston assembly, however the piston assembly is subject to extremes of temperature and the operating environment is chemically complex, whereas the factors determining valve-train friction and wear are ostensibly mechanical. The valve-train is also of particular interest in that the high wear components are serviceable and replaceable in most valve-train arrangements. This makes them ideal for the application of thin-film coatings such as DLC and  $CN_x$ , which can be challenging to apply to large or complex components. The valve-train is the engine system responsible for controlling the timing of valve opening and closing and will be discussed in greater detail in chapter 2.

The main focus of this research will be the use of DLC coatings for providing a low-friction and high-wear contact in the valve-train. DLC coating technology has benefitted from a great deal of research and industrial interest and represents the solution closest to application. The investigation of  $CN_x$  represents an extension of this investigation.  $CN_x$  coating is a similar but much more recent coating and is still very much experimental, but it offers some unique coatings properties. For the investigation of these two potential solutions this research has the following aims:

- Develop a cam-tappet testing rig for assessing coating performance in the valve-train;

- Establish, from a range of candidate coatings, those which have the best durability and friction performance;
- Categorise the tribological and mechanical properties of coatings;
- Establish any links that may exist between coating properties and valve-train performance;

Ionic liquid lubrication represents a distinct and different approach to the thin-film coating techniques described above. The use of ionic liquids as lubricants is a very recent concept and for the specific ionic liquids considered in this research this is the first-time their potential as lubricants has been investigated. This investigation therefore represents an initial assessment of a technology which may in time grow to be an effective solution to the problem of valve-train friction and wear.

The work that follows in this thesis has been broken down into a number of chapters, these chapters can be considered to be split into two groups: (i) the initial chapters provide the context and background information necessary to follow the investigations conducted in this research, and (ii) experimental chapters providing information specific to the technologies under investigation, methodology specific to the solutions under investigation, the results of these investigations, conclusions and suggested future work.

The following chapters of this thesis are as follows:

*Chapter 2 – Valve-train tribology and cam-tappet test rig development* – is an introduction to the tribological systems of the valve-train and a discussion of the stepwise development of a testing rig for the cam-tappet contact.

*Chapter 3 – Experimental techniques and methodology* – describes the background to the experimental techniques utilised in the investigations described in chapters 6, 7 and 8. Details are given of the equipment and methodologies used.

*Chapter 4 – Microscopy, spectroscopy and spectrometry* – introduces the techniques used to observe surface detail and measure aspects of coating composition and microstructure.

*Chapter 5 – Carbon based coatings – Common tribological properties and deposition processes* – discusses the properties that are common to the carbon-based coatings

considered in this thesis, their microstructure, and their mechanical and tribological properties. This chapter goes on to discuss the role that deposition technique plays in determining these properties.

*Chapter 6 – Diamond-like carbon coatings* – describes investigation of the performance of diamond-like carbon (DLC) coatings for valve-train applications. A number of studies have been carried out looking at various aspects of performance but for all studies the friction and wear experienced by DLC coatings in the valve-train testing rig is compared to coating properties determined by the techniques described in chapters 3 and 4. This approach highlights properties of significance when selecting or designing DLC coatings for valve-train applications.

*Chapter 7 – Carbon nitride coatings* – is similar in structure to chapter 6. This chapter describes an initial assessment of the performance in the valve-train for the more experimental coating technology of carbon nitride (CN<sub>x</sub>) coatings.

*Chapter 8 – Ionic liquid lubrication* – describes the investigation of novel ionic liquid based lubricants for steel-on-steel contacts. Chapter 8 differs from chapters 6 and 7 in that the investigation is not specific to valve-train lubrication. Chapter 8 is instead a feasibility study of two specific ionic liquids being used for the lubrication of steel. The role that surface texture plays in retaining ionic liquid lubricants is also investigated.

*Chapter 9 – Conclusions* – discusses the major findings of this work and their context in current research. This chapter also discusses methods by which the research aims of this work can be furthered, with a focus on how this study can be improved and extended in a systematic manner.

1.4 Chapter references

- 1 Kyoto Protocol. (United Nations Framework Convention on Climate Change, 1997).
- 2 Kyoto Protocol Ratification. (United Nations Framework Convention on Climate Change, 2009).
- 3 Stern, N. Stern Review on the economics of climate change. (Cabinet Office - HM Treasury, 2006).
- 4 European Environment Agency statement. (European Environment Agency, 2006).
- 5 Energy white paper: meeting the energy challenge. pp. pp 235-252 (Department of Trade and Industry, 2007).
- 6 Pershing, J. and Levin, K. Climate Science: Major New Discoveries. (World Resources Institute, 2006).
- 7 Environmental statement. (European Environment Agency, 2006).
- 8 Mobility 2030: meeting the challenges to sustainability. (World Business Council for Sustainable Development, 2004).
- 9 King, J. King review: Low carbon cars. (Cabinet Office - HM Treasury, 2008).
- 10 Tung, S.C. and McMillan, M.L. Automotive tribology overview of current advances and challenges for the future. *Tribology International*, 2004, **37**(7), 517-536.
- 11 Andersson, B.S. Company perspectives in vehicle tribology - Volvo. 17<sup>th</sup> Leeds-Lyon Symposium on Tribology, pp. pp.503-506 (Vehicle tribology, Elsevier, The University of Leeds, 1991).

# CHAPTER 2

## Valve-train and the cam-tappet test rig

---

### 2. Valve-train and the cam-tappet test rig

#### 2.1 The automotive valve-train

#### 2.2 Tribology of the cam-tappet contact in DOHC systems

#### 2.3 The cam-tappet test rig

##### 2.3.1 *Determining friction coefficient – modelling forces*

##### 2.3.2 *Signal noise*

###### 2.3.2.1 Initial findings

###### 2.3.2.2 Investigating the source of the noise

##### 2.3.3 *Data filtration*

#### 2.4 Chapter references

---

### 2.1 The automotive valve-train

Chapter 1 discussed the need for improvement in engine efficiency. This chapter will discuss the role that the internal combustion engine valve-train plays in achieving that aim.

The valve-train comprises the engine components that control the timing of the engine through the combustion stages. The stages of a four stroke combustion cycle are: **intake** of the air-fuel mix into the combustion chamber; **compression** of the fuel gases; **power** generation by ignition and expansion; and **exhaust** of the burnt gases (see figure 2.1 for an illustration).

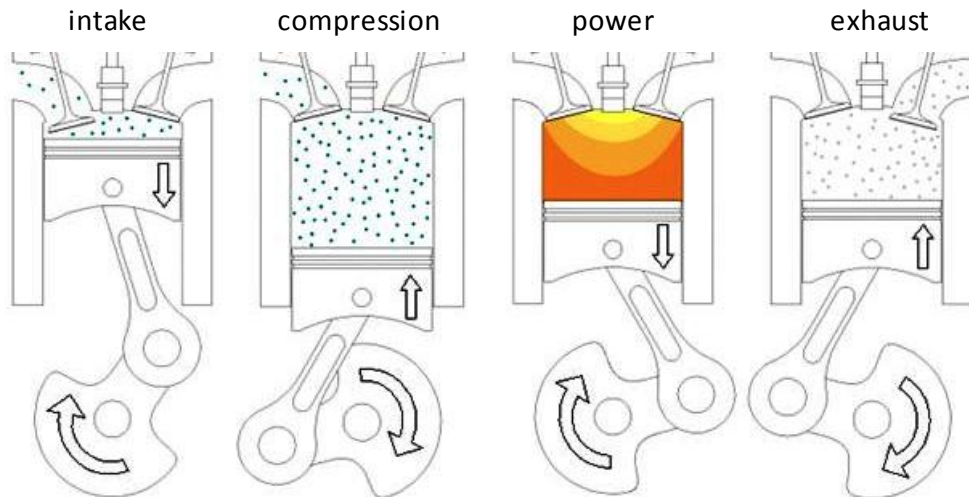


Figure 2.1 –Illustration of the stages of a four stroke combustion cycle with detail of the valve and cam positions of a DOHC system.

For proper operation, the combustion chambers must be supplied with fuel-air mix in precise quantities, all valves must be completely closed during ignition and combustion, and the exhaust gases must be evacuated completely. This requires very tight control of the valve opening and closing times. Many systems have been employed for controlling valve timing and designs have commonly used the application of cams with a combination of pushrods, rocker-arms and/or lifters in a variety of configurations, a few of the most common are shown in figure 2.2. This work is focused on the dual overhead camshaft (DOHC) arrangement also known as a direct-acting overhead camshaft arrangement, see figure 2.2(d) for an illustration of the key components. In this arrangement, the camshaft is mounted above the combustion chamber with the cams acting on bucket tappets mounted directly onto the valve-stems. The DOHC has become popular in recent years due to its mechanical simplicity and low number of moving components, which keeps the overall mass low and improves valve-train stiffness.

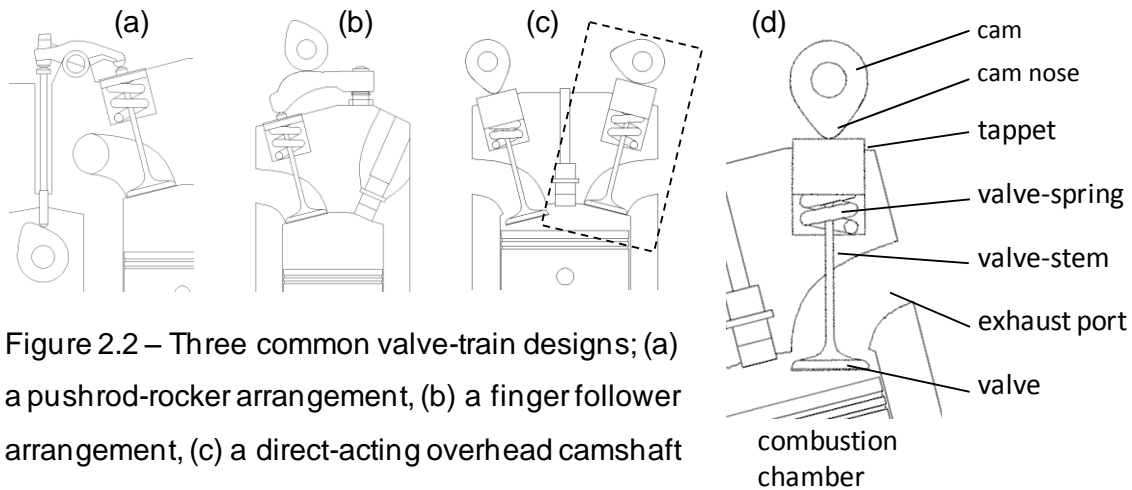


Figure 2.2 – Three common valve-train designs; (a) a pushrod-rocker arrangement, (b) a finger follower arrangement, (c) a direct-acting overhead camshaft arrangement, and (d) component details of (c).

## 2.2 Tribology of the cam-tappet contact in DOHC systems

This section discusses the tribological issues relating to DOHC valve-train arrangements, with a focus on the point of contact between cam and tappet. Depending upon the arrangement, the valve-train will have some, if not all, of its components at the top of the engine, which makes providing adequate lubrication challenging. Figure 2.3 shows a Stribeck curve indicating the lubrication regime commonly seen for a number of major engine components. There are four lubrication regimes typically experienced:

- (i) Hydrodynamic lubrication - where a film of lubricant completely separates two surfaces in relative sliding.
- (ii) Elasto-hydrodynamic lubrication (EHL) - surfaces are held separated by lubricant, but some interaction does occur between surface asperities. The pressure in the contact area is high and surfaces are elastically deformed, thereby enlarging the load bearing area and redistributing the load.
- (iii) Boundary lubrication - where the lubricant film thickness is smaller than the height of asperities and the majority of the load is supported by the asperities rather than the lubricant film.
- (iv) Mixed lubrication - is where there is a combination of EHL and boundary lubrication within a contact.

The valve-train falls into a mixed boundary and elasto-hydrodynamic lubrication regime [1]. As surfaces are potentially in asperity contact and experiencing rolling and/or sliding there are likely to be issues of abrasive and/or adhesive wear, and the

valve-train has traditionally been an area of high component wear and premature failure. Wear is a particular concern within the valve-train as change in component geometry, particularly cam or tappet, can affect valve timing and lead to improper engine function.

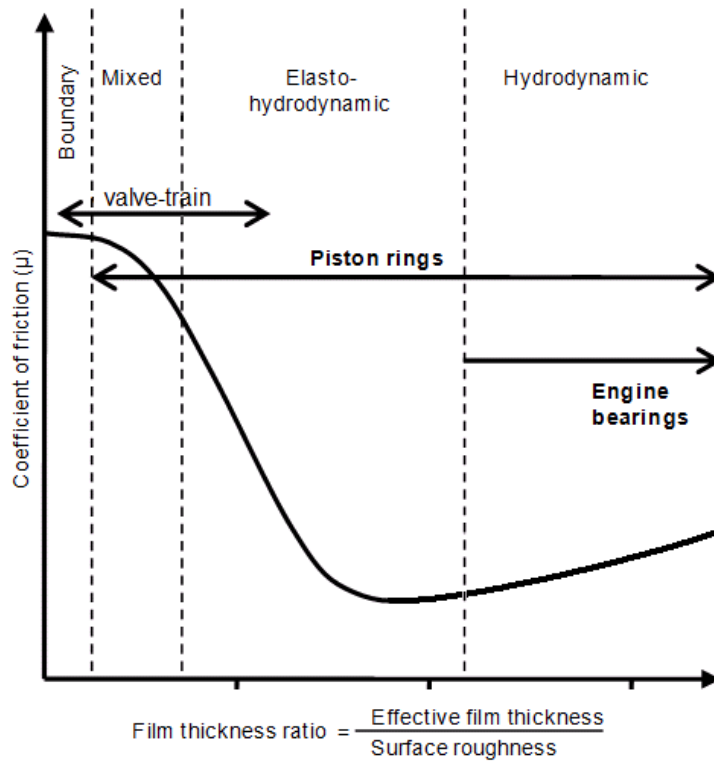


Figure 2.3 – A Stribeck curve indicating the lubrication regime of a number of key engine components.

The following section describes the mechanical operation of the DOHC in greater detail and discusses the conditions of contact between the cam and tappet surfaces.

The camshaft is rotated by a chain drive from the crankshaft, and the cam is brought into contact with the tappet surface. The cam's rotation causes depression of the tappet, compression of the valve-spring, and depression of the valve-stem, opening the valve. As camshaft rotation continues, the contact passes the cam nose, after which the force of the valve-spring assists the camshaft's motion. During a typical camshaft cycle there are a number of forces applied to the cam-tappet contact that influence the tribology of the system. The forces at the point of contact vary in magnitude depending on the point in the cycle i.e. the amount of spring compression, the lubrication regime and the steady-state camshaft rotational speed. All these factors will affect the sliding/rolling wear

regime. Also it is common for the travel of the valve-stem to be limited by the complete closing of the valve, in order to ensure complete valve-closure and keep cam and tappet surfaces separate while the valve is closed, avoiding unnecessary friction losses. In this arrangement, it is typical for the valve-spring not to reach its unstressed length and to remain compressed, with the force of keeping the spring compressed borne by the valve-stem and valve-seat. At the point where the cam rotation brings the cam and tappet back into contact, the load from the compressed spring is transferred from valve-stem and valve-seat to the cam-tappet contact very rapidly. At this point that the cam-tappet contact experiences impact loading, in excess of  $5\text{kN s}^{-1}$ . The geometry of the cam-tappet interface at the point of impact also leads to a large angle between the tappet surface and the direction of applied load, see figure 2.4. See figure 2.5 for an illustration of the motion of components through the cycle and the contact points undergo impact loading.

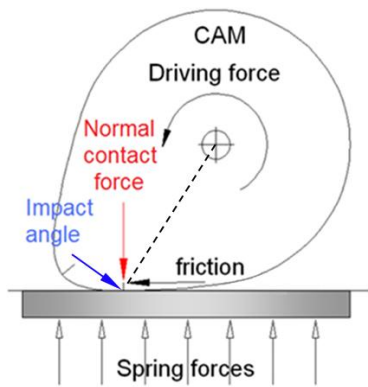


Figure 2.4 – Illustration of impact loading at a high cycle.

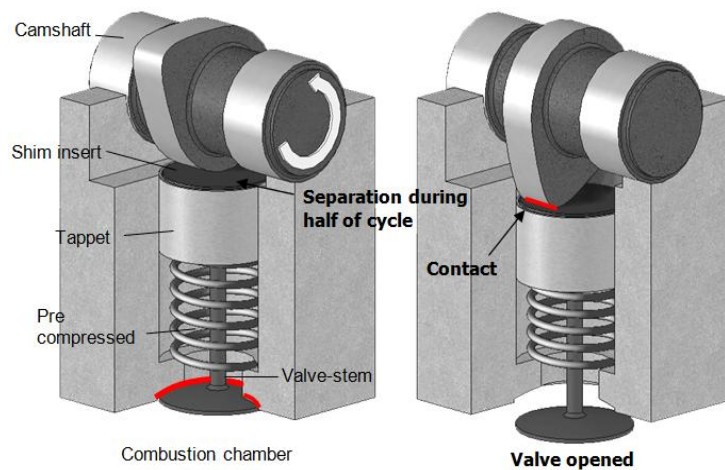


Figure 2.5 – Illustration of valve-train motion during a cycle for a single cam, with red lines indicating surfaces that experience impact loading.

Operating conditions of mixed abrasive/adhesive wear along with impact loading are potentially very harmful. This makes for a challenging environment for thin-film surface engineering techniques such as diamond-like carbon and carbon nitride coating. This research looks to identify coatings that perform well as low wear and low friction surfaces for valve-train components. An essential element of this work is therefore the development of a wear testing apparatus that realistically reproduces the in-service conditions of a DOHC valve-train, whilst allowing accurate control of test parameters

and measurement of important properties such as in-service friction coefficient. Section 2.3 discusses the test apparatus used, some of the challenges that such testing presents and the improvements and developments that have been made throughout the course of this research.

### 2.3 The cam-tappet test rig

The cam-tappet test rig is the apparatus used to test wear and friction properties of candidate coatings in a manner that recreates in-service conditions. The cam-tappet test rig can be divided into three elements, the **valve-train** itself, the **oil supply system**, and the **drive-train**, see figure 2.6.

The **valve-train** is the principle component of the cam-tappet test rig. The valve-train consists of the top-end of a cylinder-head taken from a Jaguar AJV8 engine. The section retains the top of the combustion chamber, along with the 8 inlet and 8 exhaust valves and both the inlet and exhaust camshafts, but not the piston arrangement. The oil veins that supply lubricant to the bearing faces were maintained so that tests could be conducted with realistic in-service lubrication conditions. In this research for simplicity only the inlet camshaft and the leftmost tappet are used during testing, thereby limiting contact to one cam and one tappet.

The **oil supply system** allows controlled supply of heated engine oil to the valve-train. An oil pump circulates engine oil from a sump tank, through an inline heater and into the body of the valve-train. From there it is fed directly into the camshaft bearings faces, and the runoff from this pools around the tappets and supplies lubrication to the cam-tappet contact. From there the oil drains from the valve-train body and is fed back into the sump. The sump oil can also be heated by means of a 0.5kW immersion heater. The majority of the heat is supplied by the immersion heater, with the remaining heat supplied by the more dynamic inline heater, which measures temperature at its outlet and can bring oil temperature to a relatively steady specified value. This two stage heating system allows for careful control of the energy injected into the oil so as to avoid temperature related oil degradation. The oil temperature is also measured by thermocouples at two points in the sump and a third at the base of the tappet. The two thermocouples in the sump are positioned near to and distant from the immersion heater to show heat transfer within in the sump oil. The thermocouple at the base of the

tappet sits in the oil pool that supplies the cam-tappet contact and is used to indicate lubricant temperature at the contact.

The **drive-train** of the test rig is the component that provides rotary motion to the camshaft. As will be seen in the later sections, this component of the test rig has been changed many times throughout testing in order to investigate a number of effects. The drive-train essentially consists of an electric motor, a high inertia flywheel, a contactless torque transducer, a number of flexible coupling elements and a number of supports. The motor provides rotary motion. The flywheel provides inertia, helping the motor to cope with the rapidly changing load of the camshaft and isolating the torque transducer from any high frequency torque coming from the motor. A flexible coupling is used to connect the drive-train to the camshaft; these are torsionally stiff but axially flexible and allow for angular misalignment. The introduction of a second flexible coupling, or a composite flexible coupling, also allows for lateral misalignment. These isolate the torque transducer from misalignment forces that might be damaging to the equipment or measurements. The torque transducer continuously measures the torque across the length of its shaft, i.e. from the relatively steady state of the flywheel on one side to the rapidly changing load of the camshaft rotation on the other side. This gives a measure of the torque generated by the cam's rotation. From this it is possible to determine the torque contribution from friction between the cam and tappet surfaces and allows an in-service coefficient of friction to be found. The method used to determine the coefficient of friction is laid out in the next section, section 2.3.1.

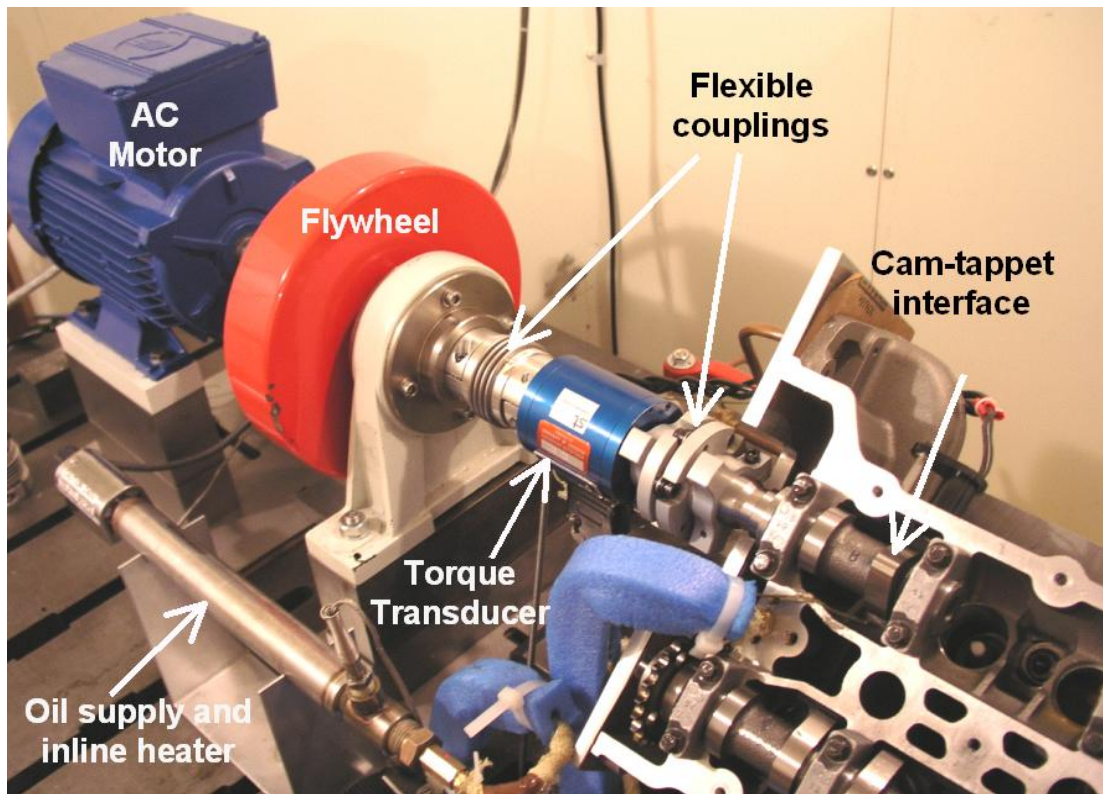


Fig 2.6 – Image of the cam-tappet test rig and its important components

### 2.3.1 Determining friction coefficient – modelling forces

By measuring the torque between the cam-tappet interface and the motor it is possible to observe all of the forces which oppose the rotary motion of the camshaft. There are many sources of resistance to the camshafts motion;

- (i) friction in the bearings,
- (ii) force of the cam depressing the tappet and compressing the valve-spring,
- (iii) force required to overcome inertia and accelerate the tappet, valve-stem, valve-spring and valve and,
- (iv) friction between the cam and tappet surfaces.

It is the last source, the cam tappet surface friction that is of particular interest. In order to isolate the friction force, all of the other sources must be understood so that their contribution can be accounted for. This work attempts to do that by modelling the individual contributions with a numerical approach in MatLab, from knowledge of the component geometries, component masses, valve-spring stiffness and operating conditions. Each can be considered in turn:

- (i) The first contribution is easily accounted for and eliminated. The friction in the bearings will be steady throughout a cycle for steady driveshaft rotational speed.

Therefore the mean torque during the unloaded portion of the cycle can be taken as a datum which includes the bearing friction contribution.

- (ii) The torque contribution from depressing the tappet can be determined directly from the cam geometry and the spring stiffness. The eccentricity of the cam's surface is known for each half degree. Therefore for any given angle of camshaft orientation,  $\alpha$ , relative to the tappet surface, the lowest point can be determined. The lowest point will be the point to make contact with the tappet, see figure 2.7 for an illustration. With knowledge of the point of contact, the eccentricity of that point,  $E$ , and angle of that point from horizontal,  $\beta$ , can be calculated. It is also possible to find the 'lift',  $L$ , i.e. the increase in effective diameter from the cam's base circle. Lift is the dimension that determines how much the tappet is displaced. The tappet displacement,  $D$ , is equal to the lift,  $L$ , less the spacing between cam and tappet. As discussed in section 2.2 the cam and tappet are held separated during approximately 55% of the cycle. The gap by which they are separated was determined to be 0.18mm, measured by inserting known thicknesses of shimming material. For any given angle the force opposing the cam's rotation is therefore the sum of tappet displacement,  $D$ , and any pre-compression of the spring, multiplied by the spring stiffness. Values of,  $E$ ,  $L$ ,  $D$ ,  $\beta$  and spring force can be generated for all 360 degrees of camshaft rotation. Tappet displacement against degrees is shown plotted in figure 2.8. For  $\sim 180^\circ$  of the cycle there is no contact between the surfaces and therefore no force, this part of the cycle has not been plotted.

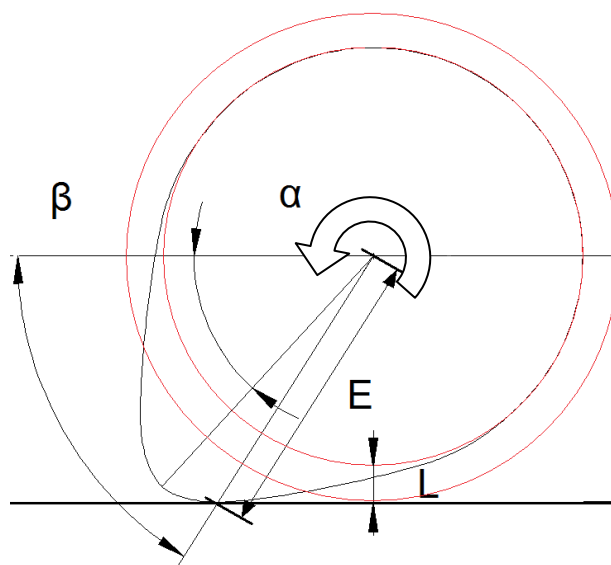


Figure 2.7 – Determining point of contact from cam angle,  $\alpha$ . Can then determine cam lift,  $L$ , eccentricity of contact,  $E$ , and angle between contact and horizontal,  $\beta$ .

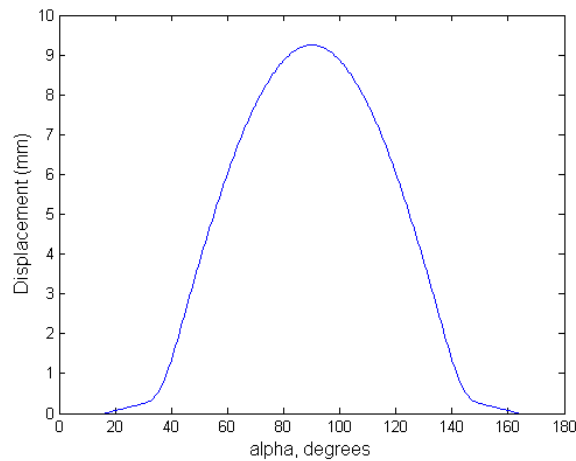


Figure 2.8 – Graph of tappet displacement against angle  $\alpha$  in degrees

(iii) With the tappet displacement known for each half degree and degrees per second being determined from the rotational speed of the camshaft, it is possible to generate values of tappet velocity and tappet acceleration for all camshaft angles (see figure 2.9 and 2.10). As tappet acceleration also determines the acceleration of the valve-stem and valve, with knowledge of the component masses the inertial forces can be found. For simplicity this approach ignores the acceleration of the springs mass as this varies across its length.

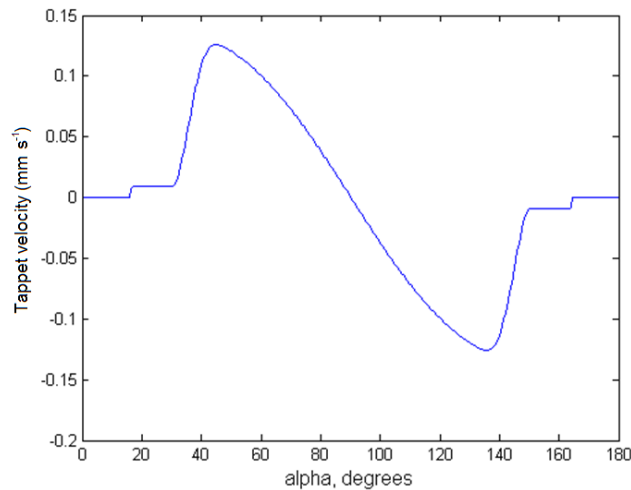


Figure 2.9 – Graph of tappet velocity against angle  $\alpha$  in degrees. Example calculated for a valve-train speed of 450 rpm

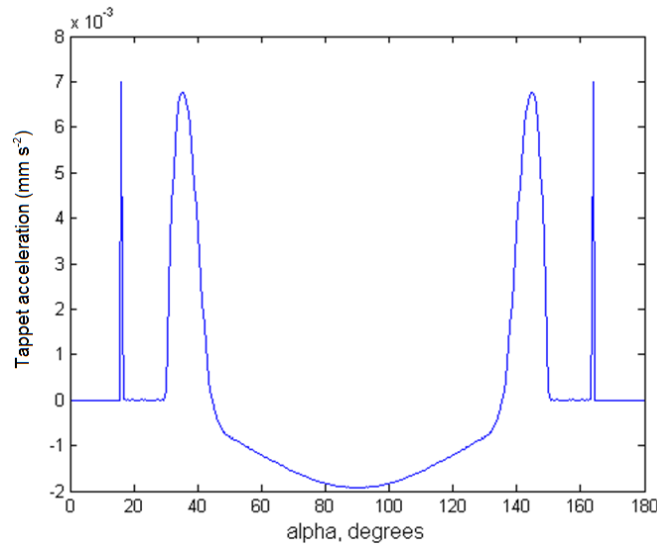


Figure 2.10 – Graph of tappet acceleration against angle  $\alpha$  in degrees. Example calculated for a valve-train speed of 450 rpm.

iv) The friction force throughout the cycle can be calculated for a specified coefficient of friction as the applied load is known from the calculations in figure 2.8 above. Figure 2.11 shows each of the force contributions, and a combined force,  $F$ .

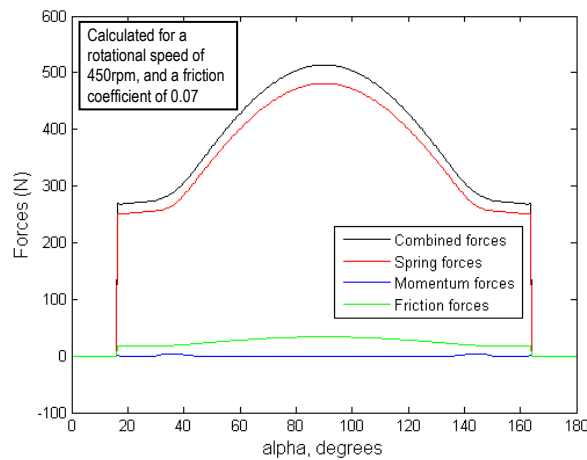


Figure 2.11 – Graph of all forces in the contact against the angle  $\alpha$  in degrees. Example calculated for a valve-train speed of 450 rpm and a friction coefficient of 0.07.

In order to find an unknown coefficient of friction the forces must be combined, and their torque contributions calculated. Then the simulated torque throughout the cycle can be compared to a recorded torque. The specified coefficient of friction can then be adjusted so that the simulated torque best matches the observed torque and in this way the actual coefficient of friction found. At this stage the process is conducted manually, but could more quickly be conducted with a least squares regression. First however the friction force, spring force and inertial force must be converted into their torque

contributions. In order to do this it is necessary to know the distance from the centre of the camshafts rotation to the point of applied load, this is given by  $E$ . Also the torque will depend upon not only the magnitude of the forces but also their direction, for example at  $\alpha = 90^\circ$ , the spring force is at its highest, however no component of that force opposes the movement of the camshaft and therefore there is no torque contribution.

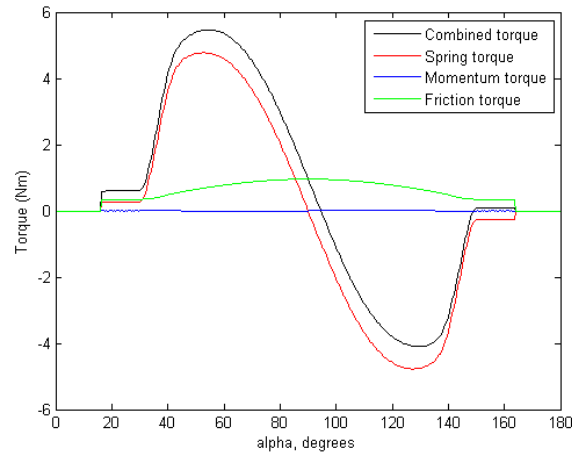


Figure 2.12 – Graph of simulated torque against the angle  $\alpha$  in degrees. Example calculated for a valve-train speed of 450 rpm and a friction coefficient of 0.07.

This approach has the advantage that it illustrates the forces in the contact, and could well be extended into a model of elastohydrodynamic film-thickness, or contact pressure. However the primary aim of calculating friction coefficient will only be possible if a good fit can be made to recorded torque data. The following section describes some of the challenges in measuring actual torque.

### 2.3.2 Signal noise

The cam-tappet testing rig was not newly constructed for this research and had been under development for a number of years. At the point where this research project took over there was known to be an issue of an unacceptable degree of noise occurring on the torque transducer signal. A large part of this research has been dedicated to investigating the source of this noise and making an attempt to eliminate it.

#### 2.3.2.1 Initial findings

Figure 2.13 shows the original set-up of the cam-tappet testing rig. The signals of the torque transducer, and rotary encoder, were converted from analogue to digital and recorded via a virtual instrument designed in National Instrument's LabView 6.1.

Whenever the cam-tappet test rig is in operation, i.e. when the motor drives the cam and tappet through a cycle, there has been observed a consistent noise superimposed upon the signal of the torque transducer. Figure 2.14 shows the torque signal generated for a single cycle at various camshaft rotational speeds and with an idealised torque curve for comparison. The first observation was that the noise signal is periodic, the second that the amplitude of the signal is affected by rotational speed. There is a trend for the amplitude to increase with rotational speed but nonlinearly, and amplitude is not constant throughout a cycle. Early investigation also showed that the noise had constant period across the working range of rotational speeds used in this investigation, see figure 2.15.

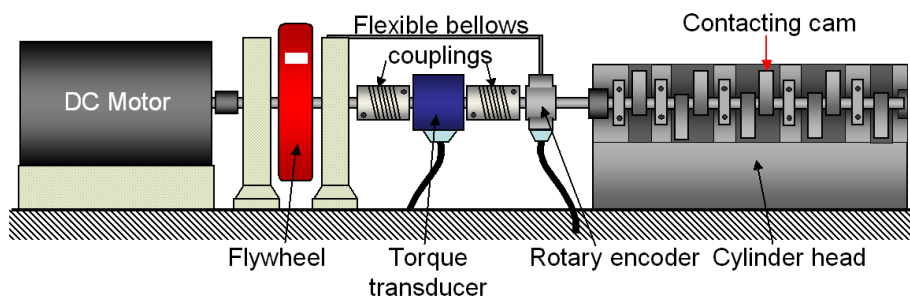


Figure 2.13 – Initial cam-tappet test rig set-up

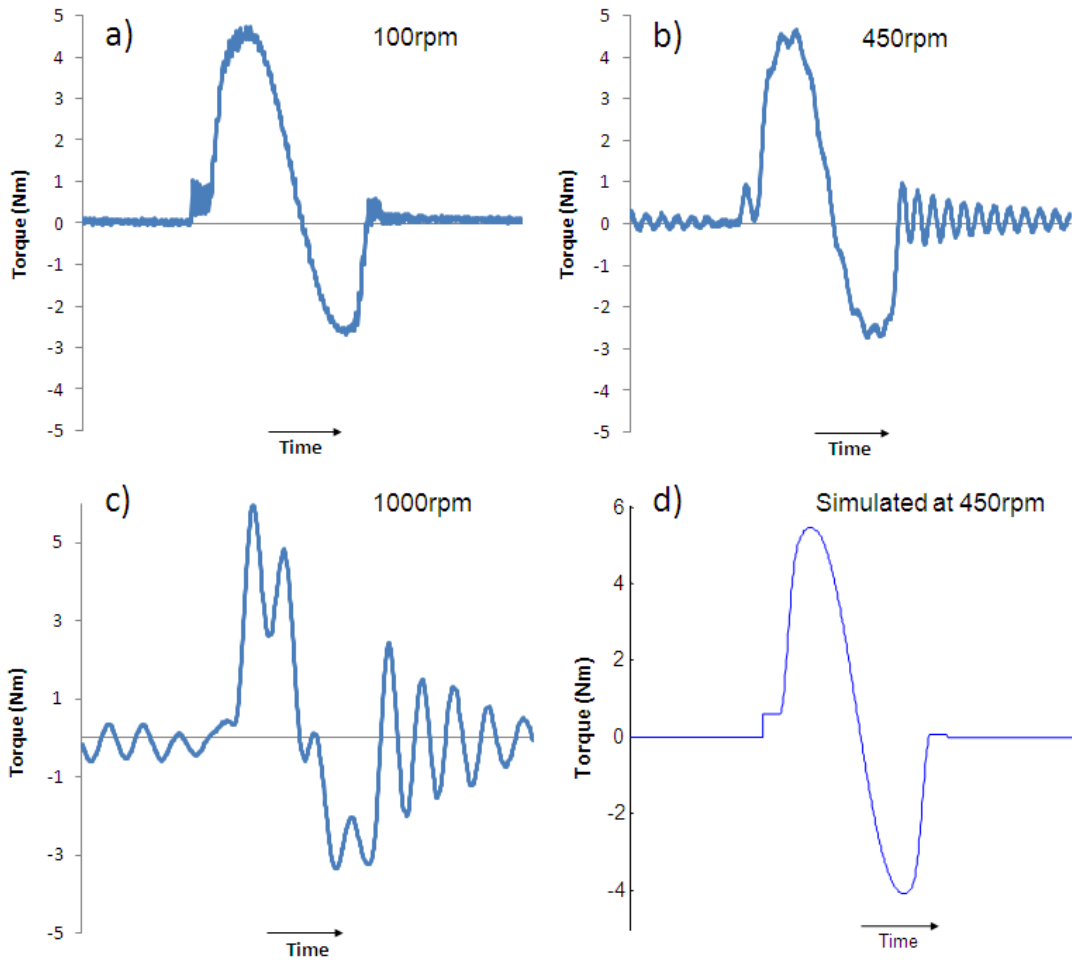


Figure 2.14 – plots of torque against time, a) at 100rpm, b) at 450rpm, c) at 1000rpm and d) a noise free simulation of torque for operation at 450rpm

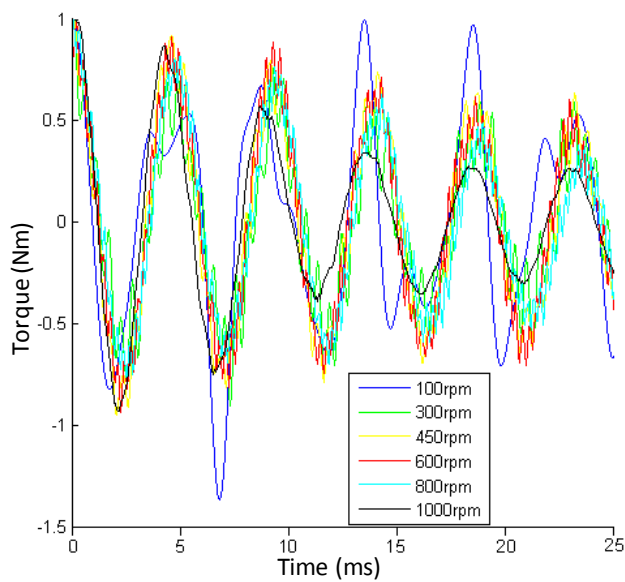


Figure 2.15 – Details of torque noise at various rotational speeds

There were many potential sources of the noise: a pulsed torque supplied from the motor; electromagnetic interference, or some mode of vibration. Each of these was investigated so that the source could be identified. The following section discusses the investigative testing conducted to find the source of the signal noise.

### 2.3.2.2 Investigating the source of the noise

What follows are illustrations of the changes that occurred in testing the cam-tappet test rig, descriptions of the affect the changes have on the noise and any other important observations. In this section all torque traces shown were generated from tests conducted with 5W30 friction modifier free engine oil, at room temperature and a rotational speed of 450rpm, unless otherwise stated. The first change was the replacement of the existing DC motor with an AC motor, see figure 2.16. The change in motor design from a DC motor to an AC motor also meant a change in control system. As the characteristic noise was only observed when the motor was operating it was possible that the noise signal was electromagnetic frequency (EMF) interference from the motor driver.

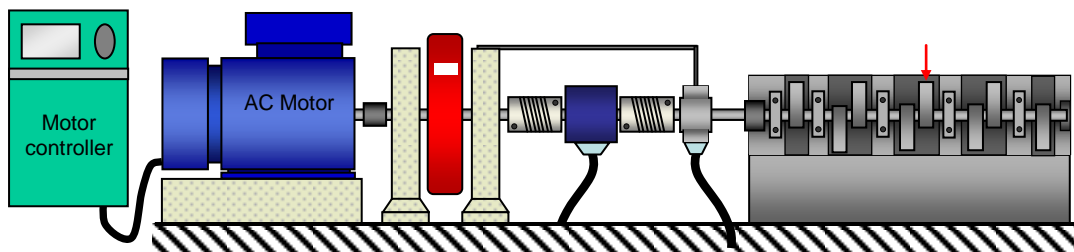


Figure 2.16 – Change of DC motor to an AC motor

As can be seen in figure 2.17 there is very little difference in noise when changing between the two motors. This indicates that it is not an oscillation in the motor torque or EMF interference from the driver, as these would likely be affected the change in motor design.

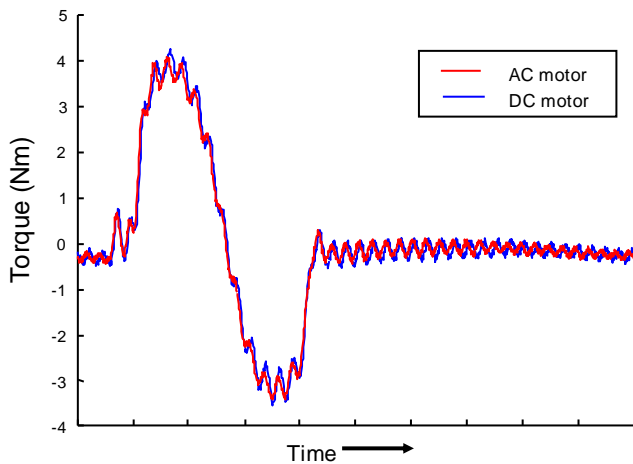


Figure 2.17 – Plot of shaft torque against time for AC and DC motors

The next suspected source was vibration, where some component of the driveshaft was being induced to vibrate at a resonant frequency. In systems such as this where there is a complex and continuously changing load there is always likely to be some resonance occurring. This is due to any complex signal being composed of a continuous spectrum of sinusoids with varying amplitude, frequency and phase. Therefore any signal that diverges significantly from a basic sinusoid will have power across a wide range of frequencies, some of which will coincide with a systems resonance. If the source of the noise is vibrational then the properties of the noise would be expected to change with change in the system dynamics. At this stage the most obvious mode of vibration is torsional, where one end of the shaft oscillates a fraction of a degree ahead and then behind the other end of the shaft, as this is the mode that will be directly detected by the torque transducer.

The torsional resonant frequency,  $f_n$ , of a shaft is a rotational analogue of the system of a mass and spring. The natural frequency of torsional vibration is determined by the shafts rotational stiffness,  $k$ , equivalent to spring stiffness, and its moment of inertia,  $I$ , equivalent to mass.

$$f_n = (1/2\pi)(k/I)^{1/2} \quad (1)$$

Therefore for increasing stiffness and decreasing mass there will be an increase in torsional natural frequency, which if the noise were vibrational in nature should be reflected in the torque transducer signal.

The next step was therefore to physically shorten the camshaft, see figure 2.18. The camshaft was reduced in length and the point of contact between cam and tappet moved to the first tappet position. The shortening of the camshaft decreased the camshaft's inertia and increased the stiffness between the driving force of the motor and the load of depressing the tappet.

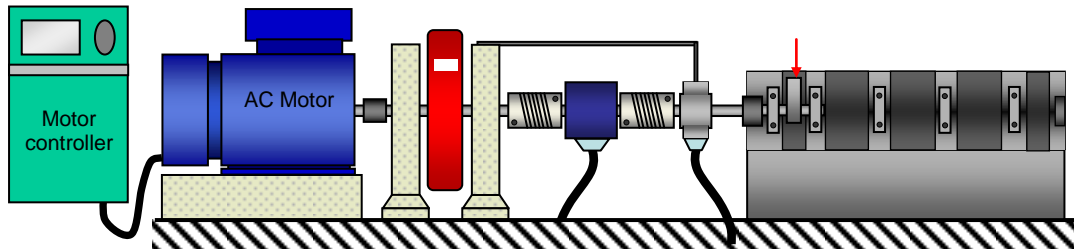


Figure 2.18 – Layout with the camshaft shortened

Figure 2.19 shows the results of changing camshaft length. The shortened cam-shaft shows a higher frequency of noise, supporting the hypothesis that a torsional vibration is the source of the noise.

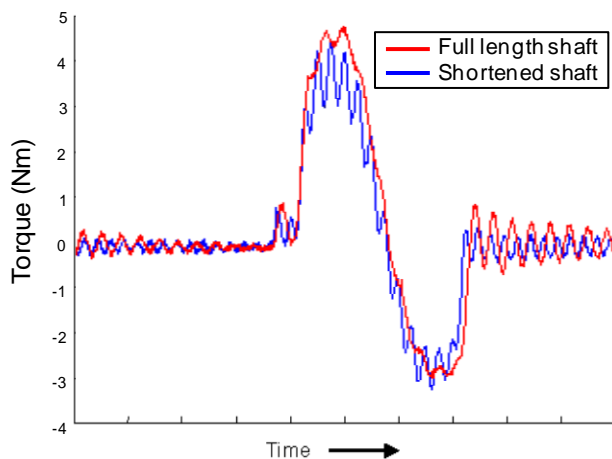


Figure 2.19 – Plot of torque against time for full length and shortened camshaft.

Once the source of the noise was established the next step was to take measures to reduce the noise or reduce the effect of the noise. By further increasing the stiffness of the system and reducing the inertia, it may be possible to drive the natural frequency of the system so high that there is little signal power of high enough frequency to cause resonance. A more reasonable expectation might be to move the natural frequency at which the vibration operates to a high enough frequency that the noise component can be successfully filtered from the signal without risking losing signal information. The next step therefore was to attempt to increase the natural frequency. The most dramatic

change in natural frequency would be achieved by removal of the flywheel, and its supports, see figure 2.20. The resulting change in torque signal is shown in figure 2.21.

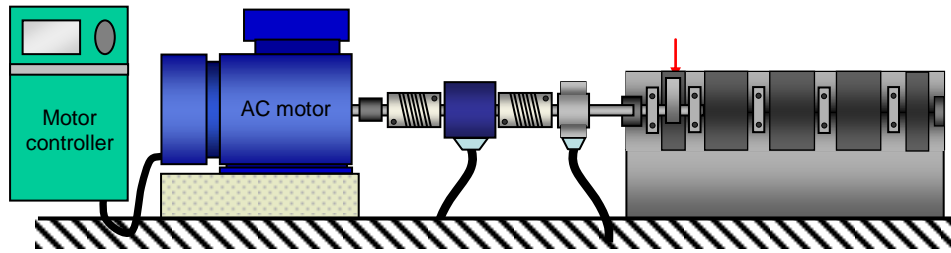


Figure 2.20 – Test rig with flywheel and supports removed

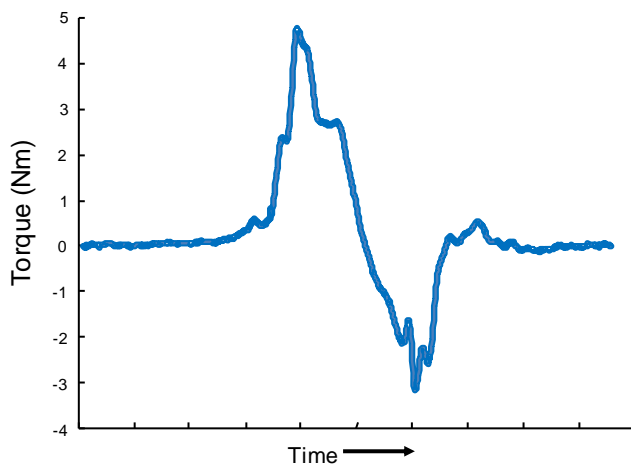


Figure 2.21 – Plot of torque against time with the flywheel and supports removed

As can be seen in figure 2.21 there is no longer a sinusoidal noise imposed upon the signal. Or rather, any noise signal that is present is of a high enough frequency and low enough amplitude so as to be indistinguishable from the noise floor. The removal of the flywheel did however expose an apparently new form of noise on the torque recordings. The flywheel's purpose is to provide a high inertia, thereby requiring a lot of energy to be accelerated or decelerated. It therefore damps high frequency components of any torque transmitted through it. In this way it smoothes any rapid changes in torque provided by the motor, ensuring a steadier rotational speed. The flywheel also acts to isolate the motor from the rapidly changing load that occurs during a cam's rotation. With the flywheel removed the motor experiences the full change in load. The noise seen when the flywheel is removed is at its highest amplitude in the second half of the loaded portion of the cycle. During this stage in the cycle the cam nose has just passed the point of greatest spring compression and the motion of the cam is then being assisted by the force of the valve-spring. It was considered that the motor controller,

which uses PID control techniques (proportional-integral-derivative), may be unable to maintain stable control when load varies magnitude and direction rapidly. This could cause the motor controller to overcompensate and create the oscillation seen in figure 2.21. It was also considered that overcompensation in applied torque from the motor could occur even with the smoothing from the flywheel and may be initiating the vibrations seen in earlier figures. This hypothesis was assessed by adjusting the gains of the PID control systems, under the controller manufacturer's supervision, until little or no feedback control occurred. No change in noise was observed.

Having eliminated unstable applied torque from the motor as an initiator of the vibration the next factor considered was vibration initiated by impact loading. As discussed above in section 2.2 the cam and tappet are out of contact for part of the cycle, during which time the valve-spring is held in compression, such that when the surfaces are brought back together the energy stored in the spring is very rapidly applied to the point of contact. This is visible in the torque traces as a small peak immediately before the primary peak. At the test speed of 1000rpm the rate of change of torque is significant,  $\sim 100\text{Nm s}^{-1}$ . In order to establish if impact loading was initiating the vibration, tests were conducted with the cam-tappet test rig in an arrangement where the cam and tappet surfaces remained in contact throughout the cycle. This arrangement saw the valve-spring released from its fixing on the valve-stem so that its minimum compression was now limited by the tappet position rather than the complete closing of the valve. The contact between the spring and the tappet was then packed out with a spacer of appropriate dimension so that the maximum and average spring compression remained the same during the loaded portion of the cycle. This effectively eliminates impact loading by keeping the cam and tappet surface in continuous contact. Figure 2.21 shows the resulting change in torque signal.

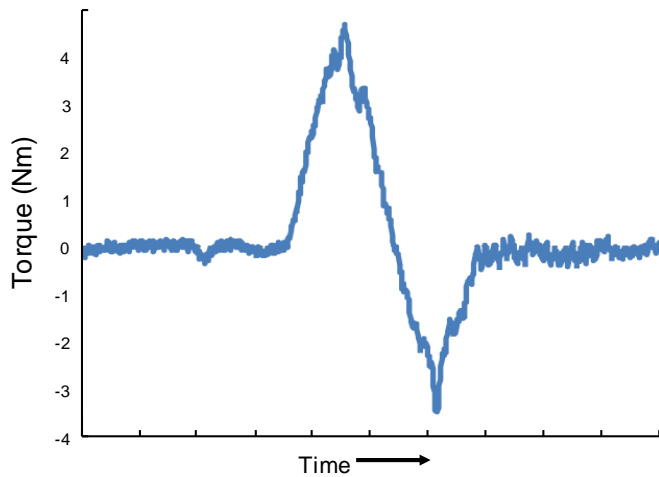


Figure 2.22 - Plot of torque against time with the cam and tappet in continuous contact.

This resulted in a dramatic reduction in the amplitude of the noise, and a loss of periodicity, with the noise on the signal more reminiscent of the testing conducted without a flywheel. This supports the hypothesis that the vibrational noise is initiated by the rapid change in load which occurs as the surfaces come back into contact. While the noise component is reduced in amplitude and is less reminiscent of a vibration, it is still present. The torque trace seen in figure 2.22 is of a single cycle and the noise component seen is unique to that cycle, whereas the vibrational noise observed with impact occurring was strongly periodic and phase locked. While this noise component does vary somewhat between cycles it cannot be entirely removed by signal averaging. It would seem that some unexpected changes in observed torque are unavoidable. Also, while continuous contact conditions remove impact and improve signal quality they are not normal operating conditions for the valve-train.

Results so far have confirmed that the nature of the noise is vibrational, and that operating conditions must be altered from in-service conditions in order to dramatically affect noise. Therefore the next step was to develop methods of working with the vibrational noise rather than eliminating it. A digital filtering technique was established in MATLAB, described in more detail in section 2.3.3, which allows the higher frequency noise to be attenuated. However at the higher rpm used in testing there remained considerable overlap in the frequency components of the noise and the underlying signal of interest. In order for filtering to be effective, the frequency at which the vibration is occurring would need to be increased. As already discussed, this can be

achieved by increasing driveshaft stiffness or reducing driveshaft inertia. This effect has been demonstrated by the removal of the flywheel in earlier testing, however there is a compromise between the inertia required to smooth torque from the motor and increase vibrational frequency. Therefore in order to increase the vibrational frequency the driveshaft must be made considerably stiffer. Many changes were made to the test rig to further improve driveshaft stiffness. The inline rotary encoder was replaced with a Hall effect tachometer, both flywheel supports were removed, and a new coupling design allowed the drive-shaft to connect directly to the camshaft, all of which contributed towards a 50% reduction in overall driveshaft length and a corresponding increase in stiffness, see figure 2.23. The result of this increased stiffness can be seen in figure 2.24 as an increase in vibrational frequency. It appears that some noise features have also been introduced, most likely from removal of the driveshaft supports, allowing more movement in the driveshaft.

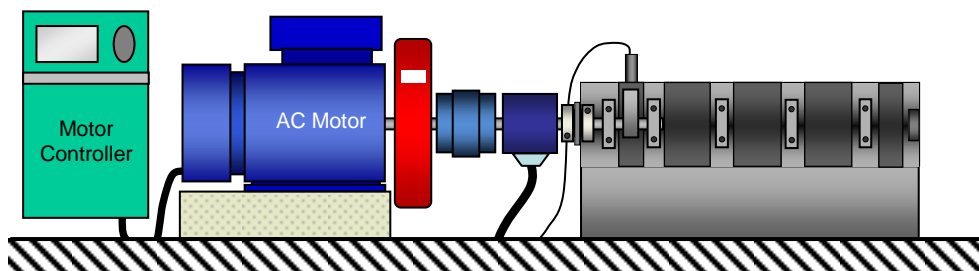


Figure 2.23 – Shortened camshaft with improved stiffness.

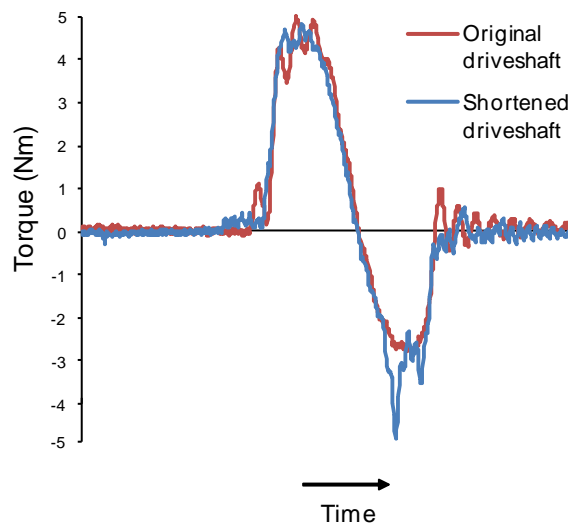


Figure 2.24 – Plot of torque against time, highlighting change in frequency with change in stiffness.

The noise reduction shown in figure 2.24 is for testing at 450rpm, as this more clearly shows the underlying signal. Figure 2.25 shows the same set-up but with testing

conducted at 1000rpm, with comparison to the torque curve shown in the previous figure 2.15c. The first observation is that the amplitude of the noise component at this rotational speed is much greater than at 450rpm, making identifying the underlying signal more challenging. The second observation is the dramatic difference that shortening the driveshaft has made to improving signal quality.

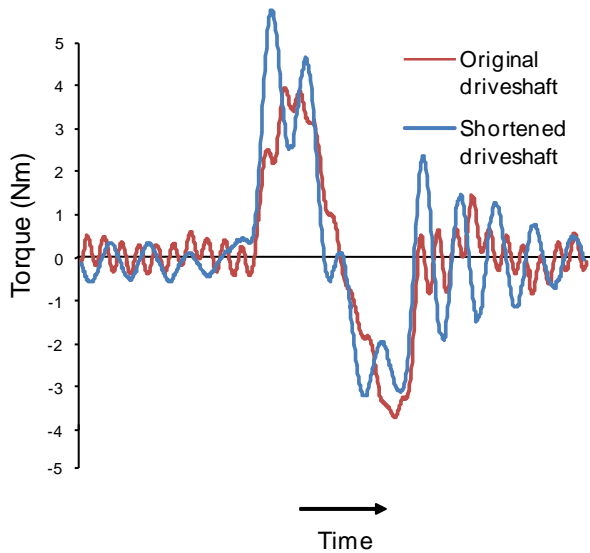


Figure 2.25 – Plot of torque against time at 1000rpm with original length driveshaft and shortened driveshaft.

Changes so far have been predominately incremental, however future improvement may well require dramatic redesign. Some of the potential issues to consider for future improvement are discussed here. There is a need to establish the minimum inertia required to smooth motor torque so as to avoid reducing the natural frequency. A system with a second shaft for the flywheel and a gear or pulley mechanism would allow the flywheel to turn at a different rotational speed, and therefore alter the inertial contribution to the driveshaft. This was attempted with a chain and sprocket mechanism, however there was found to be unacceptable noise generated by chain clatter. There is also potential to reduce the signal noise by active physical damping. The inertia of the flywheel has a damping effect on the noise from the motor, but its inertia lowers the driveshaft's natural frequency, contributing to the vibrational noise problem. Therefore a different approach is required to damp the vibrational noise. One potential approach is the use of a torsional damper, also commonly known as a 'harmonic balancer'. A torsional damper consists of a high inertia ring housed within an outer casing which mounts onto the shaft. The inertia ring is either bonded to the casing by an

elastomer or suspended in a viscous fluid, typically silicone based. As the shaft is accelerated the outer casing which is rigidly mounted onto the shaft accelerates with it. The stationary inertia ring requires a lot of energy to be accelerated, all of which must be transferred through the elastomer or fluid membrane. This causes the membrane to shear causing energy to be expended through friction and heat. Once the driveshaft and inertia ring reach a steady state no more shearing occurs and energy is conserved. However, whenever a high frequency torque is applied to the shaft, and its rate of rotation changes, the membrane is again sheared generating friction and heat. Therefore in this way the energy of the vibrational oscillations can potentially be expended, reducing resonance. Such an approach would still require an inertia which was properly matched with the motor torque fluctuations, as torsional damper systems are traditionally designed to damp low amplitude, high frequency oscillations from crankshaft vibration, not the high amplitude relatively low frequency features that have been observed in the ‘no flywheel’ testing discussed above.

Even without the physical changes suggested there is still potential to improve signal quality by the use of digital signal filtering

### 2.3.3 Data filtration

The digital filtration discussed in this section is a post-processing step, however filtration could be conducted in real-time by analogue or digital signal processing. A system was developed within the ‘Matlab’ mathematical processing platform [2] to establish if it would be possible to remove the noise component without compromising the underlying signal of interest. By conducting the filtering digitally, post collection, it can be done conscientiously with regard for retaining as much information from the signal as possible. The process used to establish the correct cut-off frequency is illustrated in figure 2.26, along with an example signal pre and post filtration. The power spectrum is calculated for a sample of data, this highlights the frequency range of the noise signal. From this an appropriate cut-off frequency can be selected and a low pass Butterworth filter can be applied.

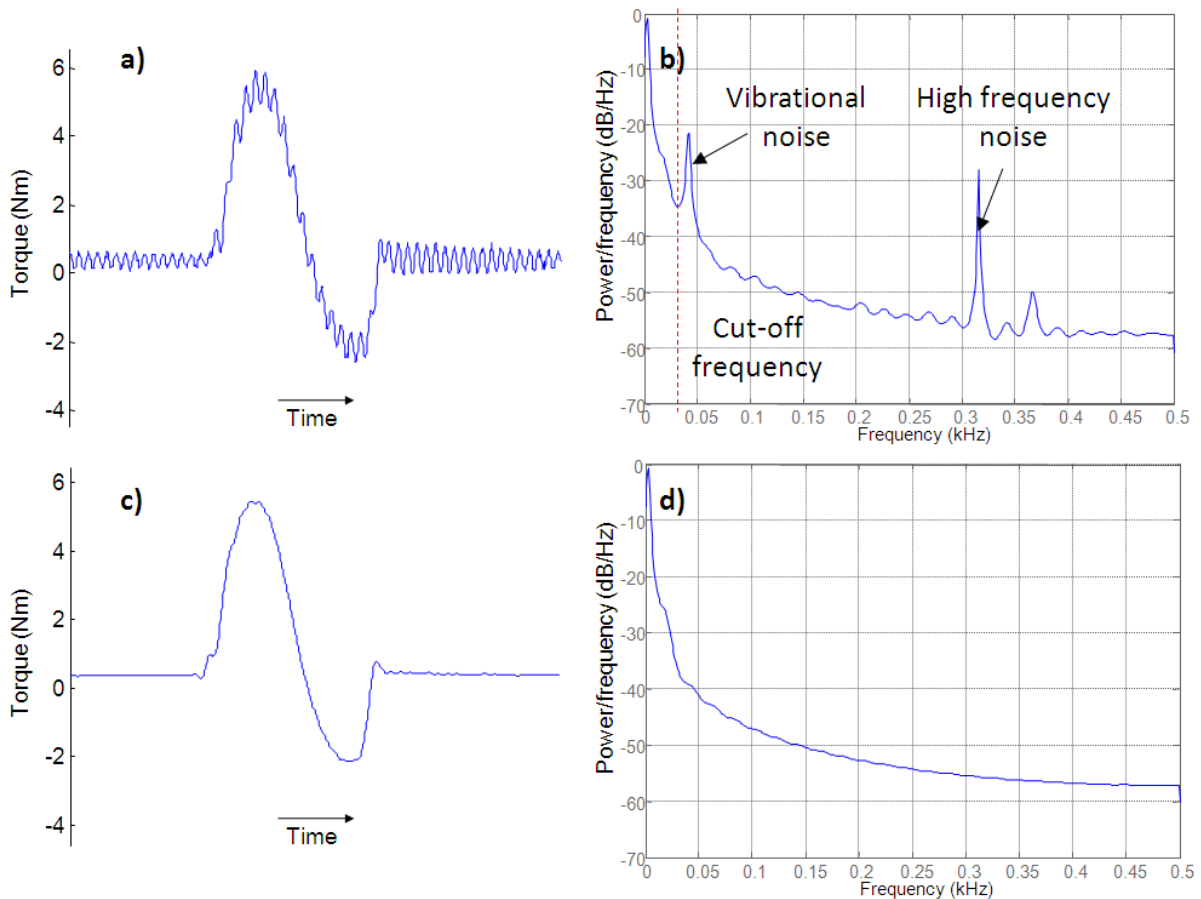


Figure 2.26 - The stages of digital filtration: a) collection of the raw unfiltered data; b) establishing a cut off frequency from the power spectrum; c) filtration, leaving the filtered data; d) the resulting power spectrum showing the removal of the noise signal.

As discussed in section 2.3.2.1, the higher the natural frequency of the driveshaft, the less overlap there will be between the frequency range of the signal of interest and the noise, allowing noise to be filtered more effectively. At this stage, much work is still to be done before the noise can be effectively filtered without having some effect on the signal of interest, particularly at higher rotational speeds.

It is important to bear in mind in this work that the noise present on torque measurement has been established to be a physical feature of the valve-train. This torsional vibration is almost certainly present in in-service conditions and is in all likelihood more severe. While these alterations are required in order to measure torque with accuracy it must be considered that the test is being idealised with respect to fired in engine tests.

This chapter has looked at the role and operation of the valve-train in the internal combustion engine. It has considered the forces acting at the contact of cam and tappet and the requirements that these place on potential thin film coatings. It has also introduced an instrumented valve-train test rig for the durability testing of thin films in a realistic environment, and the estimation of friction coefficient by torque measurement. The development of the test rig has been discussed in depth, describing the steps taken to achieve reasonable signal to noise in torque measurements. The measurements of torque from the valve-train test rig are now of a standard where friction coefficient can be identified with confidence to within 0.05. The development of this test rig has allowed for comparison between coating performance in standardised mechanical and tribological tests and coating performance in the valve-train application.

Chapter 3 looks at the properties of carbon-based coatings, including both diamond-like carbon and carbon nitride coatings. Chapter 3 also discusses a number of the properties that determine coating performance and describes details of the deposition processes.

#### 2.4 Chapter references

- 1 Priest, M. and Taylor, C.M. Automobile engine tribology -- approaching the surface. *Wear*, 2000, **241**(2), 193-203.
- 2 Mathworks. Signal processing toolset. Matlab 7.0.124704 (R14) Service Pack 1 (Mathworks, Natick Massachusetts, 2004).

# CHAPTER 3

## Carbon based coatings

---

### 3. Carbon based coatings – Common properties and deposition processes

#### 3.1 Properties of carbon based coatings

3.1.1 *The role of electron bond hybridisation*

3.1.2 *The role of coating interlayers*

3.1.3 *The role of alloying elements*

3.1.3.1 The effect of hydrogen content

3.1.3.2 The effect of silicon and fluorine content

3.1.3.3 The effect of metal content

3.1.4 *Frictional properties*

3.1.4.1 Friction and wear – The role of hydrogen and the environment

3.1.4.2 Friction and wear – The role of localised graphitisation

3.1.4.3 Friction and wear – The role of transfer layer formation

3.1.4.4 Friction and wear – Interaction with oil based lubricants

#### 3.2 Deposition processes

3.2.1 *Physical vapour deposition (PVD)*

3.2.1.1 Sputtering

3.2.1.2 Ion beam deposition

3.2.1.3 Cathodic vacuum arc

3.2.1.4 Pulsed laser deposition

3.2.2 *Chemical vapour deposition (CVD)*

3.2.2.1 Plasma enhanced chemical vapour deposition

#### 3.3 Chapter references

---

This chapter discusses the physical principles governing the properties of both diamond-like carbon (DLC) and carbon nitride ( $CN_x$ ) as carbon-based coatings. This is then followed by a discussion of the various processes by which thin-film carbon-based coatings are commonly deposited, and their affect on coating microstructure,

morphology and mechanical properties. The distinct properties of DLC and  $CN_x$  will be addressed in more detail individually in chapters 6 and 7 respectively.

### 3.1 Properties of carbon-based coatings

The terms DLC and  $CN_x$  encompass a wide variety of coating compositions and microstructures with an equally wide range of material properties. However as materials predominantly composed of amorphous carbon they share a number of properties. Both DLC and  $CN_x$  are noteworthy for their typically high hardness  $>20\text{GPa}$ , low friction coefficients, low wear rates and low thickness ( $<10\mu\text{m}$ , typically  $<4\mu\text{m}$ ). Many of the physical principles that govern their properties are the same. This section looks at those physical principles.

#### 3.1.1 The role of electron bond hybridisation

The principle component of both DLC and  $CN_x$  coatings is carbon. Carbon can exist in a number of atomic configurations, or allotropes, the most common of which are diamond and graphite. Carbon exhibits vastly different materials properties depending upon its allotrope. For example diamond is the hardest known mineral (10 on the Mohs scale), is highly abrasive, has excellent optical transparency, is an electrical insulator and a thermal conductor. Graphite is very soft (1-2 on the Mohs scale) and lubricious, is an effective solid lubricant, is optically opaque, electrically conductive and thermally insulating. Both substances are entirely composed of carbon and the variation in properties comes entirely from the change in molecular structure. Structurally diamond is formed of carbon atoms covalently bonded to four other carbon atoms in a tetrahedron, see figure 3.1a. This strong, tightly packed, three dimensional bonding gives diamond its high hardness and thermal conductivity. In graphite, the carbon atoms are arranged in covalently bonded hexagonal lattices. These lattices planes are connected by weak van der Waals forces, see figure 3.1b. The lattices are able to easily slide over each other, which makes for a substance which is easily sheared and highly lubricious.

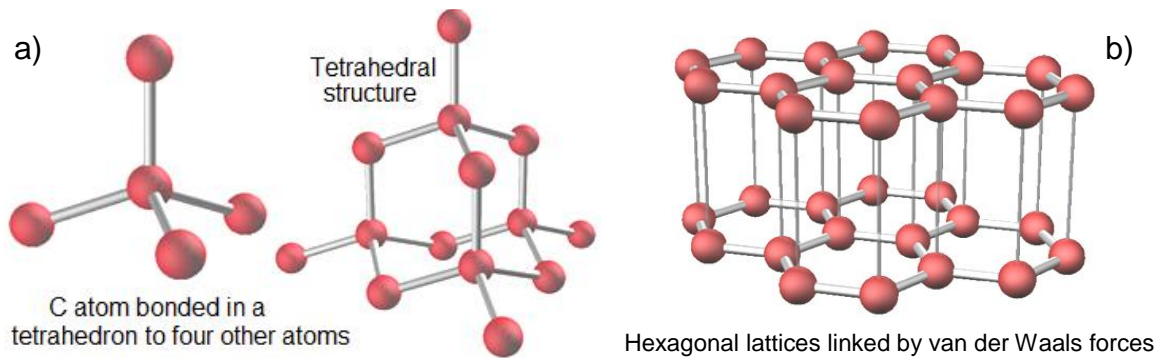


Figure 3.1- Molecular structures of a) diamond carbon and b) graphite carbon allotropes

The bonding of these allotropes is determined by the electron hybridisation that occurs. Electron hybridisation, or orbital hybridisation, is a model for explaining the available bonds in an atomic structure. The two states of hybridisation that apply to these types of carbon structures are  $sp^3$  and  $sp^2$ . These terms describe the orbitals being hybridised. For example in  $sp^3$  hybridisation, one s orbital and three p orbitals hybridise to form four bonding sites arranged three dimensionally at  $109.5^\circ$  from each other, see figure 3.2a. In  $sp^2$  hybridisation one s orbital and two p orbitals hybridise to form three bond sites at  $120^\circ$  on a plane, leaving one p orbital which forms a  $\pi$  bond at  $90^\circ$  to the plane. From this it is clear that tetrahedral structure of diamond is due to  $sp^3$  hybridisation, as  $sp^2$  hybridisation is responsible for the hexagonal structure of graphite.

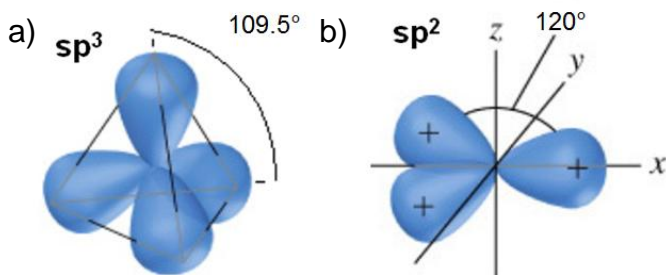


Figure 3.2 – orientation of bond sites in carbon for hybridized orbitals a)  $sp^3$  and b)  $sp^2$

There is a third common allotrope of carbon, amorphous carbon. Amorphous carbon does not have a crystalline microstructure; rather it consists of small regions of ordered atoms, which may be interlinked with other areas of different orientation or structure, e.g. tetrahedral structures and hexagonal planes. The properties of an amorphous carbon are greatly affected the proportions of tetrahedral,  $sp^3$ , bonded carbon and hexagonal,  $sp^2$ , bonded carbon. A DLC coating free of alloying elements could be

considered amorphous carbon, and the presence of tetrahedral carbon in the amorphous structure is the source of the term 'diamond-like'. In reality all DLC coatings contain some alloying elements either by unwanted or intentional inclusion.  $CN_x$  coatings share a lineage with DLC coatings and are an extension of nitrogen alloyed DLCs. The properties of both DLC and  $CN_x$  coatings are still determined in part by the relative share of  $sp^3$  bonded and  $sp^2$  bonded carbon. Coatings that are high in  $sp^3$  hybridisation tend to be harder; with higher elastic modulus. While coatings high in  $sp^2$  hybridised electron bonds are softer and more lubricious. The  $sp^3:sp^2$  ratio is a concept that will occur repeatedly throughout this work. For ease of reference, the following terminology will be used, carbon-based coatings with an  $sp^3$  proportion above 80% are termed tetrahedral amorphous carbon (ta-C), while coatings with a lower  $sp^3$  proportion are termed amorphous carbon (a-C). It is the presence of both bond types that give DLC coatings, and by extension  $CN_x$  coatings, some of their most interesting properties. The next section looks at the role that interlayers and alloying elements play in determining coating properties.

### 3.1.2 The role of coating interlayers

Carbon-based coatings typically show good adhesion to substrates with similar atomic spacing, such as silicon, but poor adhesion to engineering materials such as steel that have much greater atomic spacing. This is compounded by high residual stresses within deposited coatings. The formation of hybridised bonds in carbon-based coatings is dependent on a high degree of carbon subplantation and intermixing during the deposition process (discussed in more detail in section 3.2). This subplantation leads to dense,  $sp^3$  rich coatings but with a high degree of residual compressive stress (up to 10GPa). Residual stress limits coating thickness and poor adhesion to steel substrates can lead to delamination at unacceptably low loads. Issues of adhesion can be mitigated by introducing interlayers between the substrate and coating, which have been shown to promote adhesion and relax residual stresses. Interlayers are typically based on materials that form carbides or silicides, such as chromium, titanium, tungsten, molybdenum and silicon as these demonstrate strong bonding to both steels and carbon-based coatings. Interlayers are typically deposited by the same process used for coating deposition and with sufficient intermixing with substrate and coating, simple interlayers can dramatically improve coating adhesion [1, 2]. Further improvements in

adhesion and stress relaxation can be obtained by application of graded multilayered structures. *Xiang et al* [3] demonstrates good adhesion and load bearing for thick DLC coatings from incorporating a graded Cr/CrN/CrC/a-C interlayer structure. *Voevodin et al* [4] demonstrates a now widely adopted Ti/TiC/a-C graded interlayer for supporting ultra hard DLC coatings.

### 3.1.3 The role of alloying elements

The properties of carbon-based coatings can be expanded and tailored by the addition of alloying elements. Many alloying elements have been explored, the most common are hydrogen, silicon, fluorine, nitrogen, and various metals of which tungsten is the most common. Carbon nitride is an extension of the concept of nitrogen doped carbon coating and will be discussed separately in chapter 6. The wealth of alloying research has been conducted on DLC films, and extensive doping of CN<sub>x</sub> coatings is uncommon. There do exist a number of studies with doping of CN<sub>x</sub> coatings and the results have been varied [5-8]. The following section predominantly applies to DLC coatings.

#### 3.1.3.1 Effect of hydrogen content

The inclusion of trace amounts of hydrogen in carbon-based coatings is often unavoidable; however the inclusion of hydrogen is often intentional and desirable. The effect of hydrogen on the structure and coating properties has been studied by many researchers [9-13]. Increase in hydrogen content increases the incidence of C-H sp<sup>3</sup> bonds with a corresponding reduction in C-C sp<sup>3</sup> bonding. This leads to reduced interlinking, reduced density and a corresponding reduction in hardness and residual stresses. However the principle benefit of the hydrogen content is the role that it has in stabilizing friction response against changes in the atmospheric environment. The role that hydrogen content plays in friction is discussed further in section 3.1.4.1.

#### 3.1.3.2 Effect of silicon and fluorine content

Silicon and fluorine incorporation in the structure of carbon coatings has been shown to affect many of the film properties. Most notably these additives have been demonstrated to lower the surface coating energy and decrease internal stresses that can otherwise cause issues of coating adhesion. Extensive studies of hydrogenated silicon doped DLC films [14-20] have demonstrated coatings of up to 30 at.% Si content

show a decrease in hardness, elastic modulus and internal stress with an increase in silicon content. Fluorine doped carbon coatings (a-C:F) in particular are noted for their reduced surface energy,  $20 \text{ mN m}^{-1}$ , which is lower than that of a-C:H,  $43 \text{ mN m}^{-1}$ , and a-C:Si coatings,  $31 \text{ mN m}^{-1}$ . These surface energies are close to that of PTFE ( $18 \text{ mN m}^{-1}$ ) with only a slight drop in hardness compared to an a-C:H coating, (5-20GPa), far greater than that of PTFE (0.3GPa). This low surface energy helps to ensure a low friction coefficient that is less dependent on the atmospheric environment.

### 3.1.3.3 Effect of metal content

It has been demonstrated that carbon-based coatings can be alloyed with many different metals: Ag, Al, Au, Co, Cr, Cu, Fe, Mo, Nb, Ni, Ru, Ta, Ti and W, and coatings with such metal content are commonly termed a-C:Me [21-27]. Alloying elements that form carbides such as W, Ti and Cr are the most common. There has not been a systematic investigation of the effect of metal dopants on film formation and film properties, however, typically the addition of metal dopants can be said to reduce internal residual stress compared to un-doped carbon coatings, and reduce friction in ambient humid air conditions. Most a-C:Me films exhibit high hardness and high elasticity, alongside low surface energy. Coatings containing W in particular have shown improved interaction with some extreme pressure lubrication additives, this is discussed further in section 3.1.4.4.

This section has established that the composition and microstructure of carbon-based coatings can be extremely varied as can their mechanical properties. This next section looks at the role that those properties have on the friction and wear experienced by carbon-based coatings.

### 3.1.4 Friction and wear properties

Carbon-based coatings have been demonstrated to have perhaps the widest range of dry sliding friction coefficient of any material, 0.001 to  $>1$ , [28-30]. The variation of carbon-based coating friction coefficient has been linked to; interaction of coating and atmosphere, localised coating phase transformation and the build up of transfer layers on counterfaces. The principles behind these dependences are discussed in sections 3.1.4.1, 3.1.4.2 and 3.1.4.3 respectively, and where appropriate discussed in terms of

their affect on wear rate. Also, in many engineering applications oil based lubrication is the standard approach to friction and wear reduction. Therefore understanding the interaction of carbon-based coatings with oil based lubricants and their additives is critical, and will be discussed in section 3.1.4.4.

#### 3.1.4.1 The role of hydrogen and environment

The atmospheric environment in which carbon based coatings are tested has been shown to play an important role in the low friction performance of DLC and  $CN_x$  coatings. A number of studies of tribo-tests in ultra high vacuum (UHV) have shown that hydrogen free DLC coatings exhibit an increase in friction coefficient, while hydrogenated DLC coatings show a dramatic reduction in friction down to super-low friction coefficients [31], see figure 3.3 for an illustration. Similar results have been published for  $CN_x$  coatings [32] and the mechanism appears to be the same. The high friction of the hydrogen free DLC has been attributed to desorption of adsorbates such as hydrogen, oxygen and water from the surface at high vacuum. This leaves dangling  $\sigma$  and  $\pi$  bonds which have high bond energy and can therefore exert a large friction force. By contrast a highly hydrogenated DLC coating in UHV conditions can replenish the desorbed hydrogen and passivate all of the  $\sigma$  and  $\pi$  dangling bonds with hydrogen. In such conditions the coating surface and that of any transfer layer on the counterface will only experience hydrogen interaction through weak van der Waals forces, and friction forces will be extremely low. In humid ambient conditions, relative humidity (RH) >4%, both hydrogen free and hydrogenated DLC surfaces will be terminated by hydrogen, oxygen and water molecules, which will form hydrogen bonds with bond energies greater than weak van der Waals interactions but much less than  $\sigma$  and  $\pi$  bonding, see table 1.1. This accounts for the similar friction coefficients of hydrogenated and hydrogen free DLC coatings in ambient conditions.

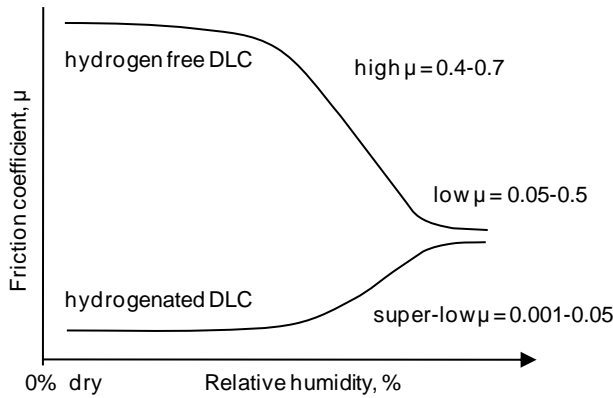


Figure 3.3 – Illustration of friction coefficient against humidity for hydrogenated and hydrogen free DLC coatings

Table 3.1	Super low friction	Typical ambient friction	High friction
Friction range	<0.02	0.1-0.2	>0.5
Interaction type	van der Waals	Hydrogen	$\sigma$ or $\pi$
Energy (eV/bond)	0.08	0.2	0.4-0.8
Material	a-C:H	a-C:H or a-C	Low H DLC
Conditions	(UHV)	(RH>4%)	(UHV)

### 3.1.4.2 The role of localised graphitisation

In the vast majority of engineering applications for carbon based coatings it is not possible to eliminate humidity from the environment, and therefore ultra low friction cannot be achieved. It is thought that carbon based coatings exhibit a low friction coefficient even in humid conditions because the two dimensionally bonded structures linked by van der Waals forces which can slide easily over each other. However carbon based coatings are amorphous and not neatly composed of lubricious layers. Therefore the contacting surfaces are likely composed of both lubricious two dimensionally bonded carbon and strong, hard three dimensionally bonded carbon. Without some other mechanism at work the soft lubricious carbon structure would quickly wear away leaving only the hard, wear resistant, high friction carbon structure intact. This additional mechanism is known as localised graphitisation.

Localised graphitisation is a phase transformation of three dimensionally bonded carbon to two dimensionally bonded carbon at the surface of the coating, leading to a higher proportion of soft lubricious carbon in the contact area. Localised graphitisation was first proposed by Miyoshi [33] and has since been observed in many studies of worn areas of coatings [34, 35], typically by means of Raman spectroscopy [36-38]. Debate exists around the mechanism of graphitisation with two competing theories having emerged. The first theory suggests that the three dimensionally bonded carbon

structures collapse to the lower density two dimensional state by desorption of hydrogen from the surface or by localised heating to 300-400°C by friction [39, 40]; the second theory suggests that transformation could occur due to repetitive straining by friction well before such elevated temperatures are achieved [41-46]. The true underlying mechanism is yet to be elucidated.

In either case the transformation of hard, three dimensional carbon to soft, easily sheared two dimensional carbon raises concerns over an increase in material wear; however for these carbon based coatings a second mechanism helps to ensure friction and wear rates remain low. This mechanism is the formation of transfer layers.

#### 3.1.4.3 The role of transfer layer formation

It has been observed in a great many studies [36-38], dating back to the early development of DLC development, that over extended periods of sliding there is often a build up of a transfer layer of carbonous material on the counterface. This transfer layer has been linked with a reduction in friction and wear rate and established, chiefly by micro-laser Raman spectroscopy, to be largely of graphitised carbon [33-35, 47]. The formation of a transfer layer of graphitised carbon provides two highly lubricious surfaces, and helps to maintain low friction and low wear sliding conditions. However the formation of this transfer layer is typically associated with significant wear of the coated component and counterface as the transfer layer builds. Successful running in of the coated surfaces can therefore prove critical in the long term wear rate of components.

#### 3.1.4.4 Interaction with oil based lubricants

Carbon based coatings such as DLC and  $CN_x$  are commonly considered to be chemically inert. While the surface energies of these coatings vary with alloying content, typically within the range 20-60mJ  $cm^{-2}$  [48], surface bonds are effectively pacified in ambient humid conditions by hydrogen and oxygen [49] and can be considered inert. This has raised debate as to whether true boundary lubrication can occur with carbon-based coating surfaces, and whether contacts can benefit from the anti-wear (AW) and extreme pressure (EP) oil additives that are traditionally used to mitigate failure in severe lubrication conditions. These additives are known to work extremely well in the lubrication of uncoated steel/cast iron/aluminium surfaces. Studies of the tribological

performance of DLC/DLC contacts and DLC/steel contacts have been conducted and the results have been varied [40, 50-58]. Most studies show that in general steel/DLC contacts benefit from the presence of AW additives, but do not benefit from EP friction modifier additives. It has been suggested that the superior thermal conduction of DLC compared to steel means that contacts do not reach the higher activation temperatures required for EP additives [55]. Metal doped DLC coatings in particular have been demonstrated to interact with additives, and form traditional additive/metal tribofilms, although they do not benefit from this interaction to the same degree as steel/steel contacts [51, 56, 58]. Novel lubricant additives have also been tested which are tailored to DLC surfaces, with impressive results, *Kano et al.* [51] report a 45% reduction in steady state sliding friction for hydrogen-free DLC against steel in specially formulated ash-free ester based oils, compared to steel/steel with EP friction modifier additives. CN<sub>x</sub> coating technology is at an earlier stage in its development and there have been no systematic studies of its interaction with engine oils, or oil additive packages. Achieving low friction and wear is an essential aspect of the applicability of DLC and CN<sub>x</sub> coatings.

It has been demonstrated that the composition and microstructure of carbon-based coatings determine their mechanical and tribological properties, which in turn will determine their performance in the valve-train testing. The compositions and microstructures that are achievable are all affected by the deposition techniques used to produce the coatings. Section 3.2 investigates many deposition techniques available, the history of their development, their individual qualities and their typical applications.

### 3.2 Deposition processes

There are a great number of potential deposition processes. Each process has its own advantages, disadvantages and peculiarities. The choice of deposition method can greatly affect the resulting coating, and the optimum deposition process will vary with component design, component composition and the desired coating properties; therefore there is no one best technique. What follows is a discussion some of the most common and promising deposition processes, which fall into one of two categories - physical vapour deposition (PVD) or chemical vapour deposition (CVD). This section also mentions where appropriate the method for inclusion of alloying elements.

### 3.2.1 Physical vapour deposition

Physical vapour deposition (PVD) techniques take place by atomic condensation of a vapour onto the component substrate in a very hard vacuum. The deposition and film growth process is governed by carbon subplantation, where ions are impacted at high energy into the atomic matrix. PVD processes typically make use of a stream of coating ions either driven off from a precursor target or directed in an ion beam from a precursor gas and this makes them largely line of sight. Such processes are therefore challenging when coating complex geometries such as holes. There are a wide variety of PVD techniques; sputter deposition, ion beam deposition, pulsed laser deposition and cathodic vacuum arc deposition are perhaps the most developed and commonly used. A critical factor in determining coating properties is controlling the  $sp^3:sp^2$  hybridisation ratio as described in section 3.1.1. For PVD processes this ratio is largely dependent on the particle impact energy and substrate temperature. The formation of  $sp^3$  hybridised electron bonds and H content are greatly affected by the average impact energy. At very low impact energies the precursor is not decomposed by impact and polymer-like C films form. At very high impact energies the precursor is fully decomposed and hybridisation does occur. Very high impact energies,  $>150\text{eV}$ , have been seen to promote  $sp^2$  hybridisation at the expense of  $sp^3$  hybridisation, generating soft lubricious films. The intermediate impact energy of  $100\text{eV}$  [59] has been demonstrated to generate the highest proportion of  $sp^3$  hybridised bonds. The substrate temperature affects the atomic mobility after impact. It has been seen that for substrate temperatures above  $250^\circ\text{C}$  there is a significant decrease in  $sp^3$  content, as the microstructure relaxes to a  $sp^2$  hybridised state and coating density decreases.

#### 3.2.1.1 Sputtered deposition

Sputtered deposition techniques are perhaps the most common method for industrial deposition of carbon-based films [60-62]. Sputtered deposition occurs in a chamber flooded with argon and held at vacuum pressures ( $10\text{mPa} - 1\text{Pa}$ ). A large negative voltage is applied to the target from which the carbon atoms are to be sputtered, typically  $-2$  to  $-5$  kV (see figure 3.4a). This polarises the argon and forms highly energised plasma of  $\text{Ar}^+$  ions.  $\text{Ar}^+$  ions are drawn to the cathode where they impact and sputter away carbon atoms. These carbon atoms travel back through the plasma and

impact the substrate, which has a considerably smaller bias voltage applied, where they form a thin film. Electrons and ions from the plasma also impact the target and help to sputter carbon atoms, causing atomic mixing. In this way, films are grown and the energy required to form  $sp^3$  and  $sp^2$  hybridised bonds is supplied. In order to improve the sputter rate, magnets are often fitted behind the target in order to hold the secondary electrons released by sputtering near to the target surface, see figure 3.4b [63]. This causes the plasma cloud near the target surface to become more highly ionised therefore increasing the sputter rate. This technique is called magnetron sputtering and is common in most sputtering processes. If the magnetic field is arranged so that it passes across the substrate as well as the target this is known as ‘unbalanced’ magnetron sputtering and the ion bombardment that occurs to the substrate promotes the formation of  $sp^3$  hybridised bonds.

Sputtering has the advantage that the atomic sputter yield rate varies little over ranges of elements for constant impact conditions. This allows for alloys to be sputtered effectively without promotion of a particular element. Sputtering processes can be used to coat both conducting targets with direct current (d.c.) diode plasma generation and insulating targets with radio frequency plasma generation. It should be noted that good cooling is required as up to 95% of the energy used in the process is dissipated in the form of heat.

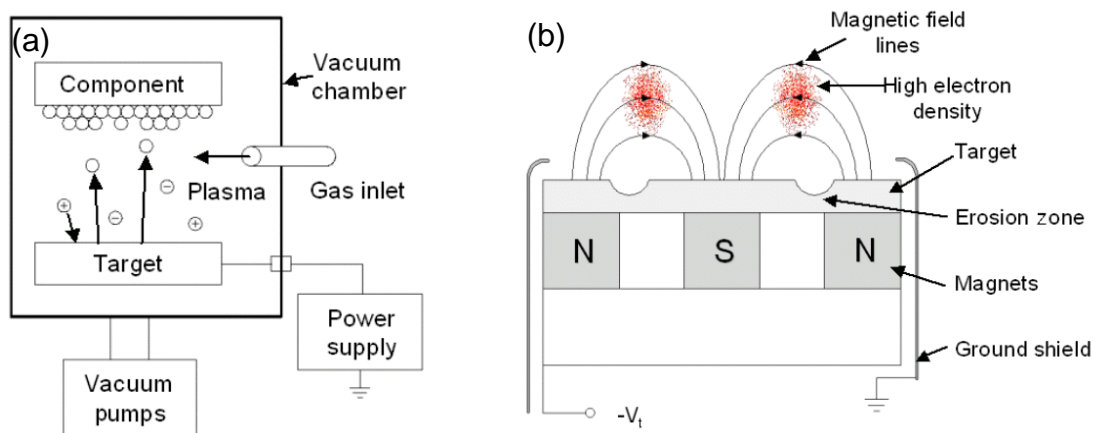


Figure 3.4 – (a) Illustration of sputtering deposition and (b) Illustration of magnetron sputtering. Magnets controlling ion position and creating areas of high ion flux near the target surface.

### 3.2.1.2 Ion beam deposition

Ion beam deposition (IBD) was established in the 1970s as one of the earliest methods for the deposition of DLC coatings. Experiments by Aisenberg and Chabot in the early 1970s [64] used an accelerated  $\text{Ar}^+$  ion beam source to sputter carbon atoms, <10% ionised, from a graphite target allowing them to condense on the substrate (see figure 3.5). Kaufmann used a similar setup to create an ionised hydrocarbon beam, accelerated by a magnetic grid into the vacuum chamber, directly impacting on the substrate and depositing an a-C:H coating (see figure 3.6) [65]. It is the impact of the ions on the growing film that impart the energy required to form  $\text{sp}^3$  hybridised bonds. These techniques both operate at a limited ion flux, where the beam contains a large flux of unionised neutral species, limiting the quality and density of coating that can be produced. Coating quality can be improved by magnetic filtering of the neutral species, improving the ratio of ions to neutrals. The magnetic filtering process can also be used to filter the mass and ion energy of the atoms in the beam. This technique is known as mass-selected ion beam deposition (MSIBD) [66]. The benefit of this method is that carbon ions of ion energy  $\sim 100\text{eV}$  can be selected to make up the majority of the ion beam, yielding high quality, highly reproducible films. The disadvantage of the filtration process is reduced ion flux and very low deposition rates, of the order  $0.001 \text{ \AA s}^{-1}$ . Except in very specialist applications, this precludes MSIBD as an industrially viable technique.

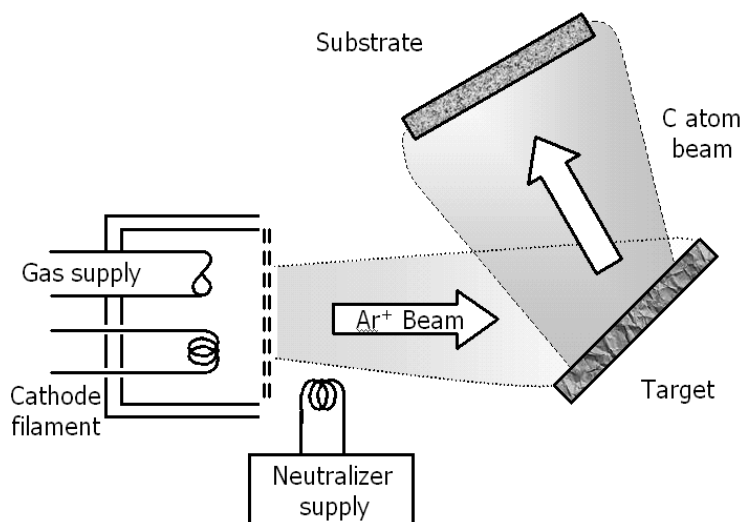


Figure 3.5 – schematic of a simple ion beam deposition technique

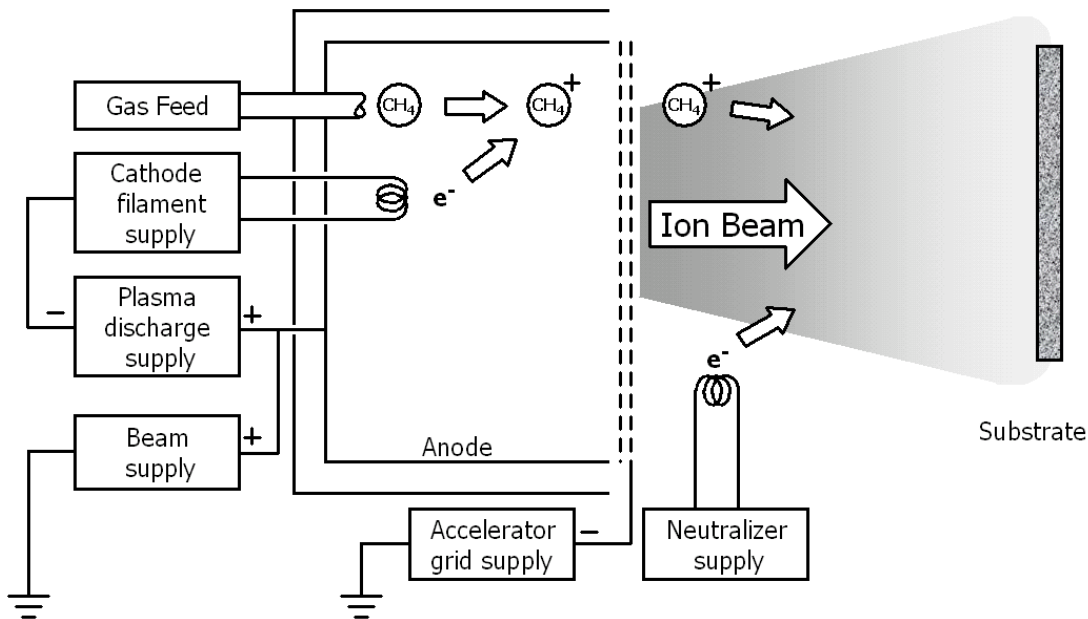


Figure 3.6 – schematic of an ion beam deposition process similar to that used by Kaufmann [65].

### 3.2.1.3 Cathodic vacuum arc

Cathodic vacuum arc (CVA), is a complex industrial scale deposition technique which results in very favourable mechanical film properties. CVA takes place within a high vacuum, typically 0.1- 10mPa. In CVA, a target cathode of very pure graphite is struck with a carbon striker electrode which is then withdrawn to generate the arc discharge. The arc is typically maintained by a low voltage, 15-150V, high current, 20-200A, power supply and results in the formation of energetic plasma. The plasma is very densely packed with ions (up to  $10^{13} \text{ cm}^{-3}$ ) [59]. The current density of the arc is very high ( $\sim 10^7 \text{ A cm}^{-2}$ ) [67] which results in the formation of micrometre sized droplets of target material. If these particulates were allowed to condense onto the substrate surface it would significantly degrade surface finish and uniformity. For many applications, these particulates would be unacceptable. The particulates can be removed by a process of magnetic filtering. A simple filtered cathodic vacuum arc (FCVA) process utilises a curve-linear axial magnetic field, generated by a toroidal duct, coupled with a radial electric field (see figure 3.7). This steers the electrons and ions in a spiral around the magnetic field lines. The particles, which are neutral, are unable to follow this path and are deposited on the walls of the filter duct. This has been demonstrated to considerably improve deposition rate and film/substrate adhesion [68]. There exist a number of more complex techniques for greater filtration which are discussed elsewhere [69].

Even with filtering, CVA is generally unsuitable for the deposition of super smooth coatings for optical applications. Work by Gupta and Bhushan [70] demonstrates that films produced by FCVA can have superior hardness, Young's modulus and scratch resistance compared to that of films produced by IBD, r.f. plasma enhanced CVD, and r.f. sputtering.

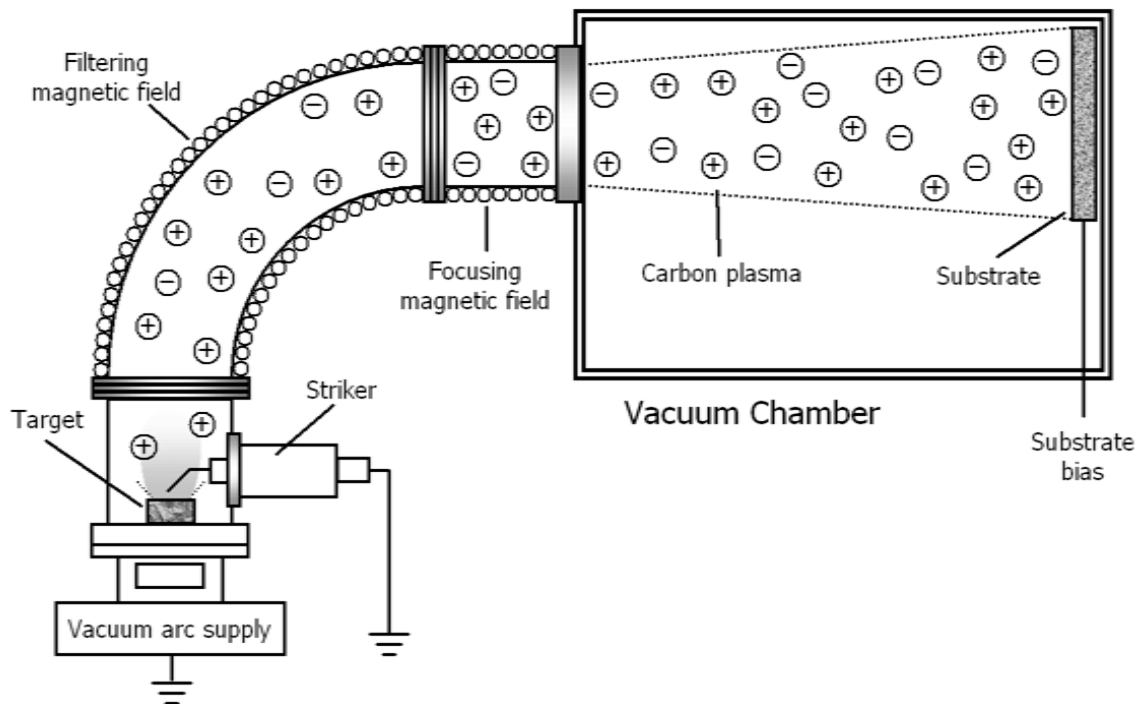


Figure 3.7 – schematic a filtered cathodic vacuum arc (FCVA) deposition process.

#### 3.2.1.4 Pulsed laser deposition

Pulsed laser deposition (PLD) is a very versatile laboratory scale deposition technique capable of depositing a wide variety of materials. The technique utilises an excimer laser beam in short pulses and with high energy to produce a plasma plume of evaporated/ablated material from the target in a high vacuum ( $1\mu\text{Pa}$  -  $10\text{mPa}$ ), see figure 3.8. Atoms are ejected from the target at very high energy in an ablation plume. Subplantation and mixing occur due to high impact energies. The properties and quality of the film are highly dependent on the fluence and wavelength of the laser, the substrate temperature and the hydrogen content [30]. PLD has been used to produce films with very high  $\text{sp}^3$  bonding content, up to 95%. Different alloying elements can be included by alternating using a carousel to change the target between laser pulses. With high rotational speeds this can be done very rapidly and well mixed coatings can be deposited.

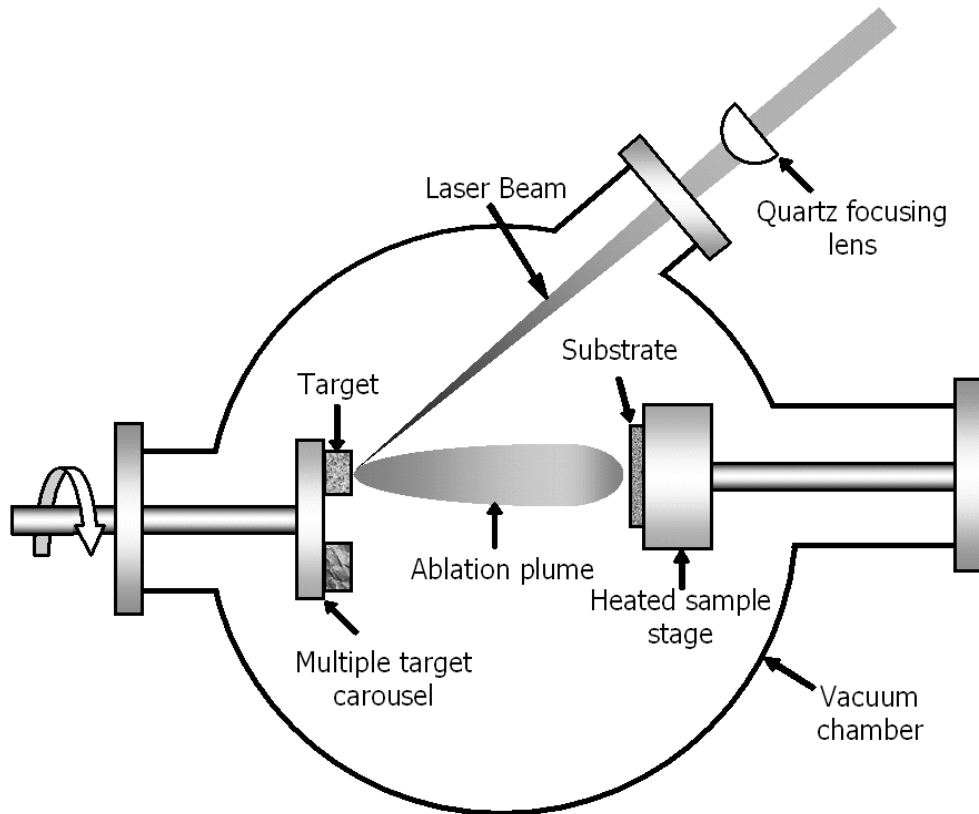


Figure 3.8 – schematic a pulsed laser deposition process.

### 3.2.2 Chemical vapour deposition

Traditional chemical vapour deposition (CVD) is process where target atoms are evaporated in a high temperature environment and decompose onto the substrate by chemical reaction. Typically the process uses a halogen based precursor gas to provide the carbon and hydrogen. This requires temperatures in the coating environment of 800-1000°C, which introduces issues with temperature induced deformation and annealing and limits the materials that can be coated. Typical CVD suitable materials include sintered carbides and some steels, i.e. stainless, A, D, S and H series tool steels if they aren't required to have very high tolerances after coating. CVD produces films with high coating hardness, good adhesion, and uniform coating thickness, however mismatches in thermal expansion can cause problems in films >10µm and at sharp corners where heat exchange is greater. Processes such as plasma enhanced chemical vapour deposition (PECVD) have been developed in an attempt to reduce the required operating temperature of CVD and are a common method for depositing these carbon-based coatings.

### 3.2.2.1 Plasma enhanced chemical vapour deposition

Plasma enhanced (or plasma assisted) chemical vapour deposition (PECVD) utilizes energetic electrons in a plasma cloud alongside thermal effects to activate chemical reaction and film deposition. This allows for considerably reduced substrate temperatures, in the range 100-600°C, typically <300°C. The reduced substrate temperature means that a greater variety of materials can be used, coating thickness and component design are no longer limited by thermal expansion differentials and post deposition tolerance is less of a concern. The plasma is generated either by direct current, microwave frequency or radio frequency fields in a relatively soft vacuum (1Pa – 600Pa, but typically < 10Pa) [59]. In a similar way to sputtered deposition, the plasma introduces ion and electron bombardment which enhance the rate of precursor evaporation and decomposition onto the substrate and also increase subplantation and intermixing.

The coatings of interest in this research were deposited by magnetron sputtering, ion beam assisted deposition, and plasma enhanced chemical vapour deposition (PECVD). The deposition method used for each coating will be described where appropriate in chapters 6 and 7, and where possible, further details of deposition conditions will be given.

This chapter has given a brief introduction to the common properties and deposition methods of the two carbon-based coatings considered in this research; DLC and CN<sub>x</sub>. Even with knowledge of the coatings deposition process it is still necessary to determine the mechanical properties, the tribological properties, the composition, and the microstructure of the coatings under investigation, in order to truly understand their performance in the valve-train. Chapter 4 describes the many experimental test procedures employed to determine the mechanical and tribological coating properties, while chapter 5 discusses the various microscopy, spectroscopy and spectrometry techniques used to determine morphology, composition and microstructure of the coatings.

---

---

### 3.3 Chapter references

- 1 Hainsworth, S.V. and Uhure, N.J. Diamond-like carbon coatings for tribology: production techniques, characterisation methods and application. *International Materials Reviews*, 2007, **52**(3), 153.
- 2 Hong, B., Kim, H.J., Park, Y.S. and Jeon, Y. Tribological Properties of Ultrathin DLC Films with and without Metal Interlayers. *Journal of the Korean Physical Society*, 2007, Vol. 51, September 2007, **51**(3), 1124-1128
- 3 Xiang, Y., Yang, L., Cheng-biao, W., Xin-chun, L. and De-yang, Y. Investigation on preparation and properties of thick DLC film in medium-frequency dual-magnetron sputtering. *Vacuum*, 2005, **80**(4), 324-331.
- 4 Voevodin, A.A., Capano, M.A., Laube, S.J.P., Donley, M.S. and Zabinski, J.S. Design of a Ti/TiC/DLC functionally gradient coating based on studies of structural transitions in Ti-C thin films. *Thin Solid Films*, 1997, **298**(1-2), 107-115.
- 5 Fernandez-Ramos, C., Sanchez-Lopez, J.C., Belin, M., Donnet, C., Pascaretti, F. and Fernandez, A. Tribological and mechanical properties of CN<sub>x</sub>- and SiCN<sub>x</sub>-TiN/Ti multilayered systems grown onto steel. *Vacuum*, 2002, **67**(3-4), 551-558.
- 6 Sarangi, D., Sanjines, R. and Karimi, A. Enhancement of the mechanical properties of the carbon nitride thin films by doping. *Carbon*, 2004, **42**(5-6), 1107-1111.
- 7 Sarangi, D., Sanjines, R. and Karimi, A. Effect of silicon doping on the mechanical and optical properties of carbon nitride thin films. *Thin Solid Films*, 2004, **447-448** Proceedings of the 30th International Conference on Metallurgical Coatings and Thin Films, 217-222.
- 8 C.Fernandez-Ramos, J.C.Sanchez-Lopez, T.C.Rojas and A.Fernandez. Structural modifications of silicon-doped carbon nitride films during postdeposition annealing. *Diamond and Related Materials* 2003, **12**(3-7), 1055-1060.
- 9 Kleinsorge, B., Rodil, S.E., Adamopoulos, G., Robertson, J., Grambole, D. and Fukarek, W. Hydrogen and disorder in diamond-like carbon. *Diamond and Related Materials*, 2001, **10**(3-7), 965-969.
- 10 Erdemir, A. The role of hydrogen in tribological properties of diamond-like carbon films. *Surface and Coatings Technology*, 2001, **146-147**(601), 292-297.
- 11 Chen, C.W. and Robertson, J. Surface atomic properties of tetrahedral amorphous carbon. *Diamond and Related Materials*, 2006, **15**(4-8), 936-938.

- 
- 
- 12 Casiraghi, C., Piazza, F., Ferrari, A.C., Grambole, D. and Robertson, J. Bonding in hydrogenated diamond-like carbon by Raman spectroscopy. *Diamond and Related Materials*, 2005, **14**(3-7), 1098-1102.
  - 13 Robertson, J. Improving the properties of diamond-like carbon. *Diamond and Related Materials*, 2003, **12**(2), 79-84.
  - 14 Goranchev, B., Reichelt, K., Chevallier, J., Hornshoj, P. and Dimigen, H. R.F. reactive sputter deposition of hydrogenated amorphous silicon carbide films, *Thin Solid Films*, 1986, **139**(3), 275.
  - 15 Hioki, T., Itoh, Y., Itoh, A., Hibi, S. and Kawamoto, J. Tribology of carbonaceous films formed by ion-beam- assisted deposition of organic material. *Surface and Coatings Technology*, 1991, **46**(2), 233-243.
  - 16 Dorfman, V.F. Diamond-like nanocomposites (DLN). *Thin Solid Films*, 1992, **212**(1), 267-273.
  - 17 Oguri, K. and Arai, T. Effect of excess carbon on the hardness of Si---C and Ti---C coatings formed by plasma-assisted chemical vapor deposition. *Thin Solid Films*, 1990, **186**(2), L29-31.
  - 18 Oguri, K. and Arai, T. Friction coefficient of Si---C, Ti---C and Ge---C coatings with excess carbon formed by plasma-assisted chemical vapour deposition. *Thin Solid Films*, 1992, **208**(2), 158-160.
  - 19 Miyamoto, T., Kaneko, R. and Miyake, S. Tribological characteristics of amorphous carbon films investigated by point contact microscopy *Journal of Vacuum Science and Technology*, 1991, **B9**(2), 1336-1339
  - 20 Grischke, M., Trojan, K., Dimigen, H. and Bewilogua, K. Application-oriented modifications of deposition processes for diamond-like-carbon-based coatings. *Surface and Coatings Technology*, 1995, **74** (1-3), 739-745.
  - 21 Dimigen, H., Hübsch, H. and Memming, R. Tribological and electrical properties of metal-containing hydrogenated carbon films *Applied Physics Letters*, 1987, **50**(16), 1056.
  - 22 Klages, C.P. and Memming, R. Microstructure and Physical Properties of Metal-Containing Hydrogenated Carbon Films, *Material Science Forum*, 1989, **52-53**, 609.

- 
- 
- 23 Dimigen, H. and Klages, C.P. Microstructure and wear behavior of metal-containing diamond-like coatings. *Surface and Coatings Technology*, 1991, **49**(1), 543-547.
  - 24 Wang, M., Schmidt, K., Reichelt, K., Dimigen, H. and Hubsch, H. Characterization of metal-containing amorphous hydrogenated carbon films *Journal of Materials Res.*, 1992, **7**, 667-676.
  - 25 Klaffke, D., Wäsche, R. and Czichos, H. Wear behaviour of i-carbon coatings. *Wear*, 1992, **153**(1), 149-162.
  - 26 Grischke, M., Bewilogua, K. and Dimigen, H. Preparation, properties and structure of metal containing amorphous hydrogenated carbon films. *Materials and Manufacturing Processes*, 1993, **8** (4) 407-417.
  - 27 Sjostrom, H., Hultman, L., Sundgren, J.E. and Wallenberg, L.R. Microstructure of amorphous C:H and metal-containing C:H films deposited on steel substrates. *Thin Solid Films*, 1993, **232** (2), 169-179.
  - 28 Enke, K. Some new results on the fabrication of and the mechanical, electrical and optical properties of i-carbon layers. *Thin Solid Films*, 1981, **80**(1-3), 227-234.
  - 29 Donnet, C., Le Mogne, T., Ponsonnet, L., Grill, A., Patel, V. and Jahnes, C. The respective role of oxygen and water vapor on the tribology of hydrogenated diamond-like carbon coatings *Tribology letters*, 1998, **4**(3-4), 259-265.
  - 30 Voevodin, A.A. and Donley, M.S. Preparation of amorphous diamond-like carbon coatings by pulsed laser depostion: a critical review. *Surface and Coatings Technology*, 1996, **82**, 199-213.
  - 31 Liu, E., Ding, Y.F., Li, L., Blanpain, B. and Celis, J.-P. Influence of humidity on the friction of diamond and diamond-like carbon materials. *Tribology International*, 2007, **40** (2), 216-219.
  - 32 Sanchez-Lopez, J.C., Donnet, C., Belin, M., Mogne, T.L., Fernandez-Ramos, C., Sayagues, M.J. and Fernandez, A. Tribochemical effects on CN<sub>x</sub> films. *Surface and Coatings Technology*, 2000, **133-134**, 430-436.
  - 33 Miyoshi, K. Studies of mechanochemical interactions in the tribological behavior of materials. *Surface and Coatings Technology*, 1990, **43-44**, 799-812.
  - 34 Bull, S.J. Tribology of carbon coatings: DLC, diamond and beyond. *Diamond and Related Materials*, 1995, **4**(5), 827-836.
-

- 
- 
- 35 Hirvonen, J.-P., Lappalainen, R., Koskinen, A., Anttila, A., Jervis, T.R. and Trakula, M. Tribological characteristics of diamond-like films deposited with an arc-discharge method. *Journal of Materials Res.*, 1990, **5**(11), 2524-2530.
  - 36 Erdemir, A., Switala, M., Wei, R. and Wilbur, P. A tribological investigation of the graphite-to-diamond-like behavior of amorphous carbon films ion beam deposited on. *Surface and Coatings Technology*, 1991, **50**(1), 17-23.
  - 37 Erdemir, A., Nichols, F.A., Pan, X.Z., Wei, R. and Wilbur, P. Friction and wear performance of ion-beam-deposited diamond-like carbon films on steel substrates. *Diamond and Related Materials*, 1994, **3**(1), 119-125.
  - 38 Erdemir, A., Bindal, C., Pagan, J. and Wilbur, P. Characterization of transfer layers on steel surfaces sliding against diamond-like hydrocarbon films in dry nitrogen. *Surface & Coatings Technology*, 1995, **76** (1-3), 559-563.
  - 39 Haque, T., Morina, A., Neville, A., Kapadia, R. and Arrowsmith, S. Non-ferrous coating/lubricant interactions in tribological contacts: Assessment of tribofilms. *Tribology International*, 2007, **40**(10-12), 1603-1612.
  - 40 Haque, T., Morina, A., Neville, A., Kapadia, R. and Arrowsmith, S. Effect of oil additives on the durability of hydrogenated DLC coating under boundary lubrication conditions. *Wear*, 2009, **266**(1-2), 147-157.
  - 41 Zhou, F., Adachi, K. and Kato, K. Sliding friction and wear property of a-C and a-CN<sub>x</sub> coatings against SiC balls in water. *Thin Solid Films*, 2006, **514**(1-2), 231-239.
  - 42 Zhou, F., Adachi, K. and Kato, K. Wear-mechanism map of amorphous carbon nitride coatings sliding against silicon carbide balls in water. *Surface and Coatings Technology*, 2006, **200**(16-17), 4909-4917.
  - 43 Zhou, F., Adachi, K. and Kato, K. Comparisons of tribological property of a-C, a-CN<sub>x</sub> and BCN coatings sliding against SiC balls in water. *Surface and Coatings Technology*, 2006, **200**(14-15), 4471-4478.
  - 44 Zhou, F., Wang, X., Adachi, K. and Kato, K. Influence of normal load and sliding speed on the tribological property of amorphous carbon nitride coatings sliding against Si<sub>3</sub>N<sub>4</sub> balls in water. *Surface and Coatings Technology*, 2008, **202**(15), 3519-3528.
  - 45 Zhou, F., Wang, X., Kato, K. and Dai, Z. Friction and wear property of a-CN<sub>x</sub> coatings sliding against Si<sub>3</sub>N<sub>4</sub> balls in water. *Wear*, 2007, **263**(7-12), 1253-1258.
-

- 46 Zhou, F., Li, K.Y., Bello, I., Lee, C.S. and Lee, S.T. Study of tribological performance of ECR-CVD diamond-like carbon coatings on steel substrates. Part 2. The analysis of wear mechanism. *Wear*, 2005, **258** (10), 1589-1599.
- 47 Grill, A. Review of the tribology of diamond-like carbon. *Wear*, 1993, **168**(1), 143-153.
- 48 Grischke, M., Hieke, A., Morgenweck, F. and Dimigen, H. Variation of the wettability of DLC-coatings by network modification using silicon and oxygen. *Diamond and Related Materials*, 1998, **7** (2), 454-458.
- 49 Erdermir, A. The role of hydrogen in tribological properties of diamond-like carbon films. *Surface and Coatings Technology*, 2001, **146-147** (601), 292-297.
- 50 Ye, J., Kenji, U., Kano, M., Yasuda, Y., G. Dalmaz, A.A.L.D.D. and Priest, M. Ultralow friction properties of DLC lubricated with ester containing oil --Part 2: Nanoscratch analysis of surface friction. *Tribology and Interface Engineering Series*, pp. 693-697 (Elsevier, 2003).
- 51 Kano, M., Yasuda, Y., Mabuchi, Y., Ye, J., Konishi, S., G. Dalmaz, A.A.L.D.D. and Priest, M. Ultra-low friction properties of DLC lubricated with ester-containing oil --Part 1: Pin-on-disc & SRV friction tests. *Tribology and Interface Engineering Series*, pp. 689-692 (Elsevier, 2003).
- 52 Miyake, S., Saito, T., Yasuda, Y., Okamoto, Y. and Kano, M. Improvement of boundary lubrication properties of diamond-like carbon (DLC) films due to metal addition. *Tribology International*, 2004, **37**(9), 751-761.
- 53 Kano, M. Super low friction of DLC applied to engine cam follower lubricated with ester-containing oil. *Tribology International*, 2006, **39**(12), 1682-1685.
- 54 De Barros Bouchet, M.I., Kano, M., Ali, E. and Jean-Michel, M. Superlubricity of diamond/glycerol technology applied to automotive gasoline engines. *Superlubricity*, pp. 471-492 (Elsevier Science B.V., Amsterdam, 2007).
- 55 Kalin, M., Roman, E. and Vizintin, J. The effect of temperature on the tribological mechanisms and reactivity of hydrogenated, amorphous diamond-like carbon coatings under oil-lubricated conditions. *Thin Solid Films*, 2007, **515**(7-8), 3644-3652.
- 56 Kalin, M. and Vizintin, J. Differences in the tribological mechanisms when using non-doped, metal-doped (Ti, WC), and non-metal-doped (Si) diamond-like carbon

- 
- against steel under boundary lubrication, with and without oil additives. *Thin Solid Films*, 2006, **515**(4), 2734-2747.
- 57 Kalin, M. and Vizintin, J. The tribological performance of DLC coatings under oil-lubricated fretting conditions. *Tribology international*, 2006, **39**(10), 1060-1067.
- 58 Kalin, M. and Vizintin, J. A comparison of the tribological behaviour of steel/steel, steel/DLC and DLC/DLC contacts when lubricated with mineral and biodegradable oils. *Wear*, 2006, **261**(1), 22-31.
- 59 Erdemir, A. and Donnet, C. (chap. 24) *Tribology of Diamond, diamond-like carbon and related materials*. In Bhushan, B., ed. *Modern Tribology Handbook* (CRC Press, 2000).
- 60 Bewilogua, K., Wittorf, R., Thomsen, H. and Weber, M. DLC coatings prepared by reactive d.c. magnetron sputtering. *Thin Solid Films*, 2004, **447-448**, 142-147.
- 61 Hans, M., Buchel, R., Grischke, M., Hobi, R. and Zach, M. High volume PVD coating of precision components of large volume at low process costs. *Surface and Coatings Technology*, 2000, **123**, 288-293.
- 62 Strondl, C., Van der Kolk, G.J., Hurkmans, T., Fleischer, W., TRinh, T., Carvalho, N.M. and Hosson, J.T.M.d. Properties and characterizartion of multilayers of carbides and diamond-like carbon. *Surface and Coatings Technology*, 2004, **142-144**, 707-713.
- 63 Renevier, M., Fox, V.C., Teer, D.G., Hampshire, J., Performance of low friction MoS<sub>2</sub>/titanium composite coatings used in forming applications, *J. Materials Design*, 2000, **21** (4), 337-343.
- 64 Aisenberg, S. and Chabot, R. Ion-Beam Deposition of Thin Films of Diamondlike Carbon, *Journal of Applied Physics*, 1971, **42** (7), 2953-2959.
- 65 Kaufman, H.R. Technology of ion beam sources used in sputtering, *Journal of Vacuum Science and Technology*, 1978, **15** (2), 272-276.
- 66 Lifshitz, Y. Hydrogen-free amorphous carbon films: correlation between growth conditions and properties. *Diamond & Related Materials*, 1996, **5**(3), 388-400.
- 67 Robertson, J. Diamond-like amorphous carbon. *Material Science and Engineering Review*, 2002, **37**, 129-281.
- 68 Sanders, D.M. and Pyle, E.A. Magnetic enhancement of cathodic arc deposition. *Journal of Vacuum Science and Technology*, 1987, **5A**, 2728-2731.
-

- 69 Anders, A. Approaches to rid cathodic arc plasmas of macro and nanoparticles: a review. *Surface and Coatings Technology*, 1999, **120-121**, 319-330.
- 70 Gupta, B.K. and Bhushan, B. Micro-mechanical properties of amorphous carbon coatings deposited by different deposition techniques. *Thin Solid Films*, 1995, **270**, 391-398.

# CHAPTER 4

## Experimental techniques and methodology

---

### **4. Experimental techniques and methodology**

#### **4.1 Cam-tappet test rig**

#### **4.2 Adhesion**

#### **4.3 Hardness and modulus**

#### **4.4 Wear**

##### *4.4.1 Abrasive wear*

##### *4.4.2 Sliding wear*

#### **4.5 Impact wear resistance**

#### **4.6 Chapter references**

---

The performance of DLC and other thin film coatings in the valve-train is dependent on the various properties of the coatings and the valve-train environment. The mechanical and tribological properties of the coatings are therefore critical to an understanding of coating performance. Chapter 2 was concerned with the valve-train and the development of the cam-tappet testing rig. This chapter discusses the test procedure used for the valve-train testing and the different test procedures used to characterise the coatings mechanical and tribological properties.

#### **4.1 Cam-tappet test rig**

The performances of the coated shims were investigated by short duration tests in an instrumented test rig described in a chapter 2. The engine oil used was standard grade SAE 5W30 that was free of friction modifier additives, and the operating temperature close to the cam-tappet contact was measured to be  $102 \pm 3^\circ\text{C}$ . In order to investigate the importance of impact loading on coating durability, testing was conducted with the test rig in two set-ups. The first set-up was the 'normal' condition, where the valve-train mechanical system allows the cam and tappet to come out of contact as described in

section 2.2. The second condition was an adaptation of normal operation where the pre-compression of the spring was released; this keeps the surfaces in contact and effectively eliminates impact loading. The total relative sliding distance between the contacting surfaces increases since the cam is in continuous contact with the tappet. Tests were conducted in 15 minute intervals at 1000rpm, after each interval the speed was dropped briefly to 450rpm and the torque was recorded, the test was then stopped and the coatings were visually inspected for evidence of coating failure. If there was no evidence of coating failure another 15 minute test was performed and this process repeated. It was not possible to conduct impact and impact free testing for all coatings and the specific details of what testing was conducted is described in the relevant chapters.

#### 4.2 Adhesion

Poor adhesion of coating and substrate can cause coating delamination early in the coatings working lifetime, therefore good adhesion is critical to durability. Many methods exist for the assessment of adhesion [1]. One of the most common quantitative methods is scratch testing. A common scratch test procedure is that of a ramped load scratch test. A stylus, typically a diamond cone, has an increasing normal load applied to it as it is drawn across the surface of the coated sample up to a maximum load (see figure 4.1). The scratch that this generates can then be assessed by microscopy to locate the points of coating failure, and the load corresponding to this point is termed the critical load,  $L_c$ . The minimum critical load is not always clear and often multiple critical loads are quoted as the failure mode evolves along the scratch length. This can make direct comparison between coating and substrate pairings difficult. In this study two critical loads are used to denote first failure and gross coating failure,  $L_{c1}$ , and  $L_{c2}$  respectively. First failure is defined as the earliest point in the scratch that coating delamination and substrate exposure occurs. Gross failure is more difficult to define as failure mechanisms often evolve steadily over the length of the scratch, for this study it is defined as the point at which the delamination in the scratch track becomes contiguous, as illustrated in figure 4.2.

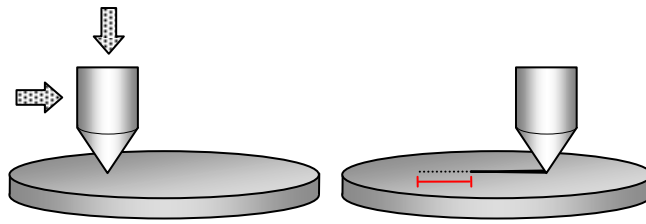


Figure 4.1 – Illustration of the scratch adhesion test procedure, with loaded stylus drawn across to create a scratch.

This distinction is arbitrary but was maintained between samples and gives a useful identifier of major coating failure. The failure modes that occur can also indicate other coating properties such as ductility, fracture toughness [2] and the load support of the substrate. The friction coefficient of stylus motion is often measured as a dramatic change in friction can occur with the onset of failure. Acoustic emission measurement can be used in a similar way to identify the onset of some failure mechanisms.

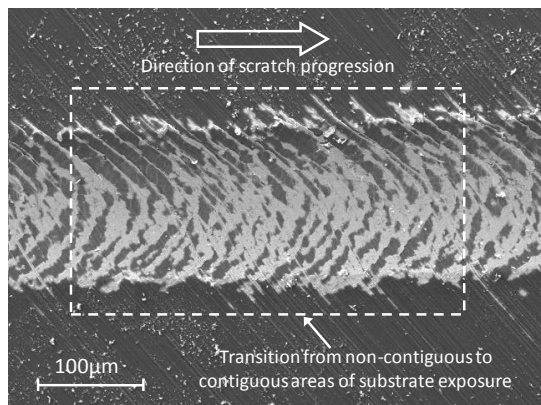


Figure 4.2 – Example of the point of second critical failure,  $L_{c2}$ , defined as the point at which substrate exposure becomes contiguous.

The scratch-adhesion testing conducted in this study was carried out on a Teer Coatings Ltd. ST-200 scratch tester (see figure 4.3). In this setup, the friction force was measured by the displacement of the bed on which the sample was mounted. This bed was supported by sprung beams which were rigid vertically but flexible in the direction of scratch progression. The displacement of the table was therefore related to the friction force between stylus and sample. The displacement of the bed was measured by the change in the width of an air gap between the bed and an aluminium support, measured by eddy current sensor. The setup was calibrated and the relationship between air gap width and applied friction force determined.

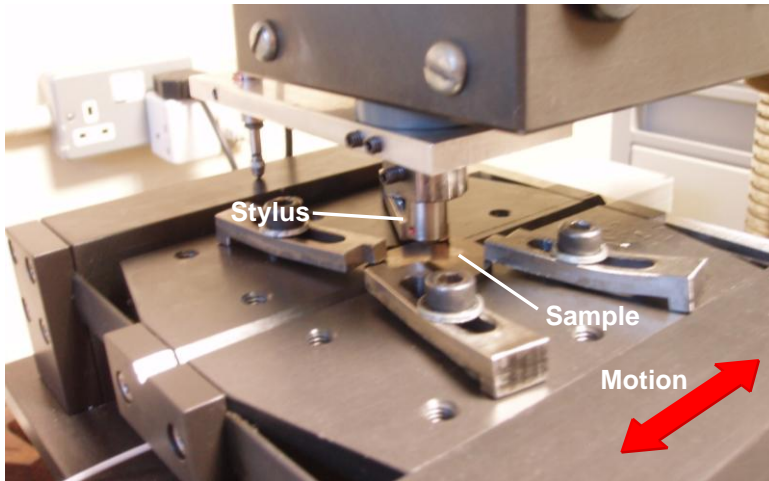


Figure 4.3– ST-200 scratch tester, detail of the point of contact

#### 4.3 Hardness and modulus

Hardness is typically assessed by generating indentations in a materials surface and measuring the resulting plastically deformed area. When measuring the hardness and modulus of thin films it is desirable to make shallow very indentations. When a component is indented there is typically a stress distribution that extends both into the coating and the supporting substrate. Therefore the observed deformation will be a combined response of coating and substrate. It is desirable for purposes of comparison to evaluate the properties of the coating in isolation of the substrate. The UK National Physical Laboratory suggested that if the indentation depth is  $<10\%$  of the coating thickness then the stress is largely confined to the coating and the hardness can be identified in isolation from the substrate [3]. However it has been demonstrated that the indentation depth must be orders of magnitude shallower in order to observe coating modulus independently of substrate [4].

The procedure used in this work produces very shallow indentations and is therefore known as nanoindentation. In recent years nanoindentation has become a widely used technique for assessing elastic modulus and hardness. In a nanoindentation test a shaped indenter, commonly a Berkovich geometry diamond, has a ramped load applied normal to the component surface. This causes initially elastic then plastic deformation as the indenter penetrates the surface, and from the depth of the residual indentation the material hardness can be estimated. Indentations of depth approaching 10% of coating thickness are often too small to be viewed by conventional microscopy and instead indentation depth is measured continuously during indentation rather than by

post inspection of the indentation. The indentation depth (or displacement) can then be plotted against applied load and the hardness and elastic modulus can be calculated by the Oliver Pharr approach [5] (see figure 4.4 for a typical load displacement curve).

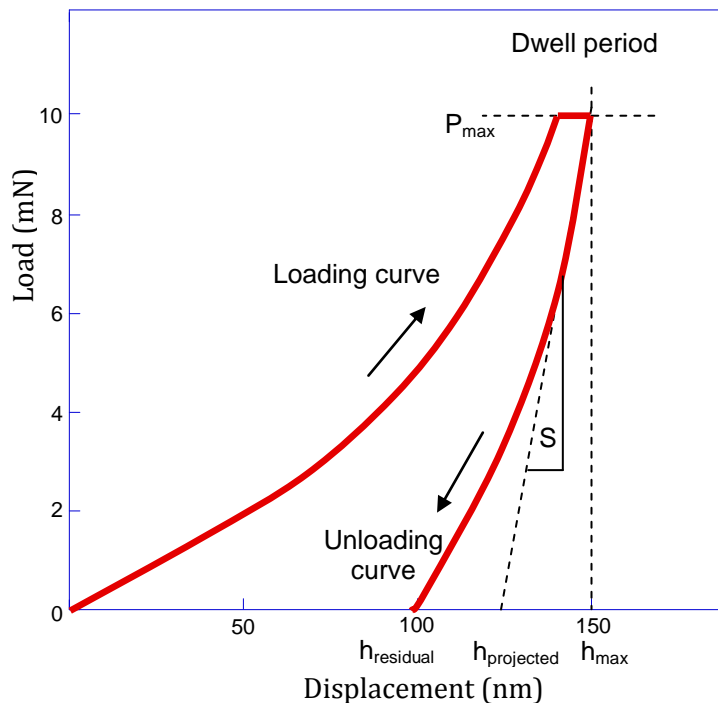


Figure 4.4- Typical load-displacement curve from a nano-indentation test.

In this approach a modified Sneddons relationship [6] is fitted to the unloading section of the load–curve. The Sneddons relationship is given by:

$$S = \frac{dP}{dh} = 2 \frac{\sqrt{A_r}}{\sqrt{\pi}} E_r \quad (1)$$

Where  $S$  is the unloading stiffness,  $P$  is the applied load,  $h$  is the indentation depth,  $E_r$  is the reduced modulus and  $A_r$  is the projected area of contact. The hardness,  $H$ , is then calculated by the applied load over the contact area, calculated from the indentation depth and a knowledge of indenter geometry.

$$H = \frac{P}{A_r} \quad (2)$$

In many cases, it is not possible to achieve reliable and reproducible load-displacement curves at very low indentation depths, as surface roughness effects and film anisotropy cause significant variance between tests. This makes direct calculations of film only hardness and modulus very difficult and a number of models have been developed to allow for separation of film and substrate properties over a wider range of indentation

depths. One of the most commonly used model was developed by Korsunsky *et al* [7] furthering a concept developed by Jönsson and Hogmark [8]. In this model, the relative volume fractions of film and substrate that are in support of the applied load are taken into consideration and calculation is made of their separate contributions to modulus and hardness. This allows data taken from indentations deeper than 10% film thickness to contribute to the calculation of film hardness. The model fits the composite hardness against the relative indentation depth,  $\beta$ , which is distinct from the  $\beta$  term in equation (1) and is the indentation depth,  $h$ , over the film thickness,  $t$ .

$$H_c = H_s + \frac{H_f - H_s}{1 + k\beta^2} \quad (3)$$

Where  $H_c$  is the composite hardness,  $H_s$  is the substrate hardness,  $H_f$  is the film hardness and  $k$  is a constant determined by experimental fitting of the data.

#### 4.4 Wear

During the operation of the valve-train the contacting surfaces of cam and tappet are exposed to a relatively high friction, high wear environment. The point of contact is typically heavily loaded and the lubrication regime is mixed boundary and elasto-hydrodynamic [9] making adhesive and abrasive wear likely. It is important to assess the wear performance of any potential coatings in terms of these different mechanisms. This section looks at the methodology for assessing abrasive wear resistance and sliding wear resistance. There is also reason to believe that impact loading may be a wear inducing process, this is discussed in detail in section 4.5.

##### 4.4.1 Abrasive wear

Microabrasion wear testing (ball cratering) is an effective way of assessing the abrasive wear resistance of coatings and is commonly used for hard thin films like DLC [10-14]. The test consists of feeding abrasive slurry, typically silicon carbide or alumina, into the contact between the component and a rotating ball, (see figure 4.5), in order to generate a spherical depression of abraded material, also known as a wear scar, (see figure 4.6). For reproducible results it is important to closely monitor and control the rotating speed, slurry feed, slurry consistency and applied load. A number of wear scars can be generated over varying sliding distances and both film and substrate wear resistance

can be assessed by investigating the diameter of the wear scars. The volume loss of the coating,  $V_c$ , and of the substrate,  $V_s$ , can then be calculated from the measured diameter,  $a$ , from equations (4) and (5).

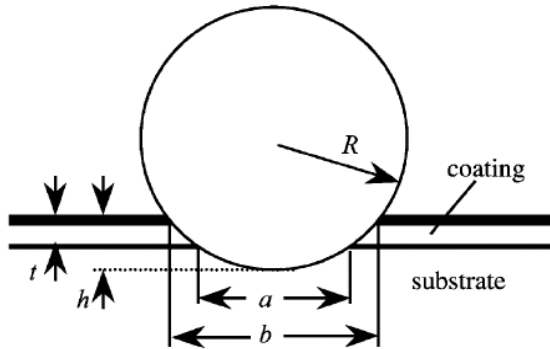


Figure 4.5 – Schematic of the measurement of micro-scale abrasion of coated substrates.

$$V_c \approx \frac{\pi t}{4} (a^2 + 4Rt) \quad (4)$$

$$V_s \approx \frac{\pi a^4}{64R} \quad (5)$$

The wear volumes for each scar can then be plotted on a graph of  $SN/V_c$  against  $V_s/V_c$ , where  $S$  is sliding distance,  $N$  is applied load. From this plot, a linear fit can be made for each sample and the specific wear rate for coating,  $k_c$ , and specific wear rate of substrate,  $k_s$ , can then be calculated from the gradient and intercept, from equation 6.

$$\frac{SN}{V_c} = \frac{1}{k_s} \frac{V_s}{V_c} + \frac{1}{k_c} \quad (6)$$

The tests carried out in this research were conducted on an in-house design of microabrasion tester pictured in figure 4.7.

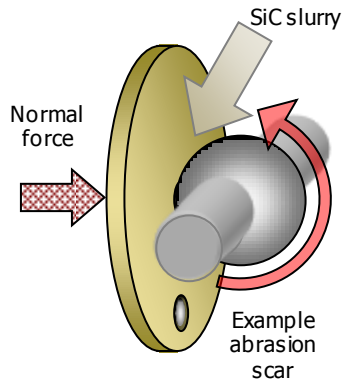


Figure 4.6 – Illustration of the microabrasion test procedure

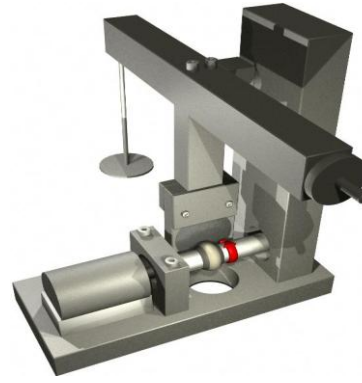


Figure 4.7 – Illustration of the microabrasion test equipment

#### 4.4.2 Sliding wear

The relative motion of two loaded surfaces is liable to cause adhesive and/or abrasive wear depending on the lubricant used, surface chemistry, loading of surfaces, relative sliding speed and surface finish. Sliding wear resistance of a surface can be assessed by a number of methods [15-19] of which pin-on-disk and reciprocating sliding wear testing are two of the most common (see figure 4.8). These test procedures both use the relative motion between the sample and a loaded stylus to generate a wear scar. The stylus is typically a hard engineering material such as steel, alumina, or silicon carbide - with a uniform surface finish. A number of geometries are common, but the testing conducted here has been limited to spherical stylus geometries. Wear scars are generated for various changes of parameters which typically include, load, sliding distance and lubrication conditions. The wear scars are then measured to determine volume loss either by: (i) profilometry, or; (ii) mass loss. The volume loss can then be related to the sliding speed and applied load to give the specific wear rate (units of  $\text{N}^{-1} \text{m}^{-2}$ ). It is common for such experiments to also measure friction force throughout testing. This is done for two reasons: (i) friction coefficient is often a property of interest in coating applications, and; (ii) a dramatic change in friction response can indicate lubrication or coating breakdown. Reciprocating sliding wear has the advantage of generating a smaller scar area, useful if available sample area is limited.

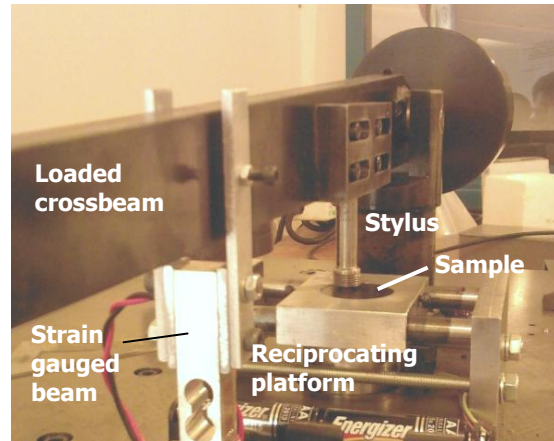
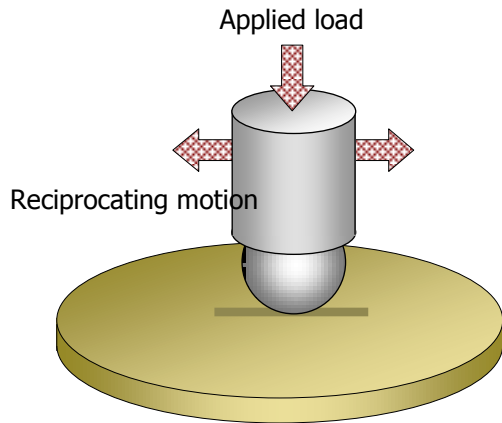


Figure 4.8 – Illustration of reciprocating wear process      Figure 4.9 – High speed wear apparatus

The reciprocating wear tests conducted in this study were carried out on one of two pieces of equipment. The first was the same Teer Coatings Ltd. ST-200 scratch tester that was used for scratch-adhesion testing. This was used for low speed sliding wear tests,  $\sim 0.005 \text{ m s}^{-1}$ , with friction measured in the same manner as is described for scratch testing, (see section 4.2). The second was a pin-on-disc wear tester that was adapted for reciprocating wear. This test equipment was used for higher sliding speeds,  $\sim 0.05 \text{ m s}^{-1}$ , and friction was measured by the deflection of a strain gauged beam (see figure 4.9).

#### 4.5 Impact wear resistance

As discussed in section 2.2, impact loading can occur in the direct-acting overhead camshaft (DOHC) valve-train and it is considered that this process may well be detrimental to coating durability. The effect of impact loading as part of the cycle is investigated in the cam-tappet test rig as described in section 2.2. However, if the impact wear resistance of coatings is to be used to indicate valve-train performance it should be measurable in the laboratory, independently of the other damaging forces of service in the valve-train. Therefore an experimental ‘impactor’ was developed to conduct impact testing in a controllable laboratory test. Impact loading with the impactor is conducted in such a way as to mimic the impact loading that occurs in the valve-train. Figure 4.10 shows the apparatus used. The stylus (A), a 25mm diameter  $\text{Al}_2\text{O}_3$  ball, is mounted on the top crosshead of the material tester. The top crosshead remains stationary during testing and thus the position of the stylus is fixed. The

bottom frame (B) that supports the sample is attached to the bottom crosshead of the tester. The bottom crosshead is oscillated to provide the cyclic impact. The supporting arm (C) on which the sample is mounted is free to move up and down the guide rails (D). The supporting arm itself sits on a spring (E) which is pre-compressed to  $\sim 80\text{N}$  and held in position between a nut (F) and stopper (G). When the sample is moved up into contact with the stylus, the motion of the supporting arm is arrested. The bottom frame continues to be displaced upwards and the spring is compressed. Since the bottom frame has moved upwards, it no longer makes contact with the stopper (G). The force of compressing the spring is transferred from the stopper (G) and bottom frame (B) to the sample and stylus (A) contact. This method allows high impact loading rates to be generated,  $\sim 40\text{kN s}^{-1}$ . The impact angle is varied between  $45^\circ$ ,  $30^\circ$ ,  $15^\circ$  and  $0^\circ$ ; where  $0^\circ$  has the applied load normal to the sample surface, by changing the angled sample holder (H).

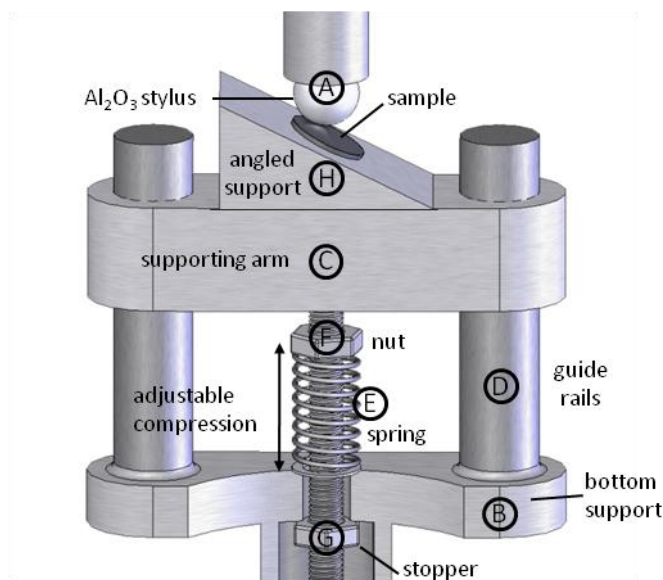


Figure 4.10 - Schematic of impact test rig.

Each of the tests described in this chapter are damaging in some way to the coatings being tested, leaving residual indentations, marks or wear scars. The visual inspection of these marks is part of the analysis of results for many of these tests and it relies upon detailed microscopy. Chapter 5 explores microscopy techniques used in this work along with the spectrometry and spectroscopy techniques used to identify coating microstructure and composition discussed in chapter 3.

---

---

#### 4.6 Chapter references

- 1 Volinsky, A.A., Moody, N.R. and Gerberich, W.W. Interfacial toughness measurements for thin films on substrates. *Acta Materialia*, 2002, **50**, 411-446.
- 2 Bull, S.J. Failure mode maps in thin film scratch adhesion tests. *Tribology International*, 1997, **30**, 491-498.
- 3 Peggs, G.N. and Leigh, I.C. Report MOM62. UK National Physics Laboratory, England, 1983.
- 4 Yu, H.Y., Sanday, S.C. and Rath, B.B. The effect of substrate on the elastic properties of films determined by the indentation test- Axisymmetric Boussinesq problem. *Journal of Mechanics and Physics of Solids*, 1990, **38**(6), 745-764.
- 5 Oliver, W.C. and Pharr, G.M. An improved technique for determining hardness and elastic modulus using load and displacement sensing indentation experiments. *Journal of Materials Res.*, 1992, **7**, 1564-1583.
- 6 Sneddon, I. The relation between load and penetration in the axisymmetric Boussinesq problem for a punch of arbitrary profile. *International Journal of Engineering and Science*, 1965, **3**, 47-57.
- 7 Korsunsky, A.M., McGurk, M.R., Bull, S.J. and Page, T.F. On hardness of coated systems. *Surface and Coatings Technology*, 1998, **99**(1-2), 171-183.
- 8 Jönsson, B. and Hogmark, S. Hardness measurement of thin films. *Thin Solid Films*, 1984, **114**(3), 257-269.
- 9 Priest, M. and Taylor, C.M. Automobile engine tribology -- approaching the surface. *Wear*, 2000, **241**(2), 193-203.
- 10 Gee, M.G., Gant, A., Hutchings, I.M., Bethke, R., Shiffman, K., van Acker, A., Poulat, S., Gachon, Y. and von Stebut, J. Progress towards standardisation of ball cratering. *Wear*, 2003, **255** (1), 1-13.
- 11 Gee, M.G. and Wicks, M.J. Ball crater testing for the measurement of the unlubricated sliding wear of wear-resistant coatings. *Surface and Coatings Technology*, 2000, **133-134**, 376-382.
- 12 Kusano, Y. and Hutchings, I.M. Sources of variability on the free ball micro-scale abrasion test. *Wear*, 2005, **258**, 313-317.
- 13 Rutherford, K.L. and Hutchings, I.M. A microabrasive wear test, with particular application to coated systems. *Surface and Coatings Technology*, 1996, **79**, 231-239.

- 14 Trezona, R.I., Allsopp, D.N. and Hutchings, I.M. Transitions between two-body and three-body abrasive wear: influence of test conditions in the microscale abrasive wear test. *Wear*, 1999, **225-229** (1), 205-214.
- 15 Psyllaki, P.P., Jeandin, M., Pantelis, D.I. and Allouard, M. Pin-on-disc testing of PE-CVD diamond-like carbon coatings on tool steel substrates. *Surface and Coatings Technology*, 2000, **130** (2-3), 297-303.
- 16 Kennedy, F.E., Lidhagen, D., Erdemir, A., Woodford, J.B. and Kato, T. Tribological behaviour of hard carbon coatings on steel substrates. *Wear*, 2003, **255** (2), 854-858.
- 17 Andersson, J., Erck, R.A. and Erdemir, A. Friction of diamond-like carbon films in different atmospheres. *Wear*, 2003, **254**, 1070-1075.
- 18 Bellido-González, V., Hampshire, J., Jones, A.H.S., Allen, T.J., Witts, J., Teer, D.G. and Pierret, B. Advances in the analysis and characterization of DLC coatings. *Surface and Coatings Technology*, 1998, **98** (1-3), 1272-1279.
- 19 Erdemir, A. and Fenske, G.R. Tribological performance of diamond and diamond-like carbon films at elevated temperatures. *Tribology Transcript*, 1996, **39**(4), 787-794.

# CHAPTER 5

## Microscopy, spectroscopy and spectrometry

---

### **5. Microscopy, spectroscopy and spectrometry**

#### **5.1 Microscopy and spectroscopy**

##### *5.1.1 Optical microscopy*

##### *5.1.2 Scanning electron microscopy*

##### *5.1.3 Scanning probe microscopy*

#### **5.2 Spectrometry**

#### **5.3 Chapter references**

---

Microscopy is an important aspect of assessing tribological problems, from measuring surface finish, to investigating wear mechanisms and coating morphology. Spectroscopy and spectrometry techniques are equally important yielding information on the chemical make-up and microstructure of coatings. The following section gives a brief introduction to the microscopy, spectroscopy and spectrometry techniques used in this research.

#### 5.1 Microscopy and spectroscopy

Microscopy is the visualisation of the minute through various types of microscope. The three most common types of microscope for materials research are: optical; scanning electron; and scanning probe, each of which has advantages, disadvantages and different areas of application.

##### 5.1.1 Optical microscopy

Optical microscopy is the oldest microscopy technique, developed in the 16<sup>th</sup> century, and it is still the most common microscopy technique today. Optical microscopy has the

advantages of relatively low price and large field of view. Optical microscopy does however have a number of limitations, which are: (i) The effect of light diffracting from features of surface finish can make imaging of topography difficult; (ii) short depth of field and; (iii) a relatively low theoretical and practical resolution.

### 5.1.2 Scanning electron microscopy

Scanning electron microscopy (SEM) overcomes many of the limitations of optical microscopy. SEM generates images by collecting the electromagnetic emissions from surfaces bombarded with an electron beam. The scanning electron microscope works by generating a source of electrons from an electron gun which are then channelled and focused by a series of electromagnetic lenses to a point on the sample surface.

Electromagnetic guides are used to steer the electron beam such that it scans a rectangular raster of the sample surface, which is used to build an image through careful monitoring of beam position and emission detection (see figure 5.1). The resolution of electron microscopy is greater than that of optical microscopy, due to the shorter wavelength of the electron beam compared to that of reflected light. With an equivalent wavelength of  $\sim 0.02\text{nm}$ , SEM has a maximum theoretical resolution of  $<1\text{nm}$ . The maximum practical resolution is actually limited by the 'spot size' of the beam, i.e. the area over which the electrons make impact. A larger spot size creates a greater the overlap in scan points, averaging and improving signal to noise ratio. There is therefore a compromise between resolution and signal quality. When the electron beam interacts with the sample surface it causes electron scattering and emission of electromagnetic radiation in a characteristic teardrop shaped volume (see figure 5.2). The different emissions can be used to gain a range of information from the sample surface. Secondary electrons are inelastically scattered from the surface, from depths of a few wavelengths. As the majority of secondary electrons are released at from a small, shallow volume they are ideal for imaging detailed surface topography of the sample (see figure 5.3). Backscattered electrons are high energy electrons that are elastically scattered through the solid to re-emerge from within the sample surface. This scattering is dependent upon the atomic number, of the material they travel through. For material with high atomic number there is a high degree of scattering and greater signal return. Therefore back-scattered electrons can be used to contrast different chemical

compositions, which is particularly useful when investigating wear regimes to clearly identify coating failure and exposure of substrate. They are released from greater depths and from a wider area than secondary electrons and therefore have reduced spatial resolution compared to secondary electrons.

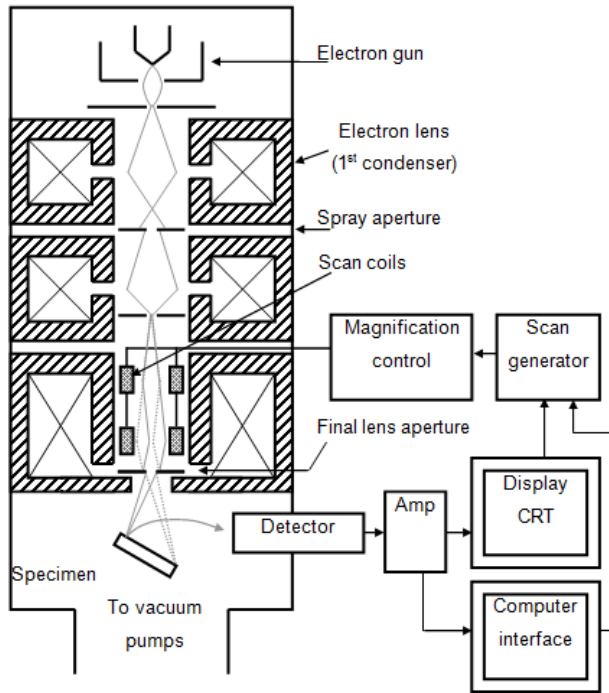


Figure 5.1 – Schematic of a scanning electron microscope showing the beam generation, focusing and scanning stages.

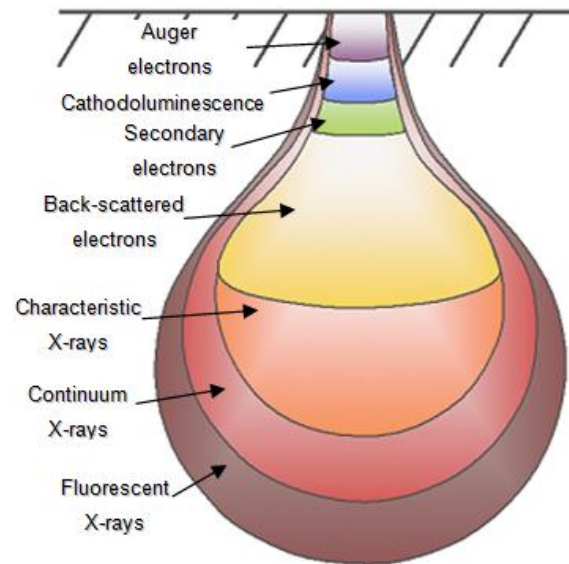


Figure 5.2 – Illustration of the emissions released by electron bombardment.

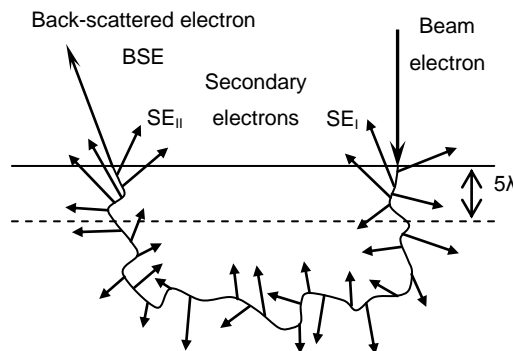


Figure 5.3 – Emission of secondary electrons and the backscattered electron path through the sample.

It is also possible to gain information about the chemical composition by spectroscopy. In this study energy dispersive X-ray analysis (EDX) was used to identify chemical

composition from the characteristic X-rays emitted from the bombarded surface. The highly energised electrons in the incident beam cause inner-shell electrons to be ejected from effected atoms creating an electron hole. The electron hole is filled from an outer-shell electron with higher energy and the energy difference is released as an X-ray quanta. The X-ray energy emitted is characteristic of the energy difference between the two shells and therefore the element from which they were released.

### 5.1.3 Scanning probe microscopy

Scanning probe microscopy (SPM) differs from optical and electron microscopy as it is a mechanical process, imaging using a physical probe in close proximity to the surface. The SPM technique used in this work was atomic force microscopy (AFM). AFM works by drawing a micron-scale cantilever, typically silicon and with a tip radius in the order of nanometres, across the specimen surface. As the tip comes into proximity with the surface it is displaced by the surface forces. A laser is reflected at an angle off the rear surface of the cantilever and displacement is measured by the motion of the reflected laser spot on a photodiode array (see figure 5.4). Similar to SEM the probe is scanned across the surface in a rectangular raster, to build an image. The use of piezoelectric actuators for controlling probe position allow for very high, often atomic, resolutions [1-3]. By measuring displacement of the cantilever during a raster it is possible to build a three dimensional image of surface topography. AFM is typically limited to small scan areas,  $<150\mu\text{m}^2$ , and is a slow image capture process compared to SEM. Depending on the AFM device it is also possible to gather information of Van der Waals forces, capillary forces, chemical bonding, electrostatic forces, friction forces and magnetic forces. In this research SPM work was limited to measurement of topography for identifying surface finish and assessing microscopic and nanoscopic wear.

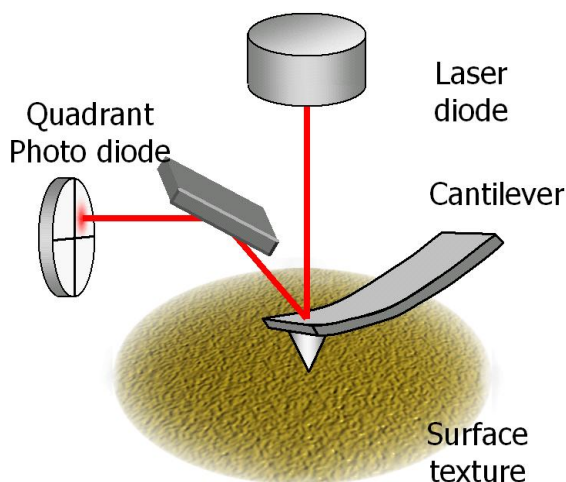


Figure 5.4 – Schematic of the principle components of an AFM system.

## 5.2 Spectrometry

In assessing the properties of diamond-like carbon and carbon nitride coatings it is important to establish the ratio of  $sp^2$  and  $sp^3$  hybridised electrons, as described in chapter 3. The  $sp^3:sp^2$  ratio affects the carbon bonding and crystallographic structure of the coating which in turn influences mechanical and tribological properties. A number of techniques exist for determining this ratio [4-6]. The technique that this study makes use of is Raman spectrometry. Raman spectrometry is a relatively quick, non-destructive technique and can be carried out with limited sample preparation. Raman spectrometry works by application of an  $Ar^+$  ion laser of monochromatic light to the surface of the sample. The majority of light that is scattered from a surface is scattered elastically by Rayleigh scattering and has the same energy after scattering as it had before. A small proportion of the light will undergo inelastic Raman scattering from the excited region. The intensity of Raman scattered light is dependent on the vibrational modes of the microstructure. By measuring the magnitude of return across resonant frequencies which are characteristic of  $sp^2$  hybridised bonds and  $sp^3$  hybridised bonds, the  $sp^3:sp^2$  ratio can be estimated. The information available from Raman spectroscopy is dependent upon the wavelength of light in the laser. Visible laser light (514nm, for this apparatus) is unable to excite the  $sp^3$  hybridised carbon structure directly and the  $sp^3$  ratio must instead be inferred from the information generated from  $sp^2$  bond excitation. Ultraviolet (UV) laser light (220-280nm) can excite the  $sp^3$  hybridised carbon bonding and the  $sp^2:sp^3$  ratio can be determined directly. However monochromatic UV

lasers are prohibitively expensive. Figure 5.5 below gives an illustration of a typical Raman spectrum for a hydrogenated DLC with high  $sp^3$  content. The scattered photons of interest have wavenumbers occurring between  $1000$  and  $1800\text{cm}^{-1}$ . In Raman spectra of amorphous carbon there are typically three features of interest: (i) the graphite G peak; (ii) the disorder D peak, and; (iii) the photo-luminescent (PL) background slope. Extensive study [5-10] has shown that the relative intensity and position of these features can be used to infer the  $sp^2:sp^3$  ratio and hydrogen content. As a rough guide a high  $sp^2$  content is indicated by a high  $I(D)/I(G)$  value and a G peak centre at higher Raman shift. High hydrogen content is indicated by a steeper PL background slope. The background slope is normalised by the intensity of the disorder peak,  $m/I(D)$ .

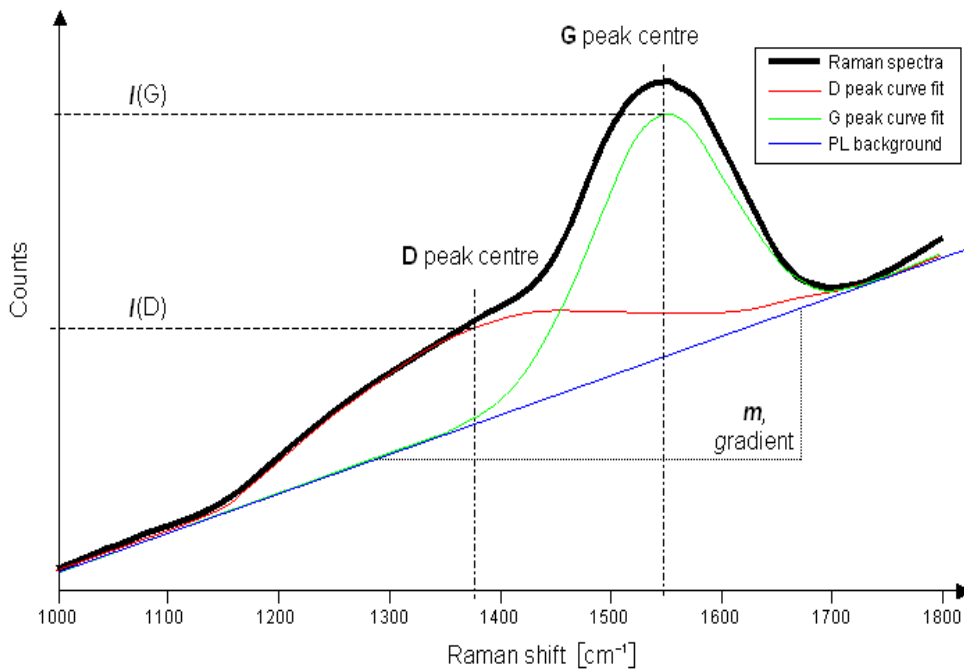


Figure 5.5 – A typical Raman spectrum for DLC

The chapters up to this point in this work have been introducing background information on the automotive valve-train, carbon-based coatings, experimental coatings and microscopy. The chapters that follow this point are the investigations of the branches of research considered in this research, i.e. diamond-like carbon coatings, carbon nitride coatings and ionic liquid lubrication; followed by a chapter summarising the conclusions made and discussing the future developments of this research.

### 5.3 Chapter references

- 1 Dagani R. Individual surface atoms identified. *Chemical and Engineering News*, 2007. p.13.
- 2 Giessibl F. Advances in atomic force microscopy. *Reviews of modern physics* 2003, **75**, 949.
- 3 Humphris ADL, Miles MJ, Hobbs JK. A mechanical microscope: High speed atomic force microscopy. *Applied Physics Letters* 2005, **86** (3).
- 4 Ferrari AC, Libassi A, Tanner BK, Stolojan V, Yuan J, Brown LM, Rodil SE, Kleinsorge B, Robertson J. Density,  $sp^3$  fraction and cross-sectional structure of amorphous carbon films determined by x-ray reflectivity and electron energy loss spectroscopy. *Physics Review B* 2000, **62B**, 11089.
- 5 Casiraghi C, Piazza F, Ferrari AC, Grambole D, Robertson J. Bonding in hydrogenated diamond-like carbon by Raman spectroscopy. *Diamond and Related Materials* 2005, **14**, 1098.
- 6 Piscanec S, Mauri F, Ferrari A. C, Lazzeri M, Robertson J. Ab initio resonant Raman spectra of diamond-like carbons. *Diamond and Related Materials* 2005;14:1078.
- 7 Thomsen C, Reich S., Double Resonant Raman Scattering in Graphite, *Physics Review Letters* 2000, **85** (24), 5214-5217.
- 8 Ferrari A. C, Robertson J. Raman spectroscopy in carbons: from nanotubes to diamond. *Philosophical Transactions of The Royal Society, A* 2004, **362**, 2267.
- 9 Tunistra F, Koenig J. L., Raman Spectrum of Graphite, *Journal of Chemical Physics* 1970, **53** (3), 1126.
- 10 Castiglioni C, Di Donato E, Tommasini M, Negri F, Zerbi G., Multi-wavelength Raman response of disordered graphitic materials: models and simulations, *Synthetic Metals*, 2003, **139** (3), 885-888.

# CHAPTER 6

## Diamond-like carbon

---

### **6. Diamond-like carbon**

#### **6.1 History of development**

#### **6.2 Properties of DLC coatings**

#### **6.3 Valve-train study**

##### *6.3.1 Coating selection – considerations*

##### *6.3.2 Study structure*

##### *6.3.3 Results*

###### *6.3.3.1 Raman spectroscopy*

###### *6.3.3.2 Atomic force microscopy*

###### *6.3.3.3 Coating thickness measurement*

###### *6.3.3.4 Valve-train testing*

###### *6.3.3.5 Nanoindentation testing*

###### *6.3.3.6 Scratch-adhesion testing*

###### *6.3.3.7 Micro-abrasion testing*

###### *6.3.3.8 Reciprocating sliding wear*

###### *6.3.3.9 Micro-impact testing and simulation*

##### *6.3.4 Collected results, comparison and discussion*

###### *6.3.4.1 Valve-train performance, key coating properties*

###### *6.3.4.1.1 Role of impact*

###### *6.3.4.2 Role of surface finish*

##### *6.3.5 Conclusions*

#### **6.4 Future work**

#### **6.5 Chapter references**

---

This chapter describes the investigation of diamond-like carbon (DLC) coatings for use in the valve-train. DLC coatings have been the primary focus of this research and a detailed study has been conducted for a variety of coatings and substrate surface finishes. The performance of coatings was determined in an instrumented valve-train test rig, detailed in chapter 2. The results of testing in the test rig have been compared to the results of mechanical and tribological testing with the aim of elucidating the

mechanical and tribological properties that are important to good valve-train performance. This chapter describes the background to DLC coatings, and presents and discusses the experimental results in terms of applicability of DLC coatings in the valve-train.

### 6.1 History of diamond-like carbon

Research into what is now termed diamond-like carbon (DLC) first began with Schmellenmeier in the early 1950s, who successfully generated amorphous carbon films [1]. However it is Aisenberg and Chabot whose work came to prominence in the early 1970s, that are commonly considered as the pioneers of DLC technology [2]. Even the earliest DLC coatings were noted as having impressive and interesting properties such as good resistance to scratching, a high index of refraction and excellent optical transparency. It was after Aisenberg and Chabot's comprehensive studies were released that researchers such as Holland *et al* developed an interest in DLC coatings [3]. A number of new deposition methods were developed, notably the first plasma based deposition techniques [3, 4]. In 1979 Weissmantel *et al* [5] conducted extensive electron microscopy and electron energy loss spectroscopy (EELS) of DLC coatings and first demonstrated the amorphous microstructure, up to that time a crystalline diamond structure had been suspected. In the late 1980s, DLC coatings were finding large scale industrial applications, with Arnoldussen and Rossi [6] correctly proposing that DLC had an application as a protective overcoat for magnetic recording media in 1985. By the early 1990s, the field of tribological DLC coatings was growing rapidly with an annual publication rate for the tribology of DLC coatings of 25 papers in 1996, which has increased yearly to date. A number of reviews exist of the major work done on DLC coatings in the intervening years [7-13]. The following section gives an overview of the current state of DLC research relevant to tribological applications.

### 6.2 Properties of DLC coatings

Chapter 3 discussed the properties of carbon based coatings and the role that microstructure, alloying elements, interlayers and deposition method plays in determining those properties. This section looks more specifically at the range of properties commonly available from commercial and experimental DLC and table 6.1

shows typical available properties for a number of different types of DLC alongside a number of other forms of carbon for comparison.

Table 6.1 - Typical properties of several carbon based materials of interest [14-28]

	sp <sup>3</sup> (%)	H (%)	Density (g cm <sup>-3</sup> )	Poisson's ratio	Young's Modulus (GPa)	Fracture Toughness (MPa m <sup>1/2</sup> )	Residual Stress (GPa)	Hardness (GPa)	Gap (eV)
Diamond	100	0	3.515	0.07	1144	3.4	-	100	55
Graphite	0	0	2.267	0.2	9-15	-	-	0.2	0
Glassy C	0	0	1.3-1.55	-	-	-	-	3	0.01
Evaporated C	0	0	1.9	-	-	-	-	3	0.4-0.7
Sputtered C	5	0	2.2	-	-	-	-	-	0.5
ta-C	80-88	0	3.1	0.12	710-805	-	<12	40-90	2.5
a-C:H hard	40	30-40	1.6-2.2	0.4	140-170	1.2-1.6	1-3	1-20	1.1-1.7
a-C:H soft	60	45-50	1.2-1.6	0.25	50	2.9-3.3	~1	<10	1.7-4
ta-C:H	70	30	2.4	0.21-0.39	251-349	-	8.4	≤50	2.0-2.5
W DLC	~50	20	2.5-16.3	0.2	100-150	1.0-2.5	0.9	13.2	-
Si DLC	60-84	15	1.85	-	100-175	-	1-2.5	14-25	-

DLC coatings with a predominance of sp<sup>3</sup> bonded carbon - up to 85% - are termed tetrahedral amorphous carbon (ta-C), as first suggested by McKenzie [10]. As hydrogen is such a common component in so many DLC coatings its inclusion or exclusion is a defining issue. DLC coatings are therefore commonly defined by a ternary phase diagram as was first used by Jacob and Moller [21], see figure 6.1.

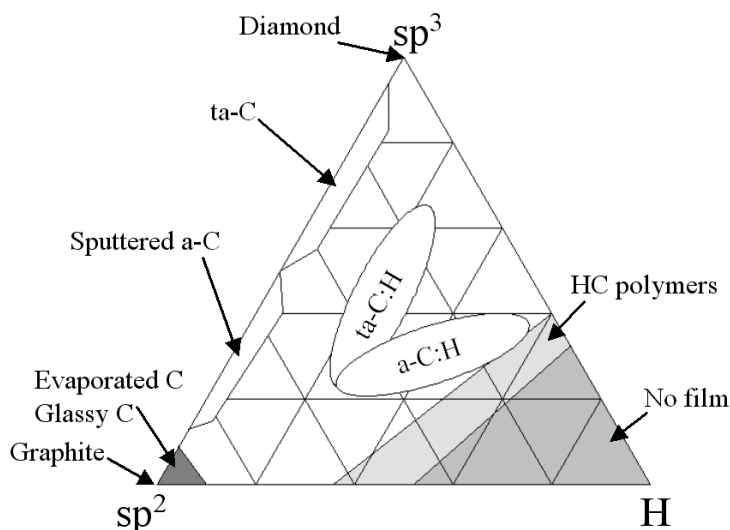


Figure 6.1 – Ternary diagram of DLC coatings and their composition

Unlike microcrystalline diamond films, which are inherently rough and cause high friction and wear in sliding contacts [8], most DLC films have a very smooth finish [29],

usually of the order of 0.1nm and are referred to as nanosmooth. As the coatings are amorphous with no preferred growth direction the roughness of the underlying substrate is usually preserved. Wear rates show a similar diversity, with a variation from easily scratchable, i.e. no wear resistance, to  $10^{-8}\text{mm}^3\text{N}^{-1}\text{m}^{-1}$  [8, 30-34].

### 6.3 Valve-train study

As discussed in chapter 1 the general aims of this research are to:

- Develop a cam-tappet testing rig for assessing coating performance in the valve-train.
- Establish, from a range of candidate coatings, those coatings which have the best durability and friction performance.
- Categorise coatings by their tribological and mechanical properties.
- Establish links between coating properties and valve-train performance.

In order to achieve these aims a systematic study of the mechanical and tribological properties of coatings was conducted, looking at the coating composition, morphology, adhesion to the substrate, hardness, modulus, sliding wear resistance, abrasive wear resistance and impact fatigue resistance. The results can then be compared to the coating performance in an in-service valve-train test rig. From comparison of in-service performance and easily measurable coating properties the properties that are key to good valve-train performance can be elucidated.

One of the key aspects of this research is its applicability to improving the performance of road cars, in an effort to reduce engine friction losses and improve CO<sub>2</sub> emissions. Therefore it is critical that the coatings tested could plausibly be adopted by automotive manufacturers. The following section looks at such practical considerations for coating selection in more detail.

#### 6.3.1 Coating selection - considerations

DLC coatings are of particular interest as a great deal of research had brought the technology to a point where DLC coatings are available in large numbers by batch production and at commercially viable prices. DLC coatings have found many very successful applications: HDD head protection; tooling; blades; diesel injection; motorsports, particularly Formula1 etc. [35]. The success of DLC coatings in Formula1 engine design is particularly encouraging for automotive applications, as operating

conditions in Formula1 engines are harsher, with higher contact forces and engine speeds. In applications such as Formula1, cost is heavily offset by performance, which allows the use of coatings produced by more expensive coatings deposition techniques, conducted in small batches and with extensive quality control to select only the best components for race engines. For a successful adoption of DLC coatings by the automotive industry they must offer significant improvement in performance and be cost effective, available in large quantities, with relatively short lead times and with reasonable quality control requirements. For applications such as diesel direct injectors DLC coatings are now standard, showing that where the gains are large enough the industry will make the necessary investment. The DLC coatings investigated in this study have therefore been limited to those which are relatively economical and readily available. The following section describes the coatings tested and the way in which the investigation was necessarily divided into a number of studies.

### 6.3.2 Study structure

Four different DLC coatings have been investigated. These were supplied by two deposition companies, which for this work will be described as company A and company B. The coatings supplied by company A are under development but intended for mass market. The coatings supplied by company A are a hydrogen free DLC (a-C) deposited by magnetron sputtering and a hydrogenated DLC (a-C:H) deposited by magnetron assisted PECVD. Neither of these coatings contained any additional alloying elements. The coatings supplied by company B were a hydrogenated and tungsten doped DLC (a-C:H:W) and a hydrogenated DLC (a-C:H) both of which were deposited by a PECVD process. In order to distinguish between the two a-C:H coatings they are to be followed by a letter denoting the deposition company, e.g. a-C:H(A) and a-C:H(B). While both a-C:H(A) and a-C:H(B) are hydrogenated, alloy free and deposited by a PECVD process, a great deal of variation is possible for DLC coatings depending upon the precise deposition conditions. These four coatings should offer a wide range of properties and different valve-train performances, and make for a good comparison of the available properties of commercially viable DLC coatings. All of the coatings were deposited onto the same substrate (shims). The shims were M2 tool steel (composition (0.95-1.05)C-(0.15-0.35)Si-(0.25-0.45)Mn-(1.35-1.65)Cr by weight), with a typical hardness of ~8.3GPa. These shims sit in a recess on the top surface of the tappet and

make up the contacting face of the tappet against the cam. Coated shims were used for the mechanical and tribological testing as well as the in-service cam-tappet tests. The shims were taken from stock used to supply the Jaguar AJ-V8 engines and had previously been treated in order to deposit a  $\sim 6\mu\text{m}$  layer of manganese phosphide (MnP). As described in chapter 1, this layer works with oil additives to provide low friction and wear. The shims were reground prior to coating deposition to remove the MnP layer. Three surface finishes were investigated, these are termed 'directionally ground' (DGnd), 'ground' (Gnd) and 'polished' (Pol). The DGnd surface finish was produced by the removal of the MnP layer on a grinding wheel and therefore has a highly directional texture. The Gnd surface and Pol surfaces were produced on a Struers TegraPol-21 polishing machine, with a bed speed of 150rpm and a co-rotating head speed of 150rpm. The applied load per sample was 30N. The Gnd texture was produced by 5 minutes of grinding with wet #220 SiC paper. The Pol surface followed the Gnd surface and is produced by a 5 minute polishing process with  $9\mu\text{m}$  diamond solution, followed by a 5 minute polishing process with  $6\mu\text{m}$  diamond solution.

With three surface finishes and four coatings, it was unfeasible to conduct a full set of mechanical and tribological tests for each coating/substrate pairing. For this reason this study can be considered to have been separated into four individual studies, each with a different set of tests. The testing that was conducted in each of the studies is shown below in table 6.2. Studies 1, 2 and 3 are concerned with coatings from company A for differing substrate finishes. Studies 1 and 2 cover a wide range of tests to establish coating: composition; microstructure; surface roughness; valve-train performance; coating thickness; hardness; modulus; adhesion, and; wear rates. Study 3 is primarily an assessment of the role that impact plays in determining valve-train performance, and therefore has less extensive testing. Study 4 is concerned with the coatings deposited by company B and like studies 1 and 2 covers a wide range of mechanical and tribological tests but also, like study 3, looks at the role of impact testing.

Table 6.2 Testing matrix

Coating supplier	A	A	A	A	A	A	B	B
Substrate finish <sup>1</sup>	DGnd	DGnd	Pol	Pol	Gnd	Gnd	Pol	Pol
Coating composition	a-C:H	a-C	a-C:H	a-C	a-C:H	a-C	a-C:H:W	a-C:H
Deposition process	Magnetron PECVD	Magnetron sputtered	Magnetron n PECVD	Magnetron n sputtered	Magnetron n PECVD	Magnetron n sputtered	PECVD	PECVD
Raman – sp <sup>2</sup> :sp <sup>3</sup>	☑	☑	☐	☐	☐	☐	☐	☐
AFM - roughness	☑	☑	☑	☑	☑	☑	☑	☑
Coating thickness	☑	☑	☑	☑	☐	☐	☑	☑
Valve-train testing								
- With impact	☑	☑	☑	☑	☑	☑	☑	☑
- Without impact	☐	☐	☐	☐	☑	☑	☑	☑
Nanoindentation	☑	☑	☑	☑	☐	☐	☑	☑
Scratch - Adhesion	☑	☑	☑	☑	☐	☐	☑	☑
Micro-abrasion	☑	☑	☑	☑	☐	☐	☑	☑
Reciprocating sliding	☑	☑	☑	☑	☐	☐	☑	☑
Micro-impact								
- Dry	☐	☐	☐	☐	☑	☑	☐	☐
- Lubricated	☐	☐	☐	☐	☑	☑	☐	☐

<sup>1</sup> Key : DGnd – ground with directional features  
 Pol – progressively polished, final stage a 6µm diamond solution  
 Gnd – ground to fine finish, no directionality to surface texture  
 ☐ - Study 1 ☐ - Study 2 ☐ - Study 3 ☐ - Study 4

The studies are separated in this way to explain the testing that was conducted. In order to gain the greatest possible information and understanding from this work it is however important to consider the results as a whole and compare and contrast the findings for the various coating/substrate pairings. Therefore the results of all studies are addressed together for each test, where available. These results are also compiled for comparison in table 6.10 in section 6.4.5.

### 6.3.3 Results

This section describes the results of the testing, which has been broken down into the individual test procedures as they are available for each coating/substrate pairing. Where necessary any additional details of testing methods are also given.

#### 6.3.3.1 Raman spectrometry

Raman spectrometry was conducted on the a-C and a-C:H(A) coatings deposited on DGnd substrates to confirm their composition. The change in substrate should not affect the results and should be considered to be representative for all of the a-C and a-C:H(A) coatings. Spectrometry was conducted using a Renishaw InVia spectroscope with a Laser Physics Ar<sup>+</sup> 514nm wavelength laser, following the methodology laid out in section 5.2. The first spectrum, see figure 6.2a, showed a shallow photo-luminescent

(PL) background slope indicating a hydrogen free film. The  $I(D)/I(G)$  ratio of 1.60 and G peak centre of  $1566\text{ cm}^{-1}$  indicated that the coating has a largely  $sp^2$  bonded structure. The second spectrum, see figure 6.2b, showed a much steeper PL background,  $m/I(G) = 17.7\mu\text{m}$ , indicating a hydrogen content of  $\sim 40\text{ at. \%}$  [36] and the  $I(D)/I(G)$  ratio of 0.26 and G peak position  $1528\text{ cm}^{-1}$ , indicated a high proportion of  $sp^3$  bonding, although not high enough to be considered a ta-C film. These results were in agreement with the information on film composition supplied by deposition company A.

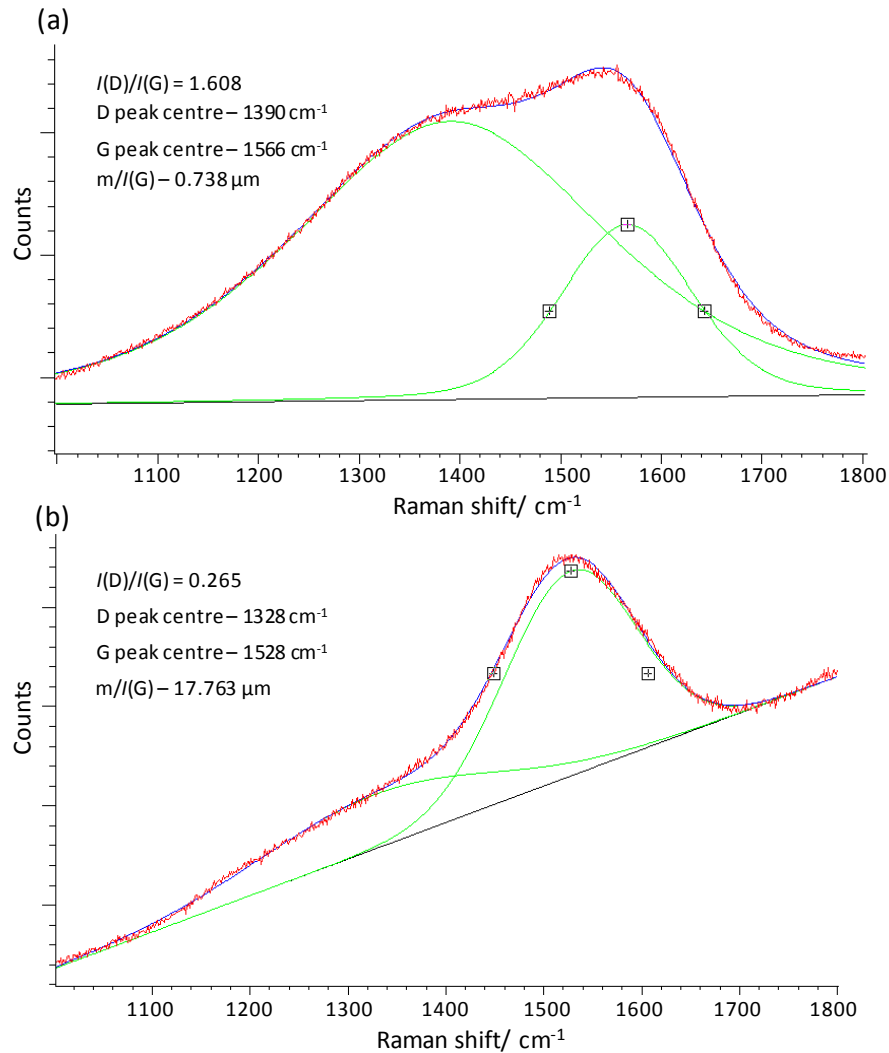


Figure 6.2 – Raman spectra of: a) the a-C, and; b) the a-C:H coatings deposited by deposition company A, fitted with mixed Gaussian/Lorentzian curves to determine position and relative amplitude of the D and G peaks.

### 6.3.3.2 Atomic force microscopy

Atomic force microscopy (AFM) was used to determine surface finish post coating deposition, using the apparatus and method described in section 5.1.3. For each sample four or more scans were performed on the surface at various positions. For each scan,

the surface roughness parameter  $R_a$  was determined, where  $R_a$  is the arithmetic mean of absolute surface amplitude. The  $R_a$  values of individual scans were then used to calculate mean values of  $R_a$  for the surfaces. Figure 6.3 shows example scans of the different surfaces with the mean values of  $R_a$  inset. The surface finish parameter  $R_a$  was chosen as it makes few assumptions about the surface texture. These values are then compiled in table 6.3

The surface finish of the a-C coated samples was found to be rougher than that of a-C:H(A) coated substrates, particularly evident for the polished substrate finish (see figure 6.3d). The a-C coating shows droplet-like formations, most likely due to the sputter type deposition process. The lower surface roughness of the a-C/Gnd surface compared to a-C/Pol, and lower incidence of sputter defects indicates variation in batch to batch coating deposition. Both of the coatings deposited by company B on polished substrates showed low surface roughness, the a-C:H:W coating was slightly rougher than the a-C:H(B) coating.

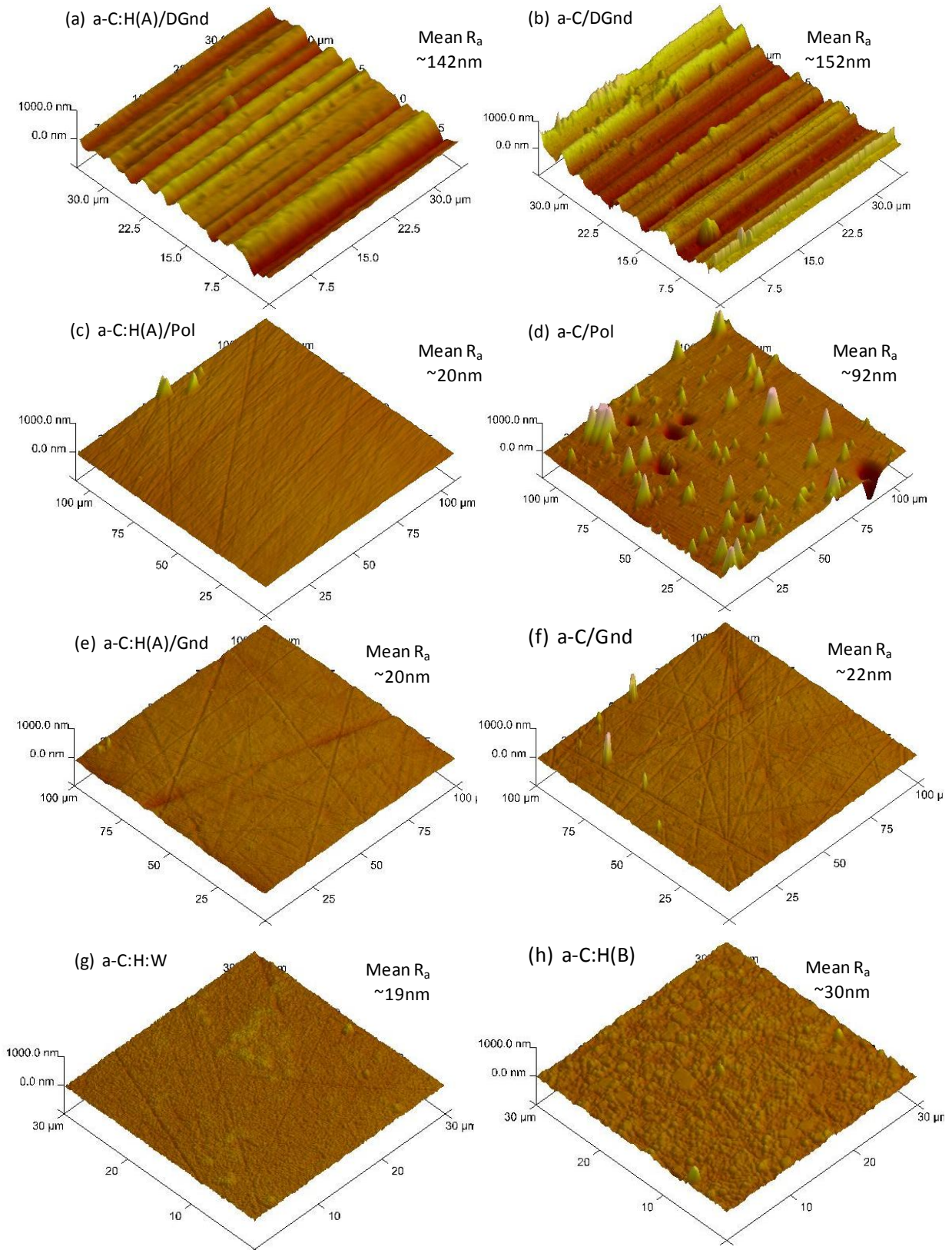


Figure 6.3 – Topographic images generated by AFM. Images a) through h) showing the various coating/surface finish combination, with mean values of surface roughness parameter  $R_a$  inset.

### 6.3.3.3 Coating thickness measurement

The next parameter to be determined was coating thickness. Thickness was determined from measurements taken by SEM of coating cross section and compared with data provided by the coating deposition companies. The coating cross section was exposed by chilled fracture of thinned sections of the sample. Chilling with liquid nitrogen to  $-196^{\circ}\text{C}$  ensures a sharp, brittle fracture, giving a representative value of thickness. Coating thicknesses were calculated from between four and six positions along the fracture and the mean thickness for the different coatings is shown in table 6.4. Figure 6.4 shows an example cross section for a-C:H(A) and a-C on polished substrates. Figure 6.4b also shows evidence of the same droplet-like particles seen in AFM scans of the surface. The size of the droplets is not insubstantial, with some approaching  $0.5\mu\text{m}$  in apparent height. These will affect the tribological performance of these samples.

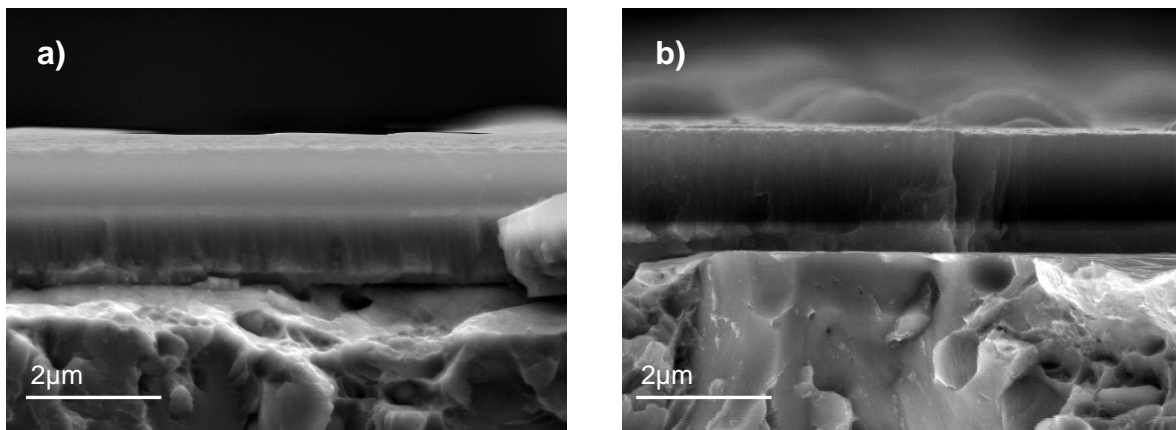


Figure 6.4 – Example cross-sectional images by SEM for: a) a-C:H(A)/Pol, and; b) a-C/Pol.

Table 6.4 – Coating thickness measurements

	a-C:H/DGnd	a-C/DGnd	a-C:H/Pol	a-C/Pol	a-C:H(B)	a-C:H:W
Thickness	$\sim 2.0\mu\text{m}$	$\sim 2.1\mu\text{m}$	$\sim 1.8\mu\text{m}$	$\sim 1.9\mu\text{m}$	$\sim 3.8\mu\text{m}$	$\sim 3.8\mu\text{m}$

### 6.3.3.4 Valve-train testing

In order to investigate the in-service friction coefficient and durability of the coatings they were tested in the cam-tappet testing rig that was described in chapter 2 and following the method described in chapter 4, section 4.1. The a-C/Gnd, a-C:H(A)/Gnd, a-C:H(B) and a-C:H:W coatings were tested under both ‘normal’ conditions and ‘impact free’ operation. The remaining coating/substrate pairings were tested under ‘normal’ conditions only. For each coating/substrate pairing and testing condition three coated

samples were tested under the same conditions. Testing was stopped if the coatings had not failed after 3¼ hours when tested under normal conditions, with impact. The coatings tested in continuous contact and not experiencing impact were stopped after 2¼ hours due to the greater sliding distance per cycle. Despite the shorter test period the continuous contact tests experienced ~50% greater sliding distances than those tested under 'normal' conditions for longer periods. After testing, the tappets were investigated by optical and electron microscopy. Figure 6.5 shows optical macrographs of the post-test condition of coatings for the a-C/DGnd, a-C:H(A)/DGnd, a-C/Pol and a-C:H(A)/Pol samples all tested under 'normal' conditions. Figure 6.6 shows optical macrographs of the post-test condition of coatings for the a-C/Gnd and a-C:H(A)/Gnd samples both for 'normal' conditions and 'impact free' conditions. Figure 6.7 shows optical macrographs of the post-test condition of coatings for the a-C:H(B) and a-C:H:W samples both for 'normal' conditions and 'impact free' conditions. As tests were stopped once coating failure was seen to have occurred, many of the tests are not of the same duration. The period of time for which each coating was tested is indicated next to the sample in the figures. Also included next to the macrograph of each sample is either a 'green tick' or a 'red cross'. The green tick indicates that the coating has survived the test duration without considerable wear and entirely without coating failure exposing the substrate. The red cross indicates that the coatings failed dramatically with large areas of coating wear or spallation, and exposure of the underlying steel substrate. Those that are unmarked typically have small localised areas where the coating has failed and the substrate has been exposed. These notations are intended purely as an aid to the reader.

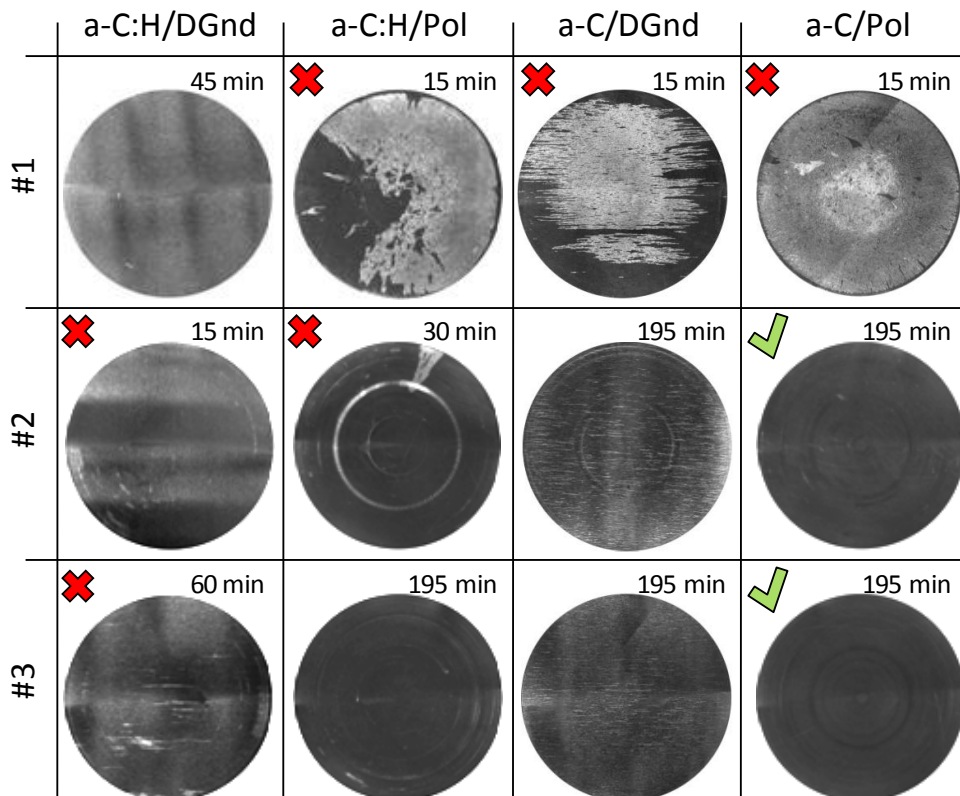


Figure 6.5 – Optical microscope images of shims worn in the valve-train test rig, for the a-C:H(A) and a-C coatings on the DGnd and Pol surface finishes.

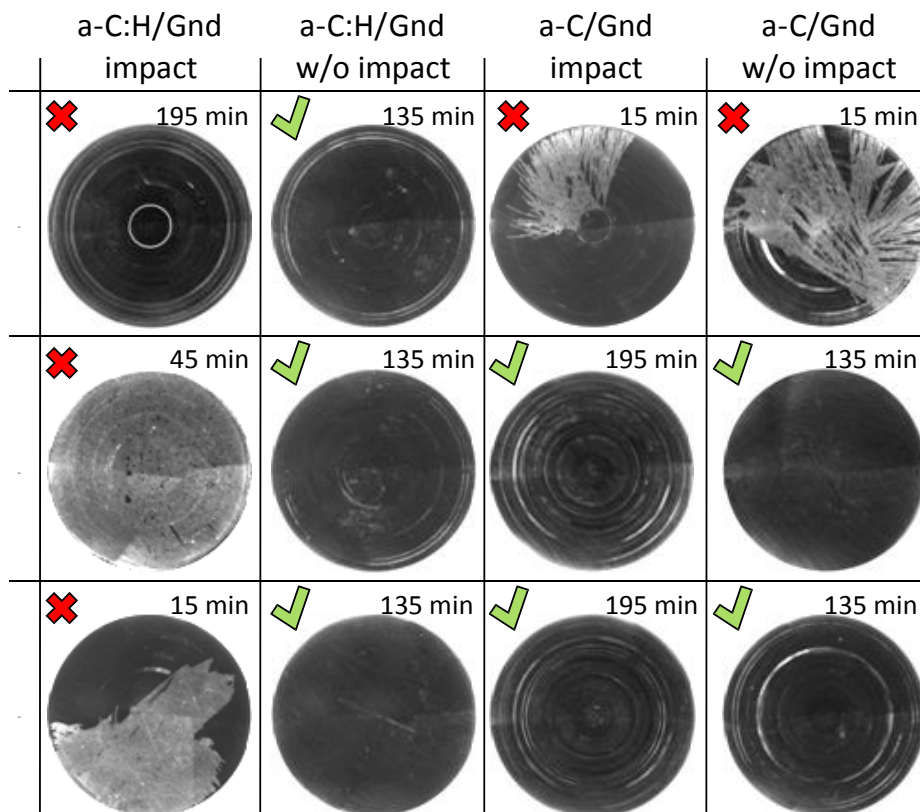


Figure 6.6 – Optical microscope images of shims worn in valve-train conditions with and without impact for the a-C:H(A) and a-C coatings on the Gnd surface finish.

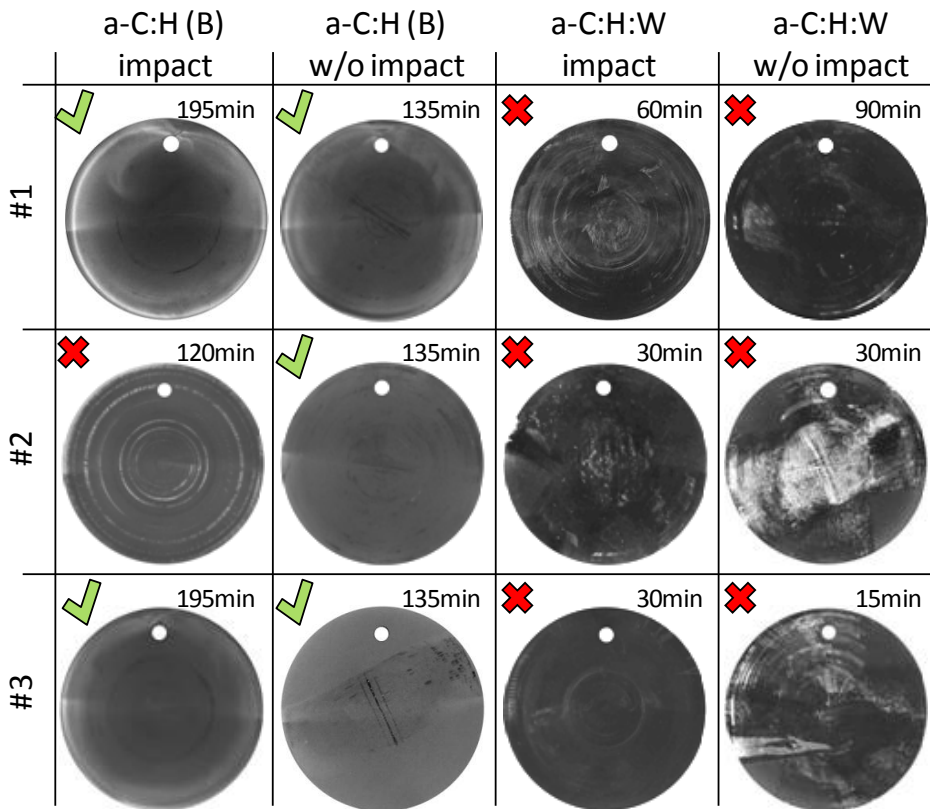


Figure 6.7 - Optical microscope images of shims worn in valve-train conditions with and without impact for the a-C:H(B) and a-C:H:W coatings on the Pol surface finish.

In addition to consideration of the coating durability, the coating friction coefficient is also of interest. To this end the torque was measured at 15 minute intervals throughout all of the valve-train tests. In each case, multiple cycles were collected, the instantaneous torque was averaged between them and the averaged result was digitally filtered following the procedure outlined in section 2.3.3. Torque was recorded and processed for all of the tests at a point 15 minutes into the test. The coefficient of friction was then estimated by fitting a simulated torque trace to the recorded data following the method described in section 2.3.1. The friction coefficient was established as the value which achieved the greatest agreement between traces. Using this fitting process the resolution of the curve fitting process was 0.005, and therefore it was not possible to differentiate fit quality for changes of friction coefficient less than this. Figures 6.8, 6.9 and 6.10 show example torque traces and the simulated traces used to calculate the coefficient of friction in each case. Figure 6.8a shows the torque trace of an uncoated bare steel tappet with a Gnd finish subjected to the same test conditions, along with the calculated coefficient of friction for comparison to the DLC coated samples. These calculations were all made for tests conducted with impact, as the simulated

model is designed for these conditions. If time were permitting friction coefficient could be calculated for impact free conditions also.

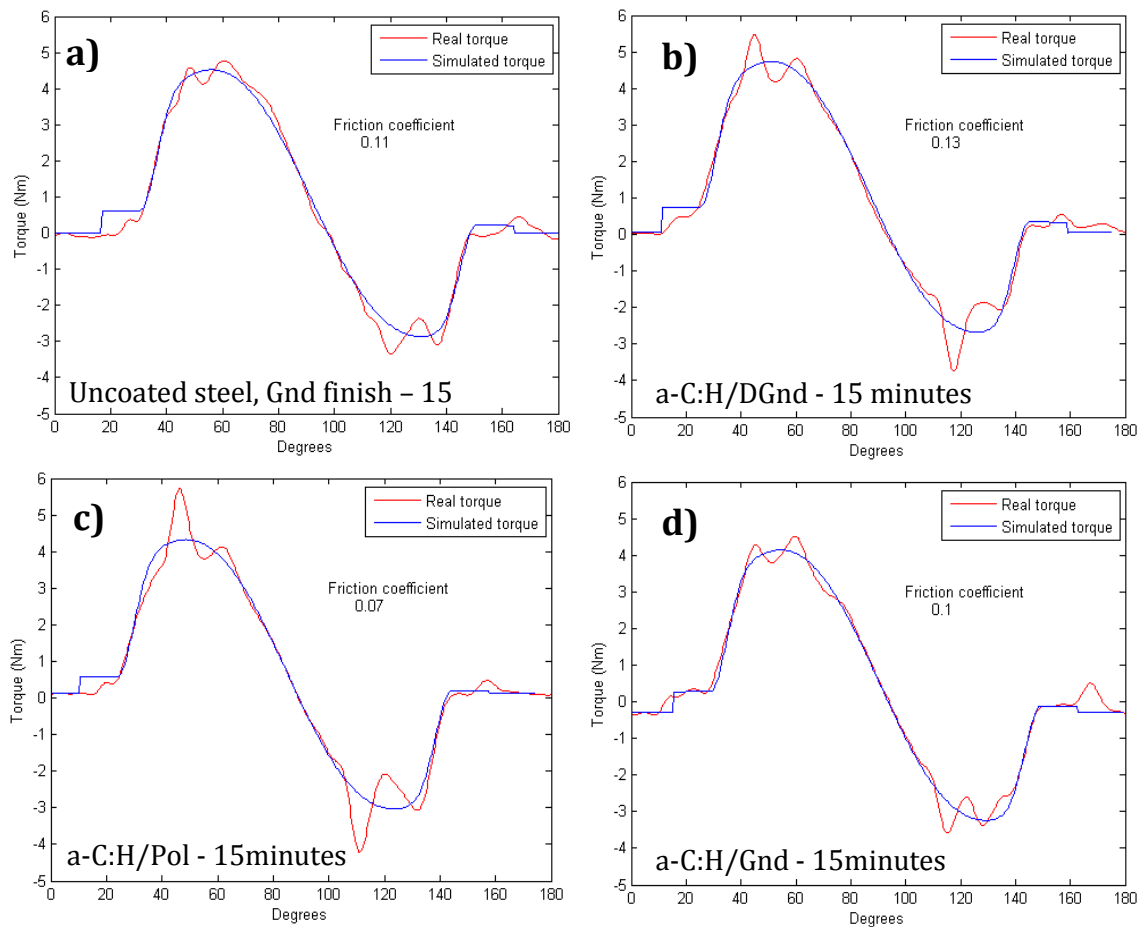


Figure 6.8 - Plots of filtered torque acquired 15 minutes into valve-train testing, with simulated torque plotted alongside. The estimated friction coefficient was recorded and inset. Plots are of: a) an uncoated steel sample; b) a-C:H/DGnd; c) a-C:H/Pol; d) a-C:H/Gnd. All data shown was collected 15 minutes into testing.

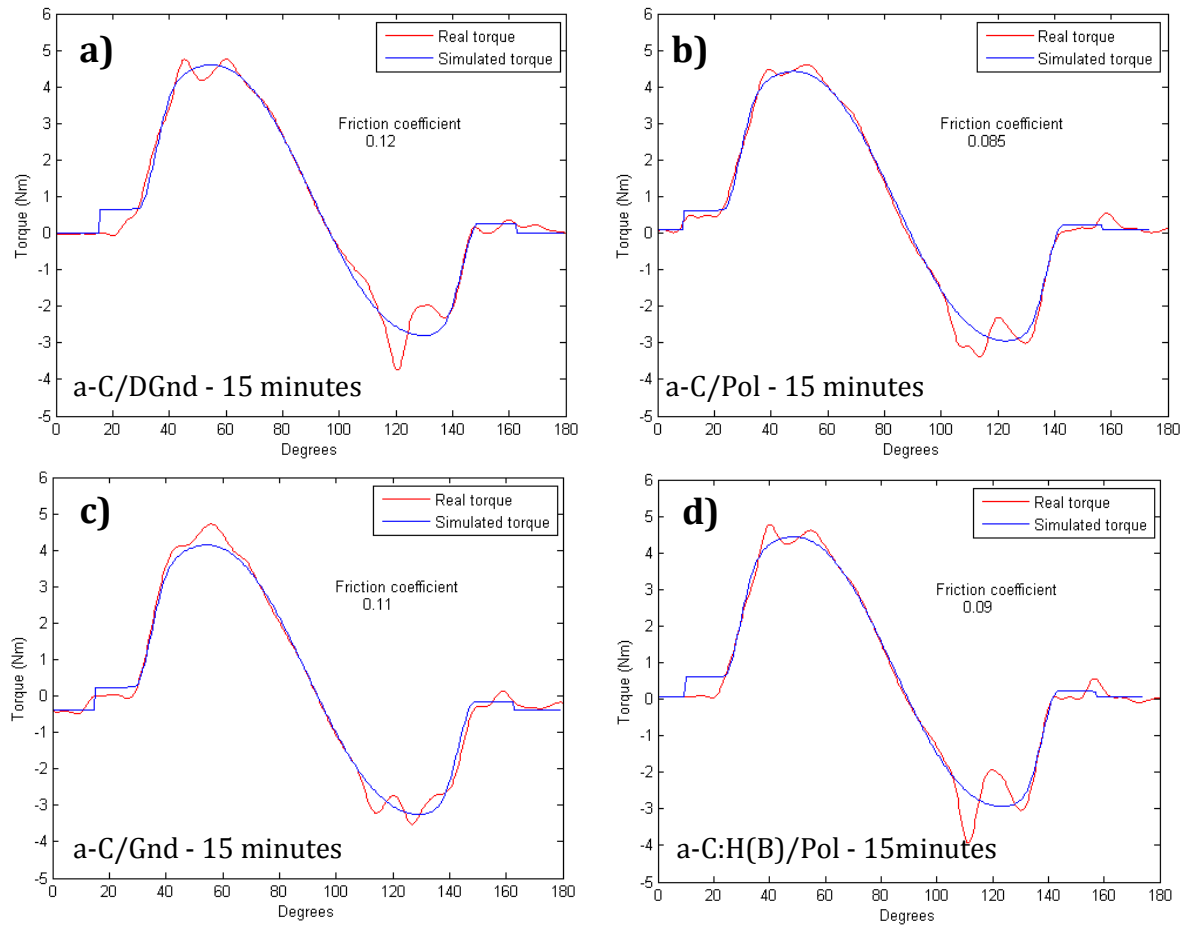


Figure 6.9 - Plots of filtered torque acquired alongside simulated torque, see figure ###. Plots are of: a) a-C/DGnd; b) a-C/Pol; c) a-C/Gnd, and; d) a-C:H(B)/Pol.

To establish if the friction coefficient changes throughout the duration of the test, for example with coating wear, torque traces were investigated at various intervals. Figure 6.10 shows the torque measured at several points in the duration of the a-C:H:W coating testing for sample #9.

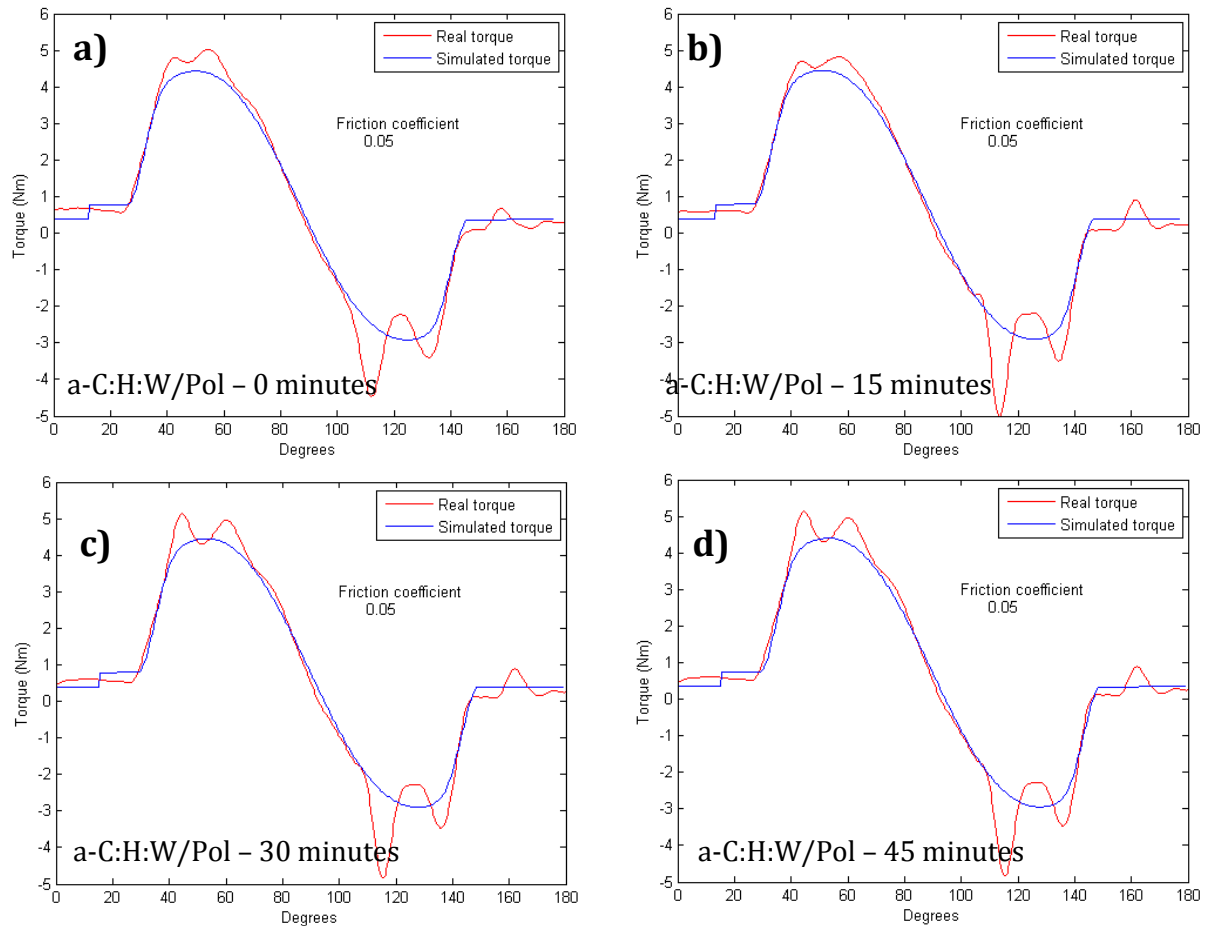


Figure 6.10 - Plots of filtered torque acquired at different time intervals into valve-train testing for the a-C:H:W/Pol DLC coatings: a) 0; b) 15; c) 30, and d) 45 minutes. Plots show the very low value of friction coefficient is maintained even after considerable wear.

As can be seen there is no change in friction coefficient throughout the testing despite the development of wear. The testing was stopped when moderate coating wear had occurred, if testing had continued for longer no doubt the friction coefficient would rise to that of bare steel once the coating was entirely removed and any residual DLC driven from the contact. A similar independence of friction coefficient and test duration was seen for all of the coated samples, with a maximum observed variation of 0.005 throughout testing, which is at the limit of resolution for this system. The single examples shown here are representative of the torque generated in all tests for each coating/surface finish pairing, with a variation between samples of no more than 0.005. To aid comparison, the total sliding distance prior to coating failure was summed for the three samples of each coating/substrate pairing in each test conditions, i.e. with or without impact, and is given alongside the surface finish parameter  $R_a$  and the calculated friction coefficient in table 6.5.

Table 6.5 - Valve-train testing results, sliding distance to failure and friction coefficient

	Uncoated steel	a-C:H/DGnd	a-C/DGnd	a-C:H/Pol	a-C/Pol	a-C:H/Gnd	a-C/Gnd	a-C:H(B)	a-C:H:W
Mean sliding distance to failure, ( $\times 10^3$ m)	$\Gamma$ ----- See fig 6.1 ----- $\gamma$					$\Gamma$ --- See fig 6.2 -- $\gamma$		$\Gamma$ -- See fig 6.3 -- $\gamma$	
- With impact	NA	2.85	9.61	5.7	9.61	6.05	9.61	12.1	2.85
- Without impact	NA	No test	No test	No test	No test	17.25	12.14	17.25	5.75
Friction coefficient	0.11	0.13	0.12	0.07	0.085	0.1	0.11	0.09	0.05
Roughness, $R_a$ (nm)	$\sim 63$	$\sim 142$	$\sim 152$	$\sim 20$	$\sim 92$	$\sim 67$	$\sim 95$	$\sim 19$	$\sim 30$

General observation of the coating durability in valve-train testing shows it to be a very demanding environment, with many coatings failing by catastrophic spallation within the first 15 to 45 minutes of testing. Figure 6.11 shows a typical worn area of the a-C/Gnd sample #3, where the light regions are areas of exposed substrate and the dark regions are areas of intact coating. The coating appears to have been spalled cleanly from the substrate, and fracture is brittle, leaving sharp well defined edges where coating has been retained. The failure shown in figure 6.11, where large areas of coating have been spalled, was typical for the failures that occur within the first 45 minutes of testing. Where samples have not shown large areas of coating spallation within the first 45 minutes of testing they have not then gone on to develop this failure mechanism later in testing. This indicates that there is an initial running-in period where spallation is more probable, most likely due to higher friction and shear stresses at the asperities. The failures that occurred after this period were predominantly by a scuffing wear mechanism that was localised to rings. Figure 6.12 shows an example of these rings of scuffing wear taken from the a-C:W/Pol sample #1. The scuffing marks are strongly directional, and scuffs appear to have been generated at the cam edges and in the direction of cam sliding motion with the ring shape being caused by tappet precession. For samples where scuffing wear was not observed, such as the a-C:H(B)/Pol samples #1 and #3 tested with impact, there was evidence of polishing wear in rings.

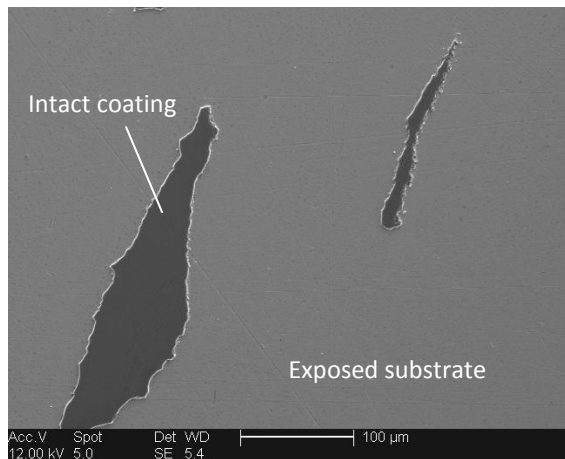


Figure 6.11 – example SEM image of early catastrophic coating failure, taken from a-C/Gnd sample #3.

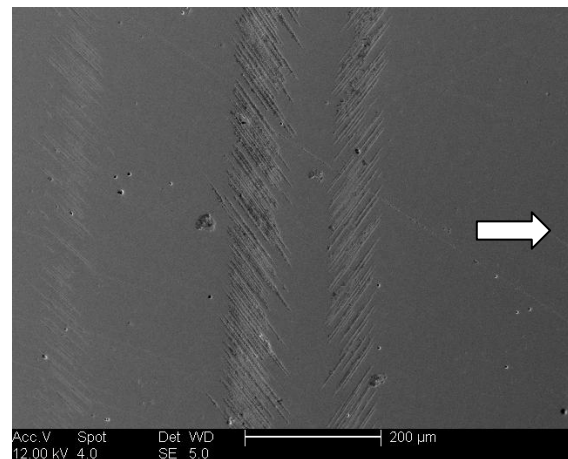


Figure 6.12 – example SEM image of scuffing wear in rings, taken from a-C:H:W/Pol sample #1. Arrow indicates direction to the centre of shim.

It is clear from these results that the a-C:H(B) coating has the greatest durability with the highest sliding distance to failure of any of the coatings, under conditions both with and without impact. Of the six a-C:H(B) samples assessed only one showed signs of coating failure and substrate exposure. The a-C coating appeared to outperform the a-C:H(A) coating for comparable surface finishes, although there were some examples of very early catastrophic coating failure. The a-C:H:W coating consistently showed the worst durability of the coatings tested, with major coating failures occurring within the first 90 minutes of testing in all test conditions. The a-C:H:W coating however also showed a dramatically lower estimated friction coefficient compared to the other DLC coatings and the uncoated steel/Gnd sample, a coefficient of friction of 0.05 indicates a 55% reduction in friction coefficient and therefore a 55% reduction in the energy lost to friction on that contact. The a-C:H(B) coating also showed a reduced friction coefficient, although it should be considered that the surfaces are also smoother than that of the uncoated steel. The a-C:H(A) DLC coating also shows a reduction in friction coefficient when compared to the uncoated steel surface, for a comparable surface finish, however the reduction is considerably smaller, and falls within the estimated error of the friction estimation approach. The surface finish appears to be the most important factor in determining friction reduction, although there is no obvious connection between surface finish and coating durability; with the a-C:H(A) and a-C coatings showing the greatest durability on the Gnd substrate finish and Pol substrate finish respectively. The a-C:H(B) for example demonstrates a friction coefficient of 0.09 with a polished

substrate surface, very slightly higher than that of the a-C/Pol sample at 0.085. By inference, the friction coefficient of an a-C:H(B) coating on a Gnd surface would be comparable to that of the steel sample.

#### 6.3.3.5 Nanoindentation testing

A series of nanoindentations were performed on the samples at a range of loads. Indentations were performed at loads of 1000, 750, 500, 250, 100, 50, 25, 10, 5, 1, 0.5 and 0.1gf, ten indentations at each load, with indent spacing's of 200 $\mu$ m for loads above 50gf and 100  $\mu$ m for 50gf and below. Following the procedures discussed in chapter 4, values of hardness and modulus were calculated from the resulting load-displacement curves. Studies have indicated that for indentations of a depth greater than a tenth of coating thickness there will be a considerable contribution from the substrate [37]. For samples with coatings that are harder than their substrates the measured hardness values will increase with decreasing indentation depth. Thickness measurements have shown the DLC coatings used in this study to be very thin, less than 4 $\mu$ m, making it difficult to achieve repeatable values of film only hardness. Korsunsky *et al* [38] suggested a model, which will be referred to as the KMBP model, for separating the individual hardness contributions made by coating and substrate from a range of indentations at various indentation depths. This model has been applied to the nanoindentation data collected in this study. Figure 6.13 shows the mean values of hardness plotted against relative indentation depth (RID), i.e. the ratio of indentation depth to coating thickness.

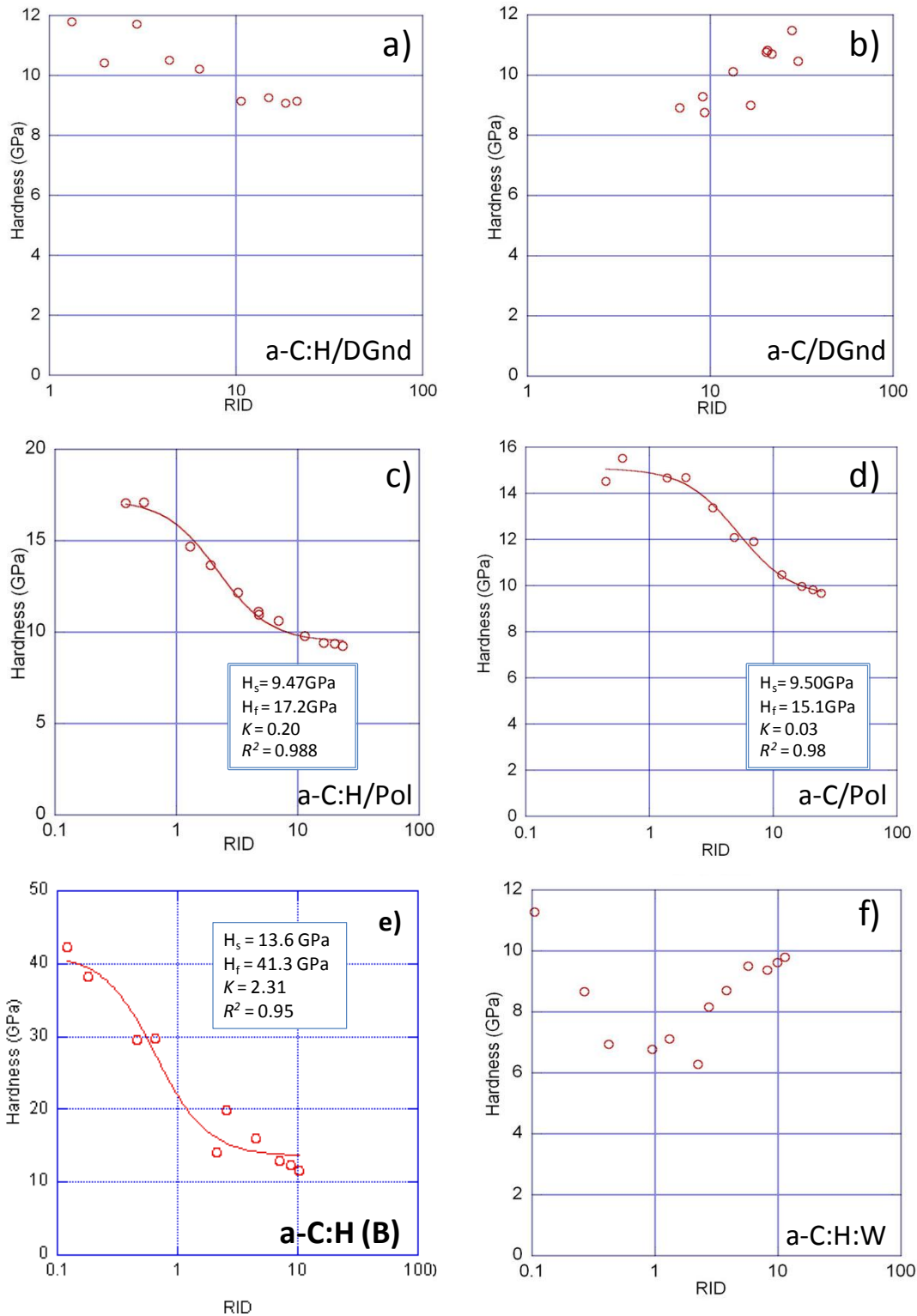


Figure 6.13 - Graphs of hardness against relative indentation depth (RID) found by nanoindentation for: a) a-C:H/DGnd; b) a-C/DGnd; c) a-C:H/Pol; d) a-C/Pol; e) a-C:H (B), and; f) a-C:H:W. The KMBP model was fitted to all data and the resulting regression coefficients are given inset for the data which gave a reasonable quality fit.

For samples with directionally ground surface finish it was not possible to achieve a realistic fit with the KMBP model, this was probably owing to difficulties in determining hardness on rough surfaces. Also, it was not possible to achieve a fit with the KMBP model for the results of nanoindentations performed on the a-C:H:W coating. This is likely to be because of the low hardness results observed for a-C:H:W coatings, which show no clear increase in hardness with decreasing indentation depth and are moderately lower than that observed for the a-C:H and a-C coatings. For the a-C:H:W coating the value of coating hardness was estimated from the known combined coating and substrate values. The hardness measured for the a-C and a-C:H(A) coatings on Pol substrates should be fairly representative of that of the coatings deposited on DGnd and Gnd surfaces excluding the effect of surface roughness. The results for the a-C:H(A)/Pol and a-C/Pol samples can therefore be referred to for the samples with the DGnd substrate finish, which were unclear, and the samples with the Gnd substrate finish which were unmeasured.

Calculations were made of modulus values for the indented coatings, however for the values of relative indentation depth and the surface roughness of the coatings the generated values of modulus will not be representative of the coating modulus. A better estimate of modulus could be obtained by acoustic methods but time was not available. The calculated and measured values of hardness are collated in table 6.6.

Table 6.6– Results of nanoindentation testing

	a-C:H/DGnd	a-C/DGnd	a-C:H/Pol	a-C/Pol	a-C:H(B)	a-C:H:W
Hardness	Refer to results for Pol substrate finish		17.2 GPa	15.1 GPa	41.3 GPa	9-11 GPa

#### 6.3.3.6 Scratch adhesion testing

Scratch testing was conducted to determine the critical loads  $L_{c1}$  and  $L_{c2}$  at which first failure and gross failure have occurred, see section 4.2 in chapter 4 for more details. Between four and six scratches were generated for each sample/surface finish pairing. The scratches were conducted with an initial load of 10N, a maximum load of 100N, loading rate of 100N min<sup>-1</sup>, and a transverse speed of 10mm min<sup>-1</sup>. For the samples with surface finishes produced by directional grinding (DGnd), two sets of scratches were performed, one parallel to the lay and the other transverse to it. Figure 6.14 and 6.15 show examples of the first and second critical load points, as imaged by SEM, for the directionally ground samples and the polished samples respectively.

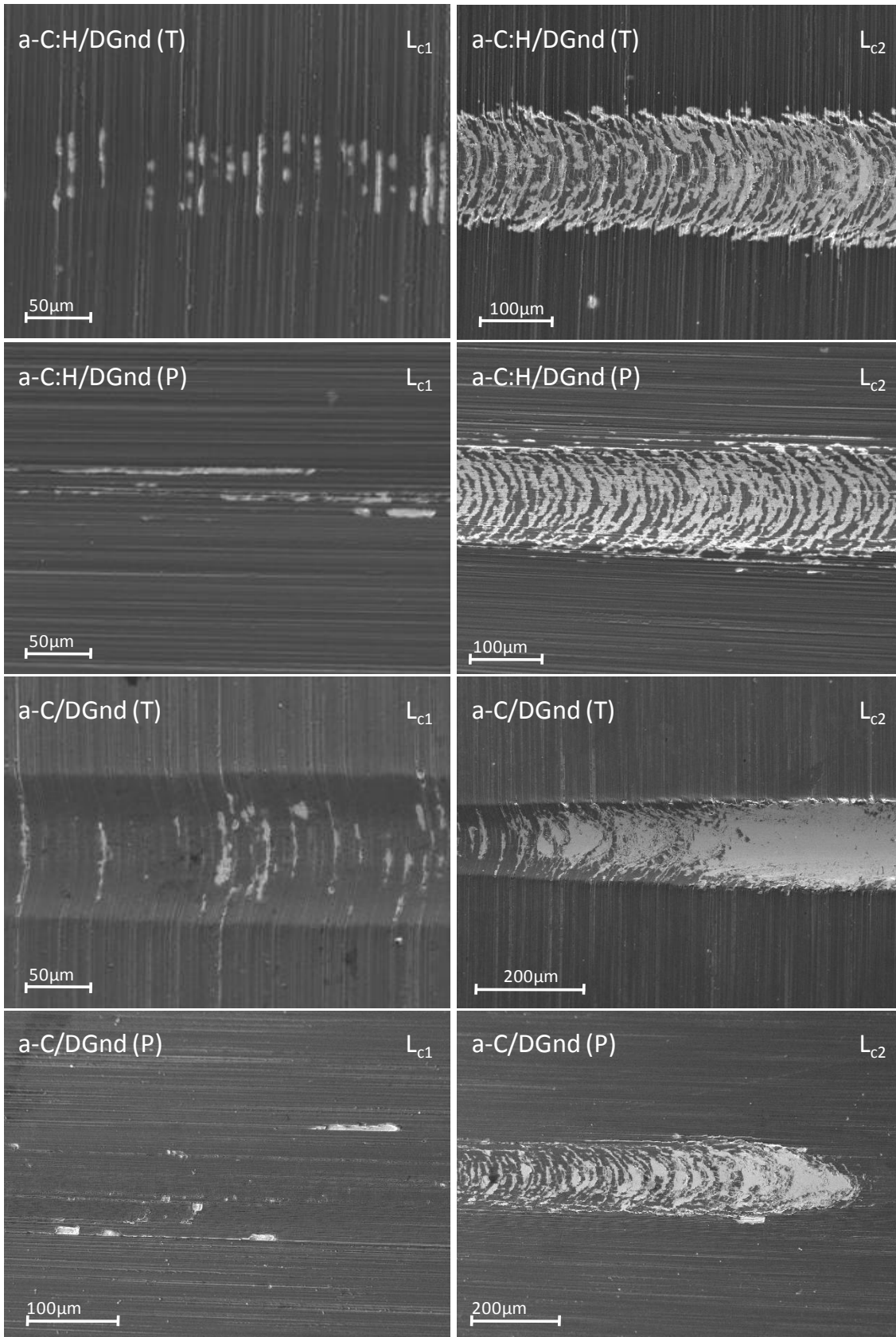


Figure 6.14 – SEM images of scratches performed on a-C, a-C:H(A) coatings on polished substrates. T denotes scratches conducted transverse to the lay of texture, and P denotes scratches conducted parallel to lay.

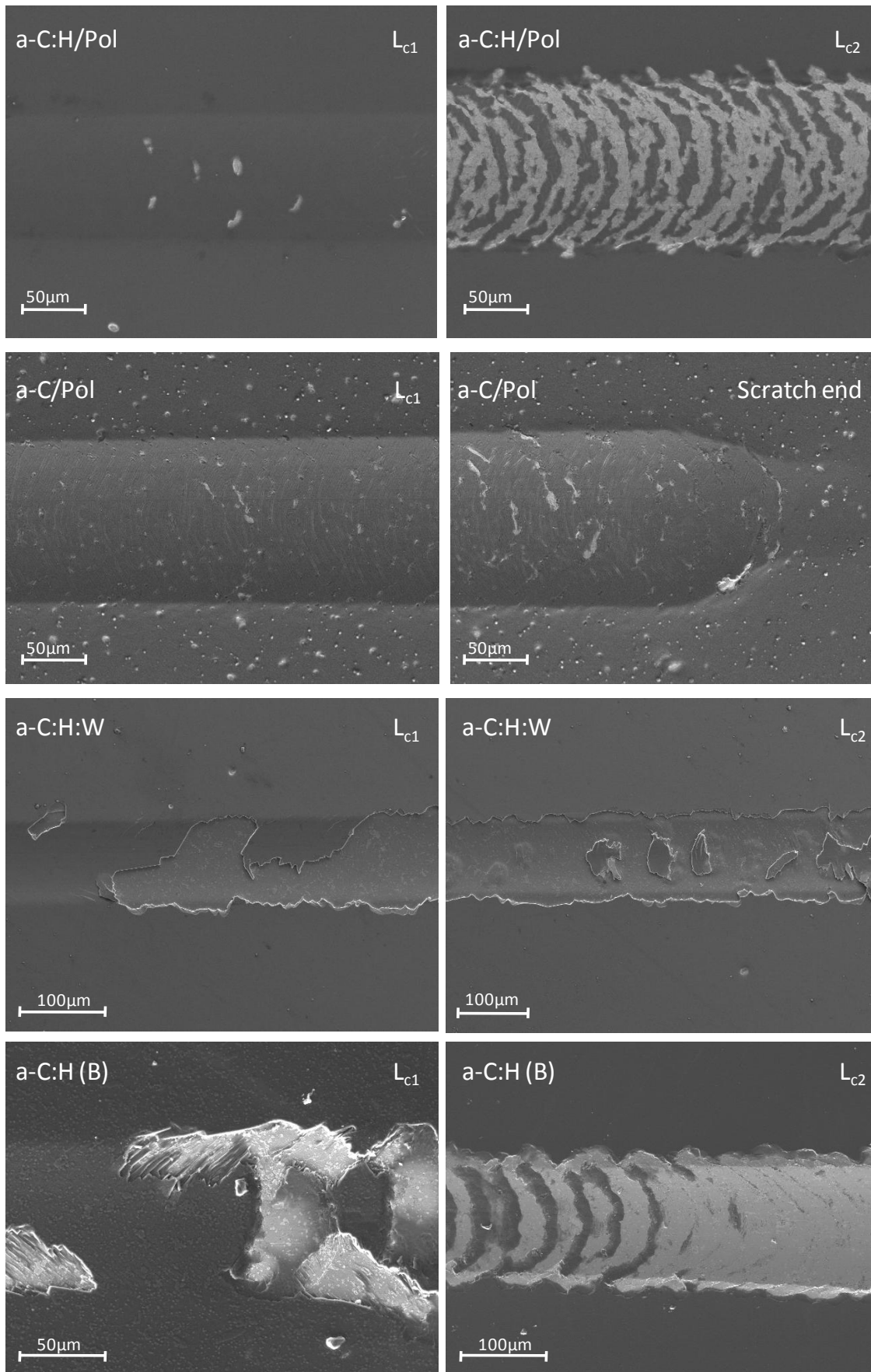


Figure 6.15 – SEM images of scratches performed on a-C, a-C:H(A), a-C:H (B) and a-C:H:W coatings on polished substrates

The resulting values of lower critical load ( $L_{c1}$ ) and upper critical load ( $L_{c2}$ ) were then averaged between scratches and the mean values of  $L_{c1}$  and  $L_{c2}$  are recorded in table 6.7. In general the coatings were very well adhered, with  $L_{c1} \sim > 40\text{N}$ , with the exception being the a-C:H(A)/DGnd [39]. The a-C:H(B) coating failed at high load by shell-shaped spallation, with considerable loss of coating material. All of the coatings produced by company A failed by the formation of micro-cracks, which were either chevron shaped or formed around features of surface roughness, followed by cohesive buckling. The a-C:H:W coating showed numerous failures, with large areas of coating exposed by brittle spallation, at relatively low loads but the coating only failed contiguously at high loads. All coatings showed very high loads for  $L_{c2}$ ,  $>75\text{N}$ . The a-C/Pol sample showed very good adhesion and did not achieve the criteria for secondary critical load within the parameters of the test, this is why no SEM image is given in figure 6.15. The a-C coating in general showed the highest adhesion of all of the coatings deposited. The two DGnd samples demonstrated lower values of  $L_{c1}$  than their Pol counterparts, with particularly low values for scratches performed in parallel to lay. The effect of substrate surface finish on  $L_{c2}$  was less clear.

Table 6.7 – Results of scratch-adhesion testing

	a-C:H/ DGnd	a-C/ DGnd	a-C:H/Pol	a-C/Pol	a-C:H(B)	a-C:H:W
- $L_{c1}$	25N (P) 17N (T)	67N (P) 63N (T)	50N	89N	48N	38N
- $L_{c2}$	77N (P) 87N (T)	Not Reached (P) 89N (T)	83N	Not reached	98N	91N

### 6.3.3.7 Micro-abrasion testing

Micro-abrasion (ball cratering) testing was conducted to assess abrasive wear rates of the coatings. Testing was conducted on samples with directionally ground surface finish, but the orientation of testing with regard to lay was not found to affect results, therefore testing was not conducted in both transverse and parallel orientation as it was for scratch-adhesion testing. The test procedure used and interpretation is described in detail in section 4.4.1. Specific details: ball radius 10mm; slurry composition, water and 5%wt.  $1\mu\text{m}$  silicon carbide particles; contact load 0.2N; counterface surface velocity  $0.05\text{m s}^{-1}$ . Between 7 and 13 wear scars were generated at various sliding distances. Sliding distances were selected such that the wear scars had diameters in the range of 0.5mm to 1.5mm. The wear scar diameters were measured by SEM and from knowledge of ball geometry and the coating thickness, the wear volume

of the coating and substrate,  $V_c$  and  $V_s$  respectively, were calculated. The results were then plotted as shown in figure 6.16. Then the specific wear rates of the coating,  $K_c$ , and the substrate,  $K_s$ , were calculated from the inverse of the intercept and gradient of a linear fit respectively. The specific wear rates are given in table 6.8.

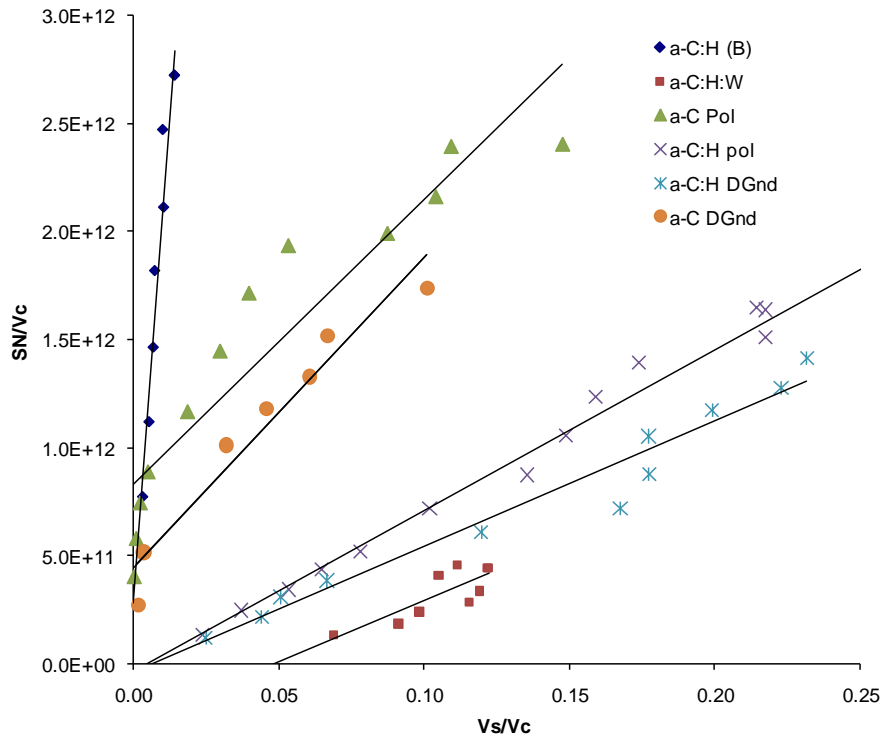


Figure 6.16 – Graph of resulting microabrasion wear, with linear curve fitting. Coating specific wear rate is determined by the inverse of the y-axis intercept; the substrate specific wear rate is determined by the inverse of the gradient.

As can be seen in figure 6.16 that this approach would generate negative values of  $K_c$  for the a-C:H(A)/DGnd, a-C:H(A)/Pol and a-C:H:W samples. This result is in contradiction to physical limits, and suggests that at a sliding distance of 0m wear should have already occurred. The appears to be due to very high wear rates at low sliding distance and the inability to truly describe the response with a linear fit. The results that generated negative values of  $K_c$  are therefore unrealistic and are listed in table 6.8 as such.

Table 6.8 – Results of microabrasion testing.

Specific wear rates (units $m^2 N^{-1}$ )	a-C:H/DGnd	a-C/DGnd	a-C:H/Pol	a-C/Pol	a-C:H(B)	a-C:H:W
For coating - $K_c$	unrealistic	2.3 e-12	unrealistic	2.15 e-12	4.5 e-12	unrealistic
For substrate - $K_s$	1.7 e-13	7e-14	1.4 e-13	1.05 e-14	5.3 e-15	1.8 e-13

The issue of poor fitting also occurs for samples showing greater abrasive wear resistance such as the a-C/Pol sample. The linear fit in figure 6.16 poorly describes the features of the data, figure 6.17 shows the same data fitted with three distinct linear lines of best fit. Very good agreement can be found for the two lower sliding distance linear regions, curve fitting parameter  $R^2 > 0.9$ . This indicates that the wear of the coating affects the wear rate of the substrate, and that wear rates are not consistent over a range of sliding distances. There is some evidence that there is a transition from coating dominated wear rates, to substrate dominated wear rates at values of  $V_s/V_c$  between 0.05 and 0.1. Where appropriate the values of  $K_s$  and  $K_c$  have been calculated from a linear fit to the initial, coating dominated region where, as suggested by [40, 41] the error from volume measurements is reduced. This method is not ideal however and does not correct for the effect of the coating on observed substrate wear rates. Therefore the values of microabrasive wear rate given here are to be considered qualitatively, being indicative of coating abrasive wear resistance. A more detailed understanding of coating and substrate wear rates could likely be gathered from generating many more wear scars over a wider range of sliding distances in order to clearly establish the transition from coating to substrate dominated abrasive wear.

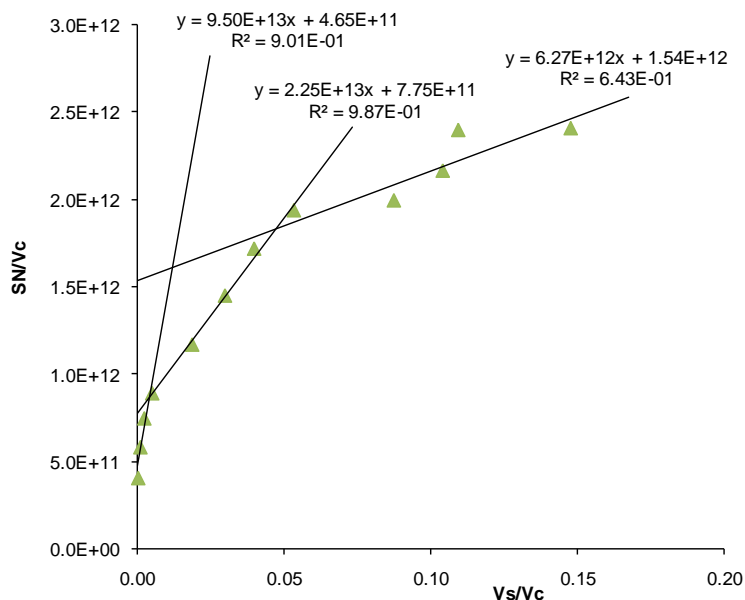


Figure 6.17 - Graph of resulting microabrasion wear, indicating difficulty in with using a linear fit to determine wear rates.

### 6.3.3.8 Reciprocating sliding wear

Reciprocating sliding wear tests were conducted for a number of the coating/substrate pairings, following the procedure described in section 4.4.2. Between four and six reciprocating sliding wear tests were conducted for the a-C, a-C:H(A), a-C:H(B) and a-C:H:W coatings on polished substrates for distances of 100m. For the a-C and a-C:H(A) coatings on directionally ground substrates, reciprocating sliding wear tests were conducted both parallel and transverse to the lay of surface features, as with scratch testing. For all tests the same parameters were used, applied load of 60N, stylus radius of 2.5mm, traverse speed of 300mm min<sup>-1</sup>, and a sliding distance of 10mm per cycle. The wear generated was investigated and friction was measured continuously throughout testing. Once the surfaces had run-in and a stable coefficient of friction was established it was used to determine a representative friction coefficient against the steel stylus. An example SEM image of wear and record of friction coefficient are shown in figure 6.18. For the majority of coatings it was also possible to conduct coherence correlation interferometry to determine surface topography and measure wear volume. From mean values of volume loss and knowledge of total sliding distance and applied load, specific wear rates have been calculated for the a-C and a-C:H(A) coatings on polished substrates and on directionally ground substrates, for both transverse and parallel sliding. The values of friction coefficient and specific wear rate are collated in table 6.9.

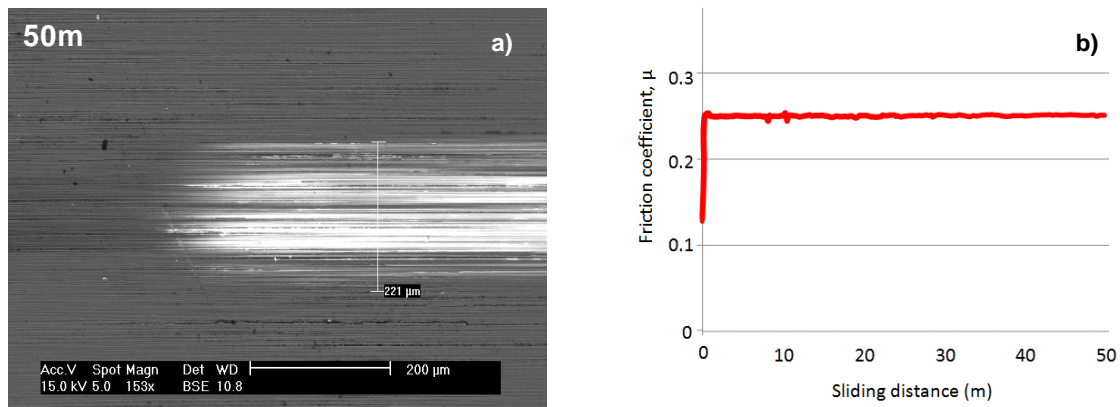


Figure 6.18 - Example reciprocating wear test conducted on a-C:H/DGnd sample parallel to the lay of surface texture: a) imaged by SEM, and; b) friction force recorded throughout reciprocating sliding test.

Table 6.9 – Results of reciprocating sliding wear testing

	a-C:H/DGnd	a-C/DGnd	a-C:H/Pol	a-C/Pol	a-C:H(B)	a-C:H:W
- Specific wear rate (m <sup>2</sup> N <sup>-1</sup> )	8.01e-17 (P) 2.81e-17 (T)	4.90e-17 (P) 6.52e-17 (T)	1.82e-17	1.10e-17	Undetermined	Undetermined
- Friction coefficient	0.26(P) 0.24(T)	0.26(P) 0.24(T)	0.24	0.24	0.23	0.16

The a-C:H(A)/DGnd and a-C/DGnd coating showed a relatively high wear rate which varied considerably with the direction of sliding. The a-C:H(A)/DGnd coating showed a greater wear rate under parallel sliding, a-C/DGnd coating conversely a lower wear rate under parallel sliding conditions. Wear testing of the a-C:H(A)/Pol and a-C/Pol showed much lower wear rates, with the a-C/Pol coating showing the lowest specific wear rate of those measured, at  $1.10 \times 10^{-17} \text{m}^2 \text{N}^{-1}$ . The friction coefficients of the a-C:H/DGnd and a-C/DGnd were the highest of those tested, when sliding wear was conducted parallel to surface lay, at 0.26. When sliding wear was conducted transverse to the surface lay the friction coefficient was the same as for the a-C:H(A)/Pol and a-C/Pol samples, at 0.24, slightly greater than that of the a-C:H(B)/Pol coating. The lowest friction coefficient was achieved for the a-C:H(W)/Pol sample, considerably lower at 0.16, which is in agreement with the dramatic decrease in friction coefficient observed in the valve-train testing.

#### 6.3.3.9 Micro-impact testing

Impact fatigue tests were conducted in addition to the valve-train tests using the apparatus and method described in section 4.5 of chapter 4. The impact procedure consisted of oscillating the impactor following a triangular wave with a frequency of 5Hz and amplitude of 1mm. All tests were conducted with a stored load of 80N in the pre-compressed spring and a 25mm diameter alumina ball as the counterface. Two sets of tests were conducted, the first set of tests was conducted dry i.e. unlubricated, and the second set of tests were performed with a continuous supply of SAE 5W30 friction modifier free engine oil to the contact. The oil was administered by a gravity feed from a pipette at a rate of  $0.3 \text{g min}^{-1}$ . Initially low numbers of impacts were performed. The contact area was then visually inspected for signs of substrate exposure, indicating coating failure, and if none was found further impacts were conducted in the same position. Repeat impacts in a fixed location allow durability to be investigated incrementally. When coating failure occurred the test procedure was repeated at a new location, and this process was repeated between 5 and 12 times dependent upon the deviation of results to establish the mean and impacts to failure with an accuracy of at least 250 cycles. The a-C and a-C:H(A) coatings were tested both with and without lubrication at  $15^\circ$ ,  $30^\circ$  and  $45^\circ$ . Figure 6.19 shows the impacts to failure in the various configurations for the a-C:H(A)/Gnd and a-C/Gnd coatings. Figure 6.20 shows example

impact craters with exposed areas of substrate where coating has failed, for the a-C and a-C:H(A) coatings tested with and without lubrication. Figure 6.21 shows examples of wear by dry impact at differing angles of impact.

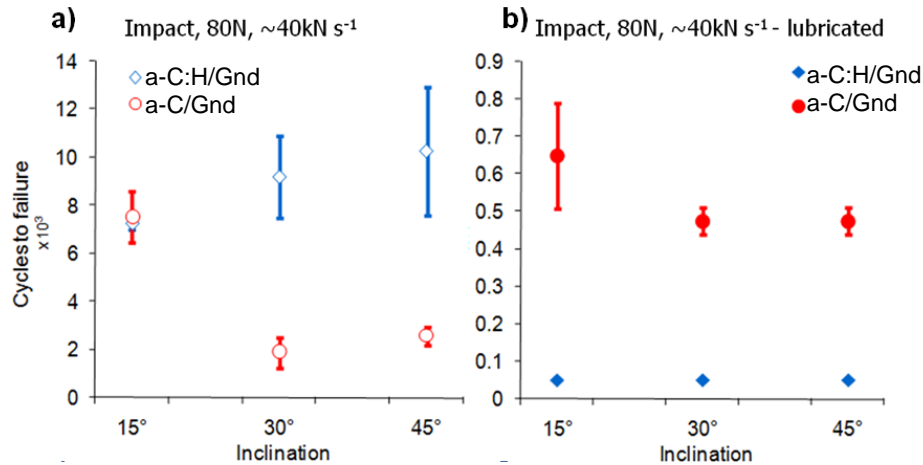


Figure 6.19- Graph of impact cycles to failure for the a-C:H(A)/Gnd and a-C/Gnd samples for: a) dry tests and b) oil lubricated tests. The error bars show one standard deviation.

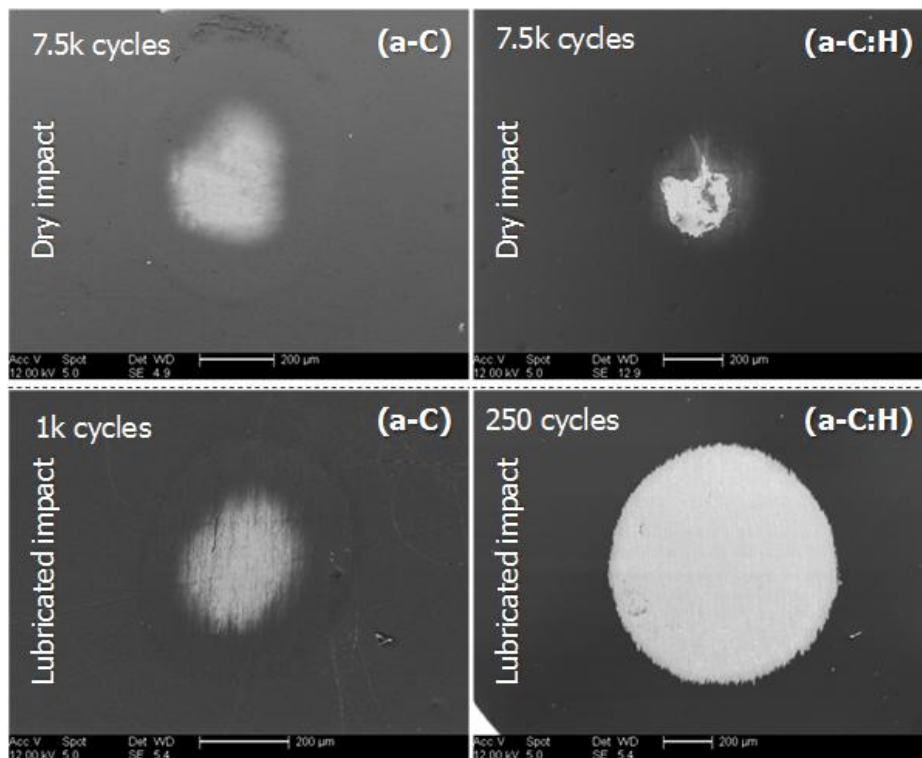


Figure 6.20 –Micrographs of example impact wear scars for a-C:H(A) and a-C coatings. Impacts conducted at 15° from normal to the surface. Each image shows inset the number of impacts that generated the wear along with coating type and presence of lubricant.

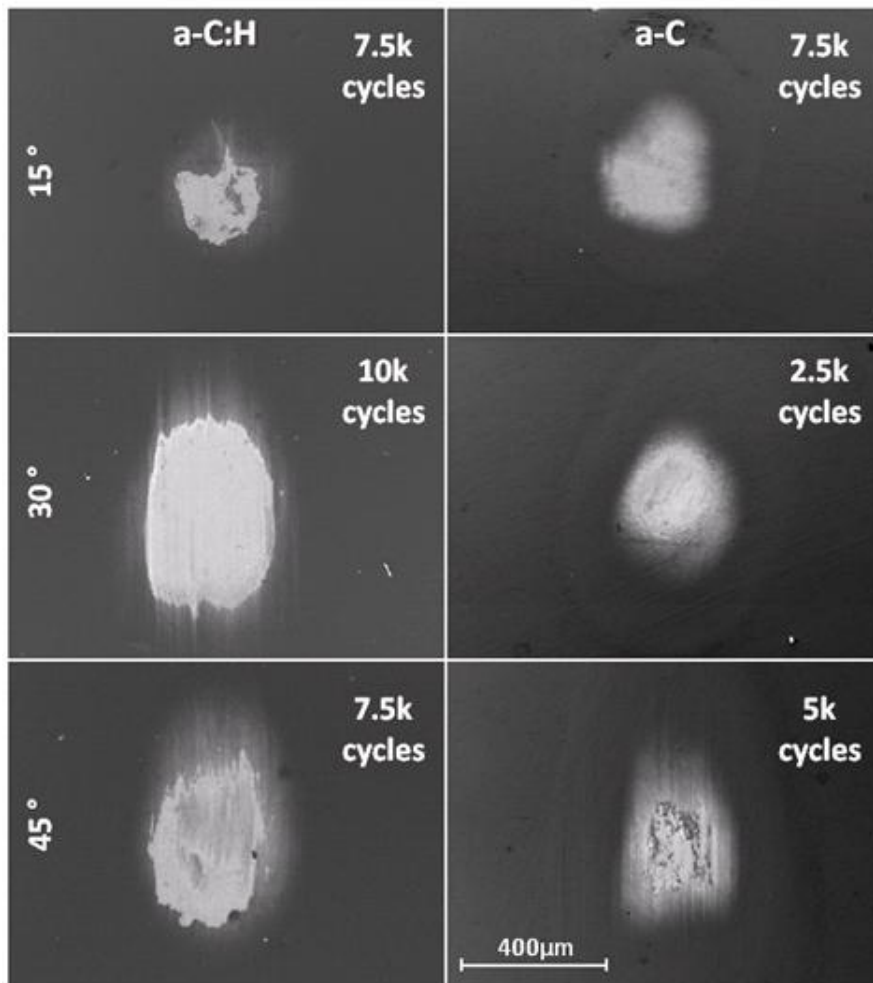


Figure 6.21 shows example images of wear by impact for the a-C and a-C:H(A) coatings at differing of angles of impact.

The role that impact angle plays is unclear from these results, with the a-C:H(A) coating showing increasing impacts to failure with increasing impact angle from normal, and the a-C coatings the opposite trend. The effect of including lubricant is much clearer, with a very large drop off in impacts to failure for both a-C:H(A) and a-C coatings. The a-C:H(A) coating in particular was highly susceptible to wear by lubricated impact, with <50 impacts to failure at any angle, a decrease of two orders of magnitude compared to un-lubricated impact. It is somewhat counter-intuitive that introducing a lubricant should increase wear, as lubricant could be expected to help distribute load and lower frictional forces, and by extension reduce shear forces that may cause wear. However the lubricant may also be acting to transport coating material away from the point of

contact, thereby eroding any build up of beneficial low friction tribofilms, or forming an abrasive slurry with any hard DLC particles that separate from the coating. The second hypothesis is supported somewhat by the fact that the wear scars formed during lubricated impact, shown in figure 6.20, are similar to those seen in the microabrasion studies.

This section has covered a wealth of results from mechanical and tribological tests as well as an assessment of coating morphology and composition. In order to assess the DLC coatings in the larger context of valve-train performance and the properties that affect valve-train performance, the results have been collated in table 6.10 below. Section 6.3.4 looks at the links that can be drawn from this information and discusses the important mechanisms in determining DLC coating performance.

6.3.4 Collated results - comparison and discussion

In order to establish how a coatings valve-train performance is affected by its composition, microstructure, and mechanical and tribological properties a wide variety of tests were conducted for a number of different coatings. The results of these tests are compiled in table 6.10 below, along with the relevant details of the uncoated steel shims performance.

Table 6.10 Testing matrix

Coating supplier	A	A	A	A	A	A	B	B
Substrate finish <sup>1</sup>	DGnd	DGnd	Pol	Pol	Gnd	Gnd	Pol	Pol
Coating composition	a-C:H	a-C	a-C:H	a-C	a-C:H	a-C	a-C:H:W	a-C:H
Deposition process	Magnetron PECVD	Magnetron sputtered	Magnetron PECVD	Magnetron sputtered	Magnetron PECVD	Magnetron sputtered	PECVD	PECVD
AFM – roughness (R <sub>a</sub> )	~142nm	~152nm	~20nm	~92nm	~20nm	~22nm	~19nm	~30nm
Coating thickness	~2.0µm	~2.1µm	~1.8µm	~1.9µm	-	-	~3.8µm	~3.8µm
Valve-train testing								
Mean sliding distance to failure, (×10 <sup>3</sup> m)	┌----- See fig 6.1 -----┐				┌----- See fig 6.2-----┐		┌----- See fig 6.3 -----┐	
- With impact	2.85	9.61	5.7	9.61	6.05	9.61	2.85	12.1
- Without impact	-	-	-	-	17.25	12.14	5.75	17.25
Friction coefficient	0.13	0.12	0.07	0.085	0.1	0.11	0.05	0.09
Nanoindentation								
- Hardness	See Pol →	See Pol →	17.2 GPa	15.1 GPa	-	-	9-11 GPa	41.3 GPa
Scratch – Adhesion								
- L <sub>c1</sub>	25N (P) <sup>1</sup> 17N (T)	67N (P) <sup>1</sup> 63N (T)	50N	89N	-	-	38N	48N
- L <sub>c2</sub>	77N (P) 87N (T)	N/A <sup>1</sup> (P) 89N (T)	83N	N/A	-	-	91N	98N
Micro-abrasion - Specific wear rate (m <sup>2</sup> N <sup>-1</sup> )								
- K <sub>c</sub>	Unrealistic	2.3 e <sup>-12</sup>	Unrealistic	2.15 e <sup>-12</sup>	-	-	Unrealistic	4.5 e <sup>-12</sup>
- K <sub>s</sub>	1.7 e <sup>-13</sup>	7e <sup>-14</sup>	1.4 e <sup>-13</sup>	1.05 e <sup>-14</sup>	-	-	1.8 e <sup>-13</sup>	5.3 e <sup>-15</sup>
Reciprocating sliding								
- Specific wear rate (m <sup>2</sup> N <sup>-1</sup> )	8.01e <sup>-17</sup> (P) 2.81e <sup>-17</sup> (T)	4.90e <sup>-17</sup> (P) 6.52e <sup>-17</sup> (T)	1.82e <sup>-17</sup>	1.10e <sup>-17</sup>	-	-	Undeter- mined	Undeter- mined
- Friction coefficient	0.24(T) 0.26(P)	0.23(T) 0.26(P)	0.24	0.24	-	-	0.16	0.23
Micro-impact								
- Dry (Impacts to failure)	-	-	-	-	7.3e <sup>3</sup> (15°) 9.2e <sup>3</sup> (30°) 10.3e <sup>3</sup> (45°)	7.6e <sup>3</sup> (15°) 1.9e <sup>3</sup> (30°) 2.6e <sup>3</sup> (45°)	-	-
- Lubricated (Impacts to failure)	-	-	-	-	<50(15°) <50(30°) <50(45°)	650 (15°) 450 (30°) 450 (45°)	-	-
Uncoated steel/Gnd	Roughness, R <sub>a</sub> (nm)				Valve-train testing friction coefficient			
	~63				0.11			

<sup>1</sup> Key : (P) denotes test conducted parallel to the lay of the texture  
(T) denotes test conducted transverse to the lay of the texture  
N/A denotes second critical failure conditions were Not Achieved during the test

It can be seen that the coatings under investigation offer a broad range of properties and durabilities in the valve-train. The results of valve-train testing demonstrate that under normal operating conditions the valve-train is a very demanding environment, with all coating/surface finish pairings having shown some evidence of severe coating wear within the period of testing. The a-C:H(B)/Pol samples showed the greatest durability in the valve-train under normal operating conditions, followed by the a-C coated samples. The a-C:H:W coated samples showed the poorest durability in the valve-train.

The a-C:H(A) coating with Gnd surface finish showed a reduced friction coefficient under lubricated cam-tappet contact when compared to the uncoated steel. The a-C coating with Gnd surface finish showed no reduction in friction coefficient compared with the uncoated steel surface of comparable surface finish. Considerable reduction in friction coefficient was also observed with a smoother surface finish, with the a-C:H(A) and a-C coatings showing a reduction in friction coefficient of ~45% and ~30% respectively from a DGnd to a Pol surface finish. This corresponds to a reduction in  $R_a$  of ~120nm and ~60nm for the a-C:H(A) and a-C coatings respectively. The a-C:H:W/Pol sample in particular showed a greatly reduced friction coefficient compared to that found for uncoated steel/Gnd, with an estimated friction coefficient, 0.05, which was ~55% lower than that found for the uncoated steel, 0.11. This contribution will be in part due to the smoother surface finish of the a-C:H:W/Pol sample,  $R_a \sim 19$ nm, compared to ~63 for the uncoated steel, however this friction coefficient is significantly lower than that observed for the a-C:H(A)/Pol which has a comparable surface finish. Section 6.3.4.1 that follows, discusses the relationship between the valve-train performance and the mechanical and tribological properties of the coatings.

#### 6.3.4.1 Valve-train performance, key coating properties

One of the chief aims of the DLC study conducted here was to establish any links that may exist between coating properties and valve-train performance. By considering the mechanical and tribological properties of those coatings that performed well in the valve-train properties of interest can be highlighted. As discussed above the two most durable coatings under normal valve-train conditions were the a-C and the a-C:H(B) coatings. Both of these coatings demonstrate very good adhesion. The a-C coating

demonstrated the highest lower critical load,  $L_{c1}$ , at 89N. The a-C:H(B) coating demonstrated comparable adhesion to that of the a-C:H(A) coating, for similar surface finish, but considerably greater durability in normal valve-train testing. The greater durability of the a-C:H(B) coated sample may in part be due to the very high coating hardness, which was considerably harder than the a-C, a-C:H(A) and a-C:H:W coatings, with values of film only hardness estimated at 41.3 GPa, 15.1 GPa, 17.2 GPa and ~10GPa respectively. The idea that hardness is an important factor is supported by the very low durability of the low hardness a-C:H:W coating, in spite of its low friction coefficient and moderate adhesion.

Good adhesion and high hardness would therefore appear to be crucial to good performance in the valve-train environment. The a-C:H(A) coating showed comparable adhesion to the a-C:H(B) coating, and slightly higher hardness than the a-C coating but consistently lower durability in the valve-train than either, with a higher incidence of early catastrophic failure. Looking at the results of the other tests in the study it can be seen that the a-C and a-C:H(B) coatings were also the only two to show good durability against microabrasive wear, so abrasive wear resistance may be a good indicator of performance. It is however interesting to note that the low values of durability for some coatings are almost entirely due to early catastrophic spallation. The two wear mechanisms observed in the valve-train were: (i) early delamination, and; (ii) steady abrasive scuffing. There is only limited evidence that the gross failure by spallation may have been initiated from areas of concentrated scuffing. The majority of cases show no obvious connection between the two wear processes, although the site of initial failure may have been obscured by further wear. There were however no examples of coatings which survived the apparent running-in period then going on to develop failure by spallation, even with the later development of considerable scuffing. It is therefore possible that the lower abrasive wear rates of the a-C and a-C:H(B) coatings decrease the rate of material loss to scuffing, which in turn inhibits the development of gross-delamination. The results of impact free valve-train operation and micro-impact testing may shed more light on the issue. The role that impact plays in the durability of the coatings is considered in detail in section 6.3.4.1.1 below.

#### 6.3.4.1.1 Role of impact

Valve-train wear testing has demonstrated that the impact loading that occurs in normal operation of a direct-acting overhead camshaft has a deleterious effect on the durability of the coatings. All coatings showing improved sliding distance to failure when valve-train tests were conducted without impact. When the valve-train test was adapted to remove impact loading, the a-C:H(A)/Gnd and a-C:H(B)/Pol coatings showed the greatest durability, with 100% of the tested coatings remaining intact.

In order to better understand the role of impact on coating durability a number of micro impact tests were conducted, investigating the effect of inclination angle and lubrication on impact fatigue resistance. These results are shown in figures 6.19 through 6.21, and discussed in section 6.3.3.9. From these it is clear that inclined impact in the presence of lubrication is very damaging to the coatings, with both coatings showing better durability under inclined impact without lubrication present for all impact angles. The a-C:H /Gnd coating appears particularly susceptible to wear by lubricated impact, with <50 impacts to failure compared to <500 impacts to failure for the a-C coating.

In order to better understand the contact conditions of inclined impact, a two dimensional finite element model has been developed in the modelling package FEMLab. The model was developed to investigate the forces at the contact, and Von Mises stress intensity in the substrate and coating near the contact, when loaded at various angles of inclination. This modelling has been conducted for the angles at which impact occurs and at 0°, normal loading. The simulations are limited to static loading, as opposed to the rapidly changing loads experienced during impact, however the results should be indicative of the changes in internal stress magnitude and stress distribution that occurs with change in impact angle. The contact conditions were determined by the load used during impact testing, i.e. 80N, and the component geometry, see figure 6.22. Body A represents the Al<sub>2</sub>O<sub>3</sub> stylus and body B the sample held at an angle of  $\alpha$  from horizontal.

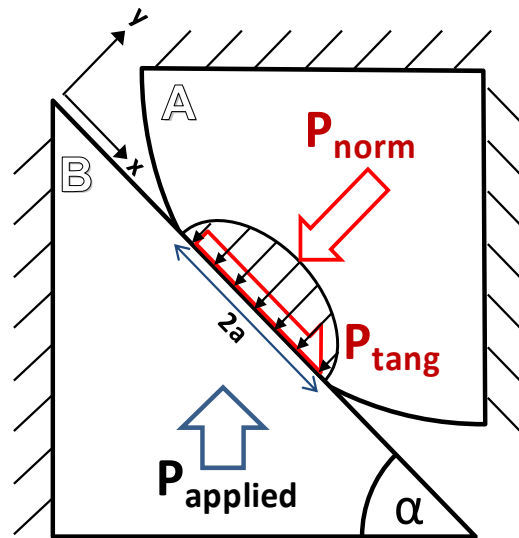


Figure 6.22- Illustration of impact contact conditions.

$P_{\text{applied}}$  is the applied load and  $P_{\text{norm}}$  and  $P_{\text{tang}}$  are the normal and tangential components of the resulting force which balance the applied load. The magnitudes of these reaction forces are determined by equation (1),

$$P_{\text{applied}} = P_{\text{norm}} \cos\alpha + P_{\text{tang}} \sin\alpha \quad (1)$$

As the surfaces are not adhered to one another, the tangential component of reaction force is limited to that which can be conferred by friction.

$$P_{\text{tang}} = \mu P_{\text{norm}} \quad (2)$$

Therefore (1) becomes,

$$P_{\text{applied}} = P_{\text{norm}} (\cos\alpha + \mu \sin\alpha) \quad (3)$$

and ,

$$P_{\text{norm}} = \frac{P_{\text{applied}}}{(\cos\alpha + \mu \sin\alpha)} \quad (4)$$

From equations (4) and (2) the normal and tangential components of the reaction force can be calculated for various angles. A value of coefficient of friction was determined by reciprocating sliding against a 5mm diameter  $\text{Al}_2\text{O}_3$  ball, a representative value was taken as 0.15. Figure 6.23 shows the resulting normal and tangential loading components. It is worth noting that the two load components both increase rapidly at

angles above 45°, and that the conditions under which impact occurs in the valve-train indicate impact may be occurring at angles as high as 85°.

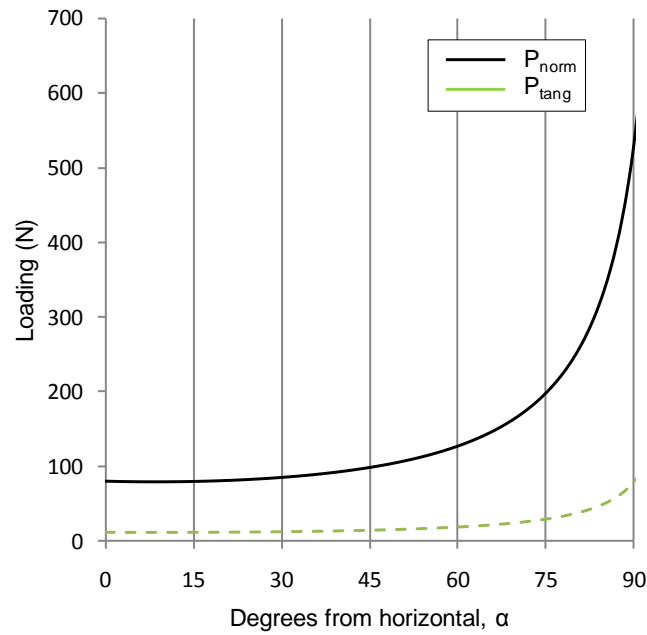


Figure 6.23 – Graph of the normal and tangential load components for a friction coefficient of 0.15

With knowledge of the normal and tangential components of load on the sample surface, the contact can be treated as a Hertzian ball-on-flat. The half contact width,  $a$ , maximum normal load,  $P_{max}$  and load distribution across the contact,  $P(x)$ , can therefore be determined from Hertzian contact mechanics.

$$a = \left( \frac{3P_{norm} R}{4E^*} \right)^{1/3} \quad (5)$$

Where  $R$  is the stylus radius and  $E^*$  is the combined contact stiffness.  $E^*$  was calculated from modulus values of 300GPa and 207GPa, and poisons ratio values of of 0.21 and 0.27 for the alumina stylus and steel sample respectively.

$$P_{max} = \frac{3P_{norm}}{2\pi a^2} \quad (6)$$

$$P(x) = P_{max} \left( 1 - x^2/a^2 \right)^{1/2} \quad (7)$$



FE simulations indicate that with a departure from normal impact there is a repositioning of maximum von Mises stress intensity, towards the coating substrate interface, due to the tangential loading component. The point of maximum stress intensity does not continue to move towards the interface with increasing impact angle as normal and tangential components are proportional. However stress intensity does continue to increase with increasing angle of inclination. Considering again the wear scars shown in figure 6.21, the effect of increased tangential loading can be seen in the elongated wear scars. At low impact angles, the a-C:H(A) coating showed failure by micro-cracking and spallation, at higher impact angles the wear scars were elongated and may indicate a transition to wear dominated by abrasive sliding. The a-C coating by contrast appeared to fail by an abrasive wear mechanism at all angles, which became more severe with increasing impact angle. The wear mechanism of high angle impact is therefore somewhat analogous to that of the reciprocating sliding wear, however the contact pressure and the normal and tangential components of load are very different.

Both of the coatings demonstrated very low coating durability with the addition of lubricant to the micro-impact site, severely reducing the number of impacts prior to coating failure for both coatings tested. It should be considered that the effect that lubricant has upon inclined impact is only part of the more complex wear process that occurs in the valve-train, and from these results it should not be interpreted that unlubricated valve-train operation is desirable. What these tests do show is that inclined impact of thin-film DLC coatings, particularly in the presence of lubricant, is a factor in their overall performance in the valve-train. The results of lubricated inclined impact appear to be in agreement with the valve-train test results; having impact in the cycle is deleterious to coating durability and the a-C:H(A) coating is more susceptible than the a-C coating, showing a greater difference in sliding distance to failure in valve-train testing with and without impact. The micro-impact test procedure is therefore of great potential benefit in coating selection, helping to indicate valve-train performance of candidate coatings. A few adjustments are suggested. Lubricant flow rates were low, and this may have caused additional retention of hard DLC particles, encouraging the formation of abrasive slurry. Also, despite efforts to select an impact stylus of relatively

large radius, the geometry of the stylus will have led to a considerably greater contact pressure than that experienced in the valve-train, by adopting a stylus geometry closer to that of the cam, the conditions will be made more realistic.

In spite of these considerations the results of micro-impact and valve-train impact studies clearly show that a coating's durability against lubricated inclined impact has a role to play in determining overall coating durability in the valve-train.

#### 6.3.4.2 Role of surface finish

It appears that the surface finish of the coating has an important role to play primarily in determining the friction coefficient observed in the valve-train and also the durability of the coatings. As described in section 6.2 the surface finish of the coated surfaces is largely dependent upon the surface finish of the shims prior to coating deposition, with the DGnd samples showing the highest surface roughness followed by the Gnd coatings and the Pol. The values of friction coefficient determined in the valve-train are consistently greatest for the DGnd samples and lowest for the Pol. The effect of surface finish is considerable, with a change in friction coefficient for the a-C and a-C:H(A) coatings of 0.035 and 0.06 respectively between the DGnd and Pol surface finishes.

Processes for super-finishing of surfaces are likely to be competing with thin-film deposition processes as methods of solving the issue of friction and wear in the valve-train. The testing conducted here does not allow for direct comparison between the effect of improving surface finish and low-friction DLC coatings, it does demonstrate that both are capable of greatly reducing the energy lost to friction in the valve-train.

The effect of coating surface finish on coating durability is less clear than its effect on friction coefficient with the a-C coated shims having shown the same durability independent of surface finish, while the a-C:H(A) coated shims that performed best had the intermediate Gnd surface finish. The large sharp features of the DGnd surface finish may act as initiators of wear, for which there is some evidence, while the Pol surface finish does not leave crevice volume for good entrainment and retention of engine oil.

#### 6.3.5 Conclusions

This chapter has discussed the investigation of DLC coatings for application as a low-friction, low-wear solution to the problem of valve-train wear. This study has covered the valve-train performance of the investigated coatings and their mechanical and

tribological properties, with the aim of establishing the key properties for determining good valve-train durability. The results of this study have shown that the valve-train environment is a harsh and highly destructive environment for thin-film coatings, with relatively hard and well adhered coatings showing many examples of gross delamination and severe abrasive wear. There have also been examples of DLC coatings performing well over the period of valve-train testing, with no severe wear mechanisms being initiated. The mechanical and tribological properties that may determine this dramatic change in durability have been investigated and it was found that the hardness, coating adhesion and abrasive wear rate were good indicators of performance. The role that impact plays in determining coating performance was also investigated and the high angle inclined impact that occurs in standard operation of the valve-train was determined to be highly damaging to the thin-film coatings. The wear mechanics of inclined impact were investigated further in a micro-impact test. Inclined impact in the presence of lubricant was found to generate extremely high rates of coating wear. This technique requires further development to better mimic the impact and lubrication regime found in the valve-train and the results are to be treated with caution at this stage. These findings were expanded upon by the construction of a finite element model of the contact forces and stresses. It was found that a transition to an abrasive sliding wear regime can be expected at high impact angles.

#### 6.4 Future work

The apparatus and techniques used in this study have demonstrated that very low values of friction coefficient in the valve-train are possible with the application of commercially available DLC coatings. These techniques are however not perfected, and the determination of friction coefficient would be improved with the reduction of torsional vibration in the camshaft and the development of more sophisticated methods of fitting real and simulated torque data. The improvement of both these issues was discussed in chapter 2.

The most important aspect of furthering this investigation is to broaden the range of candidate coatings that are tested. The study conducted here has aimed to be systematic in its approach and much information has been collected on a relatively small selection of coatings. A real understanding of the properties which effect coating performance in the valve-train will only come from the systematic study of a wide variety of different

coatings, deposited by a number of means and covering the spectrum of mechanical and tribological properties that are available from DLC coatings. Two factors not considered in depth in this study are the role of coating interlayer and the tribo-chemistry of the coatings. The careful design of coating interlayers can yield benefits in coating adhesion, stiffness and toughness [34, 42-45], and the selection of coating chemistries which are attractive to lubricants and lubricant additives has been shown to dramatically improve the friction coefficient and wear rates of DLC coatings [46-48]. The detrimental effect of impact on coating durability indicates that use of coatings with a high impact fatigue resistance may be of particular benefit in the valve-train.

The greatest potential for DLC coatings in the valve-train will come from sympathetic design, where the valve-train mechanism is developed with consideration of the weaknesses and strengths of DLC. For example a valve-train system incorporating hydraulic dashpot tappets will help to alleviate impact loading, thereby improving DLC coating durability, while maintaining valve-train operating conditions. The combination of mechanism design and coating design offers a wealth of research and development opportunities.

In summary, this investigation has demonstrated the great potential improvements in efficiency and durability of the automotive valve-train, available from study of thin-film coatings such as DLC.

---

---

## 6.5 Chapter references

- 1 Schmallenmeier, H. Exp Technik Physik, Die Beeinflussung von festen Oberflächen durch eine ionisierte Gasatmosphäre, 1953, **1**, 49-68.
- 2 Aisenberg, S. and Chabot, R. Ion-Beam Deposition of Thin Films of Diamondlike Carbon, Journal of Applied Physics, 1971, **42** (7), 2953.
- 3 Holland, L. and Ojha, S.M. Deposition of hard and insulating carbonaceous films on an r.f. target in a butane plasma, Thin Solid Films, 1976, **38** (2), L17.
- 4 Spencer, E.G., Schmidt, P.H., Joy, D.C. and Sansalone, F.J. Ion-beam-deposited polycrystalline diamondlike films, Applied Physics Letters, 1976, **29** (2) 118.
- 5 Weissmantel, C., Bewilogua, K., Schurer, C., Breuer, K. and Zscheile, H. Characterization of hard carbon films by electron energy loss spectrometry, Thin Solid Films, 1979, **61** (2), L1-L4.
- 6 Arnoldussen, T.C. and Rossi, E.M. Materials for Magnetic Recording, Annual Review Material Science, 1985, **15**, 379-409.
- 7 Donnet, C. Recent progress on the tribology of doped diamond-like and carbon alloy coatings: a review. Surface and Coatings Technology, 1998, **100**, 180-186.
- 8 Erdemir, A. and Donnet, C. (chap. 24) Tribology of Diamond, diamond-like carbon and related materials. In Bhushan, B., ed. Modern Tribology Handbook (CRC Press, 2000).
- 9 Grill, A. and Patel, V. Wear Resistant Fluorinated Diamond Like Carbon, Diamond Films and Technology, 1996, **6**, 13-21.
- 10 McKenzie, D.R. Tetrahedral bonding in amorphous carbon. Prog. of Physics, 1996, **59**, 1611-1664.
- 11 Robertson, J. Diamond-like amorphous carbon. Material Science and Engineering Review, 2002, **37**, 129-281.
- 12 Silva, S.R.P., Carey, J.D., Khan, R.U.A., Gerstner, E.G. and Anguita, J.V. Handbook of Thin Film Materials. (Academic Press, New York, 2002).
- 13 Hainsworth, S.V. and Uhure, N.J. Diamond-like carbon coatings for tribology: production techniques, characterisation methods and application. International Materials Reviews, 2007, **52**(3), 153.

- 14 Wang, J.S., Sugimura, Y., Evans, A.G. and Tredway, W.K. The mechanical performance of DLC films on steel substrates. *Thin Solid Films*, 1998, **325**(1-2), 163-174.
- 15 Weiler, M., Sattel, S., Jung, K., Ehrhardt, E., Veerasarmy, V.S. and Robertson, J. *Applied Physics Letters*, 1994, **64**, 2797.
- 16 Ashby, M.F. and Jones, D.R.H. *Engineering materials*. (Pergamon Press, Oxford, 1980).
- 17 Li, F. and Lannin, J.S. Radial distribution function of amorphous carbon, *Physics Review Letters*, 1990, **65** (15), 1905-1908.
- 18 Pharr, G.M., Callahan, D.L., McAdams, S.D., Tsui, T.Y., Anders, S., Anders, A., Ager, J.W., Brown, I.G., Bhatia, C.S., Silva, S.R.P. and Robertson, J. Hardness, elastic modulus, and structure of very hard carbon films produced by cathodic-arc deposition with substrate pulse biasing, *J. Applied Physics Letters*, 1996, **68** (6), 779.
- 19 Fallon, P.J., Veerasarmy, V.S., Davis, C.A., Robertson, J., Armarantunga, G.A.J., Milne, W.I. and Koskinen, J. Properties of filtered-ion-beam-deposited diamondlike carbon as a function of ion energy, *J. Physics Review B*, 1993, **48** (7), 4777-4782.
- 20 Green, D.C., McKenzie, D.R. and Lukins, P.B., *The Microstructure of Carbon Thin Films*, *Material Science Forum*, 1990, **52-53**, 103-124.
- 21 Jacob, W. and Moller, W., On the structure of thin hydrocarbon films, *Applied Physics Letters*, 1993, **63** (13), 1771.
- 22 Jiang, X., Fassbender, J. and Hillebrands, N. Elastic constants of WC-a-C:H composite films studied by Brillouin spectroscopy. *Physics Review B*, 1994, **49B**(19), 13815-13819.
- 23 Cho, S.J., Lee, K.R., Eun, K.Y., Han, J.H. and Ko, D.H. Determination of elastic modulus and Poisson's ratio of diamond-like carbon films. *Thin Solid Films*, 1999, **341**(1-2), 207-210.
- 24 Harry, E., Rouzand, A., Ignat, M. and Juliet, P. Mechanical properties of W and W(C) thin films: Young's modulus, fracture toughness and adhesion. *Thin Solid Films*, 1998, **332**(1-2), 195-201.
- 25 Varma, A., Palshin, V. and Meletis, E.I. Structure-property relationship of Si-DLC films. *Surface and Coatings Technology*, 2001, **149**(2-3), 305-314.

- 
- 26 Abbas, G.A., McLaughlin, J.A. and Harkin-Jones, E. A study of ta-C, a-C:H and Si-a-C:H thin films on polymer substrates as a gas barrier. *Diamond and Related Materials*, 2004, **13**(4-8), 1342-1345.
  - 27 Damasceno, J.C., Camargo, S.S., Freire, F.L. and Carius, R. Deposition of Si-DLC films with high hardness, low stress and high deposition rates. *Surface and Coatings Technology*, 2000, **133-134**, 247-252.
  - 28 Lee, K.R., Kim, M.G., Cho, S.J., Eun, K.Y. and Seong, T.Y. Structural dependance of mechanical properties of Si incorporated diamond-like carbon films deposited by RF plasma-assisted chemical vapour deposition. *Thin Solid Films*, 1997 ICMCTF congress, **308-309**, 263-267.
  - 29 Salvadori, M.C., Martins, D.R. and Cattani, M. DLC coating roughness as a function of film thickness. *Surface and Coatings Technology*, 2005, **200** (16-17), 5119-5122.
  - 30 Erdemir, A. Genesis of superlow friction and wear in diamond-like carbon films. *Tribology International*, 2004, **37**(11-12), 1005-1012.
  - 31 Gee, M.G. and Wicks, M.J. Ball crater testing for the measurement of the unlubricated sliding wear of wear-resistant coatings. *Surface and Coatings Technology*, 2000, **133-134**, 376-382.
  - 32 Kennedy, F.E., Lidhagen, D., Erdemir, A., Woodford, J.B. and Kato, T. Tribological behaviour of hard carbon coatings on steel substrates. *Wear*, 2003, **255** (7-12), 854-858.
  - 33 Psyllaki, P.P., Jeandin, M., Pantelis, D.I. and Allouard, M. Pin-on-disc testing of PE-CVD diamond-like carbon coatings on tool steel substrates. *Surface and Coatings Technology*, 2000, **130** (2-3), 297-303.
  - 34 Voevodin, A.A. and Zabinski, J.S. Superhard, functionally gradient, nanolayer and nanocomposite diamond-like carbon coatings for wear protection. *Diamond and Related Materials*, 1998, **7**(2) 463-467.
  - 35 Hainsworth, S.V. and Uhure, N.J. *Diamond-Like Carbon Coatings for Tribology: Production Techniques, Characterization Methods and Applications*. *International materials reviews*, 2007, **52**, 153-174.
  - 36 Casiraghi, C., Piazza, F., Ferrari, A.C., Grambole, D. and Robertson, J. Bonding in hydrogenated diamond-like carbon by Raman spectroscopy. *Diamond and Related Materials*, 2005, **14**, 1098-1102.
  - 37 Peggs, G.N. and Leigh, I.C. Report MOM62. UK National Physics Laboratory, England, 1983.
-

- 
- 38 Korsunsky, A.M., McGurk, M.R., Bull, S.J. and Page, T.F. On hardness of coated systems. *Surface and Coatings Technology*, 1998, **99**(1-2), 171-183.
- 39 Chang, C.-L. and Wang, D.-Y. Microstructure and adhesion characteristics of diamond-like carbon films deposited on steel substrates. *Diamond and Related Materials*, 2001, **10**(8), 1528-1534.
- 40 Kusano, Y. and Hutchings, I.M. Sources of variability on the free ball micro-scale abrasion test. *Wear*, 2005, **258**, 313-317.
- 41 Kusano, Y., Van Acker, K. and Hutchings, I.M. Methods of data analysis for the micro-scale abrasion test on coated substrates. *Surface and Coatings Technology*, 2004, **183**, 312-327.
- 42 Voevodin, A.A., Capano, M.A., Laube, S.J.P., Donley, M.S. and Zabinski, J.S. Design of a Ti/TiC/DLC functionally gradient coating based on studies of structural transitions in Ti-C thin films. *Thin Solid Films*, 1997, **298**, 107-115.
- 43 Yu, H.Y., Sanday, S.C. and Rath, B.B. The effect of substrate on the elastic properties of films determined by the indentation test- Axisymmetric Boussinesq problem. *Journal of Mechanics and Physics of Solids*, 1990, **38**(6), 745-764.
- 44 Strondl, C., Van der Kolk, G.J., Hurkmans, T., Fleischer, W., TRinh, T., Carvalho, N.M. and Hosson, J.T.M.d. Properties and characterizartion of multilayers of carbides and diamond-like carbon. *Surface and Coatings Technology*, 2004, **142-144**, 707-713.
- 45 Hong, B., Kim, H.J., Park, Y.S. and Jeon, Y. Tribological Properties of Ultrathin DLC Films with and without Metal Interlayers. *Journal of the Korean Physical Society*, 2007, Vol. 51, September 2007, **3**, 1124-1128
- 46 Haque, T., Morina, A., Neville, A., Kapadia, R. and Arrowsmith, S. Non-ferrous coating/lubricant interactions in tribological contacts: Assessment of tribofilms. *Tribology International*, 2007, **40**(10-12), 1603-1612.
- 47 Haque, T., Morina, A., Neville, A., Kapadia, R. and Arrowsmith, S. Effect of oil additives on the durability of hydrogenated DLC coating under boundary lubrication conditions. *Wear*, 2009, **266**(1-2), 147-157.
- 48 Neville, A., Morina, A., Haque, T. and Voong, M. Compatibility between tribological surfaces and lubricant additives--How friction and wear reduction can be controlled by surface/lube synergies. *Tribology International*, 2007, **40**(10-12), 1680-1695.
-

# CHAPTER 7

## Carbon nitride coatings

---

### **7. Carbon nitride coatings**

#### **7.1 CN<sub>x</sub> coatings - History of development and properties**

#### **7.2 Importance of hardness and elasticity in wear**

#### **7.3 Valve-train study**

##### *7.3.1 Coating selection*

##### *7.3.2 Testing*

###### 7.3.2.1 Valve-train testing

###### 7.3.2.2 Mechanical and tribological testing

##### *7.3.3 Results*

###### 7.3.3.1 Valve-train testing

###### 7.3.3.2 Nanoindentation testing – H/E

###### 7.3.3.3 Scratch-adhesion testing

###### 7.3.3.4 Reciprocating sliding wear

##### *7.3.4 Discussion*

##### *7.3.5 Conclusions*

#### **7.4 Future work**

#### **7.5 Chapter references**

---

As described in chapter 3, carbon nitride (CN<sub>x</sub>) coatings are an experimental coating principally composed of carbon and nitrogen. They have the potential to be deposited with a microstructure that offers a unique coupling of high hardness and rubber-like elasticity. This chapter looks at the development of CN<sub>x</sub> coatings, their structure, their mechanical properties and an investigation of how suitable this makes them for valve-train applications. CN<sub>x</sub> coatings offer the opportunity to investigate the importance of high elasticity and high hardness, acting as a counterpoint to DLC coatings which are typically hard but also stiff and relatively inelastic.

### 7.1 $CN_x$ coatings - History of development

Interest began in the deposition of carbon nitride substances after Liu and Cohen (1989,1990) [1, 2] predicted, using a first principles model, a new crystalline carbon nitride structure - cubic beta carbon nitride  $\beta-C_3N_4$ , see figure 7.1. The predicted structure has very short covalent intermolecular bonds due to the small radii of carbon atoms.

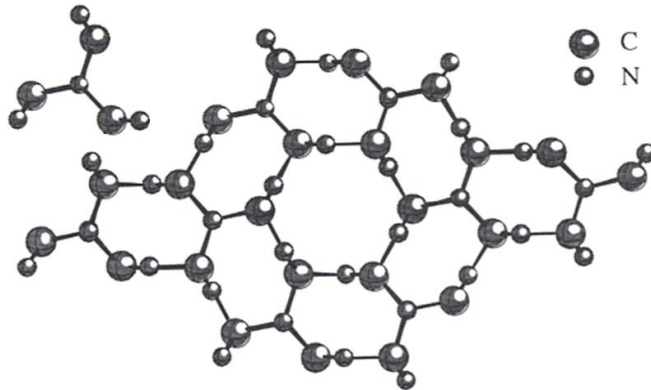


Figure 7.1 – predicted structure of the  $\beta-C_3N_4$  crystal [3].

The bonds of this molecular arrangement are predicted to be shorter than that of diamond. As molecular bond length is known to be an indicator of elastic modulus and hardness, a hardness higher than that of natural diamond was predicted for  $\beta-C_3N_4$ . This was of clear interest to the scientific and industrial communities and the generation of  $\beta-C_3N_4$  gained considerable research effort. There have however been no verified examples of  $\beta-C_3N_4$  crystallographic structure being produced in bulk. The principle reason cited is the difficulty in introducing more than 30at.% nitrogen, 57at.% nitrogen being required to produce the crystalline  $\beta-C_3N_4$  structure. This is in part due to a necessary compromise in deposition conditions; high substrate temperatures,  $T_s$ , are required to provide the energy to form a crystalline structure with high N content,  $C_N$ , however deposition rate and N absorption tend to decrease with an increase with substrate temperature. These limits are indicated in figure 7.2. Attempts to form  $\beta-C_3N_4$  have instead led to amorphous or even porous structures. The introduction of a greater bias voltage to raise the kinetic energy of the ions is ineffective due to a low re-sputtering limit of carbon nitrides [4, 5], see figure 7.3. Examples exist where small crystalline particles with high nitrogen content have been found in an amorphous

matrix but they do not demonstrate the extreme hardness expected for crystalline  $\beta$  –  $C_3N_4$  [6]. The amorphous carbon nitride coatings that were deposited have however gained interest of their own, and include the  $CN_x$  coatings under discussion in this study. These  $CN_x$  coatings demonstrate a wide variety of material properties but are characterized by a high hardness, typically 15-60GPa, similar to that of DLC coatings, combined with an extremely high elasticity.

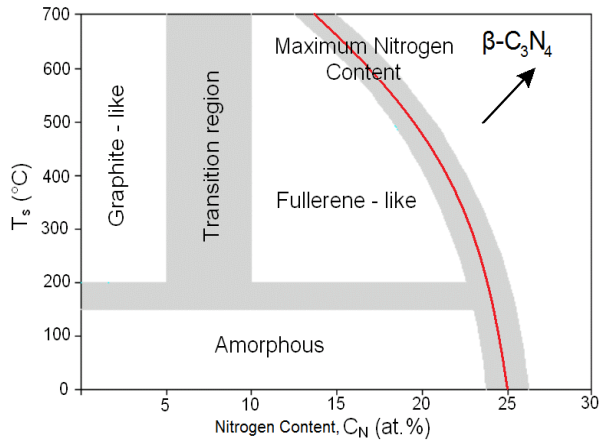


Figure 7.2 – as deposited nitrogen content against substrate temperature.

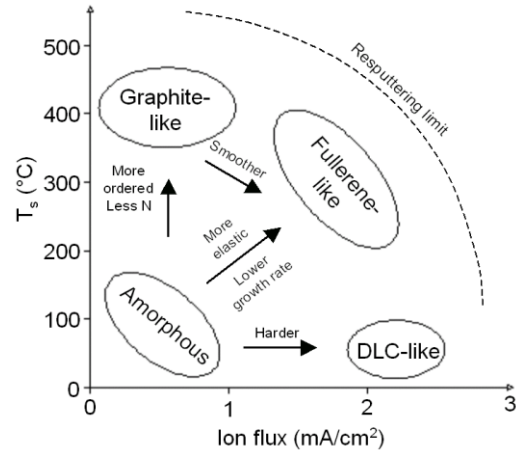


Figure 7.3 – microstructure of as deposited  $CN_x$  coatings, indicating the role of ion flux and substrate temperature.

The extreme elasticity of amorphous  $CN_x$  coatings has been suggested to be due to the formation of fullerene-like structures. Fullerene is an allotrope of carbon where all of the atoms form a closed shell or a single plane (see figure 7.4 for an example). Graphene, a singular layer from a graphite structure, is an example of a fullerene. Fullerenes are most commonly considered to be curved, for example consider a layer of graphene; it consists of a structure of hexagonally bonded carbon atoms on a plane. If some of those hexagonal structures were replaced with pentagonal structures the layer of atoms must curve to accommodate the shorter spacing. This form of curving gives rise the classic example of a fullerene, the  $C_{60}$  molecule, see figure 7.4. Fullerenes demonstrate some very impressive and unique properties in terms of their electrical and thermal conduction, chemical solubility and mechanical properties. Mechanically, fullerene molecules are of interest as their curved structure allows them to accommodate a certain amount of deformation by bond rotation, unlike crystalline structures which must undergo bond breakage in order to accommodate deformation. This gives rise to the high elasticity of fullerene molecules.

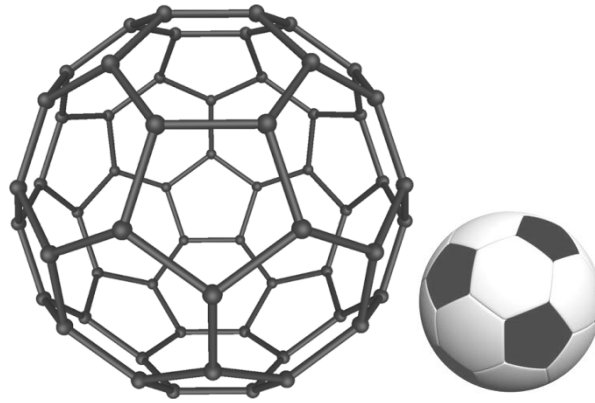


Figure 7.4 – the carbon allotrope C-60, composed of hexagonally and pentagonally bonded carbon atoms. This takes the same form as the segments of a football shown inset.

It has been demonstrated that carbon nitride coatings can be deposited which possess a fullerene-like structure [7-10]. Figures 7.2 and 7.3 indicate the conditions required for the deposition of carbon nitrides with a fullerene-like microstructure. For the case of amorphous carbon nitride it is thought that the nitrogen atoms encourage the formation of pentagonal structures in otherwise hexagonal layers and cause curvature, as with the example of graphene above. This leads to a structure of buckled and interlinked turbostratic layers. This structure can accommodate some strain by bond rotation rather than bond breakage and while there is interlinking it is much less numerous than in crystalline structures and the lack of numerous highly ordered bonds allows for the large elastic strains. Fullerene-like carbon nitride (FL-CN<sub>x</sub>) coatings demonstrating a high hardness,  $H$ , whilst maintaining a relatively low elastic modulus,  $E$ , represent an opportunity to investigate the importance of high elastic strain on coating performance in the valve-train.

## 7.2 Importance of hardness and elasticity in wear

For many years, development of wear resistant coatings has concentrated on achieving the highest possible values of coating hardness, as hardness has long been known to affect wear resistance [11]. In recent years however, it has been recognised that hardness is not necessarily the only requirement for good wear resistance. Leyland et al (2000) [12] drew attention the role that  $H/E$  plays in determining yield pressure and crack propagation and the benefits of reducing Young's modulus. A highly elastic substance can accommodate greater strain without permanent deformation. This has

clear benefits in a contact experiencing sliding wear and asperity interaction, allowing asperities to elastically deform to accommodate motion, rather than plastically deform or fracture. A low value of  $E$  is particularly beneficial if it can be closely matched to the elastic modulus of the substrate [13], as this will reduce interfacial stress discontinuities and improve the load support from the substrate. Because of this recognition, interest in coating materials that can provide a high  $H/E$  ratio is growing. This study looks at how a low  $H/E$  ratio affects the performance of hard, wear-resistant coatings in the valve-train.

### 7.3 Valve-train study

This study is very similar in structure to that conducted for the DLC carbon coatings. Two  $CN_x$  coatings were tested in the cam-tappet testing rig, and the results compared to those found for a variety of mechanical and tribological tests. Where possible the test conditions used for the DLC coatings have been maintained so that the performance of FL- $CN_x$  and DLC coatings can be compared. This section looks at the test procedures used and gives details specific to testing with FL- $CN_x$ .

#### 7.3.1 Coating selection

Two fullerene-like carbon nitride coatings were deposited by plasma assisted chemical vapour deposition (PACVD). Substrates were the same M2 tool steel shims used for DLC deposition, see section 6.4.2. The shims were polished prior to coating deposition to an #800 grit SiC finish and then annealed at 600°C for two hours to relieve stress and destroy absorbed dirt, in order to aid coating adhesion. A ~60nm thick interlayer of Ti was then deposited prior to the deposition of the FL- $CN_x$  coatings. Two sets of FL- $CN_x$  coatings were deposited at the University of Linköping, Department of Thin Film Physics, Sweden. The two coatings were deposited with two different precursor atmospheres: (i) atmosphere containing 16 at.% N, 84at.% Ar, and; (ii) atmosphere containing 66 at.% N, 34at.% Ar. This resulted in a set of low nitrogen content FL- $CN_x$  coatings and a set of high nitrogen content  $CN_x$  coatings. Coatings were deposited to a thickness of ~300nm by controlling growth rate. Two precursor nitrogen contents were selected, which will determine the nitrogen content of the deposited coatings. The nitrogen content will determine the coating microstructure, hardness and adhesion.

It should be noted that the coating deposition apparatus used at present cannot accommodate coating of the entire shim surface. Coated samples therefore have a

circular subset of their total area that is coated, this is clearly visible in the optical macrograph images of the shims tested in the valve-train, figure 7.7 in section 7.3.3.1.

The as deposited FL-CN<sub>x</sub> coatings were investigated by microscopy using the same equipment used in chapter 6 and described in section chapter 5. Scanning electron microscopy (SEM) was used to image surface morphology and the features created by the mechanical and tribological testing. Energy dispersive X-ray (EDX) analysis was used to confirm coating composition. Atomic force microscopy (AFM) was conducted on the samples before and after coating deposition. Figure 7.5a shows the results of AFM conducted on shims prior to coating deposition and identified roughness parameter R<sub>a</sub> to be ~25nm. Figure 7.5(b) and 7.5(c) shows AFM scans of surfaces post coating deposition for the 16 at.% N CN<sub>x</sub> coating and the 66 at.% N CN<sub>x</sub> coatings respectively. The 16 at.% N CN<sub>x</sub> coating shows a smooth surface finish, with an R<sub>a</sub> of ~20nm. The coating has filled some of the troughs left by polishing and the coated surface is smoother than the uncoated substrate. The 66 at.% N CN<sub>x</sub> coating however has produced a much rougher finish, which is evident in figure 7.5(c). The surface has large flat areas where surface roughness is low, interspersed with very rough areas with some high asperities and many deep troughs. AFM scans indicate that the trough depth of the rough areas approaches the thickness of the coatings. Figure 7.6 shows low and high magnification SEM images of the post deposition surface finish, prior to any testing. The rougher areas found by AFM are shown as the brighter regions in the SEM images (see figure 7.6(c) and 7.6(d)). The contrast differences could arise from differing electronic properties of the different regions or additional electron scattering from the rough edges of asperities. Figures 7.6(e) and 7.6(f) show EDX analysis of two regions of the 66 at.% N CN<sub>x</sub>. These indicate a higher proportion of iron in the rough regions and lower proportion of carbon and titanium, indicating coating thinning and substrate exposure. It can be seen that these areas cover a high proportion, ~50%, of the coating surface.

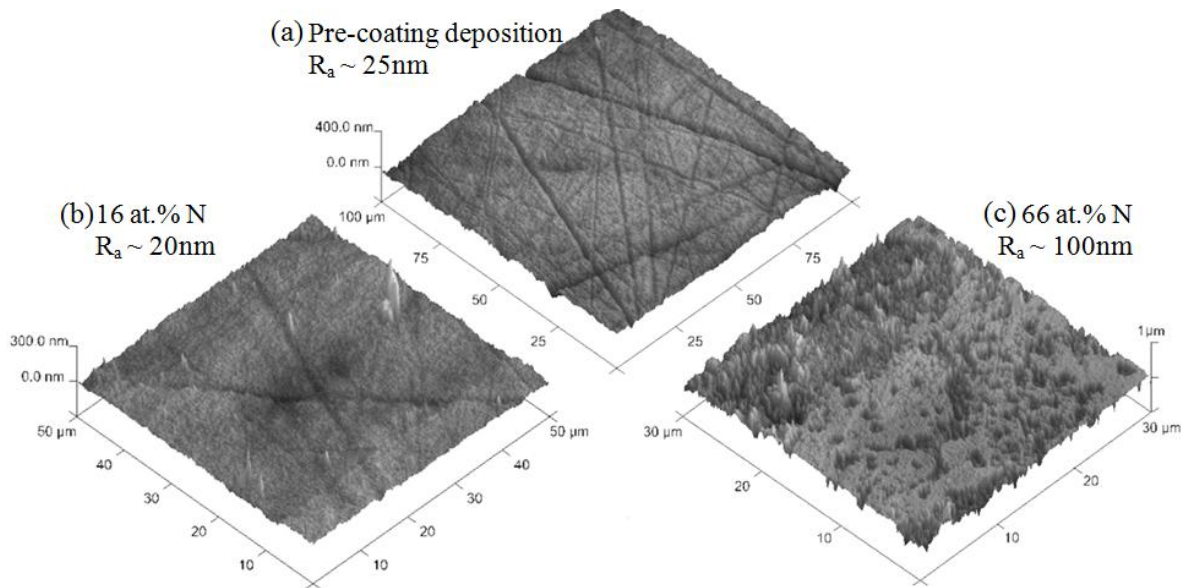


Figure 7.5 – AFM scans of unworn surfaces of: (a) the shim surface pre coating deposition; (b) the 16 at.% N  $\text{CN}_x$  coating and; (c) the 66 at.% N  $\text{CN}_x$  coating. Images have surface roughness parameter  $R_a$  inset. Note the change of scale for each scan.

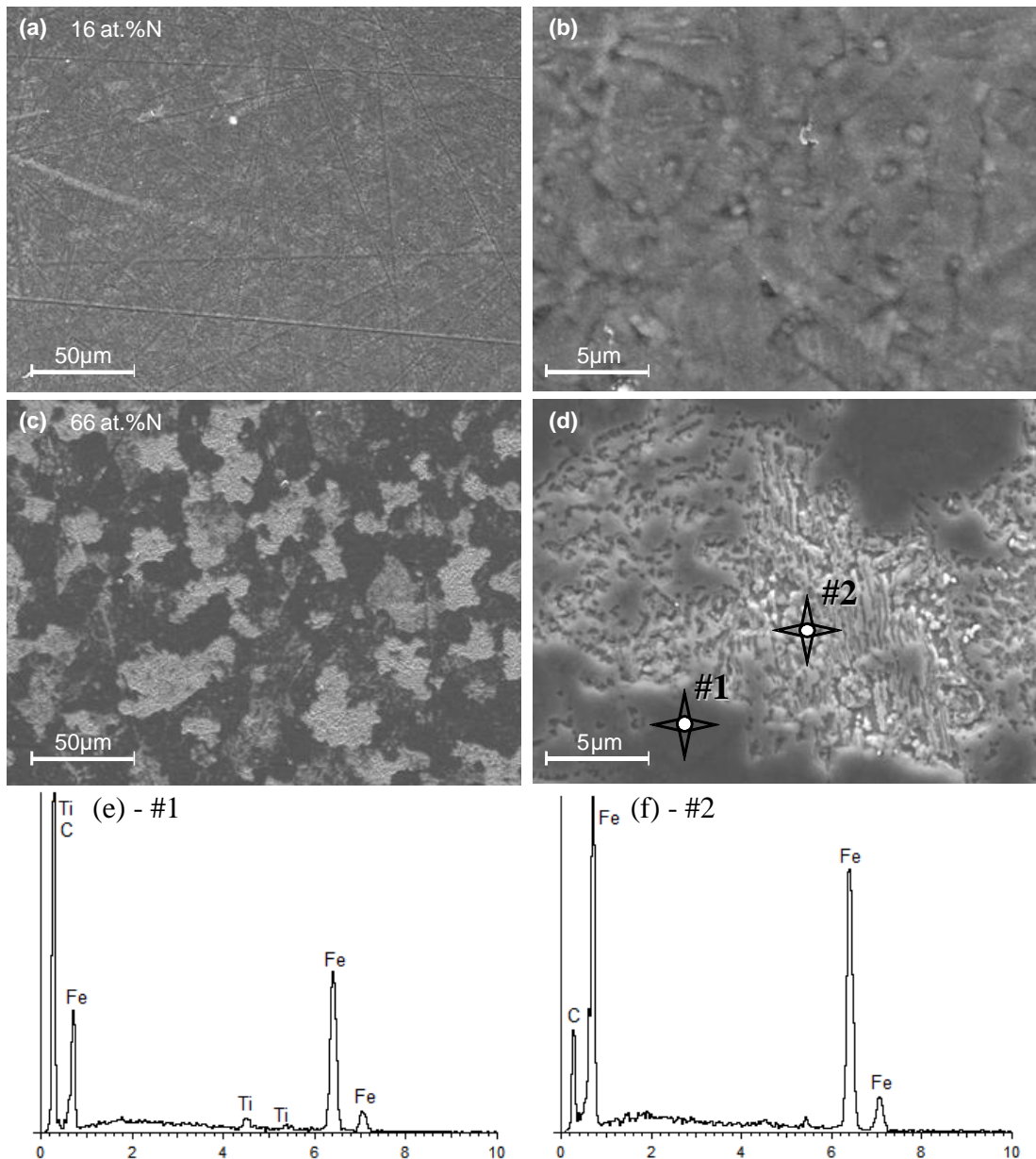


Figure 7.6 – SEM images of surface finish, (a) and (b) are images of the 16 at.% N  $CN_x$  coating, (c) and (d) are images of the 66 at.% N  $CN_x$ . (e) and (f) are EDX spectra of the smooth and troughed areas respectively.

### 7.3.2 Testing

The following section describes the tribological and mechanical testing conducted on the FL- $CN_x$  coatings.

#### 7.3.2.1 In situ valve-train testing

As part of this study, the coatings are to be tested for short duration in-service valve-train performance. The apparatus that was used for the testing is as described in chapter 2 and under the test conditions described in chapter 4, section 4.1. The DLC

work had shown that impact loading has a deleterious effect on coating durability, and therefore for this preliminary study the  $CN_x$  coatings were tested in the less harsh, 'no impact', condition. Test intervals were also shorter, 5 minutes, to assure that the evolution of wear would be captured. If there was no evidence of coating failure another 5 minute test was performed and this process repeated until it was clear that there had been significant wear. After testing the tappets were investigated by optical and electron microscopy. In this study, focus was given to the durability of the coatings, rather than their frictional properties. As with the DLC coatings tested under non-standard, continuous contact, conditions, a model does not exist at present to accurately simulate the torque, and determine a friction coefficient.

### 7.3.2.2 Mechanical and tribological testing

Mechanical properties of the coatings were determined by nanoindentation testing, scratch-adhesion testing, and reciprocating sliding wear testing.

Scratch-adhesion testing was performed on a Teer Coatings Ltd. ST-200 scratch tester. The applied normal load was ramped from 1N to 35N as the 200 $\mu$ m radius Rockwell diamond stylus was drawn across the surface. Loading rate was 40N min<sup>-1</sup> and traverse speed was 10mm min<sup>-1</sup>, giving a final scratch length of 8.5mm. Four scratches were performed on each coating, and applied load and friction force were monitored and recorded during testing. Scratches were then investigated by scanning electron microscopy to identify the points of coating failure and from this critical failure loads were found.

Nanoindentation tests were used to investigate the hardness and modulus of coated shims. Nanoindentation was performed using an MTS Nanoindenter. Indentations were made at a range of loads from 1mN to 500mN, ten indentations at each load, in a grid structure with an indentation spacing of 100 $\mu$ m and hardness and modulus determined by the Oliver and Pharr method [14].

Reciprocating sliding wear testing was performed on the same Teer Coatings Ltd. ST-200 scratch tester that was used for the scratch adhesion testing. The ST-200 was used in a reciprocating mode where a stainless steel stylus, hardness ~8.3GPa, radius 2.5mm, at constant load is drawn back and forth across the surfaces. The reciprocating displacement was 5mm, and the traverse speed 0.005m s<sup>-1</sup>. Two sets of tests were conducted: (i) high load, 60N, and total sliding distance of 3m and (ii) low load, 10N, and

a total sliding distance of 10m. The resulting scratch tracks were investigated by scanning electron microscopy to assess wear mechanism and stylus profilometry was used to measure scratch track cross-sections to indicate wear volume.

### 7.3.3 Results and discussion

#### 7.3.3.1 In-situ valve-train testing

Figure 7.7 shows the wear experienced by the coated samples during the in-situ valve-train testing. Under normal operating conditions the tappets precess around by a fraction of a degree with each pass of the cam face. This helps to distribute the wear. The SEM images in figure 7.7 show that in some cases, notably (a) #1, (a) #2 and to a degree (a) #3, this is not occurring most likely due to the non-standard setup of the valve-train. It is clear from the results of these tests that coating durability is low. The 16 at.% N CN<sub>x</sub> coatings fail by excessive scuffing wear of small areas, predominantly in the shim centre where the loading is highest, and around the edge of the coated area. By comparison the 66 at.% N CN<sub>x</sub> coatings appear relatively intact in the macrograph images, but close inspection in an SEM reveal that there is sample wide abrasion of the coating. Wear was greater in some areas but coating removal had occurred all across the surface. This seems to have been exacerbated by the differences in coating surface finish described in the coating selection section, section 7.3.1. In the areas of the shim that were heavily worn during valve-train testing all areas of the coating were heavily abraded. However where wear was less severe the smoother areas of intact coating appear relatively intact. From these results it would appear that the 16 at.% N coating has the greatest durability of the two coatings in valve-train wear testing, with wear limited to relatively small areas of rough coating.

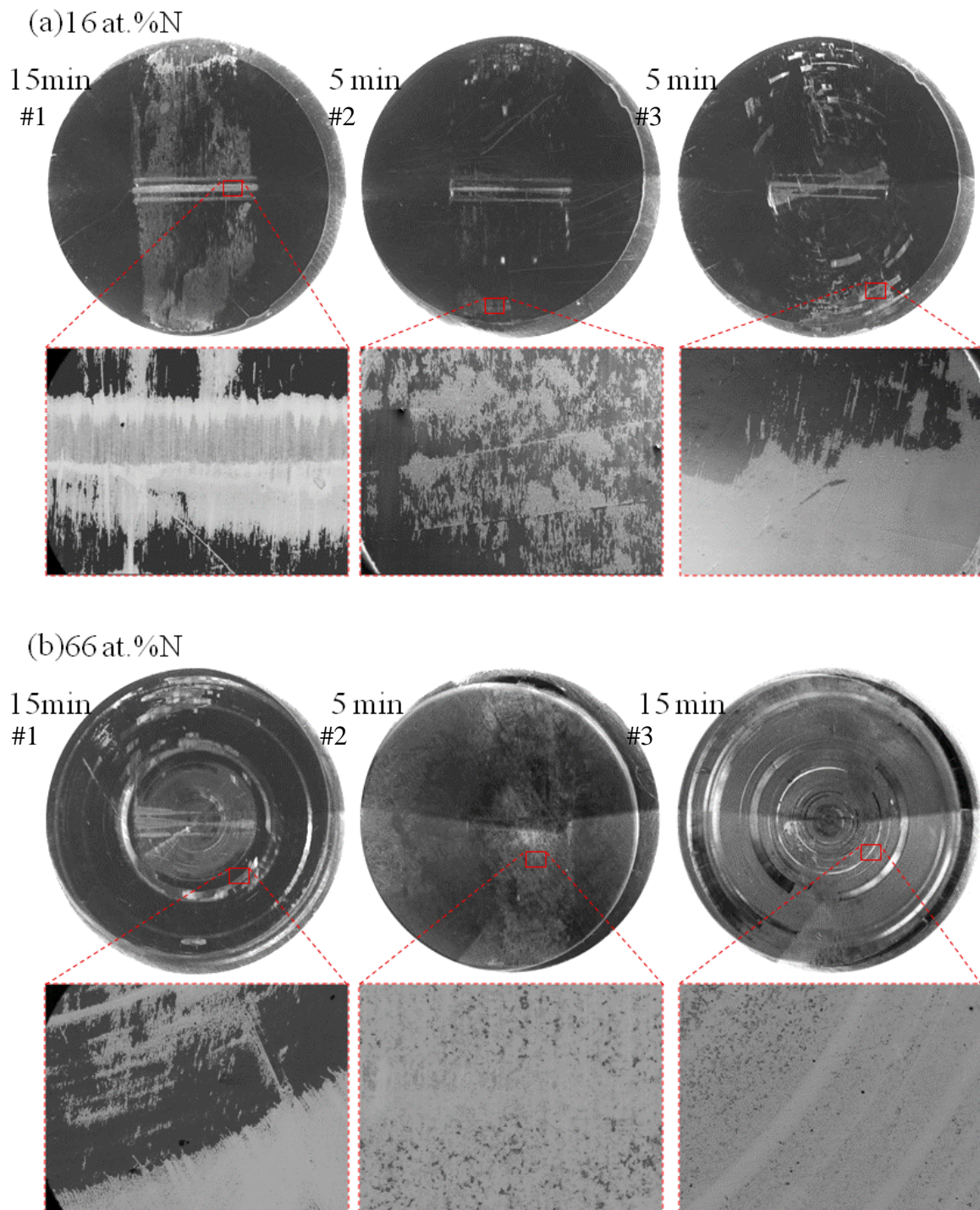


Figure 7.7 – Optical macrographs of coated shim inserts post in-situ valve-train testing. Images are labelled with the duration of the test and with inserts showing more detailed SEM images of wear. Images are collected by back-scattered electron detector: (a) the three 16 at.% N  $CN_x$  coatings tested and; (b) the three 66 at.% N  $CN_x$  coatings tested.

### 7.3.3.2 Nanoindentation testing – H/E

Nanoindentation testing gave values of hardness plotted against relative indentation depth (RID) on a semi-logarithmic scale. RID is the indentation depth over the coating thickness. Error bars show one standard deviation within the data. Figures 7.10 and 7.11 show images taken in an SEM of typical residual indentations for both coatings, at various loads. Residual indentation marks from indentations conducted at <5gf were not detectable by SEM imaging.

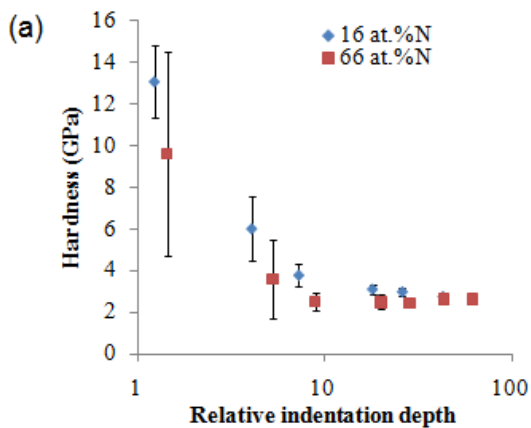


Figure 7.8 – As measured hardness of coated shims against relative indentation depth, showing error bars of a standard deviation.

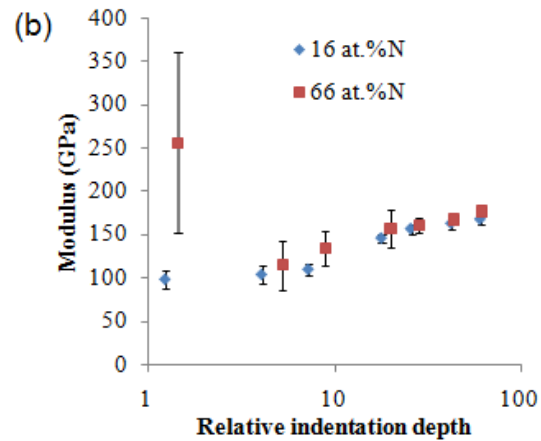


Figure 7.9 – As measured modulus of coated shims against relative indentation depth showing error bars of a standard deviation.

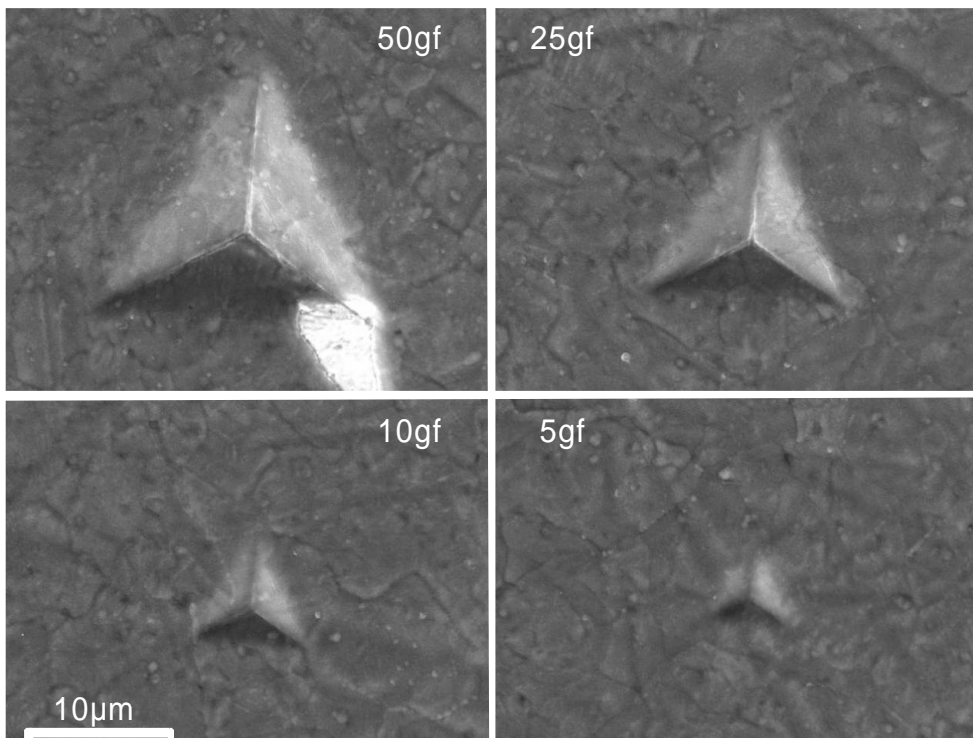


Figure 7.10 – Secondary electron detector image of typical residual indentations of the 16 at.% N  $\text{CN}_x$  coating.

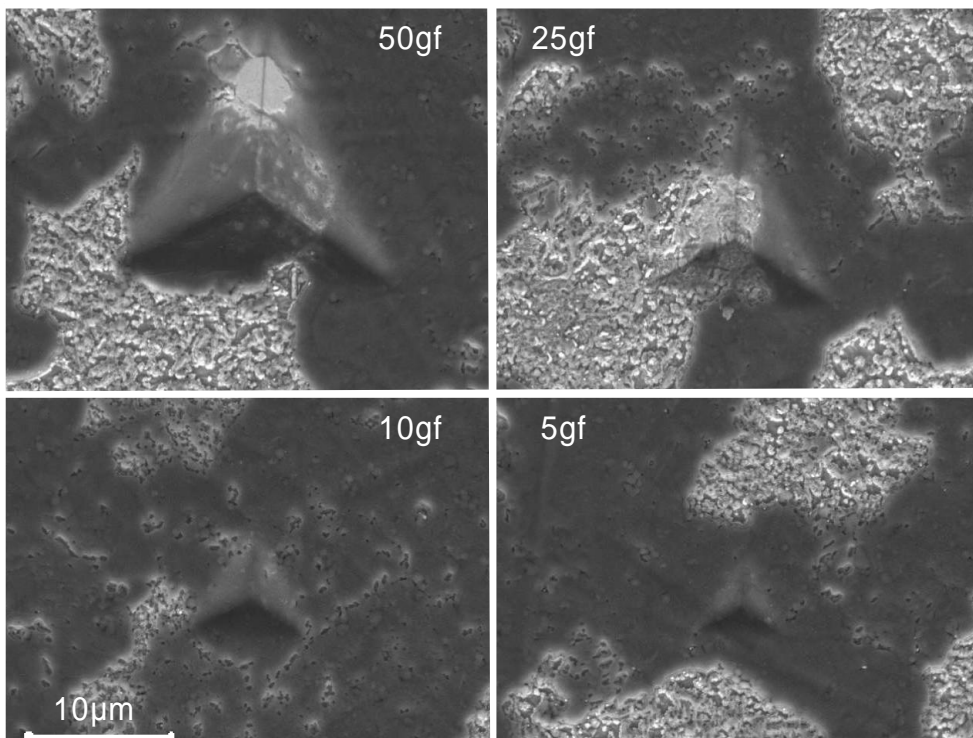


Figure 7.11 – Secondary electron detector image of typical residual indentations of the 66 at.% N  $\text{CN}_x$  coating.

Both coatings show low hardness that rises with decreasing RID indicating that the hardness seen here is the joint contribution of substrate and coating. For indentations with low RID of 1 and below, the hardness of the coatings will begin to dominate the response. It has not proved possible however to obtain accurate, repeatable, load-displacement data for very shallow indentations on these relatively rough surfaces, as shown by the increased error at low RID. It was therefore not possible to directly establish the coating only hardness or modulus of the coatings, with the 66 at.% N  $CN_x$  coating in particular showing very large standard deviation at low RID. It is clear however that the 16 at.% N  $CN_x$  coating has a slightly higher hardness compared to the 66 at.% N  $CN_x$  coating. It should also be noted that there is a relatively low hardness at higher RID, where the substrate response is dominant. This substrate hardness is due to the annealing process that is conducted on shims prior to coating deposition, which significantly tempers the hardness of the M2 steel substrate. Figure 7.12 shows example load displacement curves taken from the indentations conducted at a load of 1mN. While calculation of coating only modulus was not possible, it is clear from the load-displacement curves in figure 7.12 that at low loads the 16%N  $CN_x$  demonstrated the more elastic response.

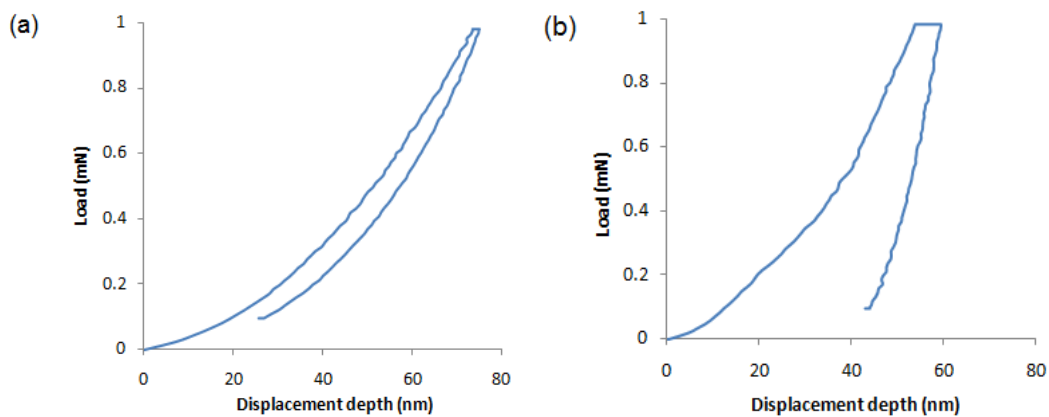


Figure 7.12 – Example load displacement curves at 1mN maximum load, for (a) 16 at.% N  $CN_x$  and (b) 66 at.% N  $CN_x$ . The 16 at.% N  $CN_x$  coating in particular shows a highly elastic response.

In an attempt to characterise the hardness and modulus response of the coatings, values of  $H/E$  were calculated from the mean values of hardness and modulus for the lowest RID. The  $H/E$  values for the two coatings are 0.133 and 0.038 for the 16 at.% N  $CN_x$  and 66 at.% N  $CN_x$  coatings respectively

### 7.3.3.3 Scratch-adhesion testing

Scratch-adhesion testing was used to produce four scratches on each sample. The scratches were investigated in a SEM and showed two critical failure loads, the first,  $L_{c1}$ , is the lowest load at which there is coating removal and substrate exposure. The second critical load,  $L_{c2}$ , is the load at which there was determined to be gross failure of the coating. Figure 7.13(a) and 7.13(b) show SEM images of the scratch track for the 16 at.% N  $CN_x$  coating and the 66 at.% N  $CN_x$  coating respectively. The corresponding critical loads were found, and the mean and standard deviation calculated. For the 16 at.% N  $CN_x$  coating;  $L_{c1} \sim 7.7 \pm 3.6N$ , and  $L_{c2} \sim 18.7 \pm 8.5N$ . For the 66 at.% N  $CN_x$  coating;  $L_{c1} \sim 9.8 \pm 2.4N$ , and  $L_{c2} \sim 17.1 \pm 2.08N$ . Although there is little difference in the critical load values found for the two  $CN_x$  coating compositions, the failure mechanisms were somewhat different. For the 16 at.% N  $CN_x$  the coating fails by a conformal buckling which develops with increasing load. At the point of major coating failure, coating material is spalled from the scratch track where it can be seen as debris alongside. The 66 at.% N coating instead shows initial failure by the micro coating fracture and spallation of small areas of coating from the smooth regions described earlier. Major failure occurs by conformal buckling of both rough and smooth coating regions, with some small areas of coating remaining intact but pressed into the substrate and partially subsumed by plastic deformation of the steel.

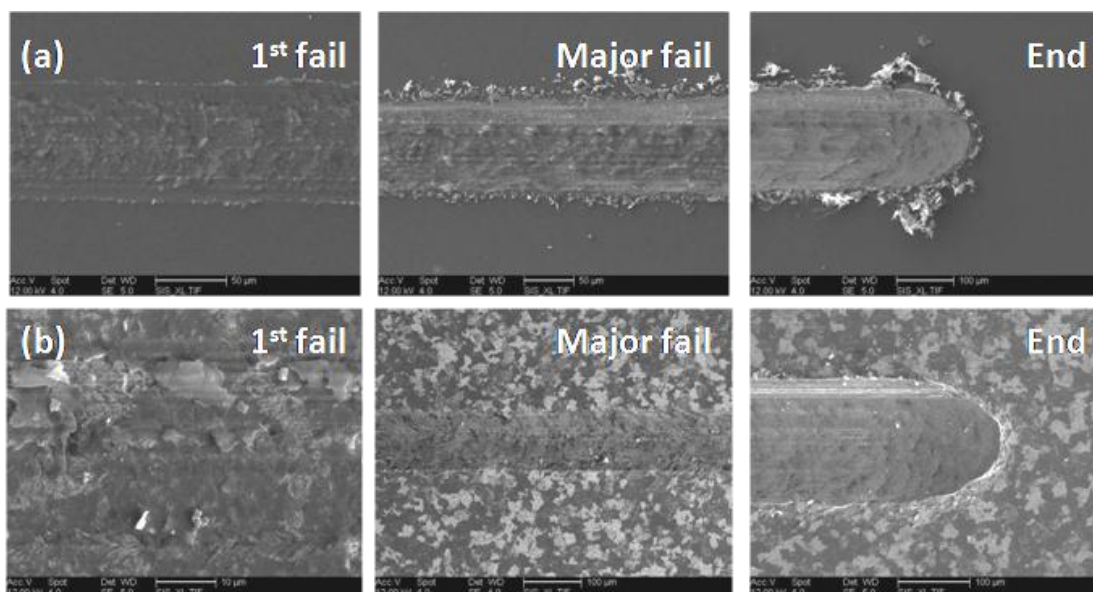


Figure 7.13 – SEM image of the stages of scratch progression for: (a) the 16 at.% N  $CN_x$  coating and; (b) the 66 at.% N  $CN_x$  coating

#### 7.3.3.4 Reciprocating sliding wear

Reciprocating sliding wear testing was conducted and the resultant wear scars were examined by scanning electron microscopy and stylus profilometry was used to measure scratch track cross-sections. Four equally spaced profiles were measured for each wear scar, and from these an average cross section of removed material was calculated, see figure 7.14 for an example. This area was then multiplied by the track length, 5mm, and an approximate wear volume found. The specific wear rate was also calculated. The results are collated in table 7.1. The friction force was also logged during testing and plot of coefficient of friction against number of cycles have been generated, see figure 7.15 for example friction plots. Each cycle represents two 5mm traverses, i.e. 1cm of sliding. It is clear from the graphs in figure 7.15 that for both compositions of coating there is a high coefficient of friction in both high load and low load conditions. For the reciprocating sliding wear tests conducted at 60N it appears that after 150-200 cycles the friction coefficient settles, probably due to complete penetration of the coating and a change to steel on steel contact. It is interesting to note that the specific wear rate of the 66 at.% N CN<sub>x</sub> coating is lower, despite its rougher initial surface finish. This corresponds with the relatively low friction coefficient maintained for the initial stages of the 10N testing. This indicates that the coating survived the initial contact and provided reduced friction before the failure started to occur. Figure 7.16 shows SEM images of the coated samples after wear testing, clearly indicating coating failure. Figure 7.16 (b) and (d) show examples of wear from the 10N, 10m tests where there are isolated regions of coating still intact in the wear track. Figure 7.16(a) and (c) show examples of wear from the 60N, 3m tests and the coatings have been completely removed from the scratch track and the steel substrate severely worn and deformed, polished smooth by plastic deformation.

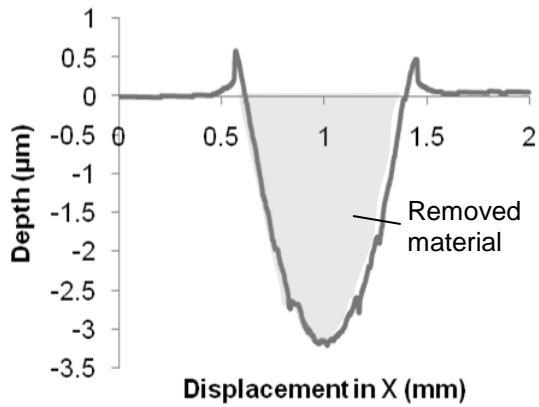
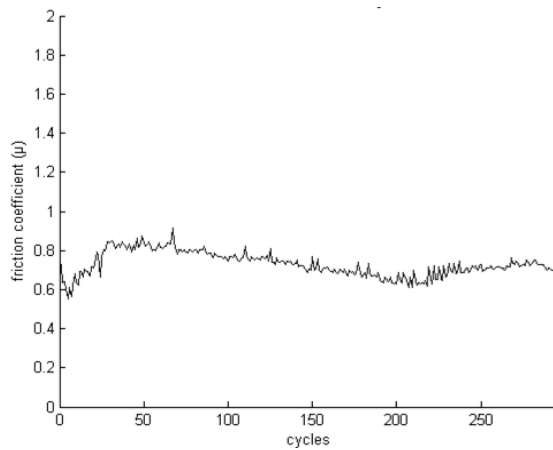
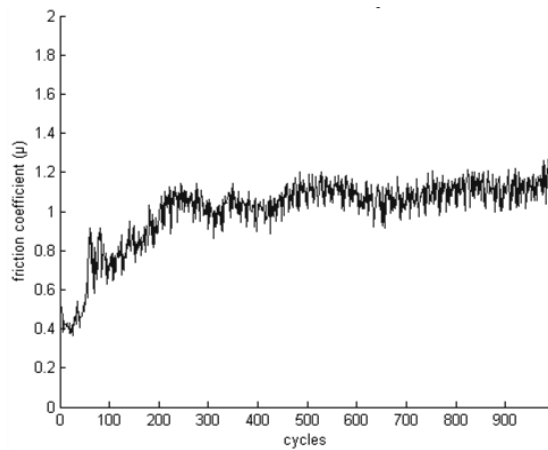


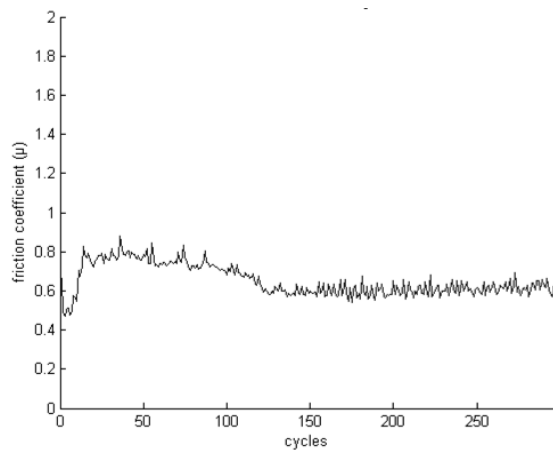
Figure 7.14 – an example profile taken from 16 at.% N, 3m sliding distance at 60N



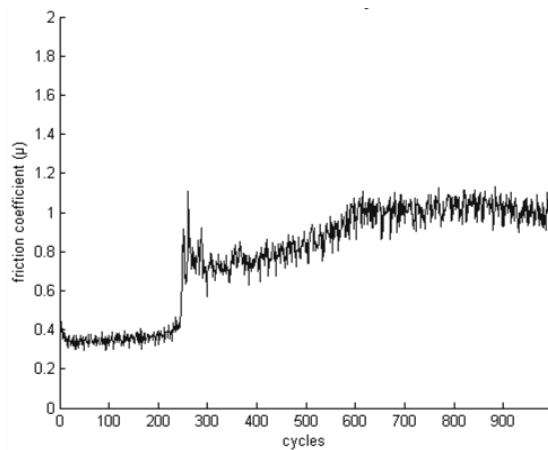
(a) 16 at.% N CN<sub>x</sub>, 60N, 3m



(b) 16 at.% N CN<sub>x</sub>, 10N, 10m



(c) 66 at.% N CN<sub>x</sub>, 60N, 3m



(d) 66 at.% N CN<sub>x</sub>, 10N, 10m

Figure 7.15 – Graphs of friction coefficient against cycles completed, for reciprocating wear tests: (a) and (b) 16 at.% N, 60N-3m and 10N-10m respectively and; (c) and (d) 66 at.% N, 60N-3m and 10N-10m respectively.

Coating	Wear volume (m <sup>3</sup> )		Specific wear rate (m <sup>3</sup> m <sup>-1</sup> N <sup>-1</sup> )
	60N, 3m test	10N, 10m test	
16 at.% N CN <sub>x</sub>	7.97e-05	5.55e-06	2.49e-07
66 at.% N CN <sub>x</sub>	4.93e-05	2.50e-06	1.49e-07

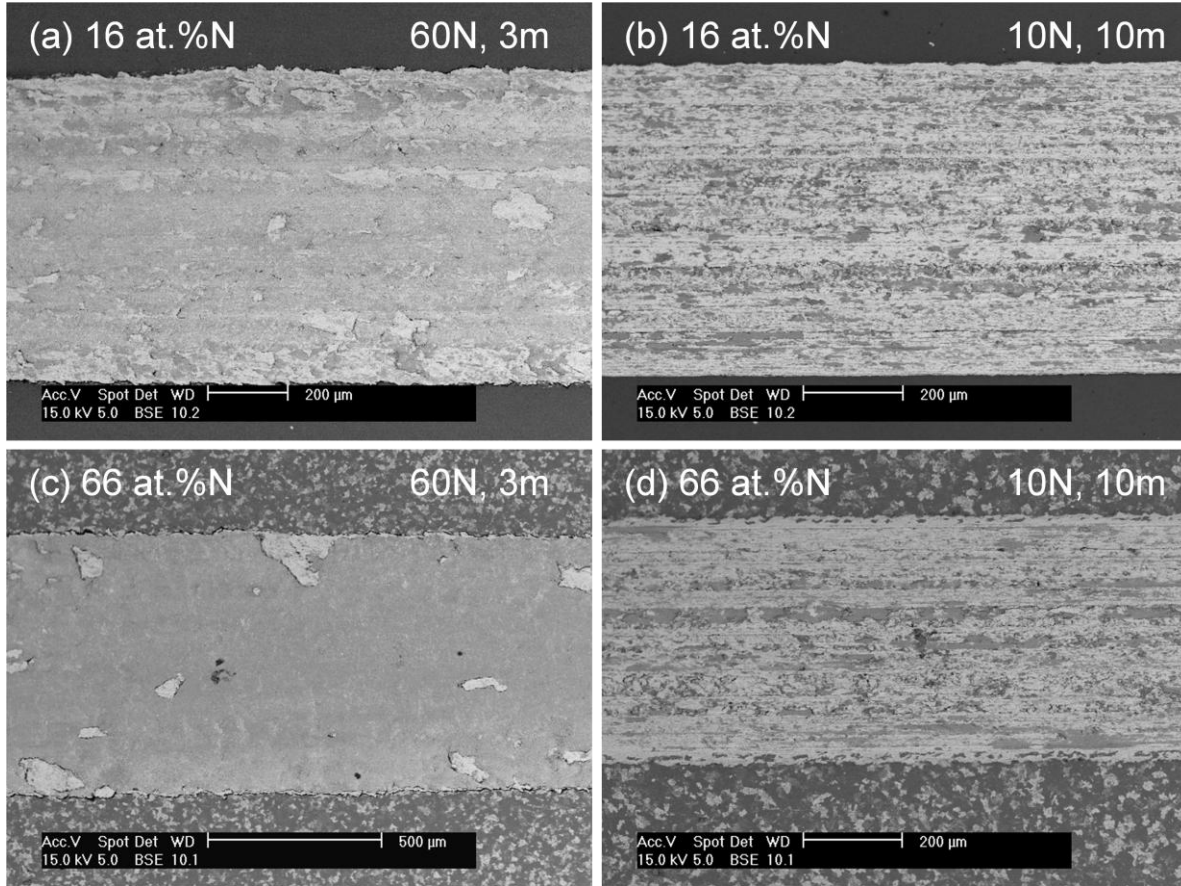


Figure 7.16 – SEM images of reciprocating wear tests: (a) and (b) 16 at.% N, 60N-3m and 10N-10m respectively and; (c) and (d) 66 at.% N, 60N-3m and 10N-10m respectively.

### 7.3.4 Discussion

In-situ valve-train testing of the coated shims showed the 16 at.% N CN<sub>x</sub> coating had a greater durability in the valve-train test compared to the 66 at.% N CN<sub>x</sub> coating. The 16 at.% N CN<sub>x</sub> coating was found to be smoother with a considerably better consistency of coating surface roughness and coating thickness compared to the 66 at.% N CN<sub>x</sub> coatings. The two coatings showed similar adhesion, with L<sub>c1</sub> 7.7N and 9.8N for the 16 at.% N CN<sub>x</sub> and 66 at.% N CN<sub>x</sub> coatings respectively. The 16 at.% N CN<sub>x</sub> coating was found to be slightly harder and with a lower modulus compared to the 66 at.% N CN<sub>x</sub> coating. The 16 at.% N CN<sub>x</sub> showed a highly elastic load-displacement response and the value of H/E was found to be 0.133 and 0.038 for the 16 at.% N CN<sub>x</sub> and 66 at.% N CN<sub>x</sub>

coatings respectively, when calculated from the lowest RID indentations. Unlubricated reciprocating wear testing indicated that the 66 at.% N CN<sub>x</sub> was retained for longer and had a lower specific wear rate compared to that of the 16 at.% N CN<sub>x</sub> coating. The greater durability of the coating with the higher  $H/E$  value and more elastic response would seem to indicate the importance of high elastic strain to failure.

In order to understand the performance of the FL-CN<sub>x</sub> coatings in their context as an experimental coating it is important to consider the performance of other coatings. The results of the DLC testing clearly show that the in-situ valve-train is a very challenging environment. The DLC coatings under investigation in chapter 6 were an order of magnitude thicker and demonstrated much higher values of adhesion,  $L_{c1}$ , of >40N, and the coatings still showed signs of considerable wear after short testing periods (<3½ hours). The performance of the FL-CN<sub>x</sub> coatings is therefore promising. With further work to improve the adhesion and thickness of the FL-CN<sub>x</sub> coatings a better investigation of high elasticity coatings should be possible.

### 7.3.5 Conclusions

- 1) The 16 at.% N CN<sub>x</sub> coating was found to be smoother with a more consistent coating thickness and lower surface roughness compared to the 66 at.% N CN<sub>x</sub> coatings.
- 2) The two coatings showed similar adhesion, with a lower critical load of 7.7N and 9.8N for the 16 at.% N CN<sub>x</sub> and 66 at.% N CN<sub>x</sub> coatings respectively.
- 3) The 16 at.% N CN<sub>x</sub> coating was found to be slightly harder, with a lower modulus and therefore higher value of  $H/E$ , 0.133 compared to 0.038 for the 66 at.% N CN<sub>x</sub> coating.
- 4) The studies of diamond-like carbon coatings in chapter 6 have demonstrated how demanding application in the valve-train is, and the FL-CN<sub>x</sub> coatings showed not unreasonable valve-train performance when revealed by testing to be relatively thin and poorly adhered, in comparison to commercial DLC coatings.
- 5) The 16 at.% N FL-CN<sub>x</sub> coating which showed the higher  $H/E$  value and more elastic response also showed greater durability in the valve-train, indicating the benefit of a high elastic strain to failure.

#### 7.4 Future work

This study was a rudimentary investigation of the performance of  $CN_x$  coatings as low-friction, low wear coatings in the automotive valve-train, and was the first assessment of FL- $CN_x$  coatings in such an application. FL- $CN_x$  coatings were considered as part of the wider study described in this thesis in order to test the experimental FL- $CN_x$  coatings in a practical engineering application and to assess the importance of relatively high values of  $H/E$  on the performance of thin-film coatings in valve-train applications. The durability of the FL- $CN_x$  coatings was relatively poor, as described above, though in the light of the coatings' low adhesion to the substrate, low hardness and relative thinness, this is not unexpected. In order to determine the role that  $H/E$  plays in the durability of hard thin-film coatings the adhesion and hardness and thickness of the coatings will require improvement. The hardness of the coated system was compromised by the tempering process conducted prior to coating deposition, however the intent of tempering was to improve coating adhesion. Early investigations with a sample 500nm thick  $CN_x$  coating showed excessive delamination. It would appear therefore that the controlling factor is the adhesion of the  $CN_x$  coating to the steel. In this case the coatings are deposited on a very thin, 60nm, titanium interlayer. Further research into low residual stress deposition and/or more effective interlayer design may well yield improved adhesion, allowing for thicker coatings to be deposited and alleviating the need for a tempering process, dramatically lowering the hardness of the substrate. If this can be achieved, so that comparable levels of adhesion and coating thickness can be generated, it would allow for a more direct analysis of the role of  $H/E$ .

7.5 Chapter references

- 1 Liu, A.Y. and Cohen, M.L. Prediction of new low compressibility solids. *Science*, 1989, **245** (841).
- 2 Liu, A.Y. and Cohen, M.L. Structural properties and electronic structure of low-compressibility materials: beta -Si<sub>3</sub>N<sub>4</sub> and hypothetical beta -C<sub>3</sub>N<sub>4</sub> *Physics Review B*, 1990, **41** (15), 10727.
- 3 Hellgren, N. Sputtered carbon nitride thin films, (Thesis) Thin Films Physics Division (Linköping University, Linköping, 1999).
- 4 Malkow, T., Arce-García, I., Kolitsch, A., Schneider, D., Bull, S.J. and Page, T.F. Mechanical properties and characterisation of very thin CN<sub>x</sub> films synthesised by IBAD. *Diamond and Related Materials*, 2001, **10**(12), 2199-2211.
- 5 Hellgren, N., Johansson, M.P., Broitman, E., Sandström, P., Hultman, L. and Sundgren, J.-E. Effect of chemical sputtering on the growth and structural evolution of magnetron sputtered CN<sub>x</sub> thin films. *Thin Solid Films*, 2001, **382**(1-2), 146-152.
- 6 Lan, A.Z., Hui-Zhong, A.M., Hui-Jun, A.L., Shi-E, A.Y., Ning, A.Y., Huan-Ling, A.H. and Bing-Lin, A.Z. Nano-crystalline CN<sub>x</sub> Films and Field Electron Emission Properties. *Chinese Physics Letters*, 2003, **20** (4), 579-581.
- 7 Broitman, E., Hellgren, N., Wänstrand, O., Johansson, M.P., Berlind, T., Sjöström, H., Sundgren, J.E., Larsson, M. and Hultman, L. Mechanical and tribological properties of CN<sub>x</sub> films deposited by reactive magnetron sputtering. *Wear*, 2001, **248** (1-2), 55-64.
- 8 Sjöström, H., Ivanov, I., Johansson, M., Hultman, L., Sundgren, J.E., Hainsworth, S.V., Page, T.F. and Wallenberg, L.R. Reactive magnetron sputter deposition of CN<sub>x</sub> films on Si(001) substrates: film growth, microstructure and mechanical properties. *Thin Solid Films*, 1994, **246** (1-2), 103-109.
- 9 Zheng, W.T., Broitman, E., Hellgren, N., Xing, K.Z., Ivanov, I., Sjöström, H., Hultman, L. and Sundgren, J.E. Reactive magnetron sputtering of CN<sub>x</sub> thin films at different substrate bias. *Thin Solid Films ICMCTF special issue*, 1997, **308-309**, 223-227.
- 10 Zheng, W.T., Hellgren, N., Sjöström, H. and Sundgren, J.E. Characterization of carbon nitride thin films deposited by reactive d.c. magnetron sputtering on various substrate materials. *Surface and Coatings Technology*, 1998, **100-101** (1-3), 287-290.
- 11 Archard, J.F. The temperature of rubbing surfaces. *Wear*, 1959, **2** (6), 438-455.

- 12 Leyland, A. and Matthews, A. On the significance of the H/E ratio in wear control: a nanocomposite coating approach to optimised tribological behaviour. *Wear*, 2000, **246** (1-2), 1-11.
- 13 Ramalingam, S. and Zheng, L. Film-substrate interface stresses and their role in the tribological performance of surface coatings. *Tribology International*, 1995, **28** (3), 145-161.
- 14 Oliver, W.C. and Pharr, G.M. An improved technique for determining hardness and elastic modulus using load and displacement sensing indentation experiments. *Journal of Materials Res.*, 1992, **7** (6), 1564-1583.

# CHAPTER 8

## Ionic liquid lubrication

---

### **8. Ionic liquid lubrication**

#### **8.1 Ionic liquids – development and properties**

#### **8.2 Lubrication feasibility study**

8.2.1 *Ionic liquid formation*

8.2.2 *Lubrication- test procedure*

8.2.3 *Lubrication - initial observations*

8.2.4 *Surface texturing*

8.2.5 *Wettability*

8.2.6 *Results and discussion*

#### **8.3 Conclusions and future work**

#### **8.4 Chapter references**

---

The aim of this research as described in chapter 1 is to “*Investigate solutions to provide low-friction, low-wear contact conditions in the automotive engine valve-train, without recourse to lubricant additives that are damaging to the catalytic converter* “. There has been a growing interest in the use of ionic liquids to provide lubrication for challenging contacts. Ionic liquid lubricants offer the potential to use a new lubricant chemistry, which could in time work with traditional oil-based additives or replace them and allow a departure from the chemistries that are known to harm the catalytic converter. This chapter introduces the background of ionic liquids and their development followed by the testing used to evaluate the lubrication of shims by two candidate ionic liquids.

#### **8.1 Ionic liquids – development and properties**

The term ‘ionic liquids’ is commonly taken to describe a variety of salts which possess very low melting temperature, such that they are molten below 100°C [1-3]. The term is also typically considered to include substances known as deep eutectic solvents (DESs), which are mixtures of higher melting point substances which when combined possess a

similarly low melting point. This work is concerned with the study of ionic liquids which are molten in ambient conditions; these are commonly known as room-temperature ionic liquids (RTILs). Ionic liquids are of particular interest because their properties are to some degree tuneable, i.e. differing compositions allow for a wide variety of viscosity, melting point and acidity.

The first reported ionic liquid was documented in 1914 although real interest in ionic liquids did not emerge until the 1980's. Early ionic liquids were typically chloroaluminate [4] or phosphonium-halides melts, which were highly sensitive to atmospheric moisture and relatively toxic. In the 1990's and more recently, the design of ionic liquids has developed and new compositions have emerged such as: tetrafluoroborate melts, which have reduced moisture sensitivity, and; ammonium salt DESs which make use of non-toxic choline cations. This has helped to expand the applications of ionic liquids and they are now used in a wide variety of laboratory and industry applications. The strongest current interest in ionic liquids is their potential use as a solvent media and there have been numerous studies investigating ionic liquids for use in metal plating, electro-polishing, metal reprocessing and phase media transfer [5-10]. They typically have a number of properties that make them well suited to such applications: they are good solvents for a wide range of both organic and inorganic materials; they can be tailored to a specific viscosity; they are immiscible with a large number of organic solvents; and they are generally considered non-volatile with a very low vapour pressure [11], which makes them suitable for applications in high vacuum and at elevated temperatures. Some of these properties also make them ideal for application as lubricants in challenging contacts as demonstrated in a number of studies [12-15]. Many of the studies conducted so far on ionic liquid lubrication have focused on the formation of low friction monolayers which are potentially highly susceptible to wear. These approaches also typically employ ionic liquids based on organic compounds such as alkylimidazolium hexafluorophosphate and pyridinium tetrafluoroborate that are relatively expensive [16-18]. This study looks to investigate lubrication from larger liquid reservoirs retained at the contact surface and employs ionic liquids based on ammonium salt DESs, with choline chloride cations. Choline chloride is a non toxic organic compound that is in mass production as a vitamin supplement in poultry and pig feed and is therefore readily available in bulk and at

relatively low cost. This makes choline chloride based ionic liquids ideally positioned for large scale applications, such as those found in the automotive industry.

This study is an initial assessment of the application of two ionic liquids based on choline chloride cations to be used as ionic liquid lubricants for engineering contacts, in this case steel on steel. The procedures used to form the ionic liquids and test their ability to act as lubricants in automotive applications are described in section 8.2 below.

## 8.2 Lubrication feasibility study

Unlike the studies described in chapters 6 and 7 this study is not focused specifically on application in the automotive valve-train. The study of ionic liquid lubrication of steel/steel contacts is very recent, and the study of these particular liquids is entirely novel, therefore the scope is limited purely to lubricating the simple mechanism of a reciprocating sliding contact between a flat steel and a spherical steel stylus. The lubrication ability of the ionic liquids were assessed in terms of friction coefficient of the contact, duration of lubricant retention and observed wear of surfaces. Assessment was conducted for a number of reciprocating sliding wear tests, under two testing regimes, low-speed/high-load and high-speed/low-speed. A detailed description of all of the testing parameters is given in section 8.2.2. The ionic liquids used for testing are described in the following section.

### 8.2.1 Ionic liquid formation

The ionic liquids used in this study are termed **ethaline** and **reline**. Both of these ionic liquids have the organic compound choline chloride as their cation. The anions of the two ionic liquids are: (i) ethaline - ethylene glycol(EG), and; (ii) reline – urea. This gives the ethaline and reline compounds the composition of (2EG:1ChCl) and (2(urea):1ChCl) respectively, the chemical structures of the components are shown in figure 8.1. These ionic liquids are formed by mixing the pure components using the following experimental protocol:

Choline chloride [ $\text{HOC}_2\text{H}_4\text{N}(\text{CH}_3)_3\text{Cl}$ ] (ChCl) (Aldrich 99%) was, when necessary, recrystallised from absolute ethanol, filtered and dried under vacuum. Urea (Aldrich > 99%) was dried under vacuum prior to use. Ethylene glycol (EG) (Aldrich 99+%), was

used as received. The mixtures were formed by stirring the two components together, in the stated (mole ratio) proportions, at 50 °C until a homogeneous, colourless liquid had formed.

Physical properties including viscosity, conductivity, density and surface tension for various choline chloride eutectic-based ionic liquids have been reported in detail previously [17, 19-21]. Viscosity is of particular importance for lubrication, and the viscosity of the two ionic liquids is ~36 mPa·s and ~120 mPa·s for the ethaline and reline ionic liquids respectively.

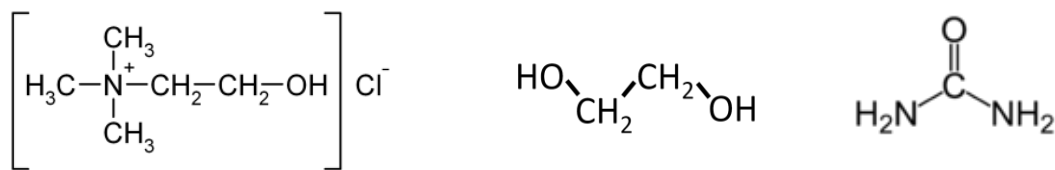


Figure 8.1 – Chemical structure of: a) choline chloride; b) ethylene glycol; c) urea

Testing was also conducted with the same SAE 5W30 friction modifier free engine oil described in chapters 6 and 7, for the purposes of comparison to ionic liquid lubrication.

### 8.2.2 Lubrication – test procedure

Reciprocating sliding wear tests were performed between two steel surfaces, a flat 'shim', and a spherical stylus (radius 2.5mm); these were composed of M2 steel (hardness ~8.3GPa) and a hardened steel (hardness ~8.9GPa) respectively. Reciprocating sliding wear tests were conducted for two conditions: (i) low-speed/high-load, and (ii) high-speed/low-load. In order to achieve a reasonable range of speeds it was necessary to conduct the two test conditions on different apparatus.

The low-speed/high-load tests were conducted on a Teer Coatings ST-200 scratch tester used in fixed-load reciprocating mode. The test parameters used were a reciprocating traverse distance of 5mm, a sliding speed of 0.005m s<sup>-1</sup>, and a load of 30N. Tests were initially conducted for 1000 cycles, equivalent sliding distance of 10m, however many extended tests were conducted and are indicated in the results. The high-speed/low-load tests were conducted on an adapted pin-on-disc wear tester, where the rotary motion was converted to a reciprocating motion; allowing for much higher sliding speeds. The reciprocating traverse distance remained at 5mm, a higher sliding speed of 0.05m s<sup>-1</sup> was used, and the applied load at the point of contact was 5N. The 0.05m s<sup>-1</sup>

1/5N reciprocating tests were conducted for much greater sliding distances. Tests were either stopped when lubricant loss was observed to have occurred or after an extended period without lubricant loss. Both instruments are described in detail in section 4.2.2. All tests were conducted at ambient temperature, pressure and humidity. Between individual sliding tests the stylus was repositioned for a new contact point and cleaned with acetone for oil lubrication, or water followed by acetone for ionic liquid lubrication.

The first stage of investigation was to establish if the ionic liquids selected for this study would provide any friction and wear reduction as a lubricant in a steel-steel contact. Therefore a simple initial study was conducted.

### 8.2.3 Lubrication – initial observations

To establish whether reline and ethaline were suitable lubricants, some very simple tests were performed. Shims with a relatively rough surface finish, the surface finish described as ‘DGnd’ in chapter 6, were dipped into a reservoir of lubricant and then allowed to drip dry for a period of 5 minutes. These shims were then subjected to a low-speed/high-load reciprocating wear test for a sliding distance of 10m. The measured friction coefficient against sliding distance is shown for some example tests in figure 8.2

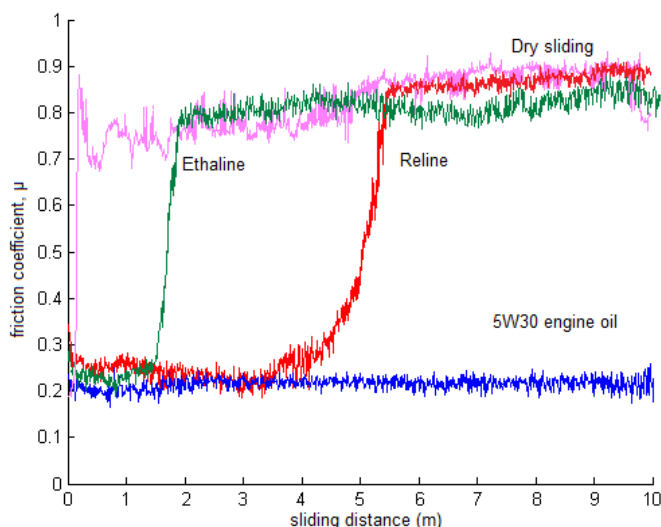


Figure 8.2 – Comparison of friction coefficient for low-speed/high-load testing of the three lubricants and dry sliding.

The reciprocating sliding wear testing conducted at both  $0.005\text{ m s}^{-1}/30\text{ N}$  showed that ionic liquid lubricants can provide low friction coefficients, comparable to that of 5W30 engine oil. A loss of lubrication was observed to occur at low sliding distances, where there was a rapid transition to a friction coefficient closer to that of dry steel/steel sliding. The wear in the sliding tracks of the ionic liquid lubricated tests was seen to be less severe than that of the dry sliding wear tests. These ionic liquids therefore demonstrate reduced friction and wear, indicating potential as a lubricant, however, the ionic liquids do not appear to be retained in the contact, and the friction coefficient quickly reaches that of unlubricated dry sliding. The lubrication that did occur was most likely provided by small reservoirs of liquid entrapped in surface features. Sliding motion would tend to push excess lubricant from the contact and wear would tend to remove features that may have entrapped lubricant. Once the amount of lubricant has dropped below a critical value a complete film cannot be formed between surfaces and high friction boundary lubrication occurs. Therefore one approach to improve ionic lubricant retention may be to provide a surface which is rich in surface features in which lubricant can be entrapped.

In the reciprocating wear tests that follow, good lubricant coverage with no large droplets of liquid was ensured by spin drying the surface after they have been supplied with a surplus of lubricant. The spin drying was achieved by spinning the samples at 15,000rpm for 10 seconds. An illustration of the apparatus used is shown in figure 8.3. The spin drying process drives off the majority of the lubricants leaving only that which is well adhered to the surface or entrapped in surface features. This procedure was used for all lubricants.

This study investigates the role that surface texture plays in lubricant retention by testing lubrication of a number of shim surface finishes, described in section 8.2.4. Another important factor is the affinity of the lubricants to the component surface, which is indicated by the wettability of the surface with the liquid. A liquid which wets a surface easily will be harder to drive off the surface during testing; section 8.2.5 investigates the wetting of the surface by the lubricants.

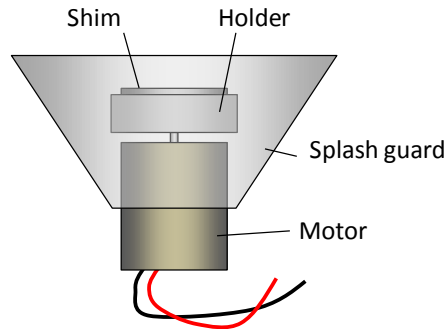


Figure 8.3 – Illustration of the spin coating equipment

#### 8.2.4 Surface texturing

This study looks at the lubricant retention of three surface finishes, with very different surface roughnesses and morphology. Surface texturing was performed in two stages, a grinding stage and then either a further polishing stage or a shot-peening stage. The surfaces produced are termed ‘ground’ and ‘polished’, i.e. those produced by the grinding and polishing stages, and ‘peened’. This section discusses the details of the texturing processes, the results section details the surfaces produced. The grinding and polishing stages were performed on a Struers TegraPol-21 polishing machine, with a bed speed of 150rpm and a co-rotating head speed of 150rpm. The applied load per sample was 30N. The ground texture was produced by 5 minutes of grinding with wet #220 SiC paper. This texture was used as a precursor to all other texturing stages. The polished surface was produced by a 5 minute polishing process with 9 $\mu$ m diamond solution, followed by a 5 minute polishing process with 6 $\mu$ m diamond solution, dispensed by a Struers TegraDoser-5. The shot peening stage was conducted in an Ellermatic 600 blast chamber, with a nozzle outer diameter of 8mm, an air pressure of 7 bar and 550g of blast media material. The samples were affixed 10cm from the nozzle and the material plume covered the total area of the shim surface ensuring even texturing. The blast media used was iron-silicate, which is a cheap and commonly available blast media with angular particles of hardness (Mohs 6-7), and a diameter range of 0.2-1.7mm. The surface textures produced were imaged in a Phillips XL30 environmental SEM, and features of interest analysed by energy dispersive x-ray analysis (EDX). Surfaces were also imaged in a Veeco Dimension 3100 AFM, which allows detailed surface topography to be investigated and surface roughness parameters calculated.

The surface textures produced were examined by SEM and AFM, see figure 8.3, and show very different surface textures. Values of surface roughness parameter  $R_a$  were found from AFM scans as were values for surface area to scan area ratio, or surface area ratio (SAR) for short. SAR is defined here as the total surface area of the topography scanned in an AFM image divided by the scan area, therefore a perfectly flat surface will have a value of SAR 1. The ground surface has an  $R_a$  of  $\approx 70\text{nm}$ , with many long overlapping troughs 1-10 $\mu\text{m}$  in width and a, of 1.0047 (10047 $\mu\text{m}^2$  over a 10000 $\mu\text{m}^2$  scan); the polished texture is much smoother, with  $R_a$  of  $\approx 8\text{nm}$  and surface area ratio of 1.0001; the surface shot peened by iron silicate blast media retains some of the trough features from the grinding process but the surface has been heavily deformed with some very angular features, giving a much increased surface roughness,  $R_a \approx 200\text{nm}$ , and surface area ratio of 1.0275.

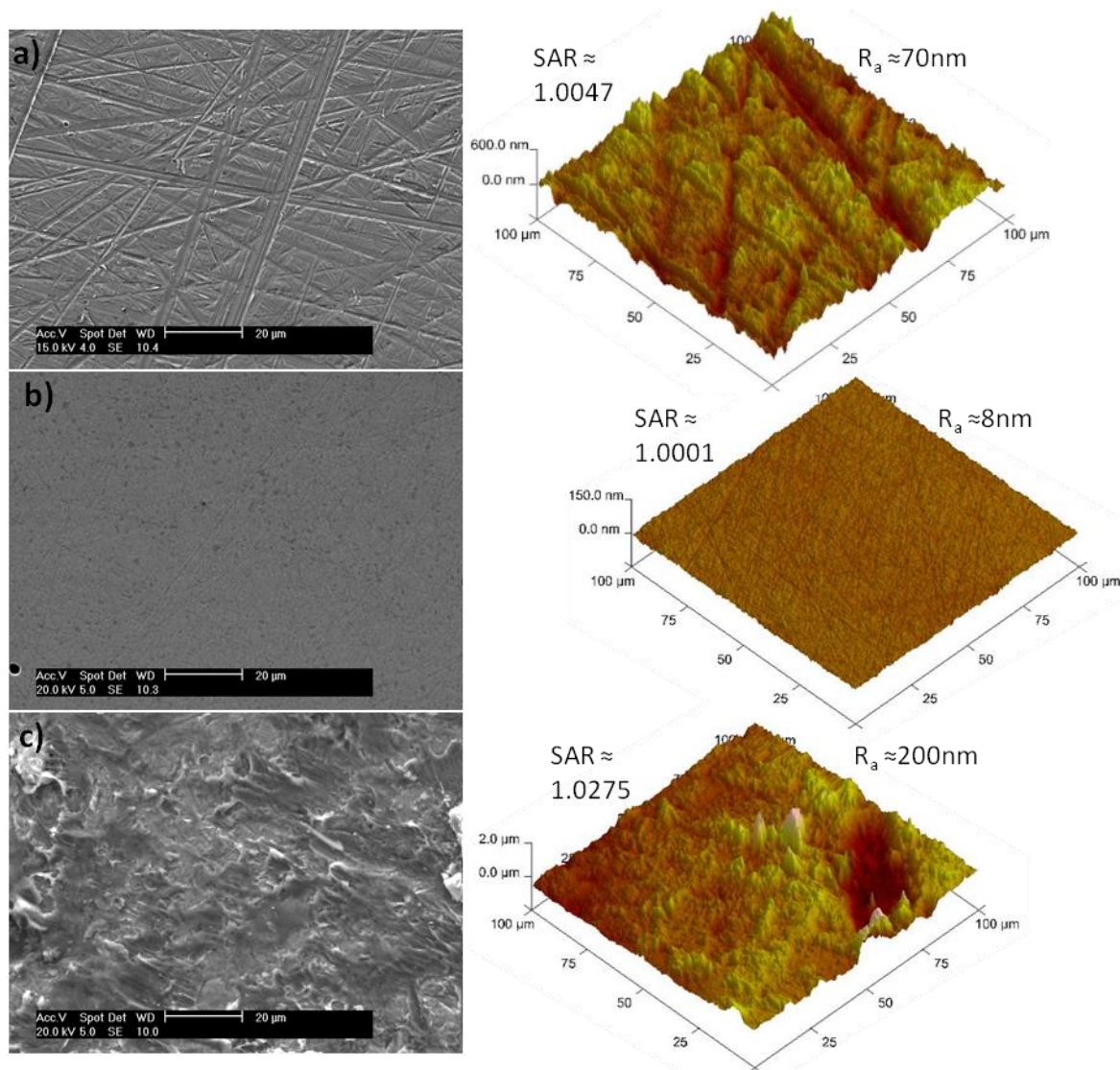


Figure 8.3 – SEM images and AFM scans of the textured surfaces with roughness parameter  $R_a$  and surface area ratio (SAR) inset: a) ground; b) polished; c) iron-silicate peened.

### 8.2.5 Wettability

In order to assess the wettability of the surfaces by the various lubricants used, a sessile drop test was conducted. In the sessile drop test a droplet of liquid was placed onto the surface, and the contact angle that was formed between the droplet and the surface was measured, in this case by observation in a shadowgraph. This contact angle is governed by the compromise between reducing the surface energy; by forming a surface with the atmosphere, and by forming a surface with the shim. A simplified interpretation gives a qualitative indication of the lubricants affinity for the surface. A low contact angle indicates poor affinity between liquid and surface, a high contact angle indicates good affinity, illustrated in figure 8.4. The lubricants affinity is of interest as it will help to

determine the ease with which liquids adhere to the surface. Sessile drop tests were conducted for both ionic liquids and the SAE 5W30 engine oil, on each of the prepared surfaces finishes.

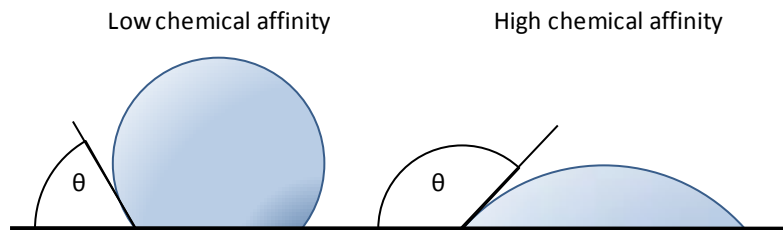


Figure 8.4 – Illustration of measuring contact angle to determine affinity between lubricants and the surface.

The sessile drop test results showed that the contact angle and by extension the lubricants affinity was not affected by the texturing processes. The contact angles for the three liquids were: (i)  $164^\circ$  for the 5W30 engine oil; (ii)  $114^\circ$  for the ethaline ionic liquid, and; (iii)  $101^\circ$  for the reline ionic liquid,  $\pm 2^\circ$  for all surface finishes. Indicating that the engine oil had by far the highest affinity for the steel surface, and the reline ionic liquid had the lowest.

### 8.2.6 Results and discussion

The reciprocating sliding tests conducted with both low-speed/high-load and high-speed/low-load showed similar results to the initial tests, with the ionic liquids demonstrating low friction coefficients and reduced wear similar to that of the 5W30 engine oil for short periods, after which conditions similar to dry sliding developed. The duration of lubricant retention is therefore important and is used in this study as a measure of lubricant effectiveness. The sliding distance achieved prior to lubricant loss was found for each pairing of surface texture and lubricant for between 4 and 6 test runs each. The sliding distances prior to lubricant loss for ionic liquids are shown in table 8.1. Values underlined are for distances where testing was stopped prior to loss of lubrication, and therefore only indicate that lubrication was retained for at least this period of sliding.

Table 8.1 – sliding distances prior to lubricant loss

		0.005m s <sup>-1</sup> /30N		0.05m s <sup>-1</sup> /5N	
		Ethaline	Reline	Ethaline	Reline
Ground	Max.	1.25	5.25	36.50	452.50
	Min.	0.47	0.24	1.70	3.20
	Mean	0.82	2.23	17.46	125.15
	$\sigma$	0.31	2.01	16.08	166.99
Polished	Max.	0.18	0.90	13.50	156.00
	Min.	0.07	0.05	0.65	7.00
	Mean	0.12	0.27	4.47	68.88
	$\sigma$	0.04	0.33	5.35	54.45
Peened	Max.	5.52	<u>30.00</u>	62.00	<u>600.00</u>
	Min.	0.25	1.25	1.50	<u>200.00</u>
	Mean	2.75	14.50	14.77	<u>368</u>
	$\sigma$	2.18	12.77	26.43	<u>208</u>

Table 8.1 does not include sliding distances prior to lubricant loss for the 5W30 engine oil, which retained lubrication for the duration of  $3 \times 30\text{m}$  sliding runs at  $0.005\text{m s}^{-1}/30\text{N}$  on each surface texture and  $3 \times 300\text{m}$  sliding runs at  $0.05\text{m s}^{-1}/5\text{N}$  on the ground surface only (due to time constraints). The 5W30 engine oil therefore showed the greatest lubricant retention of the three lubricants. The reline ionic liquid also showed good lubricant retention, comparable to that of the 5W30 engine oil in some instances, with tests run at  $0.05\text{m s}^{-1}/5\text{N}$  testing on the peened surface showing no evidence of lubricant loss within the period of any of the sliding runs. For all of the  $0.005\text{m s}^{-1}/30\text{N}$  and  $0.05\text{m s}^{-1}/5\text{N}$  tests the reline ionic liquid outperformed the ethaline ionic liquid. For  $0.05\text{m s}^{-1}/5\text{N}$  testing the mean sliding distance prior to lubricant loss was an order of magnitude greater for reline ionic liquids than for ethaline ionic liquids. The testing at  $0.005\text{m s}^{-1}/30\text{N}$  showed the same trend but less difference in mean sliding distance. These results also show that the sliding distance to lubricant loss of the reline ionic liquid varied considerably, with standard deviation,  $\sigma$ , which was an order of magnitude greater than that of the ethaline ionic liquid for most instances. High values of average sliding distance to lubricant loss do not however guarantee good performance, the minimum sliding distance is also of interest as these contacts tend to remain at high friction once de-lubricated. While the reline ionic liquid does show instances of very early lubricant loss, particularly during  $0.005\text{m s}^{-1}/30\text{N}$  testing. The incidence of early failure was greater for the ethaline ionic liquid, as evidenced by the low mean and small values of standard deviation.

The results of sliding wear testing also show an improvement in lubricant retention with an increase in surface area to scan area ratio, supporting the idea that lubricant was retained in surface features. It is only reasonable to assume that there is a limit to this trend and that there exists a compromise between the need for surface features in which to entrap lubricant and the size of surface asperities which may penetrate the lubricant film causing contact and wear. While further testing with differing surface morphologies would be required to determine the ideal surface finish, this short study has shown surface texturing can help to retain ionic liquid lubricants. Also, greater sliding distances to lubricant loss were observed for  $0.05\text{m s}^{-1}/5\text{N}$  testing, most likely due to increased entrainment velocity and a decrease in load. The higher load of the  $0.005\text{m s}^{-1}/30\text{N}$  testing means an increased contact pressure, where high pressure will likely flatten surface features, reducing surface area and squeezing lubricant from surface features.

It was also observed that for tests conducted with reline ionic liquids and surfaces textured by peening with iron silicate particles, a discoloured residual film formed around the wear debris in the sliding track and on the stylus surface. This film was noted to be larger for long duration testing. It was unclear if the development of a larger film was due to the increased sliding distance or whether the formation of this film was beneficial and aided lubrication, lengthening lubricated sliding distance. It was clear from observation that the film had high viscosity and was well retained in the sliding track.

The residual film on the stylus and in the scratch track, was imaged in an SEM and analysed by EDX, see figures 8.5 and 8.6. These images were taken from a sliding test at  $0.005\text{m s}^{-1}/30\text{N}$ , after a sliding distance of 1m, when the film was first seen to form. It is clear from the spectra that the residual film has high chlorine and silicon content, not seen in the spectra of unworn steel away from the contact area. There were dissimilarities between the observed residual film on the stylus and sample surface. The EDX spectra were nominally the same for the residual film the worn contact areas observed on the sample however on the stylus the film was not present in the centre of the contact. This is most likely to be due to the curved geometry of the stylus allowing the film to be pushed out of the contact area. The chlorine was clearly contributed by the ionic liquid; the silicon however must have been introduced by the iron silicate

peening. The greater silicon content in the residual film would appear to indicate that a chemical interaction has occurred that concentrates silicon from the sample surface into the residual film.

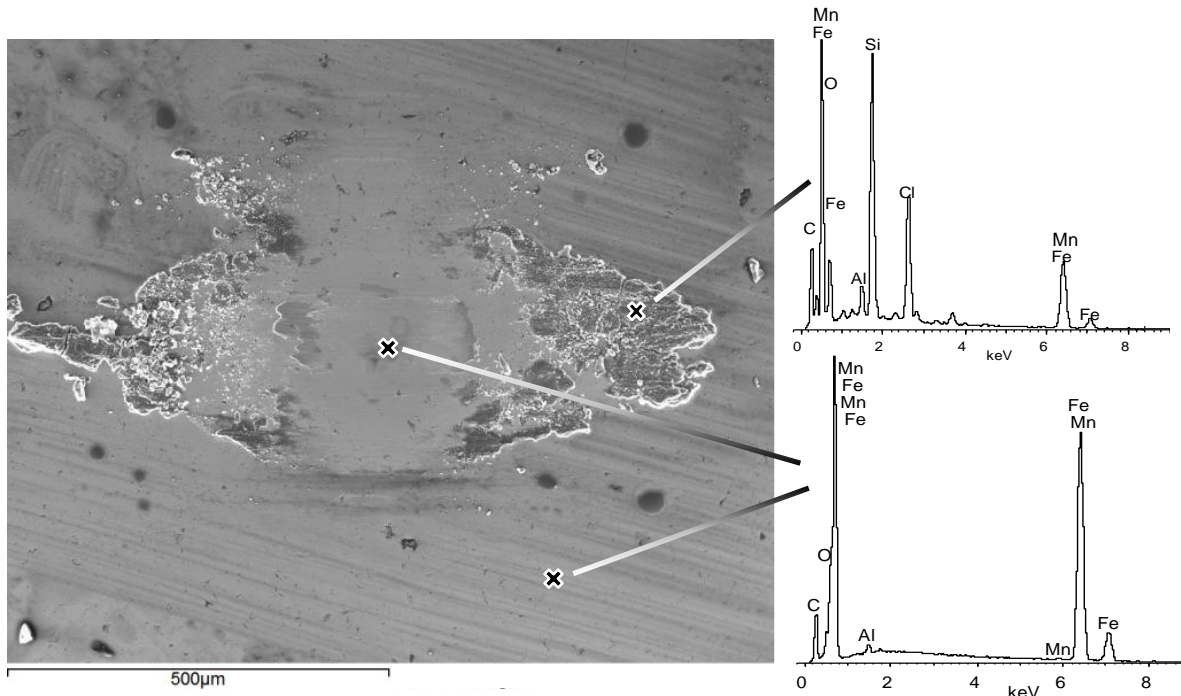


Figure 8.5 – SEM image and EDX spectra of the stylus face after testing with reline ionic liquid on iron-silicate peened surface texture. Spectra of indicated areas.

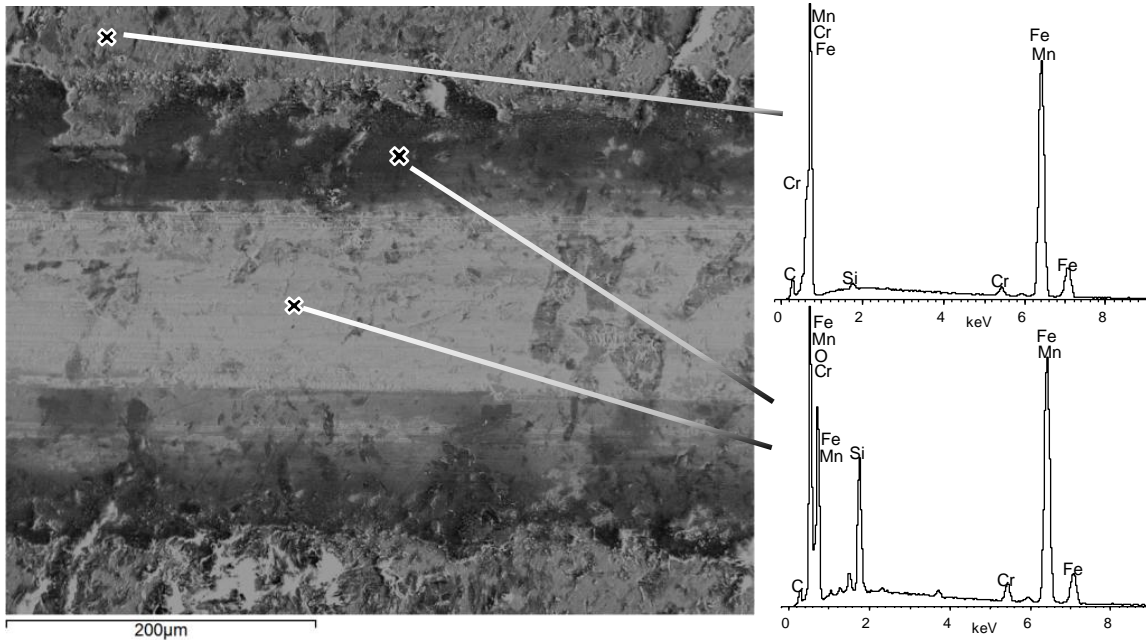


Figure 8.6 - SEM image and EDX spectra of the wear track on the sample surface after testing with reline ionic liquid on iron-silicate peened surface texture. Spectra of indicated areas.

### 8.3 Conclusions and future work

This study has shown that the ionic liquids investigated here can provide a low friction coefficient when used to lubricate a steel/steel contact, comparable to that of SAE engine oil. The ionic liquids are not however retained within the contact as well as engine oil and lubricant loss was observed to occur in most instances after relatively short sliding distances. The reline ionic liquid lubrication has been observed to be more easily sustained during sliding wear, with greater mean and maximum sliding distance for all test configurations. This was likely due in part to its higher viscosity compared to the ethaline ionic liquid, and is in contrast to its lower affinity to the surface as qualitatively determined by a modified sessile drop test. The improved lubricant retention of reline ionic liquid over ethaline ionic liquid was most pronounced at high sliding speed and low applied load where lubrication retention appeared comparable to that of SAE 5W30 engine oil. It has also been observed that the retention of lubrication was affected by surface texture and that there was an apparent increase in lubricant retention with increase in surface area ratio, as obtained by AFM. Lubricant retention was highly variable and even for the best ionic liquid/surface texture pairing very early lubricant loss still occurred in some instances.

Also it has been seen that a residual film forms during sliding wear tests of reline ionic liquid on iron silicate peened surfaces. This film has been identified by EDX analysis to have a concentration of chlorine and silicon that was not observed elsewhere on the sample or the stylus surfaces. The residual chlorine will have been from the ionic liquid and it would appear that the silicon is introduced by the iron silicate peening process and concentrated by the chemical formation of the residual film. The build up of the residual film was thickest in sliding tests where the ionic liquid was well retained and lubricant loss occurred after a large sliding distance. It is unclear if the residual film was beneficial to lubrication or if it merely developed with extended periods of sliding.

This study has looked at application of ionic liquids that are not chemically tailored to steel lubrication, and found that low friction coefficients and moderate periods of lubrication are possible. A consideration for future development is the chemical functionalising of the steel surfaces in order to promote ionic liquid retention. In this way ionic liquids could be tailored to the contact that they are to lubricate. For example

activation and functionalisation of the steel surface could be achieved in a two step process: firstly removal of surface oxide by etching or chemical pickling. In a second step the steel surface could be exposed to a single activated component of the binary liquid, binding that component to the surface of the etched steel. Exposure of this functionalised surface to the second (native) component of the binary liquid would then result in a spontaneous assembly of a layer of ionic liquid lubricant directly attached to the bearing surface. In the case of choline based binary liquids there are many chemical functionalities on either components of the binary mixture that can facilitate the desired chemical activation. The concept of spontaneous self-assembly of mono-layers and bi-layers is well known in a variety of other contexts but application here would offer a significant advantage over other strategies for surface wetting of the bearing surface with lubricant. The durability of functionalised surfaces is always a practical concern but here the self-assembled lubricant layer would serve mainly as a mechanism for lowering interfacial surface tension (*i.e.* improving surface wetting) rather than as a part of the physical load-bearing lubricant layer.

With further long-term investigation into these areas, ionic liquid lubrication is likely to develop greatly. In time development of ionic liquid lubrication may offer a new generation of lubricants with very different chemistries, potentially solving the current issues surrounding the chemistry of oil additives and their interaction with catalytic converters discussed in chapter 1.

---

---

#### 8.4 Chapter references

- 1 T., W. Room-Temperature Ionic Liquids - Solvents for Synthesis and Catalysis. *Chemistry Review*, 1999, **99**(8), 2071.
- 2 Earle, M.J. and Seddon, K.R. Ionic liquids- Green solvents for the future. *Pure Applied Chemistry*, 2000, **72**(7), 1391-1398.
- 3 Ohno H., E.A.o.I.L., Wiley-Interscience (2005),. *Electrochemical Aspects of Ionic Liquids*. In Ohno, H., ed. *Electrochemical Aspects of Ionic Liquids* (Wiley InterScience, 2005).
- 4 Wasserscheid, P. and Keim, W. Ionic liquids—new “solutions” for transition metal catalysis. *Angew. Chem. Int. Ed*, 2000, **39**(21), 3773.
- 5 Abbott, A.P., Capper, G. and Shikotra, P. Processing Metal Oxides Using Ionic Liquids. *Transactions of the Institution of Mining and Metallurgy, Section C*, 2006, **115**(1), 15-18.
- 6 Abbott, A.P., Bell, T., Handa, S. and Stoddart, B. Cationic Functionalisation of cellulose using ionic liquids. *Green Chemistry*, 2006, **8**, 784-786.
- 7 Abbott, A.P. and McKenzie, K.J. Electrodeposition of Metals using Ionic Liquids. *Physical Chemistry Chemical Physics*, 2006, **8**(37), 4265-4279.
- 8 Abbott, A.P., Capper, G., McKenzie, K.J. and Obi, S.U. Solubility of Metal Oxides in Deep Eutectic Solvents Based on Choline Chloride. *Journal of Chemical and Engineering Data*, 2006, **51**, 1280-1282.
- 9 Abbott, A.P., Capper, G., McKenzie, K.J. and Ryder, K.S. Electrodeposition of Zinc Tin Alloys from Deep Eutectic Solvents Based on Choline Chloride. *Journal of Electroanalytical Chemistry*, 2007, **599**, 288.
- 10 Abbott, A.P., Nandhra, S., Ryder, K.S. and Smith, E. Electroless Deposition of Metallic Silver from a Choline Chloride Based Ionic Liquid: A Study Using Acoustic Impedance Spectroscopy, SEM and Atomic Force Microscopy. *Physical Chemistry Chemical Physics*, 2007, **9**, 3735-3743.
- 11 Bhatt, A.I., Bond, A.M. and Zhang, J. Electrodeposition of lead on glassy carbon and mercury film electrodes from a distillable room temperature ionic liquid - DIMCARB. *Journal of Solid State Electrochemistry*, 2007, **11**, 1593.
- 12 Ye, C., Liu, W., Chen, Y. and Yu, L. Room-temperature ionic liquids: a novel versatile lubricant. *Chem Commun*, 2001, **21**, 2244-2245.
- 13 Reich, R.A., Stewart, P.A., Bohaychick, J., Urbanski, J.A.: Base oil properties of ionic Liquids. *Lubrication Engineering*, 2003, **59** (16-21).

- 14 Wang, H., Lua, Q., Ye, C., Liu, Q. and Cui, Z. Friction and wear behaviors of ionic liquid of alkylimidazolium hexafluorophosphates as lubricants for steel/steel contact. *Wear*, 2004, **256**, 48-48.
- 15 Liu, W., Ye, C., Gong, Q., Wang, H. and Wang, P. Tribological performance of room-temperature ionic liquids as lubricant. *Tribology letters*, 2002, **13**, 81-85.
- 16 Yu, G., Zhou, F., Liu, W., Liang, Y. and Yan, S. Preparation of functional ionic liquids and tribological investigation of their ultra-thin films. *Wear*, 2006, **260**(9-10), 1076-1080.
- 17 Abbott, A.P. and Macfarlane, D.R. Electrodeposition in Ionic Liquids. In Endres, F., ed (Wiley-VCH Weinheim, 2008), ISBN: 978-3-527-31565-9
- 18 Abbott, A.P., Barron, J.C., Elhadi, M., Frisch, G., Gurman, S.J., Hillman, A.R., Smith, E.L., Mohamoud, M.A. and Ryder, K.S. Electrolytic metal coatings and metal finishing using ionic liquids. *Electrochemical Society Transactions*, 2008, **16**(36), 47
- 19 Abbott, A.P., Harris, R.C. and Ryder, K.S., Application of hole theory to define ionic liquids by their transport properties, *Journal of Chemical Physics, B*, 2007, **111**, 4910.
- 20 Abbott, A.P., Capper, G., Davies, D.L., Rasheed, R.K. and Tambyrajah, V. Novel solvent properties of choline chloride/urea mixture. *Chem Commun*, 2003, **1**(70-71),
- 21 Abbott, A.P. Application of Hole Theory to the Viscosity of Ionic and Molecular Liquids. *Chemical Physical Chemistry*, 2004, **5**, 1242.

# CHAPTER 9

## Conclusions

---

### 9. Conclusions

#### 9.1 In Summary

#### 9.2 Findings and implications

#### 9.3 Future work

---

#### 9.1 In summary

This research has covered the investigation of thin-film coatings; diamond-like carbon (DLC) and carbon nitride (CN<sub>x</sub>); alongside ionic liquid as novel lubricants, in an effort to establish the efficacy of these approaches at reducing friction and wear in the valve-train. The technologies under investigation in this research have been selected for their potential to alleviate the need for present oil-additive based friction and wear reduction techniques, which can compromise catalytic converter effectiveness and increase harmful vehicle emissions.

The study of the DLC coatings has been focused on determining the potential friction reduction that these coatings offer and the mechanical and tribological properties that are key to effective performance in the demanding environment of the valve-train. CN<sub>x</sub> coatings were investigated as coatings can be deposited that have fullerene-like microstructures, and exhibit a combination of high hardness and low elastic modulus. They offer the opportunity to explore the role that  $H/E$  ratio plays in determining coating durability. Ionic liquids are a novel lubricant chemistry, very different from traditional mineral and synthetic oil based lubricants. The ionic liquids considered in this study are deep eutectic solvents that form viscous liquids stable at high temperatures such as those experienced in highly loaded contacts. They offer interesting possibilities in terms of fine tuning viscosity and pairing lubricant chemistries with surface treatments in order to aid lubricant retention. What follows is

---

a discussion of the major findings of this work, their implications and potential areas of future work.

## 9.2 Findings and implications

The research conducted here has demonstrated that by application of DLC coatings a friction reduction of the order of 10% is achievable in most circumstances. It has also been seen that a friction reduction of 55% was possible for a tungsten doped DLC coating on a well polished substrate. The durability of such coatings is still in question, with the low friction tungsten doped coating in particular showing very low durability in the valve-train testing. However early tests have revealed some examples of good durability and have helped to demonstrate a number of coating properties that are important factors in determining valve-train performance, namely adhesion, hardness, abrasive wear resistance and impact toughness. Using this information as a guide, future coating development for valve-train applications could lead to improved durability whilst maintaining major improvements in friction. The work conducted here has only been able to assess a small proportion of the diverse selection of thin-film coatings available. Further study into a wider range of available coatings will improve understanding of what is required of a coating for valve-train application. Another highlight of this study has been the importance of surface finish in determining friction in the valve-train. Surface finishing techniques such as honing, polishing and lapping can be used to produce surfaces with very low roughness, dramatically reducing the frictional force generated by sliding against the surface. So called super-finishing techniques are a competing approach to thin-film deposition for the provision of low-friction and low-wear surfaces in the automotive engine and much research is also being conducted into their effectiveness and economy. This study had not considered finishing approaches in detail. The finishes investigated here have been selected to assess the ideal finish for coating adhesion and durability. However it is worth considering that these methods are not exclusive. As described earlier, in section 6.2, the thin-films studied in this research are themselves very smooth and tend to reproduce the surface upon which they are deposited. Therefore super-finishing techniques and thin-film coatings can be additive, and indeed this study has shown the potentially vast gains that can be made from employing these two mutually beneficial techniques with a friction reduction of ~55% from a-C:H:W/Pol samples.

Carbon nitride (CN<sub>x</sub>) coatings with a fullerene-like structure were studied to assess the effect of a high  $H/E$  ratio on coating performance. The CN<sub>x</sub> coatings showed very low durability in the valve-train compared to the DLC coatings investigated, but were also approximately an order of magnitude thinner and relatively poorly adhered. For experimental coatings with poor adhesion they demonstrated some capability, and showed the potential benefit of a high value of  $H/E$ . Further development of CN<sub>x</sub> coatings on steel substrates is required to really understand the benefit of higher values of  $H/E$ .

Alongside the investigation of thin film coatings, this research has also investigated ionic liquids as a novel lubrication medium. Other research into ionic liquid lubrication has tended to focus on the generation of lubrication mono-layers. This study however has dealt with ionic liquid lubrication in the more traditional sense of a reservoir of liquid, a proportion of which is entrapped in contacts and provides lubrication. The findings showed that these ionic liquid lubricants can provide a very low friction coefficient between steel surfaces, but suffer from poor retention in the contact compared to commercial engine oil. This retention was improved by increasing the surface area of the component finish. Ionic liquids offer a great deal of promise for development of future lubricants. The novel chemistry of the ionic liquids offers a number of interesting possibilities in terms of lubricant design. The viscosities of ionic liquids are highly dependent on the composition and proportion of cations to anions in the solution and can be carefully tailored. There also exists the possibility of altering surface chemistries and promoting ionic liquid and surface interactions. In this way designer ionic liquids which are well adhered to component surfaces and tailored to suit wear conditions could represent a new field of lubrication. Again, this area of research does not stand alone as an approach for improving the lubrication of the valve-train or automotive contacts in general, offering the potential of ionic liquids designed to work with functionalised thin-film coated surfaces.

### 9.3 Future work

The work conducted here will hopefully be only the start of a systematic study of these thin-film coating technologies and their automotive applications. DLC as a technique will benefit in particular from a concentrated and systematic investigation of a number of possible engine applications and a determination of the mechanical and tribological properties that are suited for each. The future of DLC as an automotive coating is far from assured but as illustrated in this work the potential benefits are tremendous. Likewise  $CN_x$  coatings offer many potential advantages. Currently their development for engineering substrates, such as steel, is at an early stage and improvements are needed in terms of coating thickness, residual stresses and adhesion before they can hope to compete with techniques such as DLC. These advances will most likely come from development and sophistication of coating interlayer techniques. It should be noted that in order to achieve real progress in the application of these thin-films to the automotive engine it will be necessary to develop both coatings and application in concert. Only with synergistic design will it be possible to use coatings to their full advantage whilst minimising their potential failings. Impact loading in the valve-train is a primary example of this, by making use of existing techniques such as hydraulic dashpot tappets, it may be possible to effectively eliminate impact and improve coating durability.

This study of ionic liquid lubrication has barely scratched the surface of the subject. The tuneable nature of ionic liquids and the possibilities for surface functionalising offer a great many opportunities for investigation. What is needed now however is a more fundamental rationalisation of their properties as lubricants: their chemical interaction with component surfaces, both functionalised and unfunctionalised; the evolution of their properties in the challenging environment of a tribological contact and the range of operating conditions over which they may be applied. With an improved understanding of their operation, ionic liquids could become a viable alternative to oil based lubricants for specialised tribological applications.

To conclude, the importance of reducing engine losses to friction cannot be ignored. A reduction in frictional losses in the valve-train of a moderate 10% would make for an overall reduction in  $CO_2$  emissions in the UK of  $\sim 0.11\%$ , and if these principles could be extended to the commercial vehicles and public sector transport, then this could be

increased to ~0.17%. While these values appear small they would account for some ~0.57 and ~0.97 million tonnes annual CO<sub>2</sub> emission, respectively, based on 2005 CO<sub>2</sub> emissions [Source: [DEFRA](#), published [2007-01-31](#)]. The novel technologies investigated here have the potential to be an important part of achieving that goal.